Plasma Physics Reports, Vol. 26, No. 12, 2000, pp. 1000–1004. From Fizika Plazmy, Vol. 26, No. 12, 2000, pp. 1068–1073.

TOKAMAKS

ECE Measurements via B–X–O Mode Conversion: A Proposal to Diagnose the *q* Profile in Spherical Tokamaks[1]

V. F. Shevchenko

EURATOM/UKAEA Fusion Association, Culham Science Centre, Abingdon, OX14 3DB, UK

Received March 31, 2000

Abstract—Generation of electron Bernstein waves by the ordinary–extraordinary–Bernstein (O–X–B) mode conversion process has been successfully demonstrated on W7-AS. According to Kirchoff's law, the inverse process of plasma EC emission by B–X–O mode conversion at particular angles must take place in tokamak plasmas. The optical depth at electron cyclotron harmonics is generally very high for electron Bernstein waves in tokamak plasmas. Consequently the O-mode ECE spectrum measured below the plasma frequency will show steps in the emitted power when each EC harmonic coincides with the upper hybrid resonance zone, where the mode conversion occurs, giving a local measurement of the relationship between the total magnetic field and plasma density. In a spherical tokamak, there are several EC harmonics below the plasma frequency, so several such steps can be observed via the B–X–O mode conversion mechanism. This is a very promising way to get information about the *q* profile in ST plasmas. © *2000 MAIK "Nauka/Interperiodica".*

1. INTRODUCTION

The topology of plasma cut-offs and resonances in spherical tokamaks (STs) is quite different from the corresponding topologies in conventional tokamaks and stellarators (see Fig. 1). The main reason for this difference is the relatively low magnetic field used for plasma confinement in STs. As a result, in the bulk ST plasma, the electron cyclotron (EC) frequency ω_{ce} is usually an order of magnitude less than the plasma frequency ω_{pe}.

Obviously such a plasma is unable to exhibit significant electron cyclotron emission (ECE) or absorption in the framework of the conventional theory of ECE in tokamaks [1]. Indeed, the first few harmonics (up to the tenth) of ω_{ce} are usually trapped by cut-offs in the bulk plasma while the rest of them, which are not trapped, have too low an optical depth to be able to emit or absorb useful power. This situation is quite typical, and makes conventional methods of ECE diagnostics and electron cyclotron resonance heating (ECRH), difficult in STs with high-density plasmas.

There is, however, another possibility that might be used for plasma heating and diagnostic applications in STs. This possibility is based on the linear mode conversion mechanism between the electron Bernstein mode and the electromagnetic extraordinary (X) mode at the upper hybrid resonance (UHR). Via this conversion mechanism, the energy from the vacuum electromagnetic waves can be transferred to the electron Bernstein waves (EBWs) in order to heat the central layers of the plasma. Conversely, the energy from the electrostatic EBWs can be transferred to electromagnetic waves, which are able to leave the plasma, so carrying information about internal plasma layers. EBWs have no high-density cut-off and can propagate across the dense plasma experiencing a cut-off only at the UHR surface, where they can be either reflected back or, under particular conditions, the converted into the X-mode. EBWs are strongly absorbed near EC resonance layers at both the fundamental resonance and its higher harmonics. This makes them a very promising object for fusion plasma diagnostics.

There are two ways, in practice, of realizing the mode conversion mechanism in ST plasmas. The first way is the ordinary–extraordinary–Bernstein (O–X–B) mode conversion process originally proposed for plasma heating by J. Preinhaelter and V. Kopecký [2]. Experimentally the O–X–B mode conversion scheme has been successfully demonstrated on the W7-AS stellarator by Laqua *et al.* [3].

The second way is based on a direct tunnelling of the X-mode launched from the low-field side through the evanescent layer between the low-density right-hand R-cut-off and the UHR [4]. Obviously, this process can only be efficient with a narrow evanescent layer which requires a steep density gradient at the plasma edge.

At present, both schemes of mode conversion are being discussed as candidates for plasma heating and current drive in magnetically confined plasmas [3–6]. According to Kirchhoff's law, the inverse process of plasma EC emission by B–X–O or B–X mode conversion must take place in tokamak plasmas. In this paper, we consider the mode conversion processes as mechanisms giving new opportunities for plasma diagnostics in STs. Section 2 is devoted to calculations of the mode conversion efficiency. We compare some theoretical

[1] This article was submitted by the author in English.

1063-780X/00/2612-1000$20.00 © 2000 MAIK "Nauka/Interperiodica"

ideas about Bernstein mode properties and linear mode conversion processes in tokamak plasmas. Section 3 is concerned with the analysis of EC spectra emitted by high-density plasmas and their possible applications for plasma diagnostics. A summary and conclusions are given in Section 4.

2. LINEAR MODE CONVERSION IN TOKAMAK PLASMAS

As mentioned above, there are two interesting conversion mechanisms allowing Bernstein waves to leave the bulk plasma by being converted into electromagnetic waves. These waves can be detected and analyzed from the low-field side of the plasma. First, we will consider the conditions required for a high efficiency of the O–X–B mode conversion process.

The essential part of this process is the conversion of the O-wave launched from the low-field side near an optimum angle into the X-wave. Let us consider a slab geometry and suppose that the plasma density gradient defines the x-direction of a coordinate system, while the magnetic field defines the y-axis. At normal incidence, when the wave vector is parallel to the density gradient, an electromagnetic wave of ordinary polarization cannot penetrate further than the critical layer at $X = 1$, where

$$X = \frac{\omega_{pe}^2}{\omega^2}.$$

Here, ω_{pe} is a plasma frequency, and ω is the frequency of the wave. When an obliquely incident wave penetrates into the plasma, it is refracted. The critical angle θ_{cr} of incidence from vacuum is the angle for which, the wave vector at the reflection point ($X = 1$) is exactly parallel to the magnetic field [7]. From the plasma dispersion relation we know that, if the direction of the wave vector approaches the direction of the magnetic field, the O-mode cut-off is degenerate with the high-density X-mode left-hand L-cut-off, and the reflection point jumps discontinuously from $X = 1$ to $X = 1 + Y$ with:

$$Y = \frac{\omega_{ce}}{\omega},$$

where ω_{ce} is the EC frequency. Thus it is clear that, at the critical angle of incidence, the O-wave is not reflected at the level $X = 1$ but, at that point, as it is propagating parallel to the magnetic field, it can be identified with the circularly polarized left-hand mode. On further propagation, it is converted into the X-mode without having passed a region of evanescence. According to Snell's law, the y-component of the index of refraction η_y does not change during wave propagation through the plasma. This means that the wave vector component parallel to the magnetic field remains constant from the plasma edge to the $X = 1$ layer, and

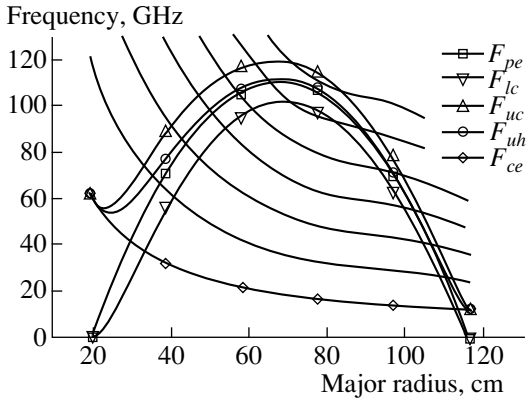

Fig. 1. The topology of resonant and cut-off frequencies for the MAST plasma: $n_{e0} = 1.5 \times 10^{20}$ m^{-3}, $B_0 = 0.63$ T, and $I_p = 0.5$ MA; parabolic density profile.

θ_{cr} can be identified with the angle of incidence from vacuum [7]:

$$\sin\theta_{cr} = \eta_{y,cr} = \left(\frac{Y}{1+Y}\right)^{1/2}. \quad (1)$$

For non-critical angles of incidence, an evanescent region always exists near the cut-off layer. The thickness of the evanescent barrier depends on the density scale length $L_n = n_e/(\partial n_e/\partial x)$, and a considerable fraction of the incident power can tunnel through this barrier when L_n becomes small. The power transmission function can be written as [5]

$$T = \exp\left\{-\pi\frac{\omega}{c}L_n\sqrt{\frac{Y}{2}}[2(1+Y)(\eta_{y,cr}-\eta_y)^2 + \eta_z^2]\right\}. \quad (2)$$

After O–X conversion, the X-mode propagates to the UHR layer, where it is totally converted into an EBW. The O–X–B conversion efficiency [see Eq. (2)] has been estimated for different launching angles and plotted as a function of frequency in Fig. 2. At the optimum angle for a particular frequency, the efficiency is close to 100%, but away from the optimum, it shows an exponential decrease. In terms of the angular deviation from the optimum angle, the condition for significant mode conversion can be written as

$$\pi\frac{\omega}{c}L_n\sqrt{\frac{Y}{2}}[2(1+Y)\delta\theta_y^2 + \delta\theta_z^2] \le 1, \quad (3)$$

where $\delta\theta_y$ is the angular deviation in the (x, y) plane and $\delta\theta_z$ is the deviation in the (x, z) plane. For a MAST plasma with a parabolic density profile, this condition defines the elliptical angular cone of efficient mode conversion with $\delta\theta_y = \pm 3.7°$ and $\delta\theta_z = \pm 5.6°$ for 60 GHz. Selecting the launching or viewing angle of ~22°, which is optimal for 80 GHz, one can expect more than 40% O–X–B conversion efficiency in the frequency range up to 100 GHz.

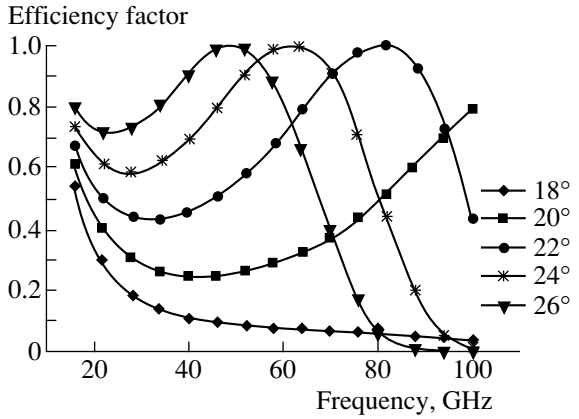

Fig. 2. B–X–O conversion efficiency for different viewing angles (MAST plasma): $n_{e0} = 1.5 \times 10^{20}$ m^{-3}, $B_0 = 0.63$ T, and $I_p = 0.5$ MA; parabolic density profile.

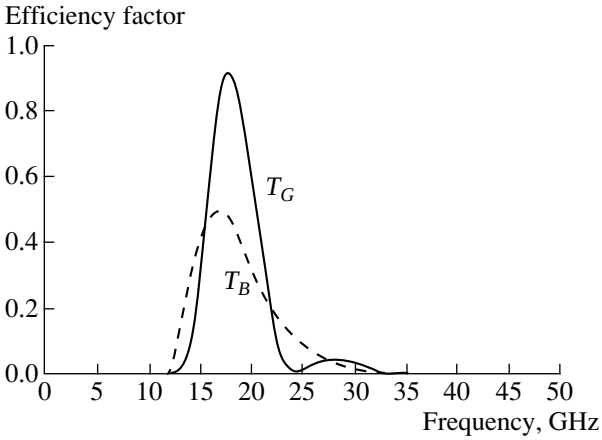

Fig. 3. B–X mode conversion efficiency for the MAST plasma: $n_{e0} = 1.5 \times 10^{20}$ m^{-3}, $B_0 = 0.63$ T, and $I_p = 0.5$ MA; parabolic density profile.

Another scheme of linear mode conversion in a tokamak plasma involves the direct coupling of an externally launched X-mode with the electrostatic Bernstein mode. This coupling mechanism is known as Budden tunnelling [8]. According to Budden's theory, the total conversion efficiency from the X-mode to the Bernstein mode can be written as [4]

$$T_B = 2e^{-\delta}(1 - e^{-\delta}), \tag{4}$$

where δ is the Budden parameter, which is proportional to $(\omega/c)L_N$. This result includes both the transmission of the low-density X-mode directly to the Bernstein mode and the transmission of the high-density X-mode, reflected back from the L-cut-off layer, to the Bernstein mode. It does not include the interference effect between high-density and low-density X-modes, so can only be applied for a strongly fluctuating plasma, when interference is not important.

The conversion efficiency of the X–B tunnelling including interference can be written in the form [7]

$$T_G = 4e^{-\delta}(1 - e^{-\delta})\sin^2\varphi, \tag{5}$$

where

$$\delta = 4\frac{\omega}{c}L_n Y^{3/2}(1 - Y)(1 + Y)^{1/2} \times \int_0^1 \sqrt{(1 - t^2)\left(1 + \frac{1 - Y}{1 + Y}t^2\right)}\,dt \tag{6}$$

and

$$\varphi = 2\frac{\omega}{c}L_n Y^{3/2}(1 + Y)(1 - Y)^{1/2} \times \int_0^1 \sqrt{(1 - t^2)\left(1 + \frac{1 + Y}{1 - Y}t^2\right)}\,dt. \tag{7}$$

From the comparison of Eqs. (4) and (5), it is easy to conclude that the interference adds an oscillating factor to the Budden conversion efficiency and increases the maximum conversion efficiency by a factor of 2. We have evaluated the phase coefficients (6) and (7) numerically for the typical plasma parameters in the MAST tokamak [9]. Both efficiencies T_B and T_G are plotted in Fig. 3. In a real plasma, the efficiency will lie between these two extremes, as the cut-off surfaces can be perturbed from nearly parallel, which is ideal for the interference regime, to totally inclined to the converted wave, which is appropriate to the Budden case. These events can be caused by either MHD activity or plasma fluctuations.

So far, we have considered conversion mechanisms, supposing that electromagnetic waves are launched into the plasma from outside and then converted into EBWs. However the inverse processes will also occur. EBWs undergo strong EC collisionless damping near resonant surfaces corresponding to the EC frequency and its harmonics [6, 10, 11], transferring all the wave energy to the plasma electrons. Conversely, in a hot plasma, EBWs will be generated by electrons near the resonant surfaces. Waves with appropriate values of η_y and η_z then will be sequentially converted into the high-density X-mode and then into the O-mode propagating from the plasma close to the critical angle. EBWs which propagate in the direction of the density gradient will be converted directly into the low-density X-mode leaving from the plasma.

3. EBW SPECTRUM IN A SPHERICAL TOKAMAK

Let us consider the EBW radiation emitted from the interior of the plasma and estimate its spectrum as it arrives at the UHR layer, viewed from the low-field side. We suppose that all EC harmonics enclosed by the

O-mode cut-off surface are totally black for EBW; i.e., each separate resonant surface emits and absorbs power as an absolutely black body. With such an assumption, each higher harmonic will partially shadow the previous one (Fig. 1). The resultant radiation shows a sawtooth-like spectrum with emissivity gradually rising with frequency (see Fig. 4). However, EBW radiation is unable to leave the plasma because of its electrostatic nature.

EBWs can escape through a small angular window determined by the B–X–O mode conversion mechanism. Thus, the ordinary polarized emission of the ST plasma will be mainly determined by the EBW spectrum multiplied by the B–X–O conversion efficiency (see Fig. 2). It is easy to see from condition (3) that the emission cone about the critical angle is narrower at higher frequencies, so the viewing angle must be chosen close to the critical angle for the highest frequency expected in the spectrum.

The extraordinary polarized emission of the ST plasma is determined by the EBW spectrum multiplied by the B–X conversion efficiency (see Fig. 3). Via the B–X conversion mechanism, EBWs most effectively transmit their energy to the X-polarized waves propagating in the direction of the density gradient. The X-mode power spectrum emitted by the plasma will have a well defined resonant structure that is mainly sensitive to the density gradient (see experiment [12]). Only the low-frequency part of the EBW spectrum can reach the outside plasma layers via B–X conversion, which makes O-mode observations more suitable for EBW spectrum studies in ST plasmas.

Obviously, the model considered above is rather simplified because it assumes all emission to be generated near the EC harmonic layers. As was shown by S. Pešić [10] (see also references therein), collisionless EC damping of EBWs is strongly dependent on the angle between the wave vector and the plasma density gradient and, in toroidal geometry, the damping region can appear away from the EC resonant position. Only for the propagation directions nearly parallel to the density gradient, the waves are completely absorbed in the vicinity of the resonant layer. On the other hand, in low-temperature plasmas ($T_e \le 10$ eV), collisional wave absorption near the UHR is strong, and the emission spectrum is predominantly determined by the UHR layer rather than EC harmonics. Nevertheless, our simplified model allows us to make a qualitative analysis of the spectrum emitted by a relatively hot plasma and to find some relationships between plasma parameters and spectrum features.

From Figs. 1 and 4 it is clearly seen that jumps in the emissivity spectrum correspond to frequencies $\bar{\omega}_l$ that are defined by the coincidence of UHR and EC harmonic resonant layers in the plasma:

$$\bar{\omega}_l = l\omega_{ce}(x) = (\omega_{pe}^2(x) + \omega_{ce}^2(x))^{1/2}, \quad l = 2, 3, \ldots, \tag{8}$$

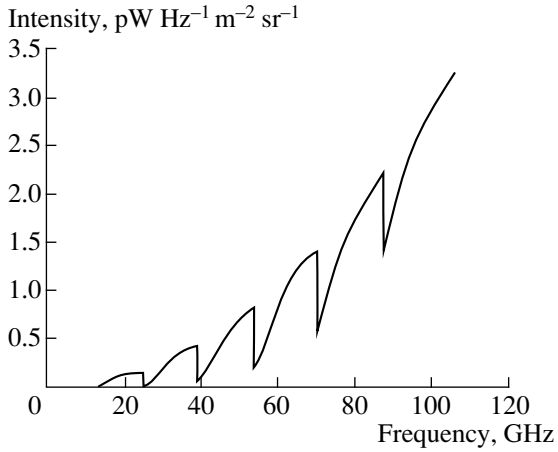

Fig. 4. EBW spectrum as it appears at the UHR for the MAST plasma: $n_{e0} = 1.5 \times 10^{20}$ m^{-3}, $B_0 = 0.63$ T, $I_p = 0.5$ MA, and $T_{e0} = 1$ keV.

where l is the number of the EC harmonic. In STs, it is possible to observe a number of such features in the emission spectrum. The central plasma frequency is typically one order of magnitude higher than the EC frequency, so one can expect up to ten jumps in the spectrum. O-mode plasma emission from STs can be measured rather precisely using a conventional ECE technique with a frequency scanning heterodyne source, with the antenna aligned at appropriate angles to the density gradient and magnetic field.

The measured spectrum gives us some important relationships between local plasma parameters. Indeed, for l measured frequencies $\bar{\omega}_l$ in the spectrum from Eq. (8) one can write l interrelations:

$$B(x_l) = \frac{m_e}{e}\frac{\bar{\omega}_l}{l}, \qquad n_e(x_l) = \varepsilon_0 \frac{m_e}{e^2}\left(1 - \frac{1}{l^2}\right)\bar{\omega}_l^2. \tag{9}$$

Here, B is the total magnetic field, x_l is the location where the lth EC harmonic and UHR coincide. Moreover, with measurements of power emitted by the plasma near spectral minima, one can estimate the electron temperature $T_e(x_l)$ at the same points, assuming that the plasma is absolutely black. It should be noted that, at the spectral minima, the point of the emission origination is strongly localized near the intersection of the UHR with the corresponding EC harmonic.

Thus, having one of the profiles $B(x)$, $n_e(x)$, or $T_e(x)$ measured with other diagnostic techniques, for example, $n_e(x)$ measured with reflectometry, one can recover the other two profiles for the low-field side of the plasma. These three profiles substantially determine the plasma equilibrium in tokamaks. Internal relationships (9) between local plasma parameters can be used as

additional constraints in plasma equilibrium reconstruction codes such as EFIT.

4. CONCLUSIONS

We have found that the EBW spectrum in STs has discrete jumps. The frequencies of these jumps are defined by the crossing of the UHR layer with EC harmonic layers. It was shown that the EBW spectrum can be measured via the B–X–O or B–X linear mode conversion mechanisms. These measurements give a set of local relationships between the most important plasma parameters $B(x)$, $n_e(x)$, and $T_e(x)$ at a number of points in the plasma. Using relations between these parameters and measurements with other diagnostics, one can localize these particular points in the plasma, making it possible to reconstruct any of the profiles $B(x)$, $n_e(x)$, or $T_e(x)$. The most efficient way of doing this would be to introduce these local relations into an equilibrium reconstruction code.

The complexity of the general theory of EBW propagation in a tokamak plasma makes it difficult to predict an exact angular behavior of the emission spectrum in the wide frequency range covering the higher EC harmonics. Nevertheless, the present analysis gives a qualitative picture of the emission and mode conversion processes in STs, allowing us to make an initial design of the experimental set-up for experimental studies of plasma emission.

ACKNOWLEDGMENTS

I would like to acknowledge useful discussions with Geoffrey Cunningham and Chris Lashmore-Devis. This work was jointly funded by the United Kingdom Department of Trade & Industry and EURATOM.

REFERENCES

1. M. Bornatici, Plasma Phys. **24**, 629 (1982).
2. J. Preinhaelter and V. Kopecký, J. Plasma Phys. **10**, 1 (1973).
3. H. P. Laqua, V. Erckmann, and H. J. Hartfuss, Phys. Rev. Lett. **78**, 3467 (1997).
4. S. Nakajima and H. Abe, Phys. Rev. A **38**, 4373 (1988).
5. E. Mjølhus, J. Plasma Phys. **31**, 7 (1984).
6. A. Montes and G. O. Ludwig, Plasma Phys. Controlled Fusion A **28**, 1765 (1986).
7. V. L. Ginzburg, *The Propagation of Electromagnetic Waves in Plasmas* (Nauka, Moscow, 1967; Pergamon, Oxford, 1970).
8. K. G. Budden, *Radio Waves in the Ionosphere* (Cambridge Univ. Press, Cambridge, 1961).
9. A. C. Darke, M. Cox, J. R. Harbar, *et al.*, in *Proceedings of the 16th Symposium on Fusion Energy, Champaign-Urbana, IL, 1995*, Vol. 2, p. 1456.
10. S. Pešić, Physica C (Amsterdam) **125**, 118 (1984).
11. R. A. Cairns and C. N. Lashmore-Davies, Phys. Plasmas (in press).
12. V. F. Shevchenko, in *Proceedings of the 27th EPS Conference on Controlled Fusion Plasma Physics, Budapest, 2000*, paper P3.120.

Plasma Physics Reports, Vol. 26, No. 12, 2000, pp. 1005–1014. Translated from Fizika Plazmy, Vol. 26, No. 12, 2000, pp. 1074–1085.

PARTICLE ACCELERATION

Effect of the Magnetic Field on the Resonant Particle Acceleration

S. V. Bulanov and A. S. Sakharov

Institute of General Physics, Russian Academy of Sciences, ul. Vavilova 38, Moscow, 117942 Russia

Received June 1, 2000; in final form, June 27, 2000

Abstract—The acceleration of charged particles trapped by a potential wave in a magnetic field is investigated as applied to the problem of the generation of fast particles in a laser plasma. The conditions for unlimited particle acceleration are determined, and the spectra of fast particles are found. *© 2000 MAIK "Nauka/Interperiodica".*

1. INTRODUCTION

It is known that a quasistatic magnetic field can violate the wave–particle resonance in a plasma. However, under certain conditions, the magnetic field can create a regime of so-called "unlimited" (without phase slippage) particle acceleration (surfotron acceleration) [1]. The situation in which the magnetic field strongly affects the acceleration of particles trapped by a potential wave is typical of space and laboratory plasmas [2, 3]. This circumstance gives rise to the wide scope of problems discussed in the literature. In this paper, attention is mainly focused on the influence of the magnetic field on the acceleration of charged particles in laser plasmas.

In the interaction of a relativistically strong electromagnetic wave (for a laser with the wavelength $\lambda = 1\ \mu m$, this corresponds to intensities $I \geq 10^{18}$ W/cm^2) with a plasma, the spontaneous magnetic field can be so high that it begins to strongly affect both the propagation of radiation [4] and the focusing of fast particles [5–9]. In [10], it was pointed out that the spontaneous magnetic field localized inside an electron vortex can violate plasma quasineutrality, which results in ion acceleration.

The generation of spontaneous magnetic fields in laser plasmas has been thoroughly studied analytically, numerically, and experimentally for both moderate [11, 12] and relativistic [4, 6, 7, 13–15] laser intensities. Quasistatic magnetic fields generated by super-high-power laser pulses possess a specific symmetry: the azimuthal magnetic field (perpendicular to the propagation direction of the laser pulse) vanishes at the axis, whereas the longitudinal magnetic field (parallel to the propagation direction of the laser pulse) generated by circularly polarized radiation due to the inverse Faraday effect (see [16]) is uniform. Charged particle acceleration occurs in the electric field of the space-charge waves. Space-charge waves propagating in the radial direction are generated in the self-focusing channel under the action of the ponderomotive force of laser radiation [17, 18] and magnetic field pressure [10]. In this case, the ions are accelerated in the direction perpendicular to the direction of the laser pulse propagation [17–19]. Behind the pulse, an electrostatic wake wave propagating in the longitudinal direction is excited [20]. This wave is responsible for the generation of fast electrons in a laser plasma.

The goal of this paper is to investigate the effect of spontaneous magnetic fields generated by a high-power laser radiation in a plasma on the charged particle acceleration. To describe charged particle motion, we use the approach that was developed by us in [21] and is based on the methods of the Lagrange mechanics on manifolds [22].

The paper is organized as follows. In Section 2, we derive the Lagrange equations for the motion of a charged particle trapped by a potential wave with a curved front in a nonuniform magnetic field and discuss the influence of the front curvature on the particle acceleration. In Section 3, we solve the problem of the motion of a particle trapped by a potential wave whose front has the shape of a surface of revolution and calculate the energy spectrum of the accelerated particles. In Section 4, we present a simple model describing the structure of a spontaneous magnetic field generated by a nonuniform flow of fast particles in a collisionless plasma. In Section 5, we consider particle acceleration by a strong potential wave in the vicinity of the null-plane of the magnetic field. In the Conclusion, the main results are summarized.

2. RESONANT ACCELERATION OF PARTICLES TRAPPED BY A POTENTIAL WAVE WITH A CURVED FRONT IN A MAGNETIC FIELD

2.1. $\mathbf{v} \times \mathbf{B}$ *Mechanism for Particle Acceleration*

The acceleration of charged particles in a magnetic field (which is also referred to as the $\mathbf{v} \times \mathbf{B}$ acceleration) is a fundamental phenomenon. The motion of charged particles trapped by a wave in a magnetic field has been studied in many papers (see, e.g., [1, 3, 21, 23–28]). In

1063-780X/00/2612-1005$20.00

[1], it was shown that, under certain conditions, a relativistic particle can pass over to the regime of unlimited acceleration.

The basic idea of the acceleration mechanism can be described as follows. In the frame of reference moving with the phase velocity of the wave V, the electric field directed along the wave front appears. The induced electric field is determined by a standard formula of the Lorentz transformation:

$$E = \beta \frac{B_\parallel}{(1-\beta^2)^{1/2}}, \quad (1)$$

where $\beta = V/c$ and $B_\parallel$ is the magnetic field component parallel to the wave front. The necessary condition for acceleration is that the particle must be trapped by the wave. The particle may be trapped due to either a regular electric field [1] or diffusion. In the latter case, the particle is localized in the vicinity of the shock wave front due to, e.g., scattering by turbulent pulsations of the magnetic field in a plasma. The diffusion mechanism for the particle trapping in the vicinity of the front of a collisionless shock wave is usually discussed in connection with the problem of charged-particle acceleration in space plasmas (see [3, 29]). It is easy to show that, for the particle to be trapped (confined), it is necessary that the component of the electric field perpendicular to the wave front, $E_\perp$, be large enough:

$$E_\perp > \frac{B_\parallel (v^2/c^2 - \beta^2)^{1/2}}{(1-\beta^2)}, \quad (2)$$

where v is the particle velocity. The condition for unlimited acceleration ($v \longrightarrow c$) is [1]

$$E_\perp > \frac{B_\parallel}{(1-\beta^2)^{1/2}}. \quad (3)$$

In this case, the energy of particle grows as $\mathcal{E} = eB_\parallel Vt/(1-\beta^2)^{1/2}$.

In a real situation, the front of the wave is always curved and its curvature changes with time. This refers equally to the wake plasma wave behind a short laser pulse [30], shock waves generated at the boundary of the self-focusing channel [31], and shock waves in space plasmas [3].

2.2. Equations of Motion

Let us consider the trajectories of particles accelerated by a strong potential wave with a curved front. The idea of the mathematical approach to the analysis of this problem was proposed in [21]. We assume that the wave front is a smooth surface whose shape and position are determined by a given function of time $S(\mathbf{r}, t) = 0$. This function is related to the structure of the electric field that affects the accelerated particle. We also assume that the wave propagates in a nonuniform magnetic field. To describe the charged particle motion, we use the methods of Lagrange mechanics. The Lagrange function L of a particle moving with relativistic velocity in the electric and magnetic fields, which can be expressed in terms of the electrostatic potential $\Phi(\mathbf{r}, t)$ and vector potential $\mathbf{A}(\mathbf{r}, t)$, has the form [32]

$$L = -mc^2\left(1 - \frac{v^2}{c^2}\right)^{1/2} + \frac{e}{c}(\mathbf{A}\cdot\mathbf{v}) - e\Phi. \quad (4)$$

Here m, e, and $\mathbf{v} \equiv \dot{\mathbf{r}}$ are the mass, charge, and velocity of the particle, respectively.

We introduce the curvilinear coordinates q_j with $j = 1$, 2, and 3, where q_1 is the coordinate along the normal to the surface and q_2 and q_3 are the coordinates along the surface. The particle motion is determined by the Lagrange function $L(q_i, \dot{q}_i, t)$, where $i = 1$, 2, and 3:

$$\frac{d}{dt}\frac{\partial L}{\partial \dot{q}_i} = \frac{\partial L}{\partial q_i}, \quad i = 1, 2, 3. \quad (5)$$

For the particle trapped by the wave, the coordinate q_1, which is a given function of time ($q_1 = q_1(t)$), determines the position of the wave front. The motion of a trapped particle along the front is described by the Lagrangian

$$L^*(q_2, q_3, \dot{q}_2, \dot{q}_3) = L(q_1(t), \dot{q}_1(t), q_2, q_3, \dot{q}_2, \dot{q}_3), \quad (6)$$

where $q_1(t)$ and $\dot{q}_1(t) = dq_1/dt$ are supposed to be known functions of time, $\dot{q}_2 = dq_2/dt$ and $\dot{q}_3 = dq_3/dt$. The corresponding system of Lagrange equations is

$$\frac{d}{dt}\frac{\partial L^*}{\partial \dot{q}_i} = \frac{\partial L^*}{\partial q_i}, \quad i = 2, 3. \quad (7)$$

In other words, we are dealing with a nonautonomous Lagrange system with holonomic constraints dependent on time [22].

Solving Eqs. (7), we find $q_2(t)$ and $q_3(t)$ as functions of time. Then, we substitute these dependences into Eq. (5) for $i = 1$

$$\frac{d}{dt}\frac{\partial L}{\partial \dot{q}_1} = \frac{\partial L}{\partial q_1} \quad (8)$$

with $L(q_i, \dot{q}_i, t)$ defined by expression (4) in order to prove for which parameters of the wave, magnetic field, and initial conditions Eq. (4) can be satisfied for the given $q_i(t)$. As a result, we obtain the condition for unlimited acceleration or estimate the maximum energy the particle gains if the trapping condition is violated during the acceleration.

2.3. Influence of the Curvature of the Wave Front

Let the position of the front be determined by the equation

$$S(\mathbf{r}, t) = x - Vt + \frac{\alpha y^2}{2} = 0, \quad (9)$$

where V is the propagation velocity of the wave and $\alpha = 1/R$ is the front curvature with R being the radius of curvature in the vicinity of $y = 0$. Further, we assume that the curvature is small so that $\alpha y \ll 1$. The magnetic field is assumed to be nonuniform in the x-direction:

$$\mathbf{B}(\mathbf{r}, t) = B_0\mathbf{e}_y - hy\mathbf{e}_x, \tag{10}$$

i.e., the magnetic field lines are parabolas. The ratio B_0/h is a characteristic spatial scale on which the magnetic field varies. The corresponding vector potential only has the component $A_z = -B_0x - hy^2/2$. It is worth noting that, for $h/B_0 = \alpha$, the wave front coincides with the isolines of the vector potential (the normal component of the magnetic field at the front equals zero). In this case, the equations of motion are somewhat simplified. For the configuration of the magnetic field and wave front under consideration, the Lagrangian L^* can be written as

$$L^*(y, z, \dot{y}, \dot{z}, t) = -\frac{eB_0}{c}\left(\left(Vt - \frac{\alpha y^2}{2}\right) + \frac{hy^2}{2B_0}\right)\dot{z} \tag{11}$$
$$- mc^2\left(1 - \beta^2\left(1 - \frac{2\alpha y\dot{y}}{V} + (1 + \alpha^2y^2)\frac{(\dot{y})^2}{V^2}\right) - \left(\frac{\dot{z}}{c}\right)^2\right)^{1/2}.$$

In the nonrelativistic case, this expression takes the form

$$L^*(y, z, \dot{y}, \dot{z}, t) = -\frac{eB_0}{c}\left(\left(Vt - \frac{\alpha y^2}{2}\right) + \frac{hy^2}{2B_0}\right)\dot{z} \tag{12}$$
$$+ \frac{m}{2}((V - \alpha y\dot{y})^2 + (\dot{y})^2 + (\dot{z})^2).$$

In the particular case of $\alpha = h/B_0$, we have

$$L^*(y, z, \dot{y}, \dot{z}, t) = -\frac{eB_0}{c}Vt\dot{z} \tag{13}$$
$$+ \frac{m}{2}((V - \alpha y\dot{y})^2 + (\dot{y})^2 + (\dot{z})^2).$$

2.4. Case of Straight Magnetic Field Lines

Let us assume that $h = 0$. Then, the Lagrange function L^* takes the form

$$L^*(y, z, \dot{y}, \dot{z}, t) = -\frac{eB_0}{c}\left(Vt - \frac{\alpha y^2}{2}\right)\dot{z} \tag{14}$$
$$- mc^2\left(1 - \beta^2\left(1 - \frac{2\alpha y\dot{y}}{V} + (1 + \alpha^2y^2)\frac{(\dot{y})^2}{V^2}\right) - \left(\frac{\dot{z}}{c}\right)^2\right)^{1/2}.$$

Since the configuration is uniform in the z-direction, the Lagrange function does not depend on the z-coordinate and the z-component of the generalized momentum is conserved:

$$P_z = m\left(\gamma\dot{z} - \Omega_c\left(Vt - \frac{\alpha}{2}y^2\right)\right) = \text{const}. \tag{15}$$

Here, $\Omega_c = eB_0/mc$ is the cyclotron frequency calculated for the magnetic field B_0 and $\gamma = \mathscr{E}/mc^2$ is the Lorenz factor of the particle, $\mathscr{E}$ being the particle energy.

For the initial conditions $y_0 = 0$ and $\dot{y}_0 = 0$, equations of motion (7) with the Lagrange function (14) have the solution

$$y^{(0)}(t) = 0, \quad \dot{y}^{(0)}(t) = 0, \tag{16}$$

$$\dot{z}^{(0)}(t) = c\frac{(1 - \beta^2)^{1/2}\beta\Omega_c t}{(1 + \beta^2\Omega^2t^2)^{1/2}}, \tag{17}$$

$$\gamma^{(0)}(t) = \left(\frac{1 + \beta^2\Omega_c^2t^2}{1 - \beta^2}\right)^{1/2}, \tag{18}$$

which is identical to that found in [1]. The particle remains at the parabola apex and is accelerated along the z-axis. In the limit $|\beta\Omega_c t| \gg 1$, the particle velocity along the z-axis is equal to $|\dot{z}^{(0)}| = c(1 - \beta^2)^{1/2}$ and the particle energy increases as $\mathscr{E}^{(0)} = |\beta\Omega_c t|/(1 - \beta^2)^{1/2}$.

For the initial conditions corresponding to $y_0 \neq 0$ and $\dot{y}_0 \neq 0$, we can represent the solution to the equations of motion in the form

$$\mathbf{r}(t) = \mathbf{r}^{(0)}(t) + \mathbf{r}^{(1)}(t) + \ldots, \tag{19}$$

where the ratio $|\mathbf{r}^{(1)}(t)|/|\mathbf{r}^{(0)}(t)|$ is assumed to be small compared to unity. The y-component of $\mathbf{r}^{(1)}(t)$ obeys the equation

$$\frac{d}{dt}\left(\gamma^{(0)}\frac{dy^{(1)}}{dt}\right) - \alpha\left(\frac{\Omega_c^2Vt}{\gamma^{(0)}} + V\frac{d\gamma^{(0)}}{dt}\right)y^{(1)} = 0, \tag{20}$$

where the function $\gamma^{(0)}(t)$ is given by expression (18). We see that the sign of the curvature α determines whether the solution (16)–(18) is stable or unstable.

In the nonrelativistic case, when $|\beta\Omega_c t| \ll 1$, the solution to Eq. (20) has the form

$$y^{(1)}(t) = y_0^{(1)}\frac{\Gamma(2/3)}{2^{1/3}}\left(\frac{t}{t_0}\right)^{1/2}Z_{-1/3}\left(\left(\frac{t}{t_0}\right)^{3/2}\right) \tag{21}$$
$$+ \dot{y}_0^{(1)}2^{1/3}\Gamma(4/3)(tt_0)^{1/2}Z_{1/3}\left(\left(\frac{t}{t_0}\right)^{3/2}\right),$$

where $\Gamma(x)$ is the gamma function, $Z_\nu(x)$ is a Bessel function, $y_0^{(1)}$ and $\dot{y}_0^{(1)}$ are the initial values of the displacement and velocity along the y-axis, and t_0 is

$$t_0 = -\left(\frac{3}{2}\right)^{2/3}(\alpha\Omega_c^2V)^{-1/3}. \tag{22}$$

For $\alpha < 0$ (concave front) in the limit $t \longrightarrow \infty$, expression (21) yields

$$y^{(1)}(t) \approx \left(\frac{t_0}{t}\right)^{1/4}\left(\left(y_0^{(1)}\frac{\Gamma(2/3)}{2^{1/3}}\cos\left(\left(\frac{t}{t_0}\right)^{3/2}-\frac{\pi}{12}\right)\right)\right.$$
$$\left.+\dot{y}_0^{(1)}2^{1/3}\Gamma(4/3)t_0\cos\left(\left(\frac{t}{t_0}\right)^{3/2}-\frac{5\pi}{12}\right)\right). \quad (23)$$

It follows from here that the particle is localized near the plane $y = 0$.

For $\alpha > 0$ (convex front) in the limit $t \longrightarrow \infty$, expression (21) yields

$$y^{(1)}(t) \approx \left(y_0^{(1)}\frac{\Gamma(2/3)}{2^{1/3}}+\dot{y}_0^{(1)}2^{1/3}\Gamma(4/3)|t_0|\right)\left(\frac{t_0}{t}\right)^{1/4}$$
$$\times\exp\left(\left(\frac{t}{|t_0|}\right)^{3/2}\right). \quad (24)$$

We see that, for $\alpha > 0$, the solution $y = 0$ is unstable.

In the ultrarelativistic limit, we have $\gamma = \beta\Omega_c t/(1-\beta^2)^{1/2}$ and the solution to Eq. (20) can be expressed in terms of zero-order Bessel functions $Z_0((t/t_1)^{1/2})$ with

$$t_1 = -\frac{\beta}{\alpha c}. \quad (25)$$

For $t \longrightarrow \infty$, we have

$$y^{(1)}(t) \propto \left(\frac{t_1}{t}\right)^{1/4}\cos\left(\left(\frac{t}{t_1}\right)^{1/2}\right) \quad \text{for} \quad \alpha < 0 \quad (26)$$

and

$$y^{(1)}(t) \propto \left(\frac{|t_1|}{t}\right)^{1/4}\exp\left(\left(\frac{t}{|t_1|}\right)^{1/2}\right) \quad \text{for} \quad \alpha > 0. \quad (27)$$

2.5. Influence of the Curvature of Magnetic Field Lines

In expression (10), the ratio B_0/h has the meaning of the curvature radius of the magnetic field line near the $y = 0$ plane. For $h \neq 0$, the equation of particle motion has the form

$$\frac{d}{dt}\left(\gamma^{(0)}\frac{dy^{(1)}}{dt}\right)$$
$$-\left(\alpha+\frac{h(1-\beta^2)}{B_0}\right)\left(\frac{\Omega_c^2 Vt}{\gamma^{(0)}}+V\frac{d\gamma^{(0)}}{dt}\right)y^{(1)} = 0. \quad (28)$$

We see that the stability of the particle motion is determined by the sign of the effective curvature

$$\tilde{\alpha} = \alpha + \frac{h(1-\beta^2)}{B_0}. \quad (29)$$

If the effective curvature is positive, then the trajectory $y = 0$ is unstable, whereas for $\tilde{\alpha} < 0$, it is stable.

2.6. Acceleration by a Wave with a Rippled Front

We assume that the wave front has the shape of a surface rippled in the y-direction, the ripple amplitude and wavenumber being δ and $k_\perp$, respectively. The curvature in this case is equal to

$$\alpha = k_\perp^2\delta\cos k_\perp y \equiv \alpha_m\cos k_\perp y. \quad (30)$$

If the magnetic field is directed along the y-axis, the charged particles move mainly along the z-axis (i.e., along the lines on which the curvature is constant) and do not undergo the action of the centrifugal force. In this case, the particles are accumulated in the regions where α is negative.

If the magnetic field is directed along the z-axis, the charged particles experience the action of the centrifugal force $m\gamma v^2\alpha$. This force results in the modification of the condition for the charged particle trapping, which, for $V \ll v$, can be written as

$$\frac{eE}{m} > \gamma v^2\alpha + \frac{eB_0 v}{mc}. \quad (31)$$

It follows from here that the maximum energy gain of the accelerated particle is

$$\mathscr{E}_{\max} \approx \min\left\{\frac{mc^2}{2}\left(\frac{E}{B_0}\right)^2, \frac{eE}{2k_\perp^2\delta}\right\} \quad (32)$$

in the nonrelativistic case and

$$\mathscr{E}_{\max} \approx \frac{eE}{k_\perp^2\delta} = \frac{eE}{\alpha_m} \quad (33)$$

in the ultrarelativistic limit.

3. MOTION OF CHARGED PARTICLES TRAPPED BY A WAVE WHOSE FRONT HAS THE SHAPE OF A SURFACE OF REVOLUTION

Now, we consider a strong potential wave whose front is described by the expression

$$r = r_f(z,t) = Vt - \frac{1}{2}\alpha(t)z^2 + \ldots. \quad (34)$$

The magnetic field has z- and φ-components, and the vector potential also has z- and φ-components:

$$\mathbf{A} = -\mathbf{e}_z\int^r B_\varphi(r)dr + \mathbf{e}_\varphi\int^r B_z(r)rdr. \quad (35)$$

In this case, the Lagrange function L^* has the form

$$L^*(z, \varphi, \dot{z}, \dot{\varphi}) = -\frac{e\dot{z}}{c}\int_0^{r_f(z,t)} B_\varphi(r)dr + \frac{e\dot{\varphi}}{c}\int_0^{r_f(z,t)} B_z(r)rdr - mc^2\left(1 - \frac{\dot{r}_f^2 + 2\dot{r}_f r_f'\dot{z} + r_f^2\dot{\varphi}^2 + (1 + (r_f')^2)\dot{z}^2}{c^2}\right)^{1/2}, \quad (36)$$

where the prime denotes differentiation with respect to the z-coordinate.

Since the Lagrange function does not depend on the φ-coordinate, the φ-component of the generalized momentum is conserved:

$$P_\varphi = r_f^2(\gamma\dot{\varphi} + \Omega(r_f)) = \text{const}, \quad (37)$$

where the function

$$\Omega(r_f) = \frac{e}{mcr_f^2}\int_0^{r_f(z,t)} B_z(r)rdr \quad (38)$$

is introduced. We note that, in a uniform magnetic field, the frequency $\Omega(r_f) = eB/2mc$ is equal to one-half of the cyclotron frequency.

If the wave front is cylindrical, then the Lagrange function is also independent of the z-coordinate. In this case, the z-component of the generalized momentum is also conserved:

$$P_z = (\gamma\dot{z} + eA_z/c) = \text{const}, \quad (39)$$

where $A_z = \int_0^{r_f(z,t)} B_\varphi(r)dr$.

3.1. Clairaut Theorem for a Particle Moving along a Spherical Surface in a Magnetic Field

Let us suppose that the propagation velocity of the wave is sufficiently low so that the radius of the front $r_f(z, t)$ changes only slightly during one circulation of the trapped particle around the z-axis. In this case, it is of interest to analyze the particle motion assuming that the front radius does not depend on time ($r_f = r_f(z)$). Under this assumption, the particle energy $\mathscr{E} = \gamma mc^2$ and, consequently, the absolute value of the particle velocity $|\mathbf{v}|$ do not change with time. We introduce the angle ψ between the velocity of a particle moving along the surface $r_f(z)$ and the direction of the meridian on this surface. Then, taking into account that $r_f(z)\dot{\varphi} = |\mathbf{v}|\sin\psi$, we obtain from Eq. (37)

$$\gamma r_f(z)|\mathbf{v}|\sin\psi + r_f^2\Omega(r_f) = P_\varphi. \quad (40)$$

In the absence of a magnetic field ($\Omega(r_f) = 0$), Eq. (40) reduces to

$$r_f(z)\sin\psi = \text{const}, \quad (41)$$

which is equivalent to the Clairaut theorem [22]. It follows from this relationship that the particle trajectory is confined within the region $|\sin\psi| \le 1$, i.e., at $r \ge r_0\sin\psi_0$. In the presence of a magnetic field, the trajectory lies in the region $r_{\min} < r < r_{\max}$. For $P_\varphi > 0$, we have

$$r_{\min,\max} = \mp\frac{\gamma|\mathbf{v}|}{2\Omega} + \left(\left(\frac{\gamma|\mathbf{v}|}{2\Omega}\right)^2 + \frac{P_\varphi}{\Omega}\right)^{1/2}. \quad (42)$$

The minimum value of the radius corresponds to $\sin\psi = +1$, and the maximum value of the radius corresponds to $\sin\psi = -1$. For $P_\varphi < 0$, the minimum and maximum values of the radius are achieved at $\sin\psi = -1$ and are equal to

$$r_{\min,\max} = \frac{\gamma|\mathbf{v}|}{2\Omega} \mp \left(\left(\frac{\gamma|\mathbf{v}|}{2\Omega}\right)^2 + \frac{P_\varphi}{\Omega}\right)^{1/2}. \quad (43)$$

3.2. Particle Trajectory

Now, we assume that the radius of the wave front depends on time as

$$r_f(z, t) = Vt - \frac{\alpha z^2}{2}. \quad (44)$$

Let the magnetic field have only the z-component. A more general case of a helical magnetic field will be considered below. The particle trajectory corresponding to the initial conditions $z_0 = 0$ and $\dot{z}_0 = 0$ lies in the $z = 0$ plane. In the limit $t \longrightarrow \infty$, it is given by relationships

$$\dot{\varphi} = -\frac{\Omega(r_f)}{\gamma}, \quad (45)$$

$$\gamma = \left(\frac{c^2 + \Omega^2(r_f)r_f^2}{c^2 - V^2}\right)^{1/2}. \quad (46)$$

If $B_z = \text{const}$, then, for $t \longrightarrow \infty$, we have

$$\gamma \approx \frac{eB_z r_f}{2(1-\beta^2)^{1/2}mc^2}. \quad (47)$$

In the ultrarelativistic limit, the trajectory has the shape of a logarithmic spiral,

$$\varphi = \frac{(1-\beta^2)^{1/2}}{\beta}\ln r, \quad (48)$$

whereas in the nonrelativistic case, it has the shape of an Archimedes spiral,

$$\varphi = \frac{eB_z}{mcV}r. \quad (49)$$

For small z, the motion along the z-axis is described by the equation

$$\frac{d}{dt}\left(\gamma^{(0)}\frac{dz}{dt}\right) - \alpha\frac{\Omega^2(r_f)Vt}{\gamma^{(0)}}\left(1 + \frac{d\ln\Omega(r_f)}{d\ln r_f}\right)z = 0. \quad (50)$$

Using Eq. (46) for the Lorenz factor $\gamma^{(0)}$ and assuming that Ω is independent of r_f, we rewrite Eq. (50) in two limiting cases. In the ultrarelativistic limit ($\gamma^{(0)} \gg 1$), we have

$$\ddot{z} + \frac{1}{t}\dot{z} - \alpha\frac{c}{\beta t}z = 0 \quad (51)$$

and, in the nonrelativistic case $\gamma^{(0)} \simeq 1$), we have

$$\ddot{z} - \alpha\Omega^2 Vtz = 0. \quad (52)$$

We see that the stability of the particle motion is determined by the sign of the front curvature. For $t \longrightarrow \infty$, in the ultrarelativistic limit, we have

$$z \sim (t_1/t)^{1/4}\cos((t/t_1)^{1/2}) \quad \text{for} \quad \alpha < 0, \quad (53)$$

$$z \sim (|t_1|/t)^{1/4}\exp((t/|t_1|)^{1/2}) \quad \text{for} \quad \alpha > 0, \quad (54)$$

where

$$t_1 = -\frac{\beta}{\alpha c}. \quad (55)$$

In the nonrelativistic case, we have

$$z \sim (t_0/t)^{1/4}\cos((t/t_0)^{3/2}) \quad \text{for} \quad \alpha < 0, \quad (56)$$

$$z \sim (|t_0|/t)^{1/4}\exp((t/|t_0|)^{3/2}) \quad \text{for} \quad \alpha > 0, \quad (57)$$

with

$$t_0 = \left(\frac{9}{4\alpha\Omega^2 V}\right)^{1/3}. \quad (58)$$

If the front curvature decreases with time as $\alpha \sim 1/Vt > 0$ (as is the case of an expanding spherical front), we obtain

$$z \sim t^{1/\beta} \quad (59)$$

in the ultrarelativistic limit and

$$z \sim \exp(\Omega t) \quad (60)$$

in the nonrelativistic case.

3.3. Energy Spectrum of Fast Particles

For $\alpha > 0$ (positive curvature), the trajectory lying in the equatorial plane is unstable. In this case, the charged particle acceleration is less effective compared to the case of negative curvature. Nevertheless, some particles can gain large energies even for $\alpha > 0$. The longer the time during which the particle stays in the neighborhood of the plane $z = 0$ (which in turn depends on z_0 and $\dot{z}_0$), the higher the energy gain. In the ultrarelativistic limit, we obtain the following estimates for the particle energy gain:

$$\mathscr{E} \simeq (\mathscr{E}_1 \ln(z^*/z_0))^2 \quad (61)$$

for α = const and

$$\mathscr{E} \simeq (z^*/z_0)^\beta \quad (62)$$

for $\alpha = 1/Vt$. Here, $\mathscr{E}_1 = e|B_z|\beta^2/2\alpha(1-\beta^2)^{1/2}$.

By virtue of the conservation of the particle flux in phase space, the differential energy spectrum is proportional to $|dz_0/d\mathscr{E}|$.

Let us assume that, at the time t_{in}, the particles are distributed uniformly along the wave front with the surface density $n_0/4\pi r_f^2(t_{in})$. For simplicity, we suppose that the initial velocity $\dot{z}_0$ is zero. We also assume that the front curvature depends on time as $\alpha = 1/Vt > 0$. Taking into account that the particle energy gain is proportional to Δt for $\gamma \gg 1$ and $(\Delta t)^2$, for $\gamma \approx 1$, we obtain the following relationships between the energy gain and the z-coordinate:

$$z = z_0(\mathscr{E}/\mathscr{E}_0)^{1/\beta} \quad (63)$$

for $\gamma \gg 1$ and

$$z = z_0\exp(\sqrt{2\mathscr{E}/mV^2}) \quad (64)$$

for $\gamma \approx 1$.

Calculating the Jacobian $|dz_0/d\mathscr{E}|$, we find that, for $\alpha = 1/Vt$, the energy spectrum of ultrarelativistic particles has a power-law form,

$$\frac{dN}{d\mathscr{E}} = \frac{n_0}{4\pi r_f^3(t_{in})}\left|\frac{dz_0}{d\mathscr{E}}\right| = \frac{n_0}{2\pi e|B_z|\beta r_f^3(t_{in})}\left(\frac{\mathscr{E}}{\mathscr{E}_0}\right)^{-(1+\beta)/\beta}, \quad (65)$$

whereas the energy spectrum of nonrelativistic particles is

$$\frac{dN}{d\mathscr{E}} = \frac{n_0}{4\pi r_f^3(t_{in})}\left|\frac{dz_0}{d\mathscr{E}}\right| = \frac{n_0}{2\pi r_f^2(t_{in})(\mathscr{E}mV^2)^{1/2}}\exp\left(-\left(\frac{2\mathscr{E}}{mV^2}\right)^{1/2}\right). \quad (66)$$

If α = const > 0, then the energy spectrum of ultrarelativistic particles has the form

$$\frac{dN}{d\mathscr{E}} \sim \exp\left(-\frac{2\alpha\mathscr{E}(1-\beta^2)^{1/2}}{e|B_z|\beta^2}\right). \quad (67)$$

For $\alpha < 0$, the particle trajectories are stable and the particle spectrum is localized in energy space. The maximum of the spectrum drifts with time, and its

width is determined by the initial particle phase distribution.

3.4. Conditions for Particle Trapping at the Wave Front

For $\mathbf{B} = B_z\mathbf{e}_z$, the Lagrange equation for the radial motion of a particle is

$$\frac{d}{dt}\left(\gamma\frac{dr}{dt}\right) = \gamma r\left(\frac{d\varphi}{dt}\right)^2 + \frac{eB_z}{mc}r\frac{d\varphi}{dt} + \frac{e}{m}E(r), \qquad (68)$$

the electric field of the wave being $E = -\partial\phi/\partial r$. We present the electrostatic potential in the form

$$\begin{aligned}\phi(r,t) &= \frac{E_0}{(rk)^{1/2}}\sin(k(r-Vt)+\epsilon)\\ &= E_m\sin(k(r-Vt)+\epsilon).\end{aligned} \qquad (69)$$

Further, we assume E_m to be constant. Substituting expression (45) for $\dot{\varphi}$ into Eq. (68), we obtain

$$\frac{d}{dt}\left(\gamma\frac{dr}{dt}\right) = -\frac{1}{\gamma}\left(\frac{eB_z}{2mc}\right)^2 r + \frac{e}{m}E(r). \qquad (70)$$

The particle trapped by the wave has a radial velocity equal to V. Assuming

$$r = Vt + r^{(1)} \qquad (71)$$

with $r^{(1)} \ll Vt$, we find

$$\begin{aligned}\frac{d}{dt}\left(t\frac{dr^{(1)}}{dt}\right) = \frac{c}{\beta^2}&\left(\frac{1-\beta^2}{Vt} - \frac{2k(1-\beta^2)^{1/2}E_m\cos\epsilon}{B_z}\right)r^{(1)}\\ &+ \frac{2(1-\beta^2)^{1/2}E_m\sin\epsilon}{B_z} - 1.\end{aligned} \qquad (72)$$

This equation has the solution $r^{(1)} = 0$ for

$$E = E_m\sin\epsilon = \frac{B_z}{2(1-\beta^2)^{1/2}}. \qquad (73)$$

Since $|\sin\epsilon| \le 1$, we find the condition for unlimited acceleration

$$\frac{E_m}{B_z} > \frac{1}{2(1-\beta^2)^{1/2}}, \qquad (74)$$

which is less stringent (by a factor of 2) than condition (3) found in [1]. This difference is related to the contribution from the centrifugal force.

3.5. Particle Acceleration in a Nonuniform Magnetic Field

Above, we have assumed that the amplitude of the wave E_m is constant. However, the amplitude of a cylindrical wave decreases as $r^{-1/2}$ and the amplitude of a spherical wave decreases as r^{-1}. If the magnetic field is uniform, then the condition for the particle trapping breaks at a certain distance r_{max}. As a result, the particle energy is limited and equals $\mathcal{E}_{max} = eBr_{max}/2(1-\beta^2)^{1/2}$. This limitation can be avoided if the magnetic field is nonuniform. We assume that the magnetic field has the form

$$\mathbf{B} = B_z(r)\mathbf{e}_z. \qquad (75)$$

In this case, the Lagrange function is

$$\begin{aligned}L = -mc^2&\left(1 - \frac{\dot{r}^2 + (r\dot{\varphi})^2}{c^2}\right)^{1/2}\\ &+ \frac{e}{c}\dot{\varphi}\int_0^r B(r)r\,dr - e\phi.\end{aligned} \qquad (76)$$

For $r_f = Vt$, the function L^* has the form

$$\begin{aligned}L^* = -mc^2&(1-\beta^2(1+(t\dot{\varphi})^2))^{1/2}\\ &+ \frac{e}{c}\dot{\varphi}\int_0^{Vt} B(r)r\,dr.\end{aligned} \qquad (77)$$

Since the system is uniform in the azimuthal direction, the φ-component of the generalized momentum is conserved:

$$P_\varphi = (Vt)^2\dot{\varphi}\gamma + \frac{e}{mc}\int_0^{Vt} B(r)r\,dr. \qquad (78)$$

From the above relationships, it follows that the angular velocity is equal to

$$r\dot{\varphi} = -\frac{(1-\beta^2)}{c}\mathrm{sgn}(B), \qquad (79)$$

and the particle energy is

$$\mathcal{E} = \frac{e}{(1-\beta^2)^{1/2}}\frac{1}{Vt}\int_0^{Vt} B(r)r\,dr. \qquad (80)$$

The condition for unlimited acceleration takes the form

$$E(r) > \left(B(r) - \frac{1}{r^2}\int_0^r B(r)r\,dr\right)/(1-\beta^2)^{1/2}. \qquad (81)$$

In particular, for a uniform magnetic field, we obtain condition (74).

3.6. Particle Acceleration by a Cylindrical Shock Wave in a Helical Magnetic Field

Let us now consider a configuration in which the magnetic field has the z- and φ-components (helical magnetic field) and the wave front is cylindrical. For a particle accelerated by a shock wave in the self-focus-

ing channel, this corresponds to taking into account both the azimuthal magnetic-field component generated by fast electrons and the longitudinal magnetic-field component arising due to the inverse Faraday effect. Applying the procedure used above for other configurations, we obtain that, for $t \longrightarrow \infty$, the particle energy increases as

$$\gamma = \left(\left(1 + \left(\frac{e}{mc^2 r_f}\int_0^{r_f} B_z r dr\right)^2 + \left(\frac{e}{mc^2}\int_0^{r_f} B_\varphi dr\right)^2\right)\Big/\left(1 - \frac{V^2}{c^2}\right)\right)^{1/2}. \quad (82)$$

The particle trajectory has the shape of a helix with varying radius and pitch.

As was shown in [4], the spontaneous magnetic field can attain the values corresponding to $\omega_{Be} \sim a^{1/2}\omega_{pe}$, where $a = eE_0/m_e\omega c$ is the dimensionless laser pulse amplitude. This estimate can be obtained by equating the energy density of the magnetic field $B^2/8\pi$ to the energy density of the electrostatic field $E^2/8\pi$, where the electric field is equal to the charge separation field $E = 4\pi neR$ ($R \approx a^{1/2}c/\omega_{pe}$ being the radius of the self-focusing channel). A petawatt laser pulse can have an amplitude of about $a \simeq 40 \simeq (m_i/m_e)^{1/2}$ [31]. From here, we obtain the estimate for the characteristic energy of fast ions accelerated in the radial direction: $\mathscr{E}_i \simeq am_ec^2 \approx$ 20 MeV. Particle-in-cell simulations of the interaction of a petawatt laser pulse with a plasma [9, 19] show that the energies of the ions accelerated in the radial direction are close to this estimate. However, the same simulations show that the energies of fast ions accelerated in the longitudinal direction are several times higher, which is related to the other acceleration mechanism—the so-called "anisotropic Coulomb explosion" [8].

4. A SIMPLE MODEL FOR THE GENERATION OF A MAGNETIC FIELD BY A NONUNIFORM FLOW OF FAST PARTICLES IN A COLLISIONLESS PLASMA

In [4, 33], based on the results of particle-in-cell simulations of the interaction of a petawatt laser pulse with a plasma, it was concluded that a quasistatic magnetic field is generated by the fluxes of fast electrons. Since the plasma is quasineutral, the electric field produced by fast electrons must be compensated by the cold-electron current flowing in the opposite direction. Such a configuration is unstable against the electromagnetic filamentation instability similar to the Weibel instability [34, 35]. Due to this instability, a quasistatic magnetic field is generated in the plasma. By virtue of the axial symmetry of the problem, this magnetic field vanishes on the axis of the laser beam.

When considering the arising magnetic-field configuration, we will assume that the density of the fast-electron current is described by the expression

$$\mathbf{j}_0 = -e(nv)_{acc} f(r, z, t)\mathbf{e}_z, \quad (83)$$

where $(nv)_{acc}$ is the flux density of fast electrons, $f(r, z, t)$ specifies the distribution of the fast-electron current, and $\mathbf{e}_z$ is the unit vector along the z-axis. We assume that the function $f(r, z, t)$ vanishes outside the region of radius R.

The evolution of the magnetic field in a collisionless plasma in the presence of an external current produced by fast electrons will be described within electron magnetic hydrodynamics [36] using the quasineutrality condition. From the equations of electron hydrodynamics and Maxwell equations, in which we neglect the displacement current, we obtain the equation for the magnetic field:

$$\partial_t \mathbf{B} = -\alpha_h \nabla \times \left[\left(\nabla \times \mathbf{B} - \frac{4\pi}{c}\mathbf{j}_0\right) \times \mathbf{B}\right], \quad (84)$$

where $\alpha_h = ec/m_e\omega_{pe}^2 = c/4\pi en$.

In the case of axial symmetry, in which we are interested here, Eq. (84) takes the form

$$\partial_t B = -\alpha_h \partial_z \left(J_z B - \frac{B^2}{r}\right). \quad (85)$$

Here, B is the azimuthal component of the magnetic field ($\mathbf{B} = B\mathbf{e}_\phi$, where $\mathbf{e}_\phi$ is the unit vector along the azimuthal direction) and J_z is the function proportional to the fast-electron current density ($J_z = (4\pi/c)j_0$).

We introduce the functions $w = \alpha_h(J_z - 2B/r)$ and $u = \alpha_h J_z$; then, Eq. (85) is transformed into

$$\partial_t w + w\partial_z w = q(z, r, t), \quad (86)$$

where $q = \partial_t u + u\partial_z u$ is a known function.

In a steady-state case, when J_z does not depend on time, we have

$$B^2 - rJ_z B = C(r), \quad (87)$$

where $C(r)$ is an arbitrary function of r. We set $C(r) = 0$, in which case the magnetic field vanishes in the region where the fast electrons are absent. In the approximation in which the magnetic diffusion is neglected, this assumption is natural. It follows from Eq. (87) that there are two steady-state solutions:

$$B = 0 \quad (88)$$

and

$$B = rJ_z. \quad (89)$$

In the first case, the fast-electron current is canceled at each point by the electric current produced by the plasma electrons. In the second case, the magnetic field (89) is not identically zero because there is no such can-

cellation, although the total electric current (i.e., the current integrated over the region where $J_z \neq 0$) is equal to zero. Note that the magnetic field (89) vanishes on the axis $r = 0$ and at the boundary of the region where the fast electrons are present.

5. PARTICLE ACCELERATION IN THE VICINITY OF THE NULL-PLANE OF THE MAGNETIC FIELD

As was noted in the previous section, the spontaneous magnetic field can vanish on the axis due to the axial symmetry of the problem.

Here, we consider a simpler configuration in which the magnetic field has only the *y*-component and vanishes in the plane $x = 0$. In the vicinity of this plane, the magnetic field can be represented in the form

$$\mathbf{B} = hx\mathbf{e}_y. \tag{90}$$

In particular, this corresponds to a magnetic configuration that is typical of two-dimensional simulations of the laser–plasma interaction. Let a plane potential wave (the influence of the front curvature was considered in [6]) propagate along the *z*-axis with the phase velocity *V*. Assuming that the *y* component of the particle velocity v_y is small in comparison with *V* and v_x, we derive (in the same way as was done in the previous sections) the equation of motion along the *x*-axis:

$$\frac{d}{dt}\left(\gamma\frac{dx}{dt}\right) = -\frac{eh}{mc}Vx, \tag{91}$$

where

$$\gamma = (1 - \beta^2 - \dot{x}^2/c^2)^{-1/2}. \tag{92}$$

Equation (91) has the integral

$$\gamma + \frac{ehV(x^2 - x_0^2)}{2mc^3(1-\beta^2)} = \gamma_0. \tag{93}$$

It is seen that, depending on the sign of the product *ehV*, the particle trajectory is either localized near the null-line (for $ehV > 0$) or moves away from the plane $x = 0$ (for $ehV < 0$). If $ehV > 0$, then the wave propagates in the same direction as the electrons producing the current due to which magnetic configuration (90) is formed.

From Eq. (93), we obtain the estimate for the energy of fast electrons:

$$\mathscr{E} = \frac{eh\beta R^2}{2(1-\beta^2)}, \tag{94}$$

where *R* is the transverse size of the wave front. In an underdense plasma ($\omega/\omega_{pe} \gg 1$), in which $h \approx 4\pi ne\beta$ and $1 - \beta^2 = (\omega/\omega_{pe})^2$, we have $\mathscr{E} = m_e c^2(\omega/\omega_{pe})^2$.

6. CONCLUSION

In this paper, we have considered a number of problems related to the $\mathbf{v} \times \mathbf{B}$ acceleration of charged particles trapped by a strong potential wave with a curved front in a magnetized plasma. Seemingly, the necessity of simultaneously taking into account the influence of both the wave front curvature and strong magnetic field on the charged particle motion is typical of most situations encountered in analyzing the processes occurring in space and laboratory plasmas. This refers equally to both the acceleration of charged particles by collisionless shock waves in the solar corona and charged particle acceleration in a laser plasma. In this paper, we have shown that, under optimal conditions corresponding to stable particle motion, the combined effect of the front curvature and magnetic field can assist in particle trapping and increase the particle energy, thus increasing the acceleration efficiency. When the particle motion is unstable, the final particle energy decreases because the particle rapidly leaves the acceleration region.

ACKNOWLEDGMENTS

We thank A.V. Gordeev for fruitful discussions. This work was supported in part by the Russian Foundation for Basic Research, project nos. 99-02-16997 and 98-02-17455.

REFERENCES

1. T. Katsouleas and J. M. Dawson, Phys. Rev. Lett. **51**, 392 (1983).
2. Y. Ohsawa and J.-I. Sakai, Geophys. Res. Lett. **12**, 617 (1985).
3. V. S. Berezinskij, S. V. Bulanov, V. A. Dogiel, V. L. Ginzburg, and V. S. Ptuskin, *Astrophysics of Cosmic Rays* (North Holland, Amsterdam, 1990).
4. G. A. Askar'yan, S. V. Bulanov, F. Pegoraro, and A. M. Pukhov, Pis'ma Zh. Éksp. Teor. Fiz. **60**, 251 (1994) [JETP Lett. **60**, 240 (1994)]; Fiz. Plazmy **21**, 884 (1995) [Plasma Phys. Rep. **21**, 835 (1995)]; Comments Plasma Phys. Controll. Fusion **17**, 35 (1996).
5. S. V. Bulanov, E. Lazzaro, and J.-I. Sakai, J. Phys. Soc. Jpn. **66**, 3696 (1997).
6. T. V. Liseikina, F. Califano, V. A. Vshivkov, *et al.*, Phys. Rev. E **60**, 5991 (1999).
7. B. F. Lasinski, A. B. Langdon, S. Hatchett, *et al.*, Phys. Plasmas **6**, 2041 (1999).
8. S. V. Bulanov, F. Califano, G. I. Dudnikova, *et al.*, in *Reviews of Plasma Physics*, Ed. by V. D. Shafranov (Consultants Bureau, New York, 2000), Vol. 22.
9. S. V. Bulanov, T. Zh. Esirkepov, F. Califano, *et al.*, Pis'ma Zh. Éksp. Teor. Fiz. **71**, 593 (2000) [JETP Lett. **71**, 407 (2000)].
10. A. V. Gordeev and T. V. Loseva, Pis'ma Zh. Éksp. Teor. Fiz. **70**, 669 (1999) [JETP Lett. **70**, 684 (1999)].
11. V. V. Korobkin and R. V. Serov, Pis'ma Zh. Éksp. Teor. Fiz. **3**, 301 (1966) [JETP Lett. **3**, 194 (1966)].

12. G. A. Askar'yan, M. S. Rabinovich, A. D. Smirnova, and V. B. Studenov, Pis'ma Zh. Éksp. Teor. Fiz. **5**, 116 (1967) [JETP Lett. **5**, 93 (1967)].
13. S. V. Bulanov, M. Lontano, T. Zh. Esirkepov, *et al.*, Phys. Rev. Lett. **76**, 3562 (1996); S. V. Bulanov, T. Zh. Esirkepov, M. Lontano, and F. Pegoraro, Fiz. Plazmy **23**, 715 (1997) [Plasma Phys. Rep. **23**, 660 (1997)].
14. Y. Sentoku, T. Zh. Esirkepov, K. Mima, *et al.*, Phys. Rev. Lett. **83**, 3434 (1999).
15. M. Borghesi, A. J. MacKinnon, O. Willi, *et al.*, Phys. Rev. Lett. **80**, 5137 (1998); M. Borghesi, A. J. MacKinnon, A. R. Bell, *et al.*, Phys. Rev. Lett. **81**, 112 (1998).
16. L. M. Gorbunov and R. R. Ramazashvili, Zh. Éksp. Teor. Fiz. **114**, 849 (1998) [JETP **87**, 461 (1998)].
17. G. S. Sarkisov, V. Yu. Bychenkov, V. N. Novikov, *et al.*, Phys. Rev. E **59**, 7042 (1999).
18. K. Krushelnik, E. L. Clark, M. Zepf, *et al.*, Phys. Plasmas **7**, 2055 (2000).
19. F. Pegoraro, S. V. Bulanov, F. Califano, *et al.*, IEEE Trans. Plasma Sci. (in press).
20. T. Tajima and J. Dawson, Phys. Rev. Lett. **43**, 267 (1979).
21. S. V. Bulanov and A. S. Sakharov, Pis'ma Zh. Éksp. Teor. Fiz. **44**, 421 (1986) [JETP Lett. **44**, 543 (1986)].
22. V. I. Arnold, *Mathematical Methods of Classical Mechanics* (Nauka, Moscow, 1974; Springer-Verlag, New York, 1989).
23. R. Z. Sagdeev and V. D. Shapiro, Pis'ma Zh. Éksp. Teor. Fiz. **17**, 389 (1973) [JETP Lett. **17**, 279 (1973)].
24. Y. Ohsawa, Phys. Fluids **28**, 2130 (1985).
25. A. T. Altyntsev, G. N. Kichigin, and I. V. Lebedev, Zh. Éksp. Teor. Fiz. **96**, 574 (1989) [Sov. Phys. JETP **69**, 324 (1989)].
26. T. Masaki, H. Hasegawa, and Y. Ohsawa, Phys. Plasmas **7**, 529 (2000).
27. B. Rau and T. Tajima, Phys. Plasmas **5**, 3575 (1998).
28. Ya. B. Faĭnberg, Fiz. Plazmy **13**, 607 (1987) [Sov. J. Plasma Phys. **13**, 350 (1987)].
29. G. F. Krymskiĭ, Dokl. Akad. Nauk SSSR **234**, 1306 (1977) [Sov. Phys. Dokl. **22**, 327 (1977)].
30. S. V. Bulanov, F. Pegoraro, A. M. Pukhov, and A. S. Sakharov, Phys. Rev. Lett. **78**, 4205 (1997).
31. S. V. Bulanov, I. A. Vshivkov, G. I. Dudnikova, *et al.*, Fiz. Plazmy **25**, 748 (1999) [Plasma Phys. Rep. **25**, 701 (1999)].
32. L. D. Landau and E. M. Lifshitz, *The Classical Theory of Fields* (Nauka, Moscow, 1988; Pergamon, Oxford, 1975).
33. D. W. Forslund, J. M. Kindel, W. B. Mori, *et al.*, Phys. Rev. Lett. **54**, 558 (1985).
34. E. W. Weibel, Phys. Rev. Lett. **2**, 83 (1959); R. C. Morse and C. W. Neilson, Phys. Fluids **14**, 730 (1971); V. Yu. Bychenkov, V. P. Silin, and V. T. Tikhonchuk, Zh. Éksp. Teor. Fiz. **98**, 1269 (1990) [Sov. Phys. JETP **71**, 709 (1990)].
35. F. Califano, F. Pegoraro, S. V. Bulanov, and A. Mangeney, Phys. Rev. E **57**, 7048 (1998); F. Califano, R. Prandi, F. Pegoraro, and S. V. Bulanov, Phys. Rev. E **58**, 7837 (1998); Y. Kazimura, J.-I. Sakai, and S. V. Bulanov, J. Phys. Soc. Jpn. **68**, 3271 (1999).
36. A. S. Kingsep, K. V. Chukbar, and V. V. Yan'kov, in *Reviews of Plasma Physics*, Ed. by B. B. Kadomtsev (Atomizdat, Moscow, 1990; Consultants Bureau, New York), Vol. 16.

Translated by the authors

Plasma Physics Reports, Vol. 26, No. 12, 2000, pp. 1015–1026. Translated from Fizika Plazmy, Vol. 26, No. 12, 2000, pp. 1085–1096.

PLASMA OSCILLATIONS AND WAVES

Wall Plasma in a Wideband Dielectric Cherenkov Maser

G. V. Mel'nikov, A. V. Petrov, and A. S. Shlapakovski

Nuclear Physics Institute, Tomsk Polytechnic University, Tomsk, Russia

Received March 21, 2000; in final form, May 28, 2000

Abstract—Results are reported of experimental investigations that have revealed the presence of a plasma in the interaction region of a model wideband relativistic microwave amplifier—a dielectric Cherenkov maser. The electrodynamic properties of a hybrid system—a waveguide with an annular dielectric liner and a plasma layer adjacent to its inner wall—are analyzed. Experiments with a high-current accelerator have revealed that the power of the emitted microwaves at the output of the system increases strongly when an external microwave source at different frequencies in the X-band is switched on. However, this effect was found to be hard to reproduce. Indirect evidence is obtained of the fact that, during the transport of an electron beam and under the action of the signal from a high-power pulsed magnetron, the plasma in the system is created at the surface of the dielectric. In the model of a cold magnetized plasma, a dispersion relation is derived for axisymmetric waves in a system with a wall plasma layer. The spectra of the waveguide and plasma modes in the system and the transverse structure of their electromagnetic fields are investigated thoroughly as functions of the plasma density and layer thickness. It is shown that even a very thin layer of a high-density plasma results in a large frequency shift of the dispersion curve of the waveguide mode, in which case the coupling impedance at a fixed frequency decreases sharply. On the other hand, a layer of a moderately dense plasma increases the coupling impedance for the waveguide mode. It is established that, in a configuration with a wall plasma layer, the longitudinal component of the electric field of a plasma mode whose power flux in the dielectric is of a volumetric nature reverses direction across the layer. © *2000 MAIK "Nauka/Interperiodica".*

1. INTRODUCTION

Among the numerous devices of superpower microwave electronics that are currently under development and construction, the class of wideband amplifiers has been poorly employed. Meanwhile, microwave sources that are capable of generating microwaves at a level of several hundred megawatts and are tunable continuously over a band covering more than half of an octave may find many important applications. Shlapakovski and Chirko [1] showed that an amplification band of 40–50% at the 3-dB level can be achieved in a dielectric Cherenkov maser (DCM)—a relativistic traveling-wave tube with a smooth slow-wave structure in the form of a waveguide with an annular dielectric liner. The criteria established in [1] for broadband microwave amplification were then used to prepare preliminary experiments aimed at demonstrating the possibility of broadband amplification in a DCM [2]. The experiments planned to amplify microwave signals from various external sources with different frequencies in an X-band (8–12 GHz), with the same parameters of a high-current electron beam.

The projected wideband DCM [2] differs from the DCM configurations implemented in earlier experiments [3–5], which were not intended to achieve amplification in the broadest possible band, in the following three ways: the use of an annular dielectric liner with a fairly thick wall, a special choice of the parameters of an electron beam, and the way of exciting the operating mode at the entrance to the interaction region. The use of a thick dielectric liner made of a material with a low permittivity (polyethylene) simultaneously ensures a weak dispersion of the synchronous wave in the range of relativistic phase velocities and a weak frequency dependence of the beam–wave coupling coefficient. Both of these slow-wave structure properties (which, according to [6], are in contradiction to conducting periodic waveguide structures) are necessary in order to achieve broadband amplification in a relativistic Cherenkov maser. At a fixed electron energy, the beam current should also be chosen in a proper manner in order to make the amplification band as broad as possible, in which case the higher the beam energy, the higher the optimum beam current (the use of beams with currents that differ from optimum may lead to a substantial narrowing of the amplification band [1]). In particular, the parameters of the high-current beams used in [4, 5] (800–900 kV and 0.5–3 kA) are unsuitable for broadband amplification because the beam currents are too low. According to [2], beam energies of about 400 keV and beam currents in the range 5–7 kA are optimum for practical purposes. Finally, a unit for launching microwaves into the interaction region should also be consistent with the amplification band (in [3–5], the experiments were carried out with conventional narrowband launchers). For this reason, in the cited experiments [2], the operating mode in a DCM was excited by a TEM wave propagating in a coaxial waveguide (in a way similar to that of exciting a plasma-filled slow-wave structure in [7]). The beam parameters were chosen so as to form the desired beams in a magnetically insu-

1063-780X/00/2612-1015$20.00

lated coaxial diode whose anode served simultaneously as an inner conductor of the coaxial waveguide, in which case the launcher not only was broadband but was also linked compactly to the accelerator and solenoid.

In this paper, we report the preliminary results of our experiments with a model wideband DCM. Our experimental data provide evidence that the characteristic features just described raise the intensity with which the plasma is produced near the dielectric surface and do not confirm the predictions that the charge stored at the surface and the surface breakdown merely shorten the duration of the amplified microwave signal but do not hamper the demonstration of amplification at substantially different frequencies. For this reason, we also analyze how the wall plasma layer affects the electrodynamic properties of the slow-wave structure of a DCM. Modeling our system as a waveguide with an annular dielectric liner and a plasma layer adjacent to its inner wall is more appropriate for quantitative calculations; note also that the propagation of the waveguide and plasma modes in such a waveguide structure differs in character from the propagation of analogous modes in a dielectric-free waveguide with an annular plasma [8, 9] and in a configuration with a dielectric waveguide entirely filled with a plasma [10, 11].

2. EXPERIMENTAL RESULTS

The experiments were carried out with the Luch high-current accelerator, which provides voltage pulses with an amplitude from 350 to 600 kV and duration from 80 to 100 ns at the output. The schematic of a DCM amplifier is shown in Fig. 1. An annular electron beam was formed in a magnetically insulated coaxial diode with a cylindrical edge cathode 18 mm in diameter and was transported through the interaction region—a 45-mm-diameter waveguide with an annular polyethylene liner with an inner diameter of 22 mm. The uniform portion of the interaction region was 24 cm in length, and the guiding magnetic field was up to 27 kG. Then, the beam was transported through a hollow drift tube 36 mm in diameter and was dumped onto the tube wall at the exit from a long solenoid. In order to prevent the formation of a virtual cathode, the drift tube was designed to be smaller in diameter than the waveguide, because the operating current was lower than the limiting current for a dielectric-filled waveguide, but, at the same time, it was higher than the limiting current for an empty waveguide 45 mm in diameter. The slow-wave structure was coupled to the drift tube through a smooth conical linking section, and the drift tube itself had a conical horn with a teflon vacuum window. As external microwave sources, we used pulsed magnetrons with operating frequencies of 9.5 and 11.0 GHz, a power up to 100 kW, and a pulse duration of 1.2 μs. The signals were fed into the interaction region through a launcher (Fig. 2), which excited a TEM wave of a coaxial waveguide. Due to the similar field structures of the TEM and TM_{01} modes (the presence of the E_r and H_φ components of the electromagnetic field near the external conducting wall), a TEM wave excited the TM_{01} operating mode of a waveguide with a dielectric liner. Microwave radiation ahead of the entrance to the launcher and at the exit from the system was recorded by cryogenic germanium detectors.

We performed measurements for the following three amplitudes of the operating voltage of the accelerator: 550, 450, and 370 kV. The principal results were obtained at a voltage of 370 kV (corresponding to a beam current of 3.6 kA) and are illustrated in Fig. 3, which displays the waveforms of the microwave pulses recorded by a detector positioned behind the output window in free space. The top waveform corresponds to the input signal from a magnetron at a frequency of 9.5 GHz, the middle waveform was obtained with another magnetron (with the input signal at a frequency of 11.0 GHz), and the bottom waveform is for micro-

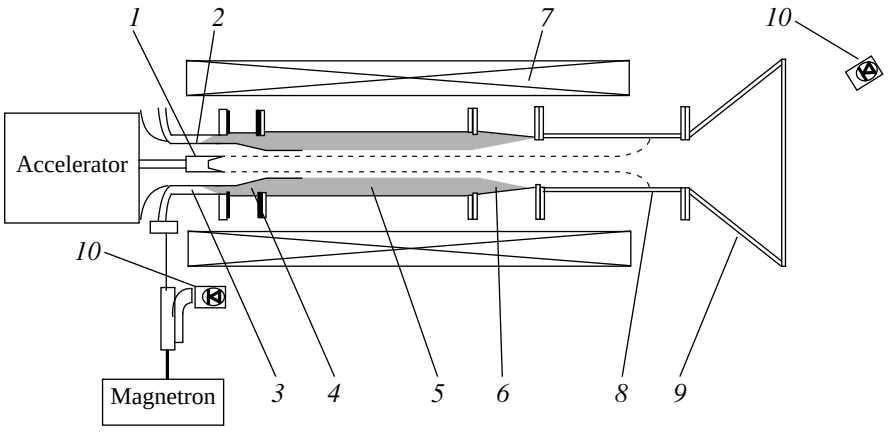

Fig. 1. Schematic of the DCM amplifier: (*1*) cathode, (*2*) anode, (*3*) coaxial waveguide, (*4*) transition section, (*5*) polyethylene liner, (*6*) output matching section, (*7*) solenoid, (*8*) place where the beam is dumped, (*9*) horn antenna, and (*10*) microwave detectors.

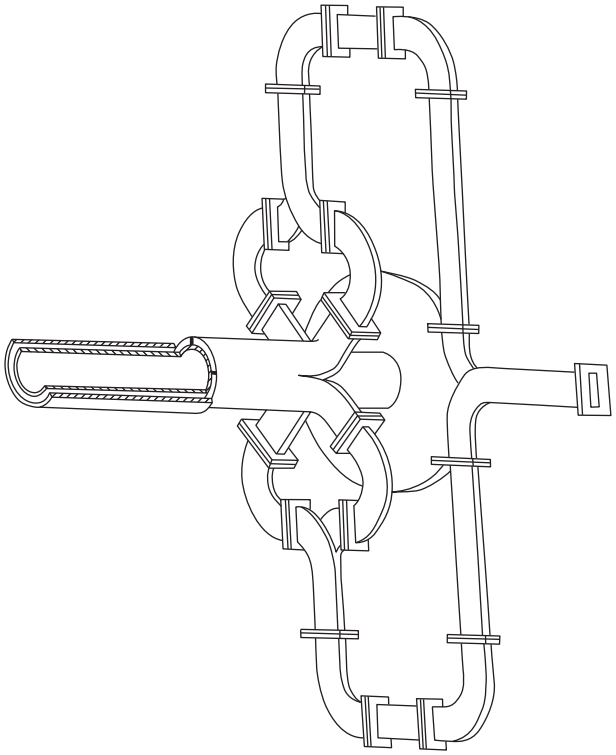

Fig. 2. Schematic of the launcher of microwave signals into a coaxial waveguide.

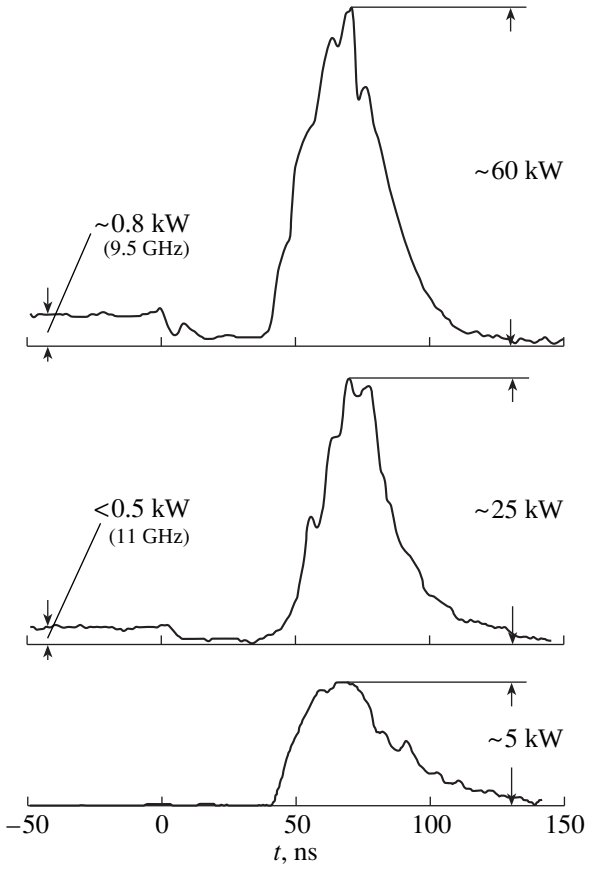

Fig. 3. Waveforms of microwave pulses at the DCM output (a, b) with and (c) without the input signal. Numerals denote the values of the microwave power measured with a detector.

wave emission from an electron beam in the absence of the input signal. The absolute values of the microwave power in Fig. 3 were determined from the calibration curve of a detector (the waveforms are plotted on a nonlinear vertical scale). A receiving horn antenna with an 8×8 cm aperture was installed at an angle of 30° to the axis of the system at a distance of 10 cm from the output window.

Before the time at which the accelerating voltage was switched on, the detector recorded the power of microwaves that passed from an external source through a launcher and the slow-wave structure of a DCM to the receiving horn (the top and middle waveforms). We can see that, in the presence of both an electron beam and input signal, the output power is about two orders of magnitude higher than that in the absence of the beam and one order of magnitude higher than that in the absence of the input signal. In this series of measurements, we found no qualitative difference between the pulses measured in the experiments with magnetrons with operating frequencies of 9.5 and 11.0 GHz. For higher operating voltages, the output power levels were found to be almost the same when the magnetron was switched on and when it was switched off.

Hence, we can conclude that this series of experiments, on the one hand, confirms the possibility of amplifying microwave radiation in a broad frequency band but, on the other hand, cannot be regarded as a practical demonstration of broadband amplification. The output microwave pulses recorded when the magnetrons were switched on were found to have a too large spread in amplitudes (in Fig. 3, we illustrate pulses with maximum powers, but we also recorded pulses that were comparable in amplitude to those obtained with the magnetron switched off). Also, our experimental data are insufficient for statistical analysis. We failed to measure the frequency of poorly reproducible output microwave pulses. In addition, increasing the magnetron power did not result in an increase in the output power, although the DCM was expected to operate in a linear regime.

Such low reproducibility is most likely attributed to the production of a plasma in the interaction region of the DCM. That the plasma was present in the system was revealed in the course of experiments. The evidence for this was, first of all, provided by the results from measurements of the beam current by a Faraday cup, which was positioned in the 36-mm-diameter drift tube immediately behind the transition section (Fig. 1). The representative waveforms of the current and voltage are shown in Fig. 4. It is seen that there is a characteristic current "tail" after the voltage pulse has ended.

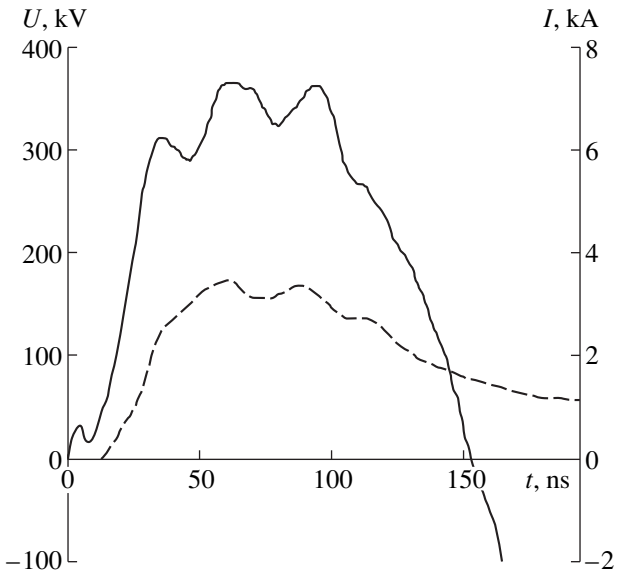

Fig. 4. Representative waveforms of the voltage pulse of the accelerator (solid curve) and the current to a Faraday cup (dashed curve).

In the experiments in which the inner wall of the polyethylene liner was protected with a copper foil, the data from the Faraday cup revealed no current tails after the voltage pulse. Of course, the recorded tails can be associated with the current carried by the plasma electrons toward the collector of a Faraday cup under the action of the longitudinal electric field, which was induced as the magnetic field of the beam current changed. The measured tails can be used to estimate the plasma density by equating the current density to the density of the electron saturation current, $j_e \approx n_p e\langle v_T\rangle$, where n_p is the plasma density and $\langle v_T\rangle$ is the electron thermal velocity. For a plasma layer with a thickness of about 1–3 mm and a temperature of 1–10 eV, the plasma density is estimated as $n_p \sim 10^{13}$–10^{14} cm^{-3}.

The wall plasma can be produced as a result of electron bombardment of the dielectric surface and/or surface breakdown in the field of microwave Cherenkov radiation, for which the Faraday cup played the role of a short-circuiting plug. In order to determine the radial current loss at the dielectric surface during the transport of a beam, we conducted a special series of experiments with a waveguide in which the section with a dielectric liner was replaced by a 36-mm-diameter tube with an array of 14-mm-long cylindrical collectors 20, 23, and 26 mm in diameter placed 1 cm apart. The collector current pulses are shown in Fig. 5: a sharp peak observed in the current in each collector corresponded to the front of the voltage pulse. The peak radial current density was about 2.5–3.0 A/cm^2. As is known [12], such a current density is high enough for a plasma of density 10^{13}–10^{14} cm^{-3} to be created as a result of the bombardment of the dielectric surface by the beam electrons in high-power ion diodes.

However, plasma could be produced not only by an electron beam but also by the surface breakdown of a dielectric during the propagation of a microwave signal from the magnetron before the accelerating voltage was switched on. The instants (with respect to the input microwave signal) at which the beam entered the interaction region varied from shot to shot; sometimes, the pulse from the magnetron terminated before the voltage pulse was switched on. When this was the case, the output microwave power in some shots was observed to be significantly higher than in the case when the magnetron was not fired at all; this experimental result may be viewed as indirect evidence of plasma production in the transport channel.

The intense production of a surface plasma is likely attributed to the parameters that were chosen to achieve broadband amplification. Lining a waveguide with a thick dielectric having a low permittivity ($\varepsilon = 2.25$ for polyethylene) meant that an electron beam propagated in the transport channel at a large distance from the conducting wall, in which case the Coulomb field of the beam increased significantly, the more so because we used beams with fairly high currents. The experiments of [3, 5], which demonstrated microwave amplification in a DCM, were carried out with thin annular dielectric liners and with beams whose currents were far below the limiting currents. In contrast to [3, 5], the launcher in our experiments was designed so as to feed microwaves into the interaction region nearly along the dielectric surface; this circumstance may also be favorable for surface breakdown.

Due to electron losses and/or microwave breakdown, the plasma was produced in a strongly unstable manner. Consequently, it is important to know how the parameters of the plasma layer influence the electrodynamics of the system under investigation. On the one hand, it is necessary to determine the parameter range in which the unstable production of plasma has no impact on the characteristics of a DCM amplifier. On the other hand, the well-known fact that, in a hybrid plasma-filled system with a slow-wave structure, the amplification may be substantially improved in comparison with the plasma-free system [13, 14] necessitates steps to determine the optimum parameter range and to establish requirements for the stability of plasma production.

3. DISPERSION RELATION FOR A SYSTEM WITH A PLASMA LAYER

We consider a circular waveguide of radius b with an annular dielectric liner of inner radius a. Let the inner radius of the plasma layer at the inner dielectric surface be r_p. The geometry of the cross section of this system is shown schematically in Fig. 6. We assume that the plasma density in the layer is uniform. In the linear approximation, we assume that the plasma is cold, collisionless, and fully magnetized and that the ions are immobile [15]. We describe the plasma by a

dielectric tensor whose off-diagonal elements are equal to zero and diagonal elements are $\varepsilon_{rr} = \varepsilon_{\varphi\varphi} = 1$ and $\varepsilon_{zz} = 1 - \omega_p^2/\omega^2$, where ω is the angular frequency and ω_p is the electron plasma frequency. The most important assumption here is that the magnetic field is infinitely strong. This assumption is valid under the conditions

$$\Omega \gg \omega, \quad \Omega \gg \omega_p, \quad \Omega \gg \omega_p \frac{\omega_p}{\omega}, \tag{1}$$

where Ω is the electron cyclotron frequency. We can see that, for a plasma density in the range $n_p > 10^{13}$ cm^{-3} and for the X-band frequencies, to satisfy the last condition in (1) requires significantly stronger magnetic fields than those in our experiments. Nevertheless, the approximation of a fully magnetized plasma can also be used to qualitatively describe the dispersion of waveguide and plasma modes and their structure in a system with a high-density plasma.

For simplicity, we restrict ourselves to considering slow axisymmetric waves with phase velocities below the speed of light c. With allowance for the continuity conditions at the boundaries of the plasma layer and the boundary condition at the conducting wall, the radial dependence of the E_z component of the electric field can be written as

$$E_z(r) = \begin{cases} E_p \dfrac{I_0(qr)}{I_0(qr_p)}, & 0 \le r \le r_p, \\ E_p \dfrac{F(\kappa r, \kappa a)}{F(\kappa r_p, \kappa a)} + E_d \dfrac{F(\kappa r_p, \kappa r)}{F(\kappa r_p, \kappa a)}, & r_p \le r \le a, \\ E_d \dfrac{F(pr, pb)}{F(pa, pb)}, & a \le r \le b, \end{cases} \tag{2}$$

where E_p and E_d are the field magnitudes at the inner plasma boundary and at the dielectric surface, respectively; $q^2 = k^2 - \dfrac{\omega^2}{c^2}$; $\kappa^2 = q^2\left(\dfrac{\omega_p^2}{\omega^2} - 1\right)$; $p^2 = \varepsilon\dfrac{\omega^2}{c^2} - k^2$; k is the longitudinal wavenumber; I_0 is the modified Bessel function; $F(x, y) \equiv J_0(x)Y_0(y) - J_0(y)Y_0(x)$; and J_0 and Y_0 are the Bessel functions.

In a vacuum channel surrounded by a plasma, the field of a slow wave decreases from the inner plasma surface toward the system axis. Inside the plasma layer, the field is an internal wave($\kappa^2 > 0$) if the wave frequency is below the plasma frequency. Inside the dielectric, the slow wave is an internal wave ($p^2 > 0$) if its phase velocity exceeds the speed of light in the dielectric medium. Consequently, the three types of waves that can exist in the system under discussion are as follows: purely plasma modes, whose field decreases in both directions away from the plasma boundaries

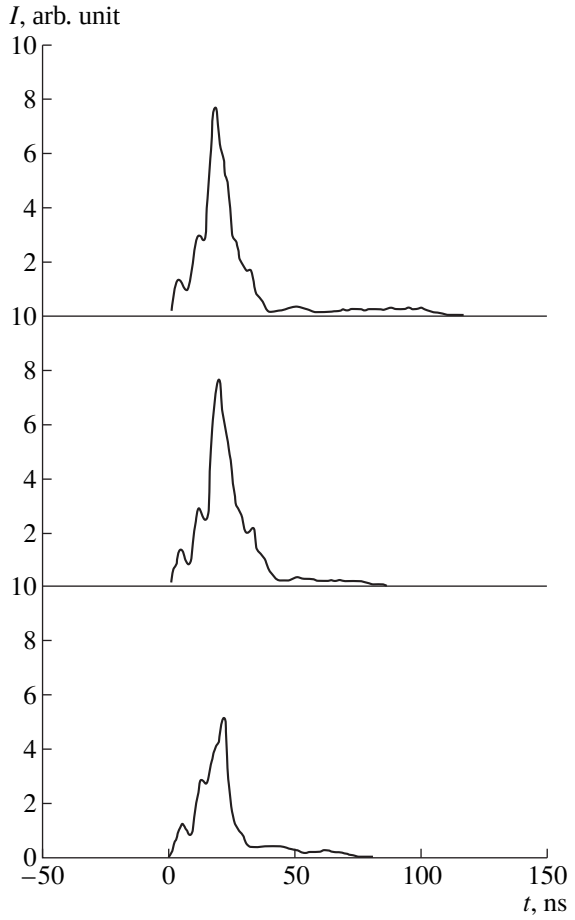

Fig. 5. Waveforms of the currents to the cylindrical collectors during the transport of an electron beam. Collectors with diameters of 20, 23, and 26 mm (top-to-bottom) were positioned along the path of the beam.

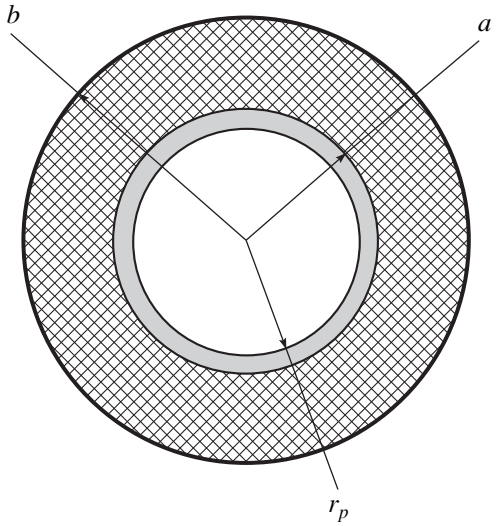

Fig. 6. Model geometry of a system with a plasma layer.

($\kappa^2 > 0$, $p^2 < 0$); purely waveguide modes, whose field is concentrated near the inner surface of the dielectric liner ($\kappa^2 < 0, p^2 > 0$); and hybrid modes, which combine the properties of the plasma and waveguide modes of a dielectric-filled waveguide ($\kappa^2 > 0$, $p^2 > 0$). This is a well-known [13, 14] characteristic feature of slow-wave structures partially filled with plasma.

Substituting expression (2) into the continuity conditions for the H_φ component of the electromagnetic field at the plasma–vacuum and plasma–dielectric boundaries,

$$\left.\frac{dE_z}{dr}\right|_{r=r_p-0} = \left.\frac{dE_z}{dr}\right|_{r=r_p+0},$$
$$\left.\frac{1}{q^2}\frac{dE_z}{dr}\right|_{r=a-0} = -\left.\frac{\varepsilon}{p^2}\frac{dE_z}{dr}\right|_{r=a+0}, \quad (3)$$

and performing simple manipulations, we arrive at the dispersion relation

$$\frac{\varepsilon}{p}\frac{F'(pa, pb)}{F(pa, pb)}$$
$$+\frac{\kappa}{q^2}\frac{F''(\kappa r_p, \kappa a) + \dfrac{q}{\kappa}\dfrac{I_0'(qr_p)}{I_0(qr_p)}F'(\kappa a, \kappa r_p)}{F'(\kappa r_p, \kappa a) - \dfrac{q}{\kappa}\dfrac{I_0'(qr_p)}{I_0(qr_p)}F(\kappa r_p, \kappa a)} = 0, \quad (4)$$

where $F'(x, y) \equiv J_0'(x)Y_0(y) - J_0(y)Y_0'(x)$ and $F''(x, y) \equiv J_0'(x)Y_0'(y) - J_0'(y)Y_0'(x)$.

In the limit $\varepsilon \longrightarrow 1$, the general dispersion relation (4) passes over to the dispersion relation for plasma modes in a dielectric-free waveguide with an annular plasma [8], and, for $\omega_p \longrightarrow 0$ or $r_p \longrightarrow a$, it passes over to the dispersion relation for TM modes in a waveguide with an annular dielectric liner. Note that the three types of waves—the hybrid waves and the plasma and waveguide modes—are described by the same dispersion relation. This indicates that, as in the case of a dielectric-free waveguide, the spectrum of the system under consideration includes the plasma and waveguide modes, in which case hybrid waves correspond to certain portions of the dispersion curves for these modes. Thus, in the wave spectrum, we can distinguish a hybrid plasma mode, which has no cut-off frequency and whose phase velocity, being maximum in the limit $\omega \longrightarrow 0$, is higher than $c/\sqrt{\varepsilon}$, and a hybrid waveguide mode, which possesses a cut-off frequency and, at the same time, satisfies the condition $\omega < \omega_p$.

It is of particular interest to examine the dispersion relation (4) in the limit $\omega \longrightarrow 0$, which characterizes the plasma mode, and in the limit $q \longrightarrow 0$, in which we can find the frequency of a waveguide mode whose phase velocity is equal to c. Using the known series expansions for the Bessel functions, we can readily derive the following equation for the maximum phase velocity of the plasma mode in the limit $\omega \longrightarrow 0$:

$$\kappa_0 a\frac{F''(\kappa_0 r_p, \kappa_0 a)}{F'(\kappa_0 r_p, \kappa_0 a)}\left[\frac{\omega_p^2(\varepsilon-1)}{c^2\kappa_0^2} - 1\right]\ln\frac{b}{a} = \varepsilon, \quad (5)$$

where the normalized phase velocity $\beta_0 = \omega_p/\sqrt{\omega_p^2 + c^2\kappa_0^2}$ can be either higher or lower than $1/\sqrt{\varepsilon}$. In the limit $q \longrightarrow 0$, the same expansions yield the following equation for the minimum frequency ω_c of the waveguide mode in the frequency band of the slowed waves:

$$\varepsilon\frac{F'(p_c a, p_c b)}{F(p_c a, p_c b)} + \frac{p_c a}{2}\left[1 - \frac{\omega_p^2}{\omega_c^2}\left(1 - \frac{r_p^2}{a^2}\right)\right] = 0,$$
$$p_c = \frac{\omega_c}{c}\sqrt{\varepsilon - 1}. \quad (6)$$

The form of Eq. (6) allows us to draw an important conclusion characterizing the hybrid waveguide mode in the system at hand. In the limit of an infinitely dense plasma ($\omega_p \longrightarrow \infty$), the solution to Eq. (6) is determined by the roots of the function $F(p_c a, p_c b)$ and is essentially independent of both the plasma density and layer thickness. Analyzing the general dispersion relation (4), we arrive at the same conclusion. In contrast, the higher the plasma frequency, the higher the frequency of the ordinary waveguide mode. This distinguishing feature of the hybrid waveguide mode can be easily explained by noting that the equation $F(pa, pb) = 0$ is the dispersion relation for high-order modes of a coaxial dielectric-filled waveguide. The high-density plasma plays the role of an inner conductor of a coaxial waveguide, in which case the dispersion of the waveguide mode is sensitive neither to the plasma density nor to the thickness of a layer (if it is not too thin).

The results of numerical calculations of the electrodynamic spectra of the system under consideration are illustrated in Figs. 7–9. In calculations, which were performed with fixed parameters of the dielectric waveguide used in our experiments, we varied the plasma density and the thickness of the plasma layer. The figures show the dispersion curves for the fundamental plasma and waveguide modes; the high-order plasma and waveguide modes are not interesting for the interaction with an electron beam at the X-band frequencies. The horizontal dashed lines in Figs. 7–9 display the operating frequency of one of the magnetrons. For convenience when comparing the results obtained in the absence of the plasma, each of these figures also presents the dispersion curve for the TM_{01} mode of a plasma-free waveguide with an annular dielectric liner.

From Figs. 7–9, we can see that the plasma of density 10^{12} cm^{-3} has an insignificant impact on the electrodynamic properties of the slow-wave structure of the

DCM. In the presence of a thin layer of such a plasma, the dispersion of the waveguide mode remains essentially unchanged. As for the plasma mode, it propagates at frequencies that are generally below the operating frequency band of the DCM and its phase velocities are too low to allow an effective interaction with a relativistic beam. However, even a 1-mm-thick layer of a plasma of density 10^{13} cm^{-3} (Fig. 7) markedly upshifts the dispersion curve of the waveguide mode along the frequency axis. For a 2-mm-thick layer (Fig. 8), the phase velocity of the waveguide mode at the magnetron frequency becomes much higher. For a 3-mm-thick layer (Fig. 9), the operating frequency leaves the frequency band within which a slow wave can propagate. For a plasma of density 10^{14} cm^{-3}, the phase velocity of the waveguide mode at the magnetron frequency is higher than c even for a 1-mm-thick layer, so that the waveguide mode cannot interact with a beam through the Cherenkov mechanism.

The dispersion curve of the plasma mode shifts toward the range of relativistic phase velocities as the plasma density and layer thickness increase. For a 1-mm-thick layer of a plasma of density 10^{13} cm^{-3} (Fig. 7), the phase velocity of the plasma mode is still low, but, for a density of 10^{14} cm^{-3}, the phase velocity is even slightly above $c/\sqrt{\varepsilon}$. In this case, the plasma mode experiences essentially no dispersion within a superbroad frequency band until the phase velocity exceeds the Cherenkov threshold, and the closeness of the phase velocity to $c/\sqrt{\varepsilon}$ indicates that the field in the dielectric is similar in structure to the field of a plane wave. For a 2-mm-thick layer of a plasma of density 10^{13} cm^{-3} (Fig. 8), the plasma mode is still a surface wave, but its phase velocity at the magnetron frequency or below is only slightly lower than $c/\sqrt{\varepsilon}$; i.e., the plasma mode is similar to a cable wave—the operating mode of a relativistic plasma oscillator or amplifier [7, 8]. For a plasma density of 10^{14} cm^{-3}, the dispersion curve of the plasma mode passes very close to the point at which the dispersion curve of a plasma-free system intersects the line corresponding to the operating frequency of a magnetron. This indicates that, for such plasma parameters, the plasma mode acts as if it were a waveguide mode in interaction with a beam, whose energy was chosen so as to provide its interaction with the waveguide mode in a plasma-free system, as is the case in our experiments. The plasma mode becomes a hybrid wave and its dispersion curve bends into a characteristic shape, which is seen most clearly in Fig. 9 (for a 3-mm-thick layer), in which the dispersion curve of the waveguide mode is also seen to bend.

Dispersion curves of similar shape are well known (see, e.g., [14]) and are used to explain the nature of hybrid waves as being due to the coupling between the waveguide and plasma modes. As is asserted, some portions of the dispersion curve of a hybrid wave are close to the dispersion curve for a vacuum slow-wave

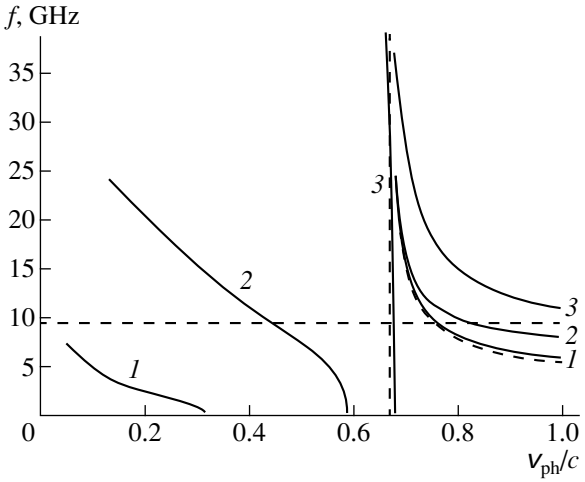

Fig. 7. Dispersion curves of the waveguide and plasma modes in a circular waveguide with an annular dielectric liner and a 1-mm-thick plasma layer for different plasma densities n_p = (*1*) 10^{12}, (*2*) 10^{13}, and (*3*) 10^{14} cm^{-3}. The dashed curve corresponds to a plasma-free system. The vertical dashed line is for the speed of light in the dielectric. The horizontal dashed line is for one of the frequencies of the input signal (9.5 GHz) in the experiment with a model DCM amplifier with the parameters $\varepsilon = 2.25$, $b = 2.25$ cm, and $a = 1.1$ cm.

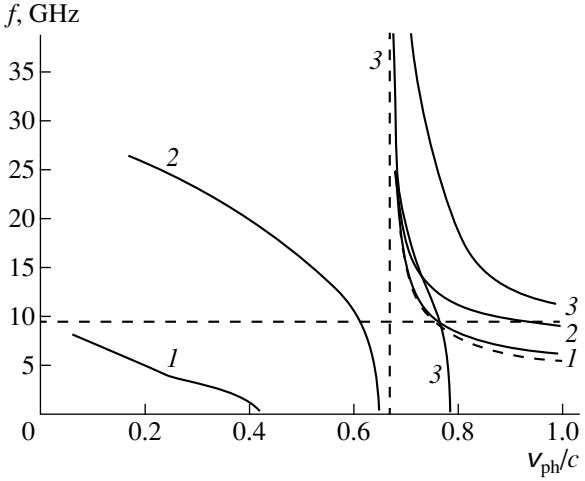

Fig. 8. Same as in Fig. 7 but for a 2-mm-thick layer.

structure and other portions are close to the dispersion curve of the plasma mode [14]. At the same time, Fig. 9 shows how strongly the dispersion of a hybrid waveguide mode differs from the dispersion in a plasma-free system. For the same parameters of the plasma layer, the presence of a dielectric changes the dispersion of the plasma mode in the same fashion. It seems unlikely that dispersion relation (4) can be reduced to a form characteristic of the method of coupled waves, when the dispersion relations for decou-

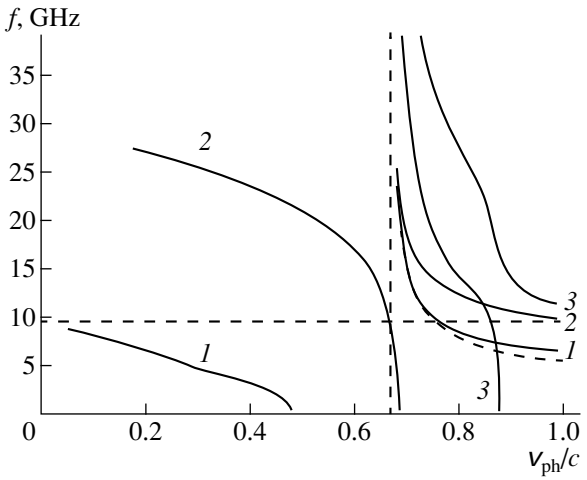

Fig. 9. Same as in Fig. 7 but for a 3-mm-thick layer.

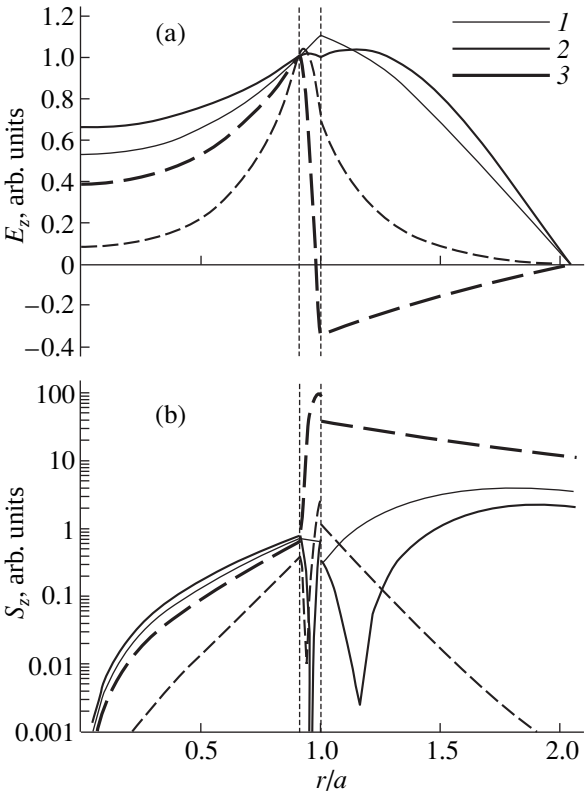

Fig. 10. Radial profiles of the longitudinal components (a) the electric field and (b) Poynting vector for the waveguide and plasma modes in the transverse cross section of a system with a 1-mm-thick plasma layer at a frequency of 9.5 GHz for different plasma densities n_p = (*1*) 10^{12}, (*2*) 10^{13}, and (*3*) 10^{14} cm^{-3}. The parameters of the dielectric liner are the same as in Figs. 7–9. The solid and dashed curves correspond to the waveguide and plasma modes, respectively. The plasma boundary is illustrated schematically by vertical dashed lines.

pled modes are derived by neglecting the wave coupling. It would be more correct to speak of the considerable transformation of waveguide and plasma modes and the resulting qualitative changes in the wave dispersion and field structure.

4. STRUCTURE OF THE FIELD AND THE POWER FLUX DENSITY

Now, we analyze the field structure and the radial profiles of the power flux density of the waveguide and plasma modes. The longitudinal component of the Poynting vector can be written as

$$S_z(r) = \begin{cases} \dfrac{\omega k}{8\pi q^2}\left[\dfrac{I_0'(qr)}{I_0(qr_p)}\right]^2 |E_p|^2, \quad 0 \le r \le r_p, \\ \dfrac{\omega k|\kappa|^2}{8\pi q^4}\left|\dfrac{F'(\kappa r, \kappa a)}{F(\kappa r_p, \kappa a)}E_p - \dfrac{F'(\kappa r, \kappa r_p)}{F(\kappa r_p, \kappa a)}E_d\right|^2, \\ r_p \le r \le a, \\ \dfrac{\varepsilon\omega k}{8\pi|p|^2}\left[\dfrac{F'(pr, pb)}{F(pa, pb)}\right]^2 |E_d|^2, \quad a \le r \le b, \end{cases} \quad (7)$$

in which case the relationship between the field at the inner surface of the dielectric and the field at the inner plasma surface is determined from the condition for the derivative of the longitudinal electric field to be continuous at $r = r_p$.

The results of numerical calculations of the radial field profiles (2) and the radial profiles of the power flux density (7) at a frequency of 9.5 GHz are illustrated in Figs. 10–12. The calculations described here were carried out for the same parameters of the dielectric liner and plasma layer as those in the previous section and for $E_p = 1$.

Figure 10 shows profiles obtained for a 1-mm-thick layer. The field of the hybrid waves is distinctly seen to differ in structure from the fields of the ordinary waveguide and plasma modes. For a plasma layer with the density $n_p = 10^{12}$ cm^{-3}, the field of the ordinary waveguide mode decreases from the dielectric surface toward the inner surface of the plasma layer essentially in the same manner as it does in the absence of a plasma. For a plasma layer with the density $n_p = 10^{13}$ cm^{-3}, the profiles of the field of the hybrid waveguide mode in the plasma and in the dielectric differ from those in the previous case. Over the entire transverse cross section of the layer, the longitudinal field component is nearly uniform; as a result, a much smaller fraction of the microwave power is transported through the layer. Unlike in the previous case, in which the E_z component decreases from the inner surface of the dielectric toward the waveguide wall, in the case at hand, the longitudinal field component, first, increases; reaches its maximum value; and, then, decreases. Over most of the dielectric volume, the radial profile of the

longitudinal component is very flat (Fig. 10a); accordingly, the fraction of microwave power that is transported through the dielectric (Fig. 10b) is also much smaller than that in the case of an ordinary waveguide mode. As a result, in a system with such a plasma density, the coupling impedance between the hybrid waveguide mode and the synchronously propagating beam increases markedly; moreover, in contrast to a system filled with a solid plasma [11, 14], this increase is attributed to the field redistribution not only in a plasma but also in a dielectric, because, in the presence of a plasma layer at the dielectric surface, the hybrid waveguide mode is similar in structure to the high-order mode of the coaxial waveguide.

Figure 10 also clearly illustrates how the field structure changes during the transformation of an ordinary plasma mode into a hybrid wave. Characteristically, for $n_p = 10^{13}$ cm^{-3}, the longitudinal and transverse fields of the plasma mode are seen to decrease exponentially away from the plasma boundaries. In contrast, for $n_p = 10^{14}$ cm^{-3}, the distribution of the power flux density inside the dielectric is similar to that in a volume mode. An important feature of the hybrid plasma mode, which makes it different from an ordinary plasma mode and a hybrid waveguide mode, is that the E_z component reverses direction across the layer. As a result, the radial profile of the flux density of the microwave power carried by the hybrid plasma mode through the layer is peaked inside the layer rather than at its boundaries. In a dielectric-free system with an annular plasma, such a profile is characteristic of the high-order plasma mode [9]. As the phase velocity increases above the speed of light in the dielectric, the radial profile of the field of the hybrid plasma mode across the layer becomes more symmetric about the layer center. This is clearly seen in Fig. 11, which displays the calculated results for a 2-mm-thick plasma layer.

As was noted in the previous section, a 2-mm-thick layer is of particular interest because, in our experiments, the phase velocity of the plasma mode at the magnetron frequency for $n_p = 10^{14}$ cm^{-3} almost coincides with the phase velocity of the waveguide mode in a plasma-free system or in a system filled with a low-density plasma. According to Fig. 11a, the distinguishing feature of the field structure in this case is that the longitudinal component of the field of the plasma mode reverses direction across the layer, while the radial profile of the absolute value of E_z in the dielectric remains essentially the same (see the profiles calculated for $n_p = 10^{14}$ cm^{-3} and $n_p = 10^{12}$ cm^{-3}), as well as the radial dependence of the Poynting vector (Fig. 11b). On the other hand, the fact that the power flux carried by the hybrid plasma mode through the plasma layer makes the dominant contribution to the total microwave power flux (even though the layer is thin) is ascribed to the abrupt change in E_z across the layer.

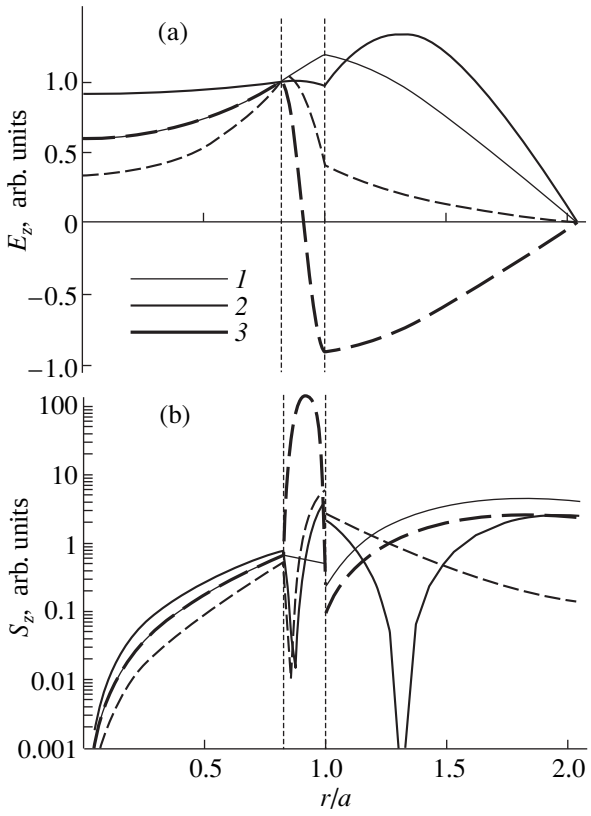

Fig. 11. Same as in Fig. 10 but for a 2-mm-thick layer.

For a hybrid waveguide mode and a 2-mm-thick layer (see the profiles for $n_p = 10^{13}$ cm^{-3} in Fig. 11), we point out not only a dip in the radial profile of the power flux density in the region occupied by a dielectric but also a fairly high degree of uniformity of the longitudinal field component in the plasma layer and vacuum channel. As in the case of a 1-mm-thick layer, the microwave power transported through the waveguide is low; consequently, the coupling impedance is high. In addition, a system with a 2-mm-thick plasma layer is especially suitable for interaction with a thick-walled electron beam, regardless of whether the beam propagates through the plasma or through the vacuum channel.

For a 3-mm-thick plasma layer with the density $n_p = 10^{13}$ cm^{-3}, the waveguide mode is no longer a slow wave; for this reason, in Fig. 12, we present only three profiles. The fields of the ordinary waveguide mode ($n_p = 10^{12}$ cm^{-3}) and hybrid plasma mode ($n_p = 10^{14}$ cm^{-3}) remain similar in structure to those in the case of a thinner layer (Figs. 10, 11). For $n_p = 10^{13}$ cm^{-3}, the longitudinal field of the plasma mode in the dielectric medium nearly vanishes, which corresponds to the transition from an ordinary plasma mode to a hybrid plasma mode.

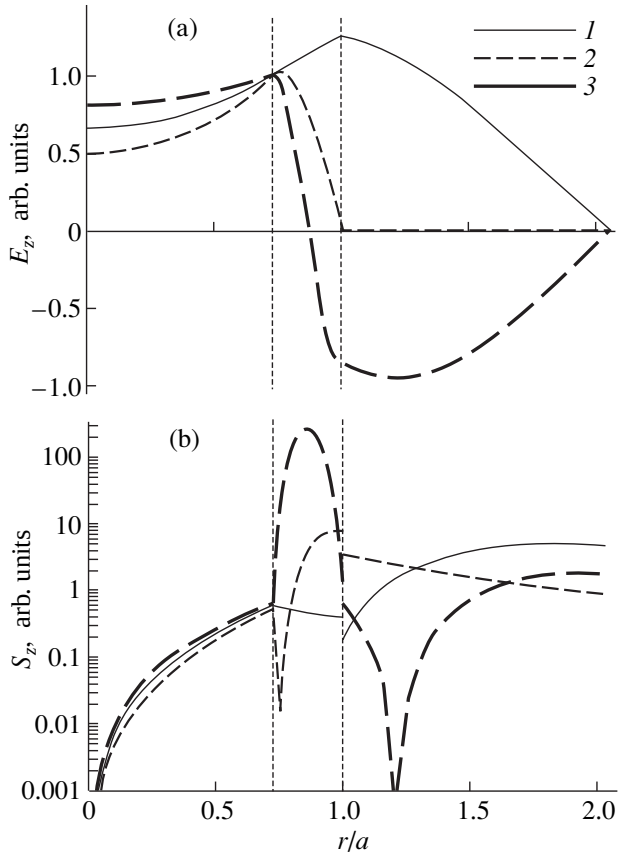

Fig. 12. Same as in Fig. 10 but for a 3-mm-thick layer.

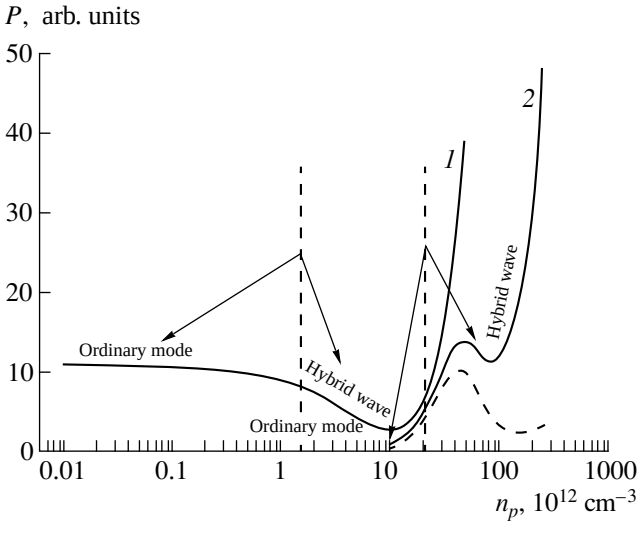

Fig. 13. Power carried through the system by the (*1*) waveguide and (*2*) plasma modes at a frequency of 11 GHz vs. the plasma density for a fixed amplitude of the longitudinal electric field at the inner surface of a 2-mm thick-plasma layer. The parameters of the dielectric liner are the same as in Figs. 7–12. The dashed curve shows the fraction of the microwave power carried by the plasma mode through the dielectric.

To better understand the possible effect of the surface plasma layer on the operation of a wideband DCM, it is necessary to calculate the total microwave power transported through the system. To do that, we must integrate the power flux density (7) over the entire transverse cross section of the system. Since, in our calculations, the field is normalized to E_p, the total microwave power carried by a certain mode is inversely proportional to the coupling impedance between this mode and an infinitely thin annular electron beam propagating along the inner surface of the plasma layer. The lower the total power at a fixed field ($E_p = 1$), the higher the gain per unit length and the interaction efficiency in a DCM. However, at high powers, the interaction is in fact disrupted. It is well known that a moderately dense plasma (rather than a high-density plasma) serves to improve to a certain extent the parameters of the Cherenkov devices. Let us analyze the total power as a function of the plasma density for the above values of the parameters of our experiments.

For a 2-mm-thick layer and a frequency of 11 GHz, this dependence is illustrated in Fig. 13, which plots the profiles of the power carried by the waveguide and plasma modes as functions of the plasma density. The fraction of power carried by the plasma mode through the dielectric is displayed by the dashed curve. The waveguide mode carries the power predominantly through the dielectric in the entire density range under consideration (curve *1*); however, for the highest plasma densities in this range, the relative fraction of power transported through the dielectric decreases. Also shown in Fig. 13 are two vertical dashed lines, which correspond to the plasma densities at which the ordinary waveguide and plasma modes transform into the hybrid waveguide and plasma modes, respectively.

We can see that, in the density range in which the properties of the waveguide mode at a fixed frequency do not change qualitatively ($n_p < 1.5 \times 10^{12}$ cm^{-3}), the plasma has essentially no impact on the total power. However, in the density range corresponding to a hybrid waveguide mode, the total power is very strongly affected by the plasma. As the plasma density increases to about 10^{13} cm^{-3}, the total power decreases by a factor of more than three and reaches its minimum value. In the range of higher densities, it increases sharply until the waveguide mode is no longer a slow wave. Consequently, there exists a density range in which a plasma layer of a given thickness may substantially improve the parameters of a DCM amplifier; however, above this range, which is rather narrow, the conditions for interaction are much worse.

The power carried by the plasma mode behaves as follows. As the plasma density increases, the power, first, increases to a certain level; then, it experiences small variations about this level; and finally, it again starts to increase very sharply. In the density range in which the plasma frequency is slightly above the fixed frequency of the input signal, the phase velocity of the

plasma mode is low and almost all of the power is transported through the plasma layer, in which case the well-known problem of extracting the power from the system arises. As the plasma density increases, the phase velocity of the plasma mode increases and approaches the speed of light in the dielectric, so that the fraction of power transported through the dielectric becomes larger, thereby substantially simplifying the problem of power extraction, as is the case in [7, 8]. The plasma mode transforms into a hybrid wave at $n_p \approx 2.1 \times 10^{13}$ cm^{-3}, in which case, as was already noted, the electric field in the dielectric becomes nearly transverse and the fraction of power transported through the dielectric amounts to 80%. Up to a density of about $n_p \approx 3 \times 10^{13}$ cm^{-3}, the total power carried by the hybrid plasma mode remains smaller than the power carried by the waveguide mode in a plasma-free system. In this density subrange, the phase velocity of the hybrid plasma mode corresponds to a fairly high (>250 keV) energy of a resonant electron. This opens up interesting prospects for microwave amplification by a hybrid plasma mode.

As the plasma density further increases, the phase velocity of the hybrid plasma mode increases to a level corresponding to the operating voltages of the accelerator in our experiments. At the same time, the fraction of power transported through the plasma layer increases abruptly. A decrease in the power transported through the dielectric even leads to the appearance of a local dip in curve *2*. At $n_p \approx 10^{14}$ cm^{-3}, the coupling impedance for the hybrid plasma mode is only slightly below that for the waveguide mode at a low plasma density, and, as was mentioned above, the phase velocities and field structures of these modes in the dielectric are almost the same. However, the fraction of power carried by the hybrid plasma mode through the dielectric is only about 27%, so that, in the case of the interaction with this mode, a significant fraction of the power extracted from the system can be lost (nevertheless, we cannot exclude that, in our experiments, we observed the interaction precisely with this mode). Finally, for plasma densities above 10^{14} cm^{-3}, the conditions for the effective Cherenkov interaction with an electron beam fail to hold: almost all of the total power, which is very high, is transported through the plasma layer, as is the case with an ordinary plasma mode at a low phase velocity.

To conclude this section, note that investigating the electrodynamics of a system with a plasma layer is certainly insufficient to completely analyze the effect of a surface plasma on the operation of a DCM amplifier. Thus, of particular importance is the question of how the power of the signal from a magnetron is redistributed between the waveguide and plasma modes at the entrance to the amplifier. The most important point here is that, in the parameter range in which both the hybrid waveguide and plasma modes can exist, they can be effectively coupled to one another through an electron beam, in which case it might be possible to achieve amplification even in a superbroad band. For this reason, it is necessary to derive and investigate the dispersion relation with allowance for an electron beam.

5. CONCLUSION

The preliminary results from our experimental investigations of a model wideband DCM amplifier show that a serious obstacle to the achievement of stable amplification is the plasma produced in the interaction region of the DCM. If an external source is switched on, the output microwave power was observed to increase substantially at two well-spaced frequencies. However, this effect is poorly reproducible and our experimental data are still insufficient to speak of the gain demonstration. We have performed a thorough theoretical analysis of the electrodynamic properties of the slow-wave structure of a DCM with a plasma layer at the dielectric surface. We have investigated the dispersion and field structure of the waveguide and plasma modes (both ordinary and hybrid). The results obtained call for a reexamination of the design parameters of the dielectric waveguide and electron beam on the basis of reliable information on the wall plasma layer and a theoretical model of a plasma-filled Cherenkov maser. Stable operation of the amplifier in the X-band can be achieved in the following two ways: first, by reducing the intensity at which the plasma is produced in order for the properties of the system to be essentially the same as those of a plasma-free system ($n_p \le 10^{12}$ cm^{-3}), possibly at the expense of narrowing (to some extent) the amplification band, and, second, by ensuring the stability of the parameters of a plasma layer both during the electron beam pulse and from shot to shot. With the optimum parameters (for a plasma density n_p of about 10^{13} cm^{-3}, depending on the layer thickness), the second way may also help to achieve amplification in a broader band with a higher gain per unit length in comparison with those in a system with a low-density plasma. Even a very thin layer of a high-density ($n_p > 10^{14}$ cm^{-3}) plasma acts to disrupt amplification in the system.

ACKNOWLEDGMENTS

We are grateful to I.I. Grushin for his help in preparing the manuscript. This work was supported in part by the Russian Foundation for Basic Research (project nos. 98-02-17931 and 00-02-17720) and the "Russian Universities–Basic Research" program (project no. 015.01.01.38).

REFERENCES

1. A. Shlapakovski and K. Chirko, IEEE Trans. Plasma Sci. **22**, 544 (1994).
2. A. Shlapakovski, G. Melnikov, A. Petrov, *et al.*, in *Proceedings of the International Workshop on High Power*

Microwave Generation and Pulse Shortening, Edinburgh, 1997, Digest of Technical Papers, p. 191.

3. E. Garate, H. Kosai, K. Evans, *et al.*, Appl. Phys. Lett. **56**, 1092 (1990).
4. W. T. Main, E. Garate, J. C. Weatherall, and R. Cherry, IEEE Trans. Plasma Sci. **20**, 281 (1992).
5. E. Kuang, T. Davis, J. Ivers, *et al.*, IEEE Trans. Plasma Sci. **22**, 511 (1994).
6. A. S. Shlapakovski, Pis'ma Zh. Tekh. Fiz. **22** (15), 8 (1996) [Tech. Phys. Lett. **22**, 602 (1996)].
7. I. A. Selivanov and A. G. Shkvarunets, Fiz. Plazmy **18**, 857 (1992) [Sov. J. Plasma Phys. **18**, 446 (1992)].
8. M. V. Kuzelev, F. Kh. Mukhametzyanov, and A. G. Shkvarunets, Fiz. Plazmy **9**, 1137 (1983) [Sov. J. Plasma Phys. **9**, 655 (1983)].
9. T. D. Pointon and J. S. de Groot, Phys. Fluids **31**, 908 (1988).
10. H. Kosai, E. Garate, and A. Fisher, IEEE Trans. Plasma Sci. **18**, 1002 (1990).
11. S. Kobayashi, T. M. Antonsen, Jr., and G. S. Nusinovich, IEEE Trans. Plasma Sci. **26**, 669 (1998).
12. V. M. Bystritskiĭ, S. N. Volkov, Ya. E. Krasik, *et al.*, Fiz. Plazmy **14**, 447 (1988) [Sov. J. Plasma Phys. **14**, 262 (1988)].
13. V. I. Kanavets, N. I. Karbushev, E. I. Ostrenskiĭ, and A. I. Slepkov, Radiotekh. Élektron. (Moscow) **35**, 2574 (1990).
14. G. S. Nusinovich, Y. Carmel, T. M. Antonsen, Jr., *et al.*, IEEE Trans. Plasma Sci. **26**, 628 (1998).
15. A. F. Alexandrov, L. S. Bogdankevich, and A. A. Rukhadze, *Principles of Plasma Electrodynamics* (Vysshaya Shkola, Moscow, 1988; Springer-Verlag, Berlin, 1984).

Translated by G. Shepekina

Plasma Physics Reports, Vol. 26, No. 12, 2000, pp. 1027–1038. Translated from Fizika Plazmy, Vol. 26, No. 12, 2000, pp. 1097–1109.

PLASMA OSCILLATIONS AND WAVES

Investigation of Low-Frequency Waves in Plasma-Filled Microwave Oscillators

A. N. Antonov, Yu. P. Bliokh, E. A. Kornilov, O. F. Kovpik, M. G. Lubarskiĭ, K. V. Matyash, V. O. Podobinskiĭ, V. G. Svichenskiĭ, and Ya. B. Faĭnberg

Kharkov Institute of Physics and Technology, National Science Center, Akademicheskaya ul. 1, Kharkov, 61108 Ukraine

Received February 16, 2000; in final form, May 25, 2000

Abstract—The excitation of microwave oscillations by an electron beam in a hybrid plasma waveguide—a slow-wave structure (a sequence of inductively coupled resonators) with a plasma-filled transport channel—is studied both experimentally and theoretically. It is shown that the governing role in the generation of microwaves and their transmission to a feeder line is played by the spatial and temporal plasma-density variations associated with low-frequency ion plasma oscillations. The microwave pressure gives rise to low-frequency plasma oscillations with a rise time shorter than their period. This nonlinear mechanism for the excitation of low-frequency oscillations has a threshold in terms of the microwave power. The unsteady character of the spatial distribution of the plasma density results in intermittent microwave generation and shortens the duration of microwave pulses. © *2000 MAIK "Nauka/Interperiodica".*

1. INTRODUCTION

Rich theoretical and experimental experience gained during more than fifty years of work in the field of plasma microwave electronics provides a deep understanding of the physical processes occurring in the interaction of charged-particle beams with plasmas. A large number of plasma-filled microwave oscillators and amplifiers have been developed that demonstrate far higher efficiencies and operate at significantly higher powers and in much broader frequency bands in comparison with vacuum analogues. However, in our opinion, some experimentally observed phenomena have received insufficient study and have not yet been understood completely. Among such phenomena, we can mention low-frequency (LF) plasma oscillations excited during the generation of high-power microwave radiation by an electron beam [1]. Such oscillations, which cannot be excited directly by an electron beam, result from the response of the plasma to high-power microwaves propagating in it; i.e., they reflect the nonlinear nature of the plasma [2–4]. According to experimental data (see, e.g., [5–7]), the onset of LF oscillations strongly affects the development of the beam–plasma instability and, as a consequence, changes the spectral and energy characteristics of the generated microwaves. This fact indicates that there is a strong interrelation between the generation of microwaves by a beam and LF plasma oscillations driven by these microwaves. In this paper, we report the results of theoretical and experimental investigations of the physical phenomena that underlie this interrelation.

In other words, we are dealing with one of the central problems in present-day high-power microwave electronics—the shortening of microwave pulses generated in various high-power sources [8]. One of the ways of overcoming this difficulty is to use plasma-filled electrodynamic structures. Changing the structure of the eigenmodes by controlling the plasma parameters makes it possible to substantially lower the microwave electric field near the metal surfaces, thereby avoiding the surface breakdown, which is one of the main causes of plasma production in the system. Loza and Strelkov [9] experimentally showed that this way in fact allows one to make the generated microwave pulses longer, but it fails to completely eliminate the problem of the pulse shortening, since microwave pulses remain shorter than the beam-current pulse. This may be explained, in particular, by the above interrelation between the plasma parameters, which change under the action of high-power microwaves, and the conditions under which microwaves are excited by an electron beam. The experimental data and theoretical models that we will present below indicate that, in an oscillator based on a plasma-filled traveling-wave tube (TWT), the self-consistent dynamics of the plasma and microwave generation causes the beam–plasma instability to evolve into the nonlinear stage, in which microwaves are generated in the form of irregular successive short pulses. As the power of the generated microwave pulses increases, their duration shortens from tens of μs to one μs or less.

1063-780X/00/2612-1027$20.00 © 2000 MAIK "Nauka/Interperiodica"

2. THEORETICAL MODEL OF THE SELF-CONSISTENT PLASMA MOTION DURING THE ONSET OF THE BEAM–PLASMA INSTABILITY

Many theoretical papers studying the beam–plasma instability in plasma-filled systems rest on the implicit assumption that the plasma parameters are independent of the amplitude of the microwave fields excited in the plasma. The related experimental data are also often interpreted based on this assumption.

Among the factors that can change the plasma parameters (the plasma density and temperature, their spatial distributions, etc.) during the propagation of microwaves through the plasma, we should, first of all, mention the microwave discharge and the ponderomotive force of the microwave field. In a strong guiding magnetic field, these two factors cause the plasma parameters to vary in the longitudinal direction. In addition, since the beam interacts with the microwave in a resonant fashion, the interaction process is very sensitive to the extent to which the waveguide structure is nonuniform. For example, let us estimate the range of the beam and plasma parameters for which the deformation of the longitudinal plasma-density profile under the action of the microwave ponderomotive force strongly affects the beam–plasma instability.

A straight monoenergetic charged-particle beam excites a synchronous wave with a phase velocity v_{ph} close to the beam velocity v_b:

$$|v_{ph} - v_b| < v_b\gamma/k, \tag{1}$$

where γ is the spatial growth rate of the instability and k is the longitudinal wavenumber of the excited wave.

In an inhomogeneous plasma, the wave phase velocity is coordinate-dependent and can be estimated from the formula

$$\Delta v_{ph} \sim \delta n \partial v_{ph}/\partial n_p.$$

Here, δn is the perturbation of the plasma density n_p under the action of the ponderomotive force $\mathbf{F} = -\nabla \frac{e^2E_0^2}{4m\omega^2}$ of the generated microwaves (here, E_0 and ω are the amplitude and frequency of the microwave field, respectively).

The perturbed plasma density δn is determined by the balance between the microwave ponderomotive force and the excessive plasma pressure $\delta n T_e$ (where T_e is the plasma electron temperature). We thus arrive at the estimate

$$\frac{\delta n}{n_p} \sim \frac{e^2E_0^2}{4m\omega^2T_e}.$$

The maximum amplitude E_m of the electric field of the wave excited during the onset of the beam–plasma instability is determined by the condition

$$\frac{e^2E_m^2}{m^2\omega^2} \sim \left(\frac{\gamma}{k}\right)^4 v_b^2. \tag{2}$$

The above formulas enable us to write condition (1) for the onset of the beam–plasma instability as

$$\lambda \equiv \left(\frac{\gamma}{k_z}\right)^3 \frac{\omega_p}{v_{ph}} \frac{\partial v_{ph}}{\partial \omega_p} \frac{eU_b}{T_e} < 1. \tag{3}$$

It is well known that the higher the beam density n_b, the higher the growth rate of the beam–plasma instability: $\gamma \sim n_b^{1/3}$. Consequently, as the beam current or the beam-electron energy increases, condition (3) may fail to hold. Note that the higher the beam current and beam-electron energy, the more important the role of the microwave ponderomotive force.

In order to estimate how difficult it is to satisfy condition (3), we consider, as an example, the excitation of a wave by a beam in a magnetized plasma waveguide and a hybrid slow-wave structure.

Magnetized plasma-filled waveguide. The dispersion relation $1 - \frac{\omega_p^2}{\omega^2} + \frac{k_\perp^2}{k_\parallel} = 0$ and condition (3) yield the estimate

$$\frac{n_b}{n_p}\left(\frac{eU_b}{T_e}\right) < 10\frac{k_\perp^4}{(k_\parallel^2 + k_\perp^2)^2} \simeq 10, \tag{4}$$

which allows us to expect that, for a system with $U_b \sim 1$ kV, $T_e \sim 3$ eV, and $n_p \sim 10^9$ cm^{-3} and a beam with a cross-sectional area of 3 cm^2, the microwave ponderomotive force will be pronounced for the beam currents $I_b > 20$ mA.

Hybrid slow-wave structure. In the previous example, such low beam currents at which the plasma density profile is already significantly deformed can be explained by the high sensitivity of the wave phase velocity to plasma density variations. In the hybrid slow-wave structure with which our experiments were carried out and which was designed as a sequence of inductively coupled resonators with a plasma-filled transport channel, the plasma occupied no more than 10% of the entire volume and had a lesser impact on the dispersion properties of the eigenmodes in comparison with a magnetized plasma waveguide [10].[1]

In order to estimate the effect of the microwave ponderomotive force, we turn to the results obtained by Bliokh *et al.* [10] from the calculations of the growth rate and dispersion parameters of a hybrid plasma-filled

[1] Here, we mean the waves that also exist in a vacuum structure. The plasma in the transport channel gives rise to new (plasma) modes, which are sensitive to plasma density variations to the same extent as the slow waves in a plasma waveguide. However, in our experiments, the plasma density was below the threshold for the direct excitation of these waves by the beam.

structure. For our experimental device (which will be described below) with the parameters corresponding to the optimum generation ($U_b \approx 20$ kV, $T_e \approx 20$ eV, and $\omega_p \sim \omega$), condition (3) takes the form $\gamma/k \leq 0.1$. This inequality fails to hold at beam currents of about 3 A, which correspond to microwaves generated at a power level of 20 kW.

Similar estimates can also be obtained for the parameter range in which the plasma inhomogeneity stems primarily from the additional ionization of a neutral gas during a microwave discharge in the fields of the beam-excited waves (i.e., during a beam–plasma discharge).

Bliokh *et al.* [11] developed a self-consistent model that takes into account the deformation of the plasma density profile under the action of the beam-excited microwaves and the inverse effect of this deformation on microwave generation. The model is based on the following two types of equations: equations that describe microwave generation in a plasma without making any assumptions about the nonuniformity of the phase velocity profile and equations that describe the onset and propagation of the plasma density perturbations in the form of LF plasma waves (ion acoustic waves, magnetosonic waves, etc.). Below, we will assume that the guiding magnetic field is strong enough for the transverse plasma motion to be neglected. In this approximation, longitudinal ion acoustic waves can only be excited.

Since the relative variations $\Delta v_{ph}/v_{ph}$ that the phase velocity should experience in order to suppress the beam–plasma instability are small, the plasma density variations that cause the phase velocity to vary are also small, $\delta n/n_p \ll 1$.[2] The characteristic time scale on which the plasma density varies is governed by the time required for an ion acoustic wave to pass through the interaction chamber or, possibly, to propagate over a length equal to the reciprocal of the spatial growth rate of the beam–plasma instability—the shortest spatial scale on which the amplitude of the generated microwaves varies. Under the conditions of our experiments, these times are short in comparison with the inverse ion plasma frequency; consequently, we can ignore the dispersion of the excited ion acoustic waves.

Based on these considerations, we can describe the excitation and propagation of plasma density perturbations by a linear wave equation with a nonzero right-hand side. The wave equation can be conveniently reduced to two first-order differential equations for the dimensionless perturbed plasma velocity (u) and density (η):

$$\begin{aligned} \frac{\partial \eta}{\partial \tau} + \frac{\partial u}{\partial \zeta} &= \lambda \Sigma(|\varepsilon|^2), \\ \frac{\partial u}{\partial \tau} + \frac{\partial \eta}{\partial \zeta} &= \lambda \Phi(|\varepsilon|^2). \end{aligned} \tag{5}$$

Here, the dimensionless functionals $\Sigma(|\varepsilon|^2)$ and $\Phi(|\varepsilon|^2)$ describe the plasma production by a microwave discharge and the microwave ponderomotive force, respectively, and the main parameter of our problem, λ, governs the character of the solutions.

Since the plasma motion is slow, we can neglect transient processes in describing the dynamics of microwave generation by an electron beam and turn to the standard equations for the saturated beam–plasma instability:

$$\begin{aligned} \frac{\partial \varepsilon}{\partial \zeta} + i\eta\varepsilon &= -\frac{1}{2\pi}\int_0^{2\pi} e^{-i\varphi} d\varphi_0, \\ \frac{\partial^2 \varphi}{\partial \zeta^2} &= \mathrm{Re}(\varepsilon e^{i\varphi}), \end{aligned} \tag{6}$$

where ε is the dimensionless complex amplitude of the beam-driven microwaves and φ and φ_0 are the instantaneous and initial phases of a beam electron in the wave.

Equations (5) and (6) with the corresponding boundary conditions were investigated analytically and numerically in the presence of either the plasma source or the microwave ponderomotive force.

The forms of the right-hand sides of Eqs. (5) were chosen so as to provide a better insight into the role of the parameter λ. In the limit $\lambda \ll 1$, the density perturbations η are small and the solutions to Eqs. (6) differ insignificantly from the solutions with $\eta = 0$. For $\lambda \gg 1$, the beam–plasma instability evolves in a different way. For example, the steady solutions $\varepsilon(\zeta)$ to the coupled equations (5) and (6) do not reach values $\varepsilon \sim 1$, which correspond to the amplitude of the saturated instability in a homogeneous plasma. This conclusion follows from Eqs. (6), which show that the dimensionless deviation η of the wave phase velocity from its resonant value cannot be significantly larger than unity; if this is not the case, then the instability is suppressed and no longer causes η to increase: the right-hand sides of (5) vanish. The fact that, in the limit $\lambda \gg 1$, the dimensionless wave amplitude is small compared to unity indicates that the mechanism for suppressing the instability is associated with the nonlinear nature of the plasma rather than the beam electron motion.

The most important factor that governs the form of the solutions is that, for $\lambda \geq 1$, the steady solutions become unstable and, at the exit from the system, the amplitude of the microwaves becomes self-modulated under the action of the ion acoustic waves, whose exci-

[2] In hybrid structures in which the plasma occupies a relatively small volume, this condition may fail to hold, because, as was noted above, the wave phase velocity is weakly sensitive to plasma density perturbations. In this case, our theory, strictly speaking, is valid only qualitatively.

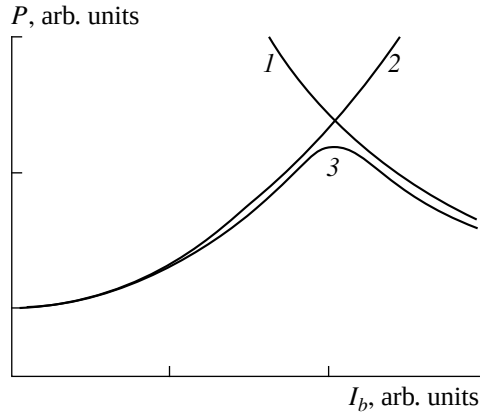

Fig. 1. Qualitative dependence of the microwave power on the beam current: (*1*) the restriction imposed by the nonlinear nature of the plasma, (*2*) the restriction imposed by the nonlinear character of the motion of the beam electrons, and (*3*) the restriction on the generated microwave power imposed by the combined action of these two mechanisms for instability saturation.

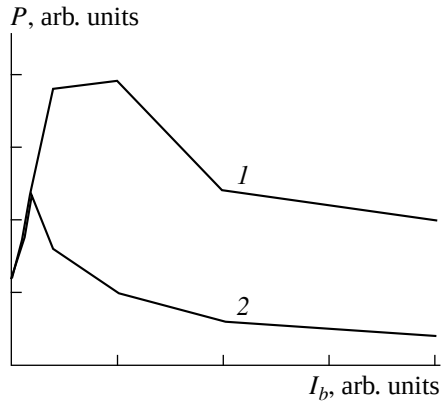

Fig. 2. Dependence of the (*1*) peak and (*2*) average microwave powers on the beam current. The profiles were obtained by solving Eqs. (5) and (6) numerically.

tation is described by the source terms Σ and Φ. The ion acoustic waves propagate in the direction opposite to the propagation direction of the beam, thereby ensuring internal distributed feedback. As a result, the system under consideration starts to function as a generator of LF waves.

Analytic estimates and numerical solutions to Eqs. (5) and (6) show that an increase in λ above the critical value gives rise to a regular LF self-modulation of the plasma density on a characteristic spatial scale equal to the length of the interaction region. Depending on the value of the reflection coefficient q of the ends of the system for an ion acoustic wave, the density perturbations are either a running or a standing wave. Since the microwave amplitude is maximum near the exit from the interaction region, the peak in the longitudinal profile of the source (Σ or Φ) of density perturbations is closer to the exit end. Consequently, for small q values, the observed waves propagate predominantly in the direction opposite to the propagation direction of the beam.

The main result of the analytic calculations can be formulated as follows. As the parameter λ increases, the mechanism for saturation of the beam–plasma instability changes: the governing role is played by the nonlinear nature of the plasma rather than the nonlinear character of the motion of the beam electrons. The plasma nonlinearity manifests itself in the dependence of the plasma density on the amplitude of the generated microwave.

In a hybrid structure, a key role in the LF plasma dynamics is likely to be played by the microwave ponderomotive force. This hypothesis is supported by the fact that, during the microwave generation by the beam, the plasma density increases considerably (by a factor of 1.5 to 2) from the entrance end to the exit end of the system (see Section 4). For this reason, we modeled the processes occurring in the slow-wave structure by solving Eqs. (5) without the source term Σ on the right-hand side.

The higher the plasma density in the hybrid structure, the stronger the coupling between the beam and the wave and, accordingly, the higher the instability growth rate. Simultaneously, the wave phase velocity becomes more sensitive to plasma density perturbations. All of these factors act to increase the parameter λ. When only the nonlinear nature of the motion of beam electrons is taken into account, the saturation level of the instability and the electron efficiency of a microwave oscillator should increase with increasing plasma density. If we take into account only the nonlinear shift of the wave phase velocity due to the plasma inhomogeneity, then the saturation amplitude and the generation efficiency should fall off as the plasma density (the parameter λ) increases. With allowance for both of these saturation mechanisms, the power of the oscillator is governed by the smaller of the corresponding two saturation amplitudes. The dependence of the microwave power on the beam current is illustrated qualitatively in Fig. 1, which also shows the resulting dependence obtained with both of the saturation mechanisms taken into account. The LF self-modulation of the plasma density acts to lower the mean power, which is illustrated in Fig. 2 as a function of the beam current. Note that, in a certain range of λ values, the peak microwave power is higher than the power of microwaves generated in a homogeneous plasma. This result stems from the self-tuning of the wave phase velocity: as the wave amplitude grows, the plasma density and, accordingly, the wave phase velocity fall off, which allows the wave to stay synchronized with the decelerated beam.

3. EXPERIMENTAL DEVICE AND DIAGNOSTIC TECHNIQUES

Microwave generation was investigated in an experimental device with a sequence of inductively coupled resonators. The device was designed according to the typical scheme of a beam–plasma oscillator in which the hybrid plasma waveguide (HPW) is formed via plasma production by an electron beam at a fixed pressure in a slow-wave structure [12–14].

The device consists of the following main elements (see Fig. 3): an electron gun (*2*) placed inside chamber (*1*), which is evacuated to a pressure of 10^{-9} torr by a turbomolecular pump; the working and auxiliary slow-wave structures—a sequence of inductively coupled resonators (*4*) with vacuum microwave feedthrough windows (*3*) placed in the magnetic field produced by solenoidal coils (*10*); diagnostic chambers (*5*); a current collector (*6*); a pipe (*9*) for controlled gas puffing into the slow-wave structure; and a power supply for an electron gun (*12*) and a solenoid (*11*).

At an accelerating voltage of 1–40 kV, the electron gun produces a beam with a current of 0.5–10 A in the pulsed mode. The duration of a current pulse is 2 ms. The cathode of the gun is a 10-mm-diameter disk made of lanthanum hexaboride and heated by the electrons from an auxiliary source. The anode of the gun is a massive copper block with a 12-mm-diameter 120-mm-long electron channel. The anode is cooled by running water. The gun is placed in the region where the magnetic field produced by the solenoid is increasing. At the location of the gun, the magnetic field is weaker than at the axis of the slow-wave structure by a factor of two. This makes it possible to squeeze the electron beam so that its diameter in the slow-wave structure attains 5 mm.

The slow-wave structures are surrounded by Bitter-like solenoidal coils made of welded copper disks. The coils are placed in a cylinder, which, together with the outer surface of the slow-wave structure, composes a chamber. A cooling agent is pumped through the chamber in order to cool both the slow-wave structure and solenoidal coils. At the axis of the slow-wave structures, the magnetic field can be maintained at a level of 1–3 kG.

The slow-wave structures have a 12-mm-diameter channel through which the beam passes. The working slow-wave structure, which is farther from the electron gun (Fig. 3), was calculated so as to ensure conditions for the interaction between a 25- to 40-keV electron beam and the first forward fundamental mode of the excited wave in the frequency band 2.4–4.7 GHz. The length of the structure (60 cm) was chosen so as to achieve the highest coefficient of the conversion of the beam-electron energy (15–40 keV) into microwave energy, with the nonlinear character of the electron motion taken into account [15]. The end resonators are matched to 72 × 34-mm rectangular waveguides through the slits in the side surface. Can-like broadband

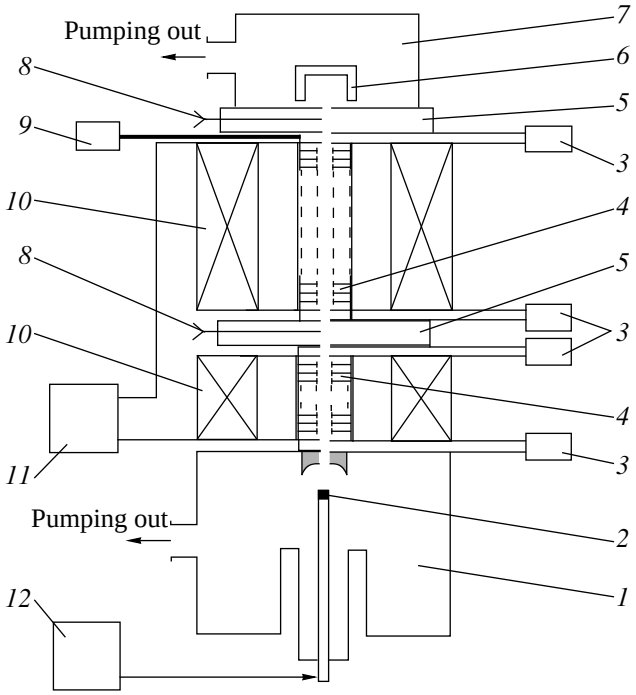

Fig. 3. Schematic of the device with a slow-wave structure in the form of a sequence of inductively coupled resonators: (*1*) electron-gun chamber, (*2*) electron gun, (*3*) vacuum microwave feedthrough windows, (*4*) slow-wave structures, (*5*) diagnostic chambers, (*6*) current collector, (*7*) collector chamber, (*8*) probes, (*9*) gas-puffing unit, (*10*) magnetic-field solenoids, (*11*) power supply for the solenoids, and (*12*) power supply for the electron gun.

feedthrough windows with 2-mm-thick sapphire disks are soldered into the waveguides. The windows are designed so as to continuously transmit microwave radiation with a power of up to 100 kW in the working frequency band. The feedthrough windows make it possible not only to output the excited microwaves but also, if necessary (when we need to measure the plasma density), to launch probing microwave signals at a fixed frequency into the structure. The pressure gauges are mounted on the waveguides near the slow-wave structures. The working gas (nitrogen, argon, or air) is puffed into the matcher of the auxiliary slow-wave structure (in front of the collector) through an automatic leak. The pressure in the structure can be varied from 10^{-5} to 10^{-7} torr at a fixed pressure of 10^{-8} torr in the electron-gun chamber. Calorimeters for measuring the microwave power are linked to all of the waveguide sections of the slow-wave structures, which makes it possible to continuously determine the mean power of the microwaves generated during operation of the device. The waveguide sections are also equipped with detectors, the current signals from which are calibrated with respect to the transmitted microwave power. This allows us to detect temporal fluctuations of the generated microwave power and to determine the absolute fluctuation amplitude. Part of the microwave power

from the waveguide sections is transmitted to the scanning analyzers of oscillation spectra with the working frequency band 8 MHz–40 GHz. In the experiments, the oscillation signals were recorded with the help of high-speed oscillographs and a video camera and then were stored in the memory of a computer. A Fourier analysis of the stored signals makes it possible to compare the averaged oscillation spectra with the "instantaneous" spectra (those recorded over short time intervals). In experiments, special attention was paid to the correlation between the parameters of the generated microwaves and the perturbations of the plasma density in a waveguide at fixed beam parameters.

In the HPW, the plasma density is measured by 2-mm-long double probes, which also allow the plasma electron temperature to be estimated. The probes are relatively insensitive to the degree to which the plasma electrons are magnetized; in magnetic fields up to 3000 G, the plasma ions remain unmagnetized [16]. Double probes with an Alundum screen are made of molybdenum wire 0.2 mm in diameter, the distance between the probe wires being 2 mm. The probes are installed on metal sylphons in two 15-mm-long diagnostic chambers on both sides of the working slow-wave structure. The sylphons allow the probes to be moved in the cross section of the transport channel of the slow-wave structure without any deterioration of the vacuum. The design of the 15-mm-long diagnostic chambers also makes it possible to carry out measurements with single and magnetic probes. Inserting the diagnostic chambers results in insignificant dips in the magnetic field profile between the waveguide sections. Either a controlled constant voltage or sawtooth voltage are applied to the probes. The signals from the probes and their characteristics are recorded and then processed by a computer. The available generators of sawtooth voltage make it possible to determine the plasma parameters on a 10 μs time scale.

In order to measure the lowest plasma density, below which the electron beam excites no oscillations, the experimental device is equipped with an auxiliary shorter slow-wave structure (closer to the electron gun), which allows the propagation of the same mode as in the working slow-wave structure. However, when the auxiliary structure is filled with a plasma, the resonant phase velocities in it are much lower than those in the working structure.

4. MICROWAVE GENERATION BY AN ELECTRON BEAM IN AN HPW

1. Our investigations show that the dependence of the averaged characteristics of the generated microwaves on the beam and plasma parameters is similar to that observed in our previous experiments [12–14]. For a fixed magnetic field and fixed electron beam energy, the maximum microwave power is achieved at certain magnitudes of the beam current and gas pressure in the slow-wave structure. Thus, for our waveguide and for a 30-keV electron beam, the maximum microwave power (41 kW) in the frequency band 3.5–4.7 GHz in the slow-wave structure was achieved at a beam current of 3.5 A and a nitrogen pressure of 8×10^{-5} torr, the central frequency being 4.3 GHz. Figures 4a and 4b show the microwave power as a function of the beam current and gas pressure in the slow-wave structure, respectively. At the maximum power, the plasma density attains 10^{11}–10^{12} cm^{-3} and the plasma electron temperature amounts to 80–100 eV. In the initial parts of the curves (at low pressures and currents), the electron temperature does not exceed 10–20 eV. According to theoretical calculations of the dispersion characteristic of the waveguide, the beam excites the first mode of the

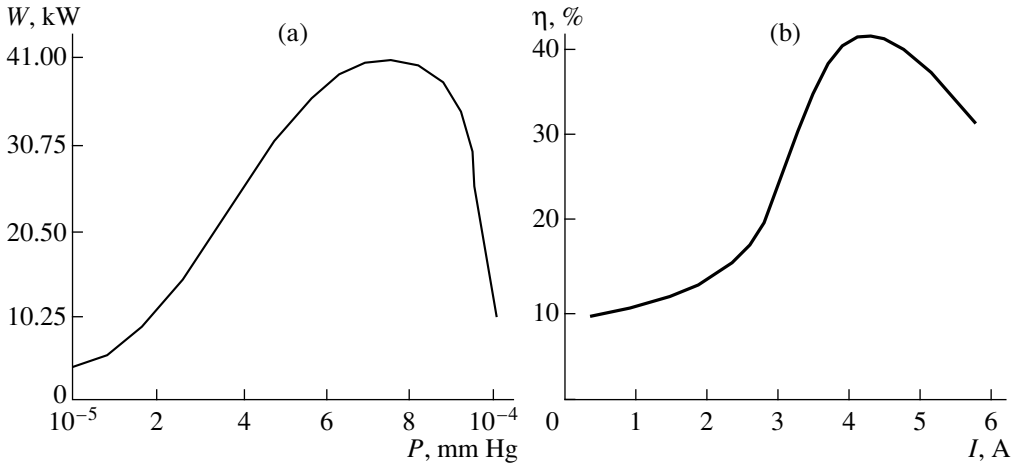

Fig. 4. (a) Output microwave power vs. the gas pressure in the HPW at an accelerating voltage of 30 kV and (b) electron efficiency vs. the beam current for a gas pressure of 8×10^{-5} mm Hg in the HPW at a fixed accelerating voltage.

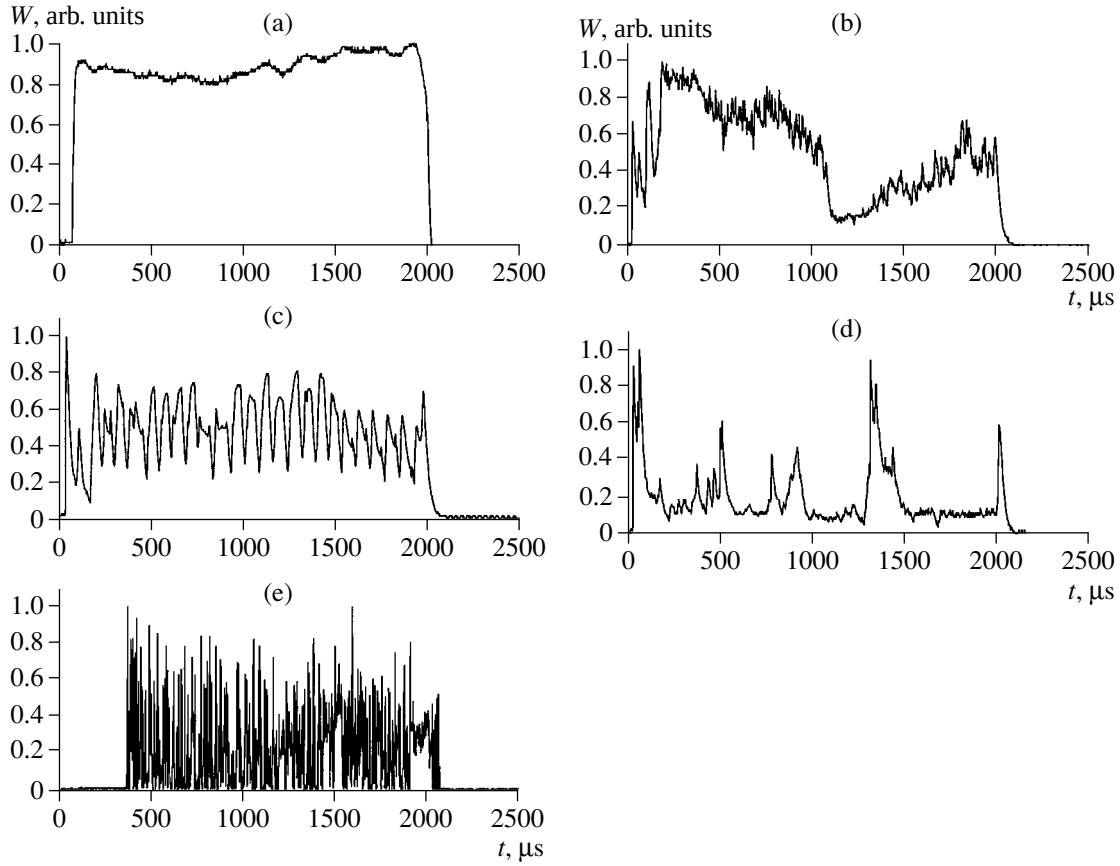

Fig. 5. Envelope of microwave pulses generated at average powers of (a) 18, (b) 20, (c) 22, and (d) 25 kW before the maximum power in Fig. 4 is achieved and (e) at an average power of 25 kW after the maximum power is reached.

E-wave. It is seen that the curves in Fig. 4 are similar in shape to those in Figs. 1 and 2.

Recorded current signals from a detector placed in the waveguide show that, as the average microwave power increases, the instantaneous value of the power starts to vary in time.

Figure 5 shows representative waveforms of the envelope of the microwave pulses generated at power levels of 18, 20, 22, and 25 kW before the maximum microwave power in Fig. 4 is achieved and at a power level of 25 kW after the maximum power is reached. The characteristic features of the generated pulses are as follows: first, as the power increases, the spectrum width increases from 3–5 MHz to 1 GHz and, second, the power experiences sharp variations during the beam-current pulse.

An analysis of the waveforms shows that there is a pedestal on the pulse envelope and power spikes above the pedestal. As the average power increases, the height of the pedestal decreases, the spikes become narrower, and their amplitude increases. After the maximum average power in Fig. 4 is achieved, the pedestal disappears and the duration of microwave pulses decreases from hundreds of microseconds to 0.5–1 μs. At certain time intervals, the rate at which microwave pulses with a nearly maximum power are generated can be as high as 1 MHz. When the average power approaches its maximum value (Fig. 4), the height of the power spikes exceeds the height of the pedestal (which corresponds to the measured average power) by a factor of 2 to 4. The efficiency with which short microwave pulses are generated during the beam-current pulse (i.e., the ratio of microwave power to the beam power) can attain 90%. Note that, according to the theoretical predictions made with allowance for the nonlinear character of the motion of the beam electrons during the excitation of waves in a homogeneous plasma (i.e., with taking into account electron trapping by the excited waves), the efficiency can be at most 30–35% [15]. The mechanism for wave excitation can be explained only in terms of the nonlinear plasma properties that ensure the self-tuning of the phase velocity of the eigenmodes of the HPW to the beam velocity, which changes during the beam–plasma interaction. This conclusion is supported qualitatively by the observed characteristic features of the spatial distribution of the plasma density during the beam-current pulse.

2. The measurements of the plasma density from the probe saturation current (the first probe is placed at the entrance end and the second probe is placed at the exit

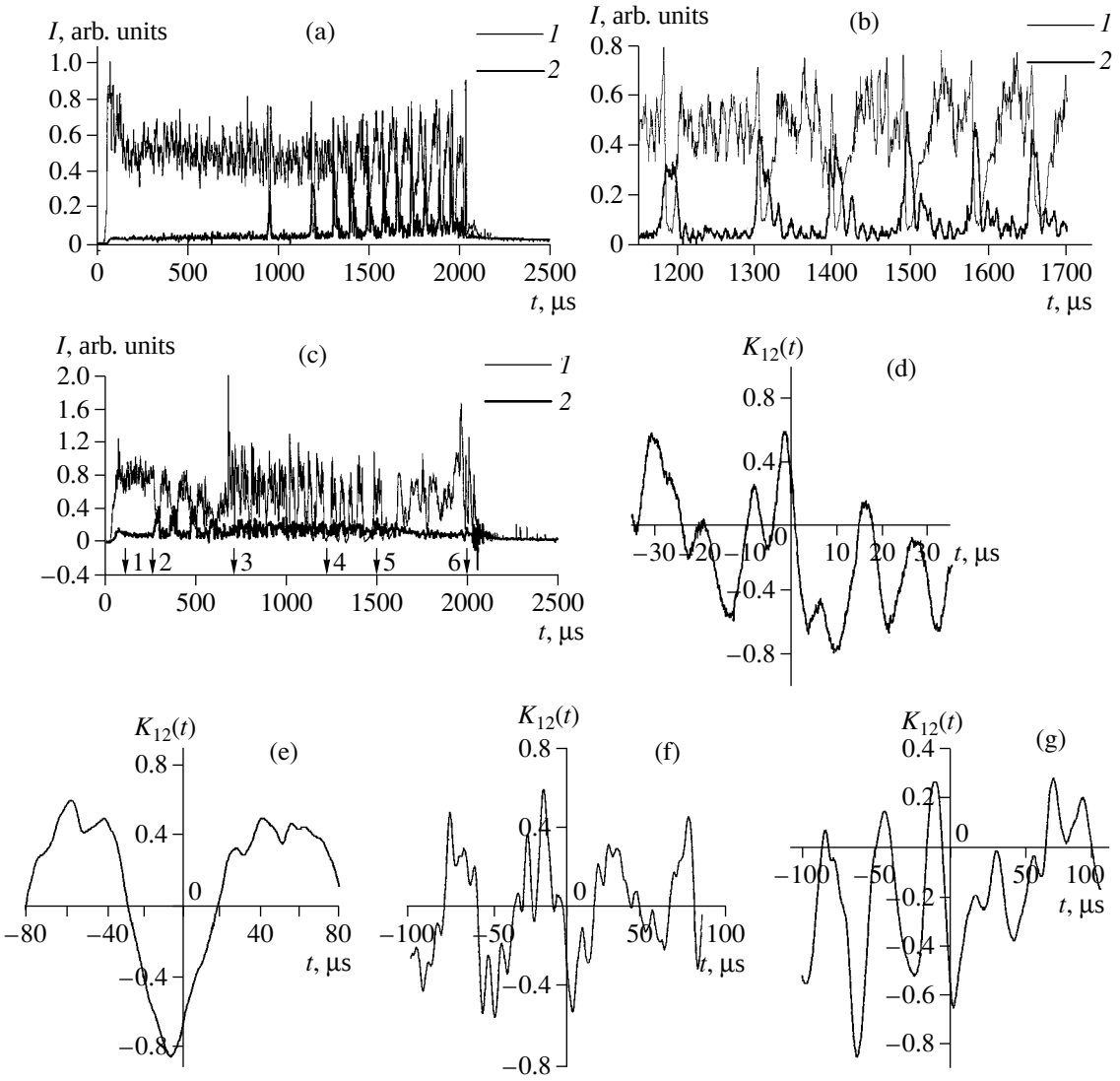

Fig. 6. (a) Waveforms of the saturation currents in the first probe (curve *1*) and second probe (curve *2*), placed at the entrance and exit ends of the waveguide, respectively, when the microwave power becomes regularly modulated (the average power being 19 kW). (b) The same waveforms over the time interval 1150–1700 μs. (c) Waveforms of the saturation currents in the first probe (curve *1*) and second probe (curve *2*) when the microwave power becomes irregularly modulated (the average power being 21 kW). Also shown is the cross-correlation function $K_{12}(\tau)$ for oscillations of the currents in the probes over time intervals of (d) 1–2, (e) 2–3, (f) 3–4, and (g) 4–5 from Fig. 6c.

end of the HPW) show that, at a power level of 5–7 kW, the plasma electron density at the waveguide ends is about 10^{10} cm^{-3}. As the power increases, the plasma electron density at the exit from the HPW increases to 10^{11} cm^{-3} (at a power of about 15 kW) and the plasma electron density at the entrance to the HPW also increases. Moreover, the plasma electron density at the entrance to the HPW becomes higher than that at the exit from the waveguide by a factor of 2 to 6. In the region where the microwave generation is most intense, the plasma density is lower. As a result, the plasma is inhomogeneous along the waveguide. A further increase in the power gives rise to a strong density modulation at frequencies of 15–200 kHz, the modulation depth being 80–100%. This is clearly seen in Fig. 6a, which shows waveforms of the plasma electron density obtained with the first probe (curve *1*) and the second probe (curve *2*) when the microwave power becomes regularly modulated (the average power being of about 19 kW), and in Fig. 6c, which shows waveforms at a higher power level (of about 21 kW). The characteristic feature of the waveforms is that the density perturbations recorded by the probes are in antiphase. This feature becomes especially pronounced if we look at the fragments of the waveforms of plasma density perturbations detected at higher sweep speeds of an oscillo-

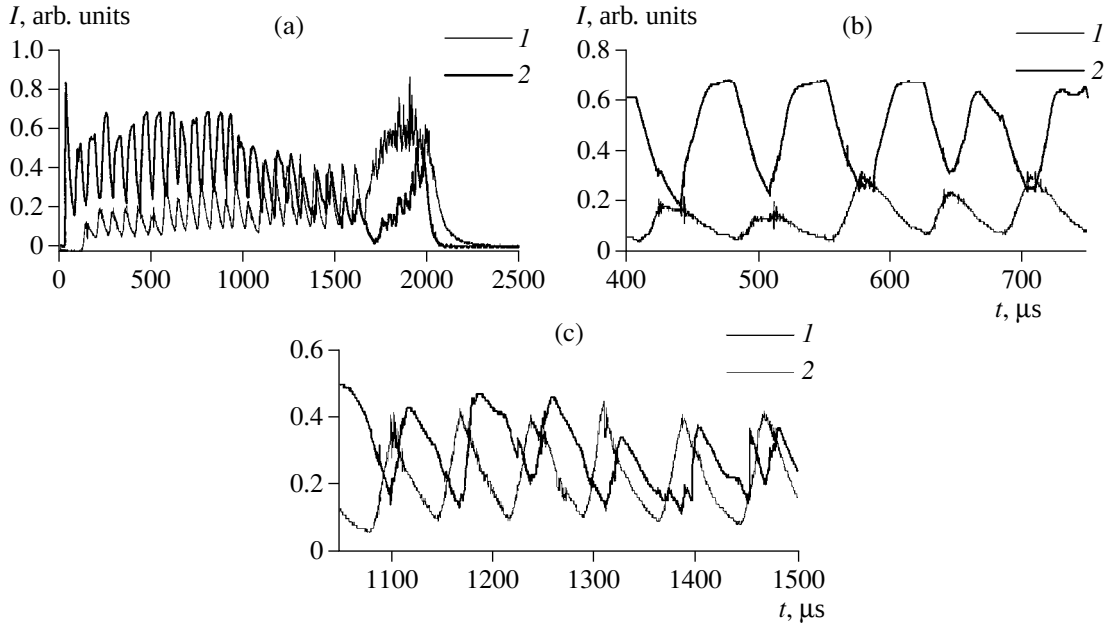

Fig. 7. (a) Waveforms of the current in the second probe (curve *1*) and microwave power in the output section (curve *2*) (the average microwave power is 21 kW). (b) The same waveforms over the time interval 400–750 μs. (c) The same waveforms over the time interval 1050–1500 μs.

graph (Fig. 6b). The same feature is characteristic of the density and power oscillations at the exit from the waveguide (Fig. 7).

A comparison between the waveforms in Figs. 6a–6c shows that, as the average microwave power increases, the frequencies of plasma density perturbations change during the beam-current pulse. Over the time interval under consideration, oscillations were recorded in two frequency bands: 0.2–0.7 and 0.03–0.1 MHz. The first probe also recorded higher frequency (up to 4 MHz) oscillations. The figures show that the frequency spectrum of the oscillations changes throughout the pulse: oscillations in the first band are followed by oscillations in the second band, and vice versa.

Figures 6d–6f show the cross-correlation function $K_{12}(\tau)$ for the plasma density perturbations recorded by the second (f_2) and first (f_1) probes over the time interval $[-T, T]$, during which the plasma density is perturbed predominantly at frequencies from one of the two bands.

The cross-correlation function is defined as

$$K_{12}(\tau) = ((\langle f_1^2\rangle - \langle f_1\rangle^2)^{1/2}(\langle f_2^2\rangle - \langle f_2\rangle^2)^{1/2}2T)^{-1} \times \int_{-T}^{T}[f_1(t) - \langle f_1\rangle][f_2(t+\tau) - \langle f_2\rangle]dt,$$

where the angular brackets denote the averaged value of a function.

We can see that the first peak in $K_{12}(\tau)$ is always shifted toward negative values of τ. This indicates that the density perturbations with complicated shapes propagate from the exit end to the entrance end of the waveguide and resemble a wave running at the velocity

$$v = \frac{l}{\tau_0},$$

where l is the distance between the probes and τ_0 is the time at which the cross-correlation function $K_{12}(\tau)$ reaches its first maximum value.

Knowing the propagation velocity of the plasma density perturbations at fixed frequencies, we can estimate the perturbation wavelength as

$$\lambda = vf^{-1} = \frac{l}{\tau_0 f},$$

where f is the mean frequency of the perturbations.

This estimate gives $\lambda \approx 15$–60 cm.

The frequency of slow magnetosonic waves can be estimated from the measured plasma electron temperature and the mass of the ions of the gas from which the plasma is produced. The estimated frequency is found to lie in the range from 15 kHz to 0.3 MHz, i.e., in the first frequency band over which oscillations were recorded in our experiments.

For powers higher than 20 kW, the electron plasma density also becomes perturbed at frequencies up to several megahertz. In this case, the first probe records perturbations at higher frequencies in comparison with the second probe. Note that, at the beginning of the beam-current pulse, the plasma density is modulated at

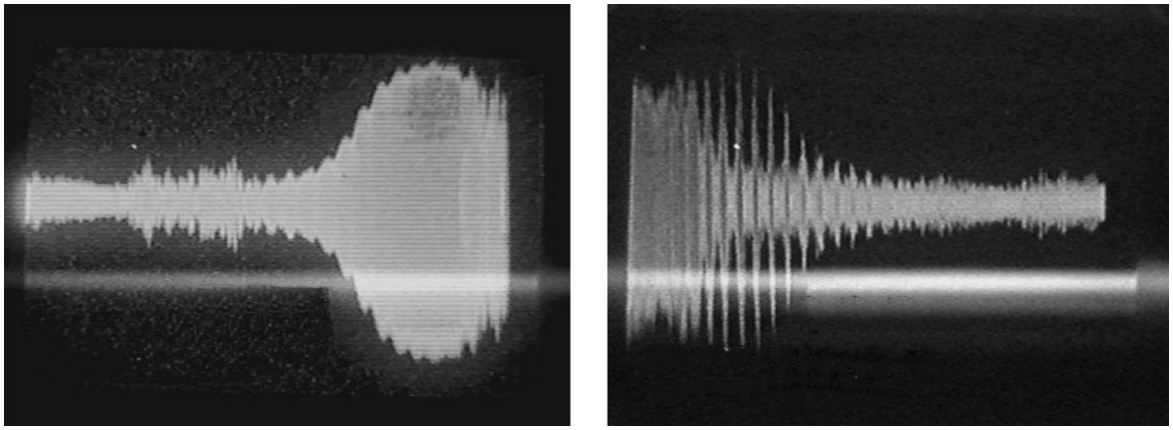

Fig. 8. Oscilloscope traces of the generated microwave pulses for each of the two halves of a 0.6-μs beam-current pulse, the sweeping time being 600 ns.

a level of 10–20% and, at the end of the current pulse, the modulation depth can amount to 100%.

Hence, the measurements of the plasma density perturbations with two probes positioned at the ends of the HPW show that the plasma maintained by a beam–plasma discharge in the waveguide is not only inhomogeneous along the waveguide but also unsteady. The density perturbations look like the waves running from the exit end to the entrance end of the waveguide.

3. Analyzing waveforms of the plasma density perturbations and microwave power during the beam-current pulse, we revealed the following characteristic features of the microwave generation.

First, note that the unsteady nature of the plasma density results in unsteady microwave generation: small perturbations of the beam current and/or plasma pressure may significantly change the recorded waveforms. Our experimental results are highly sensitive to the extent to which the slow-wave structure and the diagnostic chambers embedded in the experimental device are outgassed. The reproducibility of waveforms is in a large measure governed by the level of the microwave power recorded in the feeder lines at the exit from the waveguide.

The main feature of microwave generation is that the microwave power is governed by the plasma inhomogeneity in the HPW. The maximum power at the exit from the waveguide is achieved when the plasma density decreases from the entrance end to the exit end (Figs. 6, 7).

When the plasma density becomes modulated at frequencies of 15–200 kHz, the pulses with the maximum microwave power are recorded at the exit from the waveguide only when the plasma density decreases at the exit end and increases at the entrance end. The high-density plasma moves toward the entrance end, through which the electron beams are injected into the waveguide. As the plasma leaves the waveguide, the power level of the generated microwaves decreases. When the ratio of the plasma density at the exit end to that at the entrance end becomes approximately equal to 0.1–0.2, the microwave power starts to increase again.

The correlation between the generated microwave pulses and the plasma density perturbations is maintained almost to the end of the beam-current pulse (to the last several microseconds). The duration of microwave pulses may be several times longer than the period of the plasma density oscillations. This effect is observed when the oscillations of the plasma density and collector current at frequencies of 10–150 MHz are present in the recorded spectra. If this is not the case, the oscillations are quenched. In this spectral range, the envelope of the generated microwave pulses is also observed to experience oscillations. It is seen from the oscilloscope traces of the microwave pulses shown in Fig. 8 that oscillations at a frequency of 60 MHz appear at the front of the pulse envelope. These oscillations indicate that the end portion of the microwave pulse is modulated at a level of 100%. The oscillation amplitude decreases exponentially on a time scale equal to two oscillation periods. The modulation period coincides with the time required for a microwave signal to pass through the feedback circuit (which is associated with reflections from the ends of the slow-wave structure) and is close to the period of oscillations at frequencies near the lower hybrid resonance. It cannot be excluded that this circumstance is responsible for an additional external perturbation that promotes the effective growth of the lower hybrid waves. The wavelength of the lower hybrid waves is close to the wavelength of the generated microwaves, and the phase velocity of lower hybrid waves may be as high as the thermal velocity of the plasma electrons. These waves can be absorbed by the plasma. Microwave energy is converted to the energy of these waves and, then, to the energy of the plasma electrons. This effect can lead to

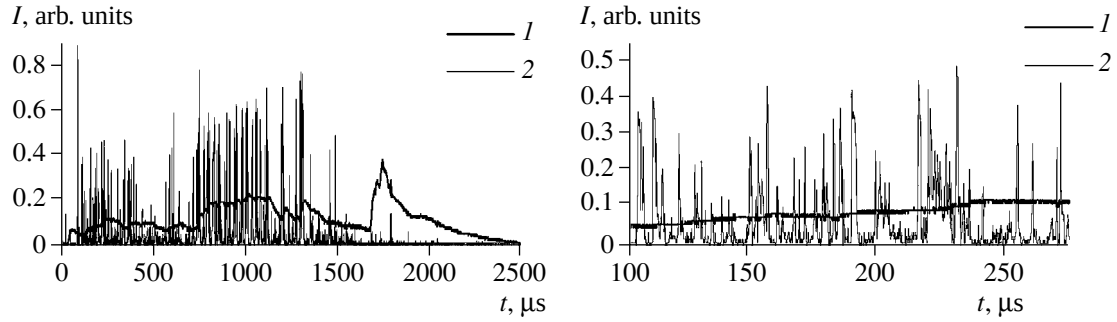

Fig. 9. (a) Waveforms of the current in the second probe (curve *1*) and microwave power in the output section (curve *2*) after the maximum power in Fig. 4 is reached. (b) The same waveforms over the time interval 200–340 μs.

additional damping of the excited microwaves, in which case the microwave generation conditions turn out to be even less favorable than would follow from the inhomogeneous and unsteady nature of the plasma.

After the maximum microwave power in Fig. 4 is achieved, the correlation between the signals from the probe currents breaks down and no correlation is observed between the plasma density perturbations and the generated microwave pulses, whose duration amounts to 0.5–1 μs. The time intervals between the generated pulses vary from 1 to 20 μs (Fig. 9). We can suppose that microwaves are emitted from local spatial regions whose length is much shorter than the waveguide length; these plasma regions travel toward the entrance end, through which the electron beams are injected into the waveguide. Also, we cannot exclude that such a periodic generation of microwaves is associated with local microwave discharges at the surface of the slow-wave structure.

5. CONCLUSION

The main result of our investigations can be formulated as follows. The inhomogeneous and unsteady nature of the LF plasma density perturbations plays an important role in microwave generation and in the transmission of the microwave power into the feeder line of the HPW. The LF perturbations are driven by the microwaves excited in the HPW by an electron beam.

The theory of beam–plasma interactions constructed with allowance for both the inverse effect of the microwave ponderomotive force on the plasma and additional gas ionization by microwaves correctly describes the development of the beam–plasma instability [12–14].

The microwave ponderomotive force and additional gas ionization give rise to LF ion oscillations (ion acoustic waves, magnetosonic waves, etc.) having rise times shorter than their half-period. The threshold power (25 kW) above which the generation of microwaves becomes stochastic was obtained by solving Eqs. (5) and (6) numerically. The accuracy with which the calculated threshold agrees with the experimentally measured one (20–22 kW) is quite satisfactory.

Our investigations show that, as a result of the excitation of high-power microwaves in the plasma created by an electron beam during a beam–plasma discharge in a slow-wave structure, the plasma density becomes nonuniform along the waveguide and varies in time. The microwave ponderomotive force drives the plasma into motion; as a result, the plasma escapes from the waveguide at the velocity of the LF ion waves. The electrodynamic parameters of the HPW also change as time elapses. Presumably, it is this circumstance that is responsible for the self-tuning of the phase velocity of the eigenmodes of the HPW to the time-varying beam velocity over the entire path of the beam through the waveguide during certain time intervals. As a result, the efficiency at which the electron beam energy is converted into microwave energy is high. Over these time intervals, the electron efficiency of microwave generation can attain 80–90%.

Under the action of a microwave field on the plasma in the HPW, the plasma density distribution is maintained in a steady state only over short time intervals. For this reason, high-power microwaves are generated in the form of short pulses. The plasma motion can be neglected only when the duration of the beam-current pulse is significantly shorter than the time scale on which the plasma density evolves to a level at which the hybrid waves of the waveguide become decoupled from the beam. Otherwise, the duration of the generated microwave pulse should be expected to decrease as the electron beam power increases. The shortening of the microwave pulse with increasing electron beam power was first observed in our previous experiments with a plasma maser [17, 18]. An increase in the power of a 0.5-μs electron beam by increasing the beam-electron energy from 150 to 200 keV and the beam current from 12 to 15 kA was accompanied by the shortening of a microwave pulse generated at a frequency of 12 GHz from 0.5 to 0.05 μs and by an increase in the pulse power from 60 to 300 MW. To achieve powers of 600–800 MW requires pulses with a duration no longer than 0.02–0.03 μs. An important point here is that short

microwave pulses were found to cause no erosion of the resonator wall or the elements of the window that links the resonator to the waveguide; luminous flames on these elements—a characteristic feature of microwave breakdown—also were not detected. On the other hand, plasma ions were always observed to be ejected from the system along the magnetic field [19].

We think that the continuous operation of high-power microwave beam–plasma oscillators and amplifiers can be made stable by creating a stable plasma whose density should increase along the waveguide in the direction opposite to the propagation direction of the beam. One of the possible ways of resolving this problem is to transfer part of the microwave power extracted from the waveguide to its entrance end and to operate with a magnetic field that is decreasing at the entrance to the waveguide. Such nonuniform local regions of the magnetic field can ensure the condition for electron cyclotron absorption of waves in a fixed frequency band [20]. This phenomenon can also be used to create selective absorbers and microwave couplers.

Controlling the length of the feedback circuit can make it possible to eliminate an unfavorable nonlinear coupling between the generated microwaves and oscillations at frequencies near the lower hybrid resonance.

The atomic numbers of the atoms of the gas from which the plasma is produced should be as large as possible. Another way is to continuously fill the slow-wave structure by a plasma from an auxiliary source.

Since, in all of the beam–plasma devices under consideration, the ions are observed to flow toward an electron gun, the cathode of the gun should be well protected from the ions or the device should be equipped with an electron gun with a plasma emitter. Additionally, the electron-gun chamber should be continuously evacuated by vacuum pumps at a rate high enough to maintain the pressure at the desired level [12, 13].

In our opinion, further research in this field should include a detailed investigation of the mechanism for spike-mode microwave generation and the mechanisms that ensure a high efficiency of conversion of the electron beam energy into microwave energy in a spatially inhomogeneous unsteady plasma. It is also necessary to seek methods for suppressing LF ion waves in order to achieve continuous generation of microwave electron waves in high-power beam–plasma devices and to develop and create slow-wave structures in which the fields would be distributed so as to prevent the onset of surface microwave discharges.

ACKNOWLEDGMENTS

This work was supported in part by the Center for Science and Technology of Ukraine, project no. 256.

REFERENCES

1. E. A. Kornilov, Doctoral Dissertation (Kharkov State Univ., Kharkov, 1974).
2. S. M. Krivoruchko, A. S. Bakaĭ, and E. A. Kornilov, Pis'ma Zh. Éksp. Teor. Fiz. **13**, 369 (1971) [JETP Lett. **13**, 262 (1971)].
3. A. S. Bakaĭ, A. K. Berezin, G. P. Berezina, *et al.*, in *Proceedings of the 5th International Conference on Plasma Physics, Madison, 1971*, Vol. 2, p. 113.
4. E. A. Kornilov, O. F. Kovpik, Ya. B. Faĭnberg, and I. F. Kharchenko, Zh. Tekh. Fiz. **35**, 1372 (1965) [Sov. Phys. Tech. Phys. **10**, 1064 (1965)].
5. E. A. Kornilov, O. F. Kovpik, Ya. B. Faĭnberg, *et al.*, Zh. Tekh. Fiz. **35**, 1378 (1965) [Sov. Phys. Tech. Phys. **10**, 1069 (1965)].
6. O. F. Kovpik and E. A. Kornilov, Zh. Tekh. Fiz. **43**, 2035 (1973) [Sov. Phys. Tech. Phys. **18**, 1284 (1973)].
7. E. A. Kornilov, O. F. Kovpik, S. M. Krivoruchko, and Ya. B. Faĭnberg, Fiz. Plazmy **24**, 1039 (1998) [Plasma Phys. Rep. **24**, 971 (1998)].
8. F. J. Agee, IEEE Trans. Plasma Sci. **26**, 235 (1998).
9. O. T. Loza and P. S. Strelkov, in *Digest of Technical Papers of International Workshop on High Power Microwave Generation and Pulse Shortening, Edinburgh, 1997*, p. 103.
10. Yu. P. Bliokh, M. G. Lyubarskiĭ, I. N. Onishchenko, *et al.*, Fiz. Plazmy **20**, 757 (1994) [Plasma Phys. Rep. **20**, 681 (1994)].
11. Yu. P. Bliokh, Ya. B. Fainberg, M. G. Lyubarsky, and V. O. Podobinsky, Proc. SPIE **3158**, 182 (1997).
12. Yu. P. Bliokh, E. A. Kornilov, L. A. Mitin, and Ya. B. Faĭnberg, Fiz. Plazmy **20**, 767 (1994) [Plasma Phys. Rep. **20**, 690 (1994)].
13. A. N. Antonov, Yu. P. Bliokh, Yu. A. Degtyar', *et al.*, Fiz. Plazmy **20**, 777 (1994) [Plasma Phys. Rep. **20**, 690 (1994)].
14. M. A. Zavjalov, L. A. Mitin, V. I. Perevodchikov, *et al.*, in *Proceedings of the 10th International Conference on High Power Particle Beams, San Diego, 1994*, Vol. II, p. 929; IEEE Trans. Plasma Sci. **22**, 600 (1994).
15. N. G. Matsiborko, I. N. Onishchenko, Ya. B. Faĭnberg, *et al.*, Preprint No. 71-40, KhFTI (Institute of Physics and Technology, Kharkov, 1971); Pis'ma Zh. Éksp. Teor. Fiz. **12**, 407 (1970) [JETP Lett. **12**, 281 (1970)].
16. O. V. Kozlov, *Electrical Probe in Plasma* (Atomizdat, Moscow, 1969).
17. Yu. E. Kolyada, Ya. B. Faĭnberg, E. A. Kornilov, *et al.*, Pis'ma Zh. Tekh. Fiz. **2**, 886 (1976) [Sov. Tech. Phys. Lett. **2**, 442 (1976)].
18. Yu. E. Kolyada, E. A. Kornilov, Ya. B. Faĭnberg, *et al.*, Fiz. Plazmy **2**, 795 (1976) [Sov. J. Plasma Phys. **2**, 442 (1976)].
19. Yu. E. Kolyada, Candidate's Dissertation (Kharkov State Univ., Kharkov, 1977).
20. O. F. Kovpik, E. A. Kornilov, and Yu. E. Kolyada, Ukr. Fiz. Zh. **17**, 820 (1972).

Translated by G. Shepekina

Plasma Physics Reports, Vol. 26, No. 12, 2000, pp. 1039–1044. Translated from Fizika Plazmy, Vol. 26, No. 12, 2000, pp. 1110–1115.

BEAMS IN PLASMA

Nonlinear Dispersion in a Plasma with a Relativistic Electron Beam

Yu. A. Volkov and V. B. Krasovitskiĭ

Keldysh Institute of Applied Mathematics, Russian Academy of Sciences, Miusskaya pl. 4, Moscow, 125047 Russia

Received April 13, 2000; in final form, May 28, 2000

Abstract—The nonlinear interaction of a relativistic electron beam with a plasma is investigated numerically on the basis of the extended notions of the physical quantities that enter the linear dispersion relation. Extending the notions of the wave frequency, wavenumber, and wave phase velocity to the nonlinear stage of an instability makes it possible to analyze the evolution of the Cherenkov and plasma resonances and to study how they affect the saturation of the wave amplitude. A model of the beam–plasma instability in which the growth rate is calculated from the corresponding linear hydrodynamic formula on the basis of the results obtained using a numerical kinetic model makes it possible to establish the applicability range of the hydrodynamic approximation for beams with different energies. © *2000 MAIK "Nauka/Interperiodica".*

The beam–plasma instability is known to occur at the intersection of the beam and plasma branches of oscillations, when small Langmuir oscillations grow exponentially with time [1–4]. The unstable mode saturates when the beam breaks up into bunches [5–11]. During this process, the wave traps resonant electrons and the electromagnetic field becomes modulated with a period of about the reciprocal of the linear growth rate. Since, in the region behind the first maximum of the wave amplitude, there is (on average) essentially no energy exchange between the beam and the wave over the period of the nonlinear oscillations [11], the beam energy is converted into the energy of the plasma wave mainly in the initial (exponential) stage of the instability. The relativistic increase in the electron mass lowers the instability growth rate, and the energy density of Langmuir oscillations becomes comparable to the beam energy density [12, 13].

The most general way of investigating the nonlinear interaction between an electron beam and a plasma is to numerically integrate the kinetic equations for the beam and plasma electrons along with the Maxwell equations for the electromagnetic field. This approach makes it possible to determine all of the physical parameters of the beam–plasma system throughout the nonlinear evolution of the beam and plasma. However, in practice, the solution of a spatially periodic one-dimensional problem is restricted to the investigation of the time dependence of the energy of Langmuir oscillations and the construction of the phase diagram of a beam [14, 15]. For this reason, most numerical studies in this area are in fact aimed at refining the maximum amplitude of oscillations in a plasma with a beam and yield less informative results in comparison with those obtained from linear theory.

Our purpose here is to interpret numerical solutions in more detail based on the extended notions of the physical quantities that are contained in the linear dispersion relation. Clearly, this approach requires that the wave frequency, wavenumber, and wave phase velocity be generalized so that, in the limit of small-amplitude perturbations, they coincide with those used in linear theory. We analyze the beam–plasma instability using a composite model in which the growth rate is calculated from the corresponding linear hydrodynamic formula on the basis of the results obtained from a numerical kinetic model. This approach enables us to establish the applicability range of the hydrodynamic approximation for beams with different energies.

For small Langmuir oscillations of the form $\sim\exp(ikx - i\omega t)$, the equations for a plasma with a monoenergetic relativistic electron beam yield the following dispersion relation, which determines the dependence of the frequency ω on the wavenumber k [1–4]:

$$1 - \frac{\omega_p^2}{\omega^2}\left(1 + \frac{3}{2}\frac{k^2 v_T^2}{\omega^2}\right) - \frac{\omega_b^2}{(\omega - kv)^2}\frac{1}{\gamma_0^3} = 0, \qquad (1)$$

where $\omega_p^2 = 4\pi n_p e^2/m$, $\omega_b^2 = (n_b/n_p)\omega_p^2$, n_b and n_p are the beam and plasma densities, v_0 is the initial beam velocity, $\gamma_0 = (1 - v_0^2/c^2)^{-1/2}$, and v_T is the thermal velocity of the plasma electrons.

We assume that all of the physical parameters to be calculated are periodic functions of the coordinate, the period being equal to the wavelength $\lambda = 2\pi v_0/\omega$ of the resonant mode. For time-dependent quantities, we

1063-780X/00/2612-1039$20.00

introduce the averaging operation

$$f(t) \equiv \langle f(t, x)\rangle = \frac{1}{\lambda}\int_0^\lambda f(t, x)dx. \quad (2)$$

The electric field $E(t, x)$ and its space and time derivatives are assumed to satisfy the Maxwell equations in the electrostatic approximation [16]:

$$\frac{\partial E}{\partial x} = 4\pi e(n_b + n_p - n_i), \quad \frac{\partial E}{\partial t} = -4\pi e(j_b + j_p), \quad (3)$$

where $n_{b,p}$ and $j_{b,p}$ are the beam and plasma current densities and n_i is the plasma ion density. Taking into account the fact that the ratios composed of the electric field and its space and time derivatives have the dimensionalities of length, time, and velocity, we define the wave frequency, wavenumber, and wave phase velocity in the nonlinear stage of the instability as

$$k(t) = \sqrt{\frac{\langle E_x^2\rangle}{\langle E^2\rangle}}, \quad \omega(t) = \sqrt{\frac{\langle E_t^2\rangle}{\langle E^2\rangle}}, \quad v_{ph}(t) = \frac{\omega(t)}{k(t)}. \quad (4)$$

We eliminate the derivatives E_x and E_t in (4) to obtain

$$k(t) = 4\pi e\sqrt{\frac{\langle (n_b + n_p - n_i)^2\rangle}{\langle E^2\rangle}},$$

$$\omega(t) = 4\pi e\sqrt{\frac{\langle (j_b + j_p)^2\rangle}{\langle E^2\rangle}}, \quad (5)$$

$$v_{ph}(t) = \sqrt{\frac{\langle (j_b + j_p)^2\rangle}{\langle (n_b + n_p - n_i)^2\rangle}}.$$

These formulas imply that $k(t)$, $\omega(t)$, and $v_{ph}(t)$ depend on the averaged moments of the beam and plasma distribution functions, which should be calculated by integrating the self-consistent set of equations numerically. The Langmuir frequencies of the beam and plasma electrons and the beam velocity can be defined in a similar manner:

$$\omega_{p,b}(t) = \frac{\omega_{p,b}}{\sqrt{n_{p,b}}}\langle\sqrt{n_{p,b}(t, x)}\rangle, \quad v(t) = \frac{\langle j_b(t, x)\rangle}{\langle n_b(t, x)\rangle}. \quad (6)$$

We continue to draw an analogy with linear theory and switch to the dimensionless variables

$$\mathrm{K} = \frac{kc}{\omega}, \quad \Omega = \frac{\omega}{\omega_0}, \quad \Omega_p = \frac{\omega_p}{\omega_0}, \quad \Omega_b = \frac{\omega_b}{\omega_0},$$

$$V = \frac{v}{c}, \quad V_{ph} = \frac{v_{ph}}{c}, \quad V_T = \frac{v_T}{c}, \quad \Gamma = \frac{1}{\sqrt{1 - V^2}},$$

$$\tau = \omega_0 t, \quad \omega_0 = \omega(0).$$

Then, we define the nonlinear dielectric function of a plasma with a beam as

$$\varepsilon(\Omega, \mathrm{K}) = \left[\Omega^2 - \Omega_p^2\left(1 + \frac{3}{2}\frac{V_T^2}{V_{ph}^2}\right)\right] \times (\Omega - \mathrm{K}V)^2 - \frac{\Omega_b^2\Omega^2}{\Gamma^3}. \quad (7)$$

The dynamics of the instability of a beam–plasma system was investigated numerically by solving the Vlasov equations for the beam and plasma electrons by a particle-in-cell method. Formula (7) makes it possible to establish the limits of applicability of the linear dispersion relation $\varepsilon[\Omega(0), \mathrm{K}(0)] = 0$ in the nonlinear stage of the instability. The positive values of the dielectric function, $\varepsilon(\Omega, \mathrm{K}) > 0$, indicate that the beam–plasma system has evolved into a nonlinear stage.

The electrons interact with the wave under the conditions of the Cherenkov and plasma resonances. Nonlinear variations of the beam modulation frequency $\mathrm{K}V$ and plasma frequency Ω_p cause the beam and plasma electrons to lose their synchronism with the wave; as a result, the wave amplitude grows at a lower rate. The role played by each of these effects in the nonlinear saturation of the instability is described by the functions

$$R_b = \Omega - \mathrm{K}V, \quad R_p = \Omega - \Omega_p \quad (8)$$

in formula (7). The time evolutions of these functions are illustrated by curves *1* and *2* in Fig. 1. Although the parameters $\mathrm{K}V$ and Ω_p correspond to the highly nonlinear stage, the dielectric function $\varepsilon(\Omega, \mathrm{K})$ (curve *3*) changes only slightly as compared to the linear theory up to the time at which the energy density of Langmuir oscillations, $W = \langle E^2\rangle/4\pi n_b mc^2\gamma_0$ (curve *4*), reaches its maximum.

For a nonrelativistic beam ($\gamma_0 < 1.75$), the field amplitude saturates because of the deviation R_b of the frequency of Langmuir oscillations from the Cherenkov resonance frequency. The higher the beam energy, the larger the deviation R_p from the plasma resonance frequency. For $\gamma_0 = 3$, these deviations become comparable in magnitude when the function $W(\gamma_0)$ reaches its maximum [11]. For a higher energy beam, the plasma resonance is destroyed earlier than the Cherenkov resonance, and the growth of the oscillation amplitude slows because the wave properties of the plasma change. However, our simulations show that, in the energy range under consideration, the nonlinear saturation of the field amplitude is always associated with the separation of the beam into individual bunches.

The beam is unstable when its phase is synchronized with the phase of Langmuir oscillations; the phase synchronization condition holds for oscillations with phase velocities $V_{ph} < V_0$. This conclusion, which

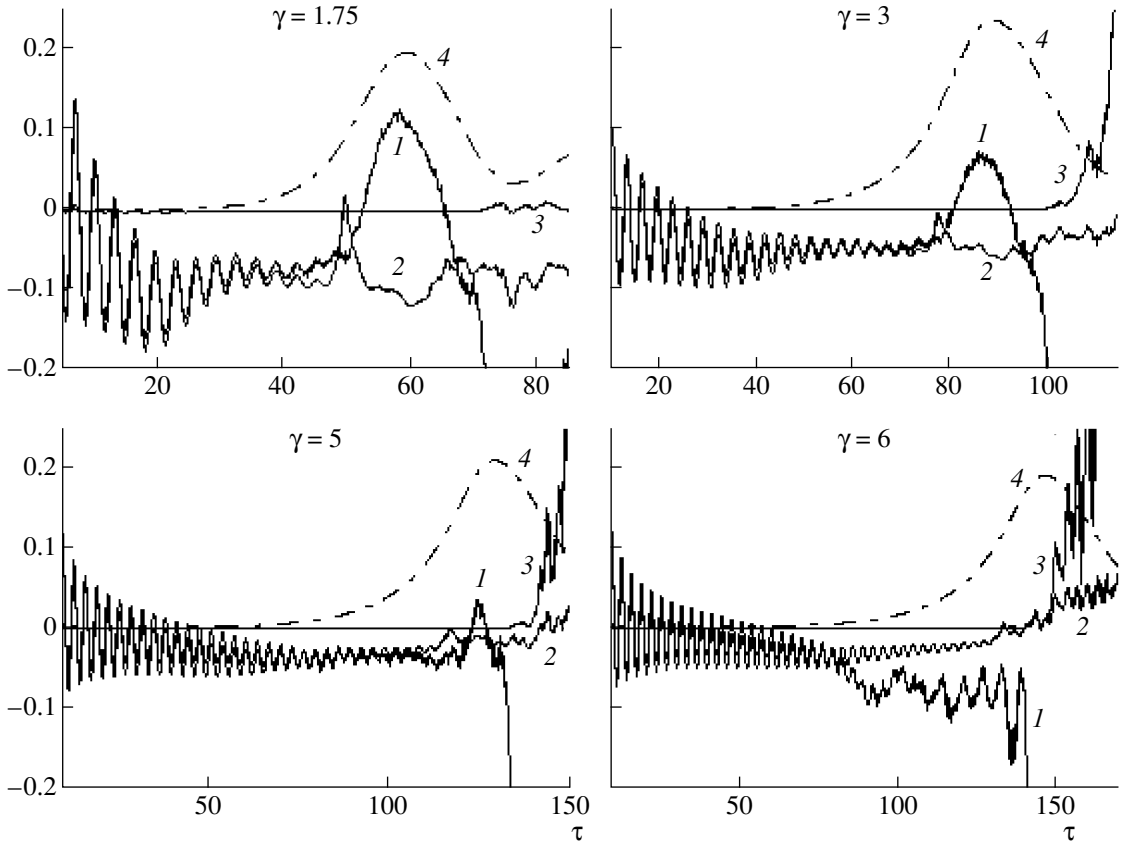

Fig. 1. Nonlinear evolution of (*1*) the deviation R_b from the Cherenkov resonance frequency, (*2*) the deviation R_p from the plasma resonance frequency, and (*3*) the dielectric function $\varepsilon(\Omega, K)$ of a plasma with a beam for different initial values of the relativistic factor γ. Curves *4* illustrate the evolution of the energy density W of Langmuir oscillations.

was drawn from linear theory, is confirmed by our numerical experiment, which, in particular, permits us to follow the evolution of the beam velocity V and wave phase velocity V_{ph} in the nonlinear stage of the instability. The numerical results obtained for beams of different energies are displayed in Fig. 2. An analysis of the results illustrated shows that, in the range $\gamma_0 \le 3$, the beam velocity decreases more rapidly than the wave phase velocity and, in the range $\gamma_0 > 3$, the situation is the opposite. In the energy range $\gamma_0 \approx 3$, the conditions for the beam–plasma interaction are optimum: the phase resonance takes place throughout the nonlinear stage of the instability [17].

According to Fig. 1, the dispersion relation $\varepsilon(\Omega, K) \approx 0$ is valid up to the time at which the beam breaks up into bunches and the "warm" correction to the electron plasma frequency in formula (7) remains small: $V_T^2/V_{ph}^2 \approx 10^{-3}$. We thus conclude that, in the first stage of the instability, the nonlinear relaxation of the beam–plasma system is governed by the time evolution of the linear growth rate. For a low-density beam propagating in a cold ($V_T = 0$) plasma, the dispersion relation has the solution $\Omega = KV + \Delta\Omega$, where the small correction to the frequency, $|\Delta\Omega|/KV \ll 1$, satisfies the equation

$$\left(\frac{\Delta\Omega}{KV}\right)^2\left[\frac{\varepsilon(KV)}{2} + \frac{\Delta\Omega}{KV}\right] = \frac{\Omega_b^2}{2\Omega_p^2\Gamma^3} = \mu,$$
$$\varepsilon(KV) = 1 - \frac{\Omega_p^2}{K^2V^2}. \tag{9}$$

For fixed μ, the complex roots of (9) depend only on the plasma dielectric function at the beam modulation frequency KV.

In Fig. 3, curves *1* illustrate the behavior of the nonlinear plasma dielectric function

$$R = R_p - R_b = KV - \Omega_p \approx \varepsilon(KV)/2 \tag{10}$$

and curves *2* reflect time evolutions of the hydrodynamic growth rate. The dotted curves *3* refer to the growth rate obtained by numerical integration.

In our hybrid model of the beam–plasma instability, the growth rate is calculated with the help of formula (9) from linear theory on the basis of the results obtained from the nonlinear numerical model. This approach makes it possible to interpret the nonlinear

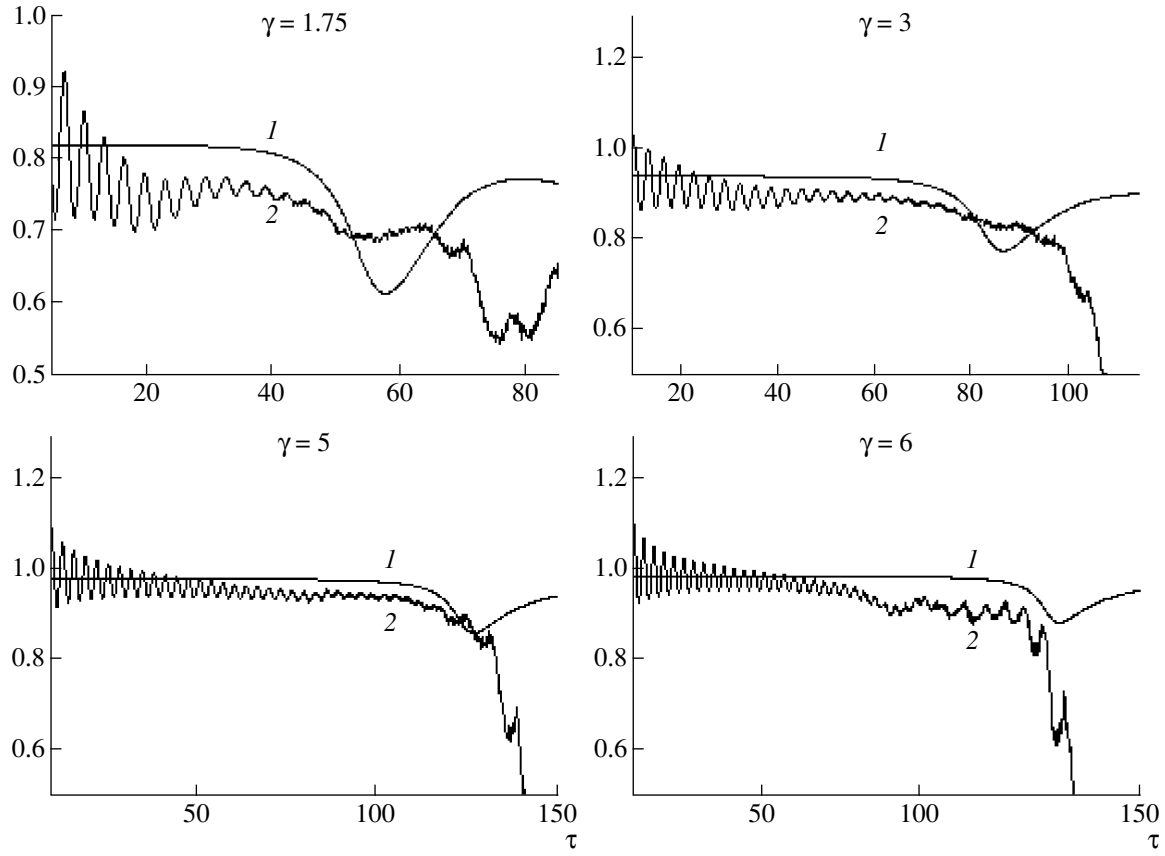

Fig. 2. Nonlinear evolution of (*1*) the beam velocity V and (*2*) the wave phase velocity V_{ph} for beams with different energies.

saturation of the oscillation amplitude as the evolution of the hydrodynamic growth rate from its maximum value $\delta_m = (\sqrt{3}/2)\mu^{1/3}\Omega_p$ to the instability threshold

$$\delta_+ = (2\mu)^{1/3}\left[1 - \frac{\varepsilon(KV)}{\varepsilon_c}\right]^{1/2}\Omega_p \quad \varepsilon_c = 3(2\mu)^{1/3}. \quad (11)$$

For a nonrelativistic beam, the plasma density can be assumed to be linear, $\Omega_p \approx 1$, and the nonlinear saturation of the oscillation amplitude is governed by the time evolution of the beam modulation frequency KV. Numerical integration shows that, as Langmuir oscillations grow, the mean beam velocity V decreases and the wavenumber K increases monotonically. The first effect dominates in the initial stage of the instability, when a significant fraction of the beam energy is expended on the excitation of Langmuir oscillations. Consequently, due to the increase in the amplitude of the fastest growing mode, the plasma dielectric function becomes negative, $\varepsilon(KV) < 0$, in which case the oscillations grow at a rate $\delta_- \approx \sqrt{2\mu/|\varepsilon(KV)|}\,\Omega_p$. The onset of the satellite modes that grow at low rates is accompanied by the redistribution of the oscillation energy among the modes in a narrow Langmuir wave packet [14] and the increase in the effective wavenumber K. Accordingly, the beam modulation frequency KV, first, falls off to its minimum value and, then, starts to increase. As the instability saturates, the dielectric function $\varepsilon(KV)$ becomes positive, in which case the growth rate equals zero.

In the high-energy range $\gamma_0 \approx 3$–5, in which the nonlinear decrease in the Langmuir frequency of the plasma electrons is already observed [10], Langmuir oscillations also saturate in an essentially hydrodynamic fashion. However, for $\gamma_0 = 6$, the correlation between hydrodynamic and kinetic (numerical) solutions is found to worsen. According to our numerical experiment, the dielectric function $\varepsilon(KV)$ increases monotonically and rapidly becomes positive, in which case unstable Langmuir oscillations should saturate nonlinearly by the time $\tau \approx 100$, at which the hydrodynamic growth rate vanishes. However, the oscillations continue to grow up to the time $\tau \approx 150$. An analysis of the phase diagram of a beam shows that multiflow motion already appears at $\tau \approx 125$; consequently, the instability saturates after the beam has broken up into bunches.

Hence, we have developed a numerical model in which the key parameters in linear theory—the wave frequency, wavenumber, and wave phase velocity—are extended to the nonlinear stage of the instability and are

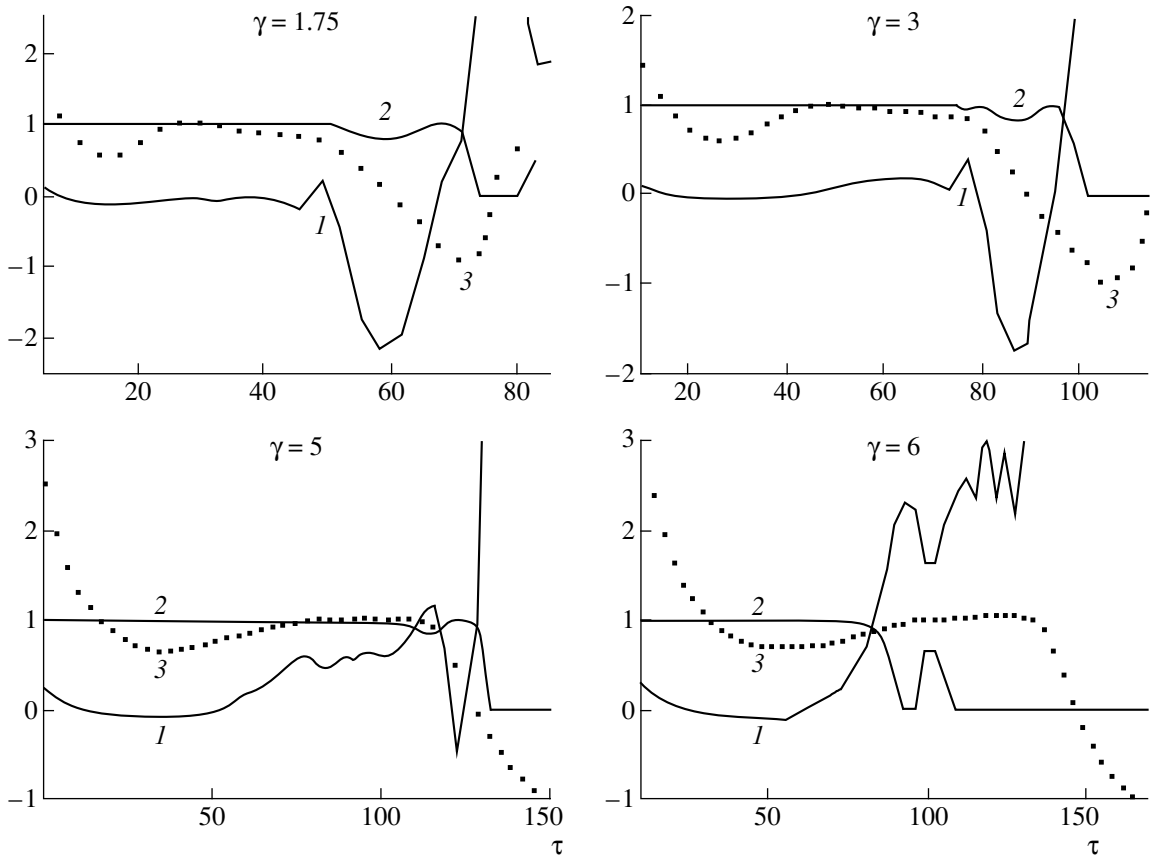

Fig. 3. Nonlinear evolution of (*1*) the plasma dielectric function $\tilde{R} = R/\mu^{1/3}$ and (*2*) the hydrodynamic growth rate $\delta(R)/\delta_m$. Curves *3* refer to the numerically calculated growth rate $\delta(\tau)/\delta_m = (2\tau)^{-1}\ln(W/W_0)$.

used, together with the field energy density, as the global parameters of an unstable beam–plasma system.

We have shown that the beam energy is converted into the energy of Langmuir oscillations and the mean beam velocity decreases. The averaged (over the spatial period of the Langmuir wave) frequency of the fastest growing mode oscillates around the initial Langmuir frequency $\Omega \approx 1$ of the plasma electrons. Consequently, when the Langmuir wave spectrum shifts toward shorter wavelengths ($K > 1$), the wave phase velocity in the nonlinear stage of the instability decreases. The asynchronous nature of these processes is the reason for the saturation of unstable Langmuir oscillations in a plasma with a nonrelativistic beam.

In the case of relativistic beams, the oscillation energy density is higher, the plasma density is modulated, and the Langmuir frequency averaged over the spatial period is lower. The last effect destroys the plasma resonance, thereby limiting the ability of the plasma to serve as a resonant waveguide structure for high-energy electron beams.

During nonlinear relaxation, the beam and plasma parameters under consideration change. However, the physical state of a beam–plasma system depends on the particular combination of these parameters that enters the plasma dielectric function: $\varepsilon(0) = 1 - \omega_p^2/k^2 v_0^2$. The instability saturates nonlinearly when the dielectric function, which is initially equal to $\varepsilon(0) = -\mu^{1/3}$, starts to increase and becomes positive, $\varepsilon(t) > 0$. In the case $n_b/n_p = 1/64$, which we have analyzed above, the time scale on which the instability saturates depends on the beam energy. For $\gamma_0 \approx 3$ (when the ratio of the energy density of Langmuir oscillations to the beam energy density is maximum), this time is the longest.

ACKNOWLEDGMENTS

We are grateful to S.S. Moiseev and A.A. Rukhadze for fruitful discussions.

REFERENCES

1. D. Bohm and E. P. Gross, Phys. Rev. **75**, 1864 (1949).
2. A. I. Akhiezer and Ya. B. Faĭnberg, Zh. Éksp. Teor. Fiz. **69**, 555 (1949).
3. Ya. B. Faĭnberg, At. Énerg. **11**, 313 (1961).

4. A. B. Mikhailovskii, *Theory of Plasma Instabilities* (Atomizdat, Moscow, 1975; Consultants Bureau, New York, 1974), Vol. 1.
5. N. G. Matsiborko, I. N. Onischenko, V. D. Shapiro, and V. I. Shevchenko, Plasma Phys. **14**, 591 (1972).
6. L. E. Thode and R. N. Sudan, Phys. Rev. Lett. **30**, 732 (1973).
7. L. E. Thode and R. N. Sudan, Phys. Fluids **18**, 1552 (1975).
8. R. N. Sudan, in *Basic Plasma Physics: Supplement to the Second Volume*, Ed. by A. A. Galeev and R. N. Sudan (Énergoatomizdat, Moscow, 1984; North-Holland, Amsterdam, 1984).
9. M. V. Kuzelev and A. A. Rukhadze, in *Electrodynamics of Dense Electron Beams in a Plasma* (Nauka, Moscow, 1990), p. 59.
10. V. B. Krasovitskiĭ, Fiz. Plazmy **22**, 728 (1996) [Plasma Phys. Rep. **22**, 659 (1996)].
11. Yu. A. Volkov and V. B. Krasovitskiĭ, Fiz. Plazmy **26**, 78 (2000) [Plasma Phys. Rep. **26**, 70 (2000)].
12. Ya. B. Faĭnberg, V. D. Shapiro, and V. I. Shevchenko, Zh. Éksp. Teor. Fiz. **57**, 966 (1969) [Sov. Phys. JETP **30**, 528 (1969)].
13. R. I. Kovtun and A. A. Rukhadze, Zh. Éksp. Teor. Fiz. **58**, 1709 (1970) [Sov. Phys. JETP **31**, 915 (1970)].
14. V. D. Shapiro and V. I. Shevchenko, Izv. Vyssh. Uchebn. Zaved., Radiofiz. **19**, 767 (1976).
15. A. A. Ivanov, in *Physics of Highly Nonequilibrium Plasma* (Atomizdat, Moscow, 1977), p. 55.
16. I. A. Akhiezer, R. V. Polovin, *et al.*, *Plasma Electrodynamics*, Ed. by A. I. Akhiezer, (Nauka, Moscow, 1974; Pergamon, Oxford, 1975).
17. V. B. Krasovitskiĭ and L. A. Mitin, Fiz. Plazmy **23**, 230 (1997) [Plasma Phys. Rep. **23**, 209 (1997)].

Translated by O. Khadin

Plasma Physics Reports, Vol. 26, No. 12, 2000, pp. 1045–1053. Translated from Fizika Plazmy, Vol. 26, No. 12, 2000, pp. 1116–1125.

ISOTOPE SEPARATION

An Efficient Method for Extracting Plasma Ions in Laser Isotope Separation Systems

N. S. Demidova and V. A. Mishin[†]

Institute of General Physics, Russian Academy of Sciences, ul. Vavilova 38, Moscow, 117942 Russia

Received November 24, 1999; in final form, May 15, 2000

Abstract—The possibility of using a Hall-current accelerator to extract ions from a partially ionized plasma produced by selective laser isotope photoionization of atomic vapor is examined. A mechanism for ion acceleration is investigated using one-dimensional time-dependent equations of two-fluid magnetohydrodynamics. The current cutoff due to the ion space charge is prevented by electron emission. It is shown that, at an accelerating voltage of 25–50 V and emission current density of several mA/cm^2, the ion component is accelerated throughout the entire plasma volume up to a velocity of ~10^5 cm/s in a few microseconds. The influence of resonant charge exchange and secondary ionization by electrons on both the acceleration dynamics and selectivity degradation is taken into account. It is shown that the Hall-current extractor allows one to avoid selectivity degradation even when the plasma size exceeds the charge-exchange mean free path by one order of magnitude.

1. INTRODUCTION

In recent years, an isotope separation technique based on atomic vapor laser isotope separation (AVLIS) has attracted considerable interest [1]. The method is based on the line shift in the electronic absorption spectra of atoms or molecules of different isotopes (isotope shift). The physics of the method lies in the selective photoionization of the atoms of an isotope to be separated out, which changes their properties with respect to the action of external factors (e.g., electric or magnetic fields). The separation technology involves the formation of a free molecular flow of the vapor of a substance to be separated through the irradiation zone, ionization of the atoms of a desired isotope with laser radiation, and extraction of the ions from the produced plasma.

The selectivity of laser ionization is very high (the degree of ionization of the desired isotope can be three to five orders higher than that of other isotopes), but it is difficult to maintain such a high selectivity in the stage of ion extraction. Thus, resonant charge exchange of the produced ions with the atoms of other isotopes or ionization of atoms by electrons decreases the selectivity of the method. In order to avoid the sputtering of the collector material and generation of secondary charged particles, the ions of the desired isotope should not acquire too much energy. Therefore, the problem of extraction is to efficiently pick up ions from the atomic flow without significant selectivity degradation.

To specify the problem, we describe the typical conditions of ion extraction. The atoms pass through the irradiation zone (which is generally a cylinder of several meters in length and 2–4 cm in diameter) with a velocity of $(0.4–1) \times 10^5$ cm/s. The density of atoms in the irradiation zone is 10^{13}–10^{14} cm^{-3}. Since the concentration of the isotope to be separated out usually ranges within 0.1–10%, the density of the ions in the plasma column ranges from 10^{10} to 10^{12} cm^{-3}. Resonant charge exchange, whose cross section can be very high (e.g., ~3×10^{-14} cm^2 for ytterbium), is the most dangerous process leading to selectivity degradation. For an atom density of 10^{14} cm^{-3}, the ion mean free path is 3 mm, which is one order of magnitude less than the characteristic diameter of the laser plasma. Under these conditions, it is necessary to either decrease the vapor density (thus reducing the capacity of an isotope separator) or accelerate the ions with a short pulse over the charge-exchange mean free path. In the latter case, the charge exchange between the accelerated ion and a neutral atom does not deteriorate the separation factor because it is not accompanied by momentum transfer. Therefore, the resulting fast neutral atom of the desired isotope will continue its motion toward the collector, whereas the newborn ion of the waste isotope will keep moving with the atomic beam. Note that this method requires simultaneous acceleration of the ions throughout the entire plasma volume.

The key role of the extraction problem was understood as soon as the AVLIS technique was proposed for industrial separation of uranium isotopes. A number of extraction methods were examined (most of them were proposed between 1973 and 1976). The most complete review of these methods is given in [1, 2]. It is noteworthy that one of the first methods was described in a patent by Janes [3], who proposed to use the Hall-current accelerator to extract ions. However, due to the specific patent language and the lack of a clear physical

[†] Deceased.

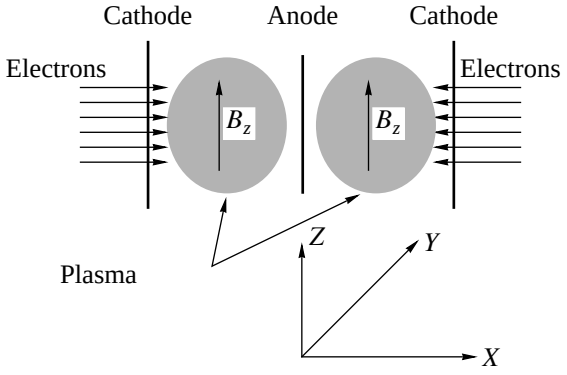

Fig.1. Schematic of a Hall-current extractor.

picture of the process, there were no publications devoted to the investigation of such an extractor. Note that, although Hall-current plasma accelerators have been known for a long time and are still used, e.g., in plasma thrusters, extraction conditions in a laser isotope separation system impose specific limitations on the acceleration regime and it is not immediately clear whether the Hall-current accelerator matches these limitations. In this paper, we will show that the Hall-current accelerator meets all the requirements and holds promise for use in laser isotope separation systems.

In order to clarify the advantages of the Hall-current extractor, we briefly consider both the process of ion extraction from an unmagnetized plasma under the action of an electric field and the applicability limits of this method. Note that, due to its simplicity, this type of electrostatic extractor (EE) is widely used [4–6]. The ions in the EE are accelerated by the electric field created by applying a voltage of 0.1–1 kV to a plasma-filled gap. Because of the fast charge separation occurring on a time scale of about the period of electron plasma oscillations, the electric field is shielded in the bulk of the plasma and only acts on the ions inside a thin sheath with a thickness on the order of $(U_0/4\pi en_0)^{1/2}$. Under these conditions, the ion current is limited by the ion space charge and is only determined by ambipolar diffusion, which depends on the electron temperature, the characteristic current velocity being $v = (2kT_e/M)^{1/2}$ [5]. As a result, the extraction time substantially exceeds that recorded in the absence of a volume charge. Thus, for an extractor with the interelectrode spacing $d = 2.75$ cm, applied voltage $U_0 = 300$ V, ion density $n_i = 10^{10}$ cm^{-3}, and electron temperature $T_e = 1$ eV, the calculated extraction time is 66 μs [5]. This time is too long to achieve high selectivity because, for an atom density of 10^{14} cm^{-3}, the charge exchange time is several microseconds. The extraction time can be reduced by heating the electron component (e.g., by an RF electric field [6]). However, an analysis of the data available in the literature shows that this method does not provide a sufficiently short extraction time. Thus, although the electrostatic method of extraction is easy to realize, it does not allow uniform ion acceleration throughout the entire plasma volume and may be applied only to a highly rarefied plasma or if a high separation factor is not required.

The above disadvantages of the EE can be eliminated if the ions are accelerated in the electric field directed perpendicular to the magnetic field such that the electrons are magnetized and the ions move freely. In order for this to take place, the condition $r_e \ll d < r_i$ must be satisfied, where r_e and r_i are the Larmor radii of electrons and ions, respectively. In this case, the electrons do not move along the electric field but drift in the $\mathbf{E} \times \mathbf{B}$ direction with the velocity cE/B, thus producing the Hall current. If this current is closed, then the charges cannot be separated during the characteristic time of the electron motion (on the order of the period of electron plasma oscillations) and the electric field penetrates into the magnetized plasma. Therefore, the magnetic field acts as if it makes the electrons heavier, thus increasing the time interval during which the electric field is not shielded due to charge separation. Within this time interval, the electric field freely penetrates into the plasma and accelerates the ions throughout the entire plasma volume. The acceleration terminates only when the ion space-charge sheath is formed near the cathode. To prevent charge separation, we propose to emit electrons from the cathode. Calculations show that, even when the plasma is weakly magnetized (the Hall factor is 10–20), a low electron emission current can substantially compensate for the ion space charge. However, the emitted electrons may cause additional nonselective ionization of atoms and decrease the separation factor. Both acceleration and secondary ionization depend strongly on the plasma and neutral-atom densities and on the electric and magnetic fields. This makes it necessary to numerically simulate the Hall-current extractor in order to optimize the extraction regime.

In this paper, we consider the above method of ion extraction within a one-dimensional model and demonstrate its feasibility. A schematic of the extractor is shown in Fig. 1. The cathode and anode are plates separated by 1–2 cm. The electrode dimensions are about 10 cm along the *z*-axis and 1 m along the *y*-axis. The laser beam ionizing the atomic vapor is directed along the *y*-axis. The free molecular flow of the atomic vapor is directed along the *z*-axis, and the Hall current is closed around the anode along the *y*-axis.

The paper is organized as follows. In Section 1, we describe the mathematical model of extraction. In Section 2, we study the dynamics of extraction without taking plasma kinetics into consideration. Finally, in Section 3, we consider the full picture of the extraction process taking into account charge exchange, secondary ionization of neutral atoms by electrons, and the influence of these processes on the plasma dynamics.

2. MATHEMATICAL MODEL OF THE EXTRACTION

To validate the model used, we specify the characteristic parameters of the problem. The neutral atom density is assumed to be $N_0 = 10^{14}$ cm^{-3}. We consider a quasineutral plasma consisting of electrons and ions of heavy elements of mass ~200 amu. The initial plasma density is $n_i = n_e = 10^{11}$ cm^{-3}. Further, we also consider the cases where the initial plasma density is one order of magnitude lower or higher. The plasma is produced in an external magnetic field. The initial temperatures of both the electron and ion components are 0.1 eV. The electric field is directed along the *x*-axis, and the magnetic field is directed along the *z*-axis. The anode is at the origin of coordinates, and the cathode is at a distance of $L = 2$ cm from the anode. According to the adopted one-dimensional model, the plasma is unbounded in the directions perpendicular to the *x*-axis. The inherent magnetic field of the plasma current is neglected. The one-dimensional approach is justified by the fact that the plasma moves freely along the *z*-axis and this motion is independent of motion along the *x*-axis. The characteristic scale length along the *y*-axis exceeds the interelectrode spacing by two orders of magnitude; hence, motion along the *y*-axis can be neglected. We plan to consider the effects related to the closing of the Hall current along the *y*-axis in a subsequent study within a two-dimensional model.

The following kinetic parameters correspond to the above initial values. The electron plasma frequency is $\omega_{Le} = 1.5 \times 10^{10}$ s^{-1}, the ion plasma frequency is $\omega_{Li} = 3 \times 10^7$ s^{-1}, the electron–ion collision frequency is $\nu_{ei} = 7 \times 10^7$ s^{-1}, the Debye radius is $r_d = 10^{-3}$ cm, and the electron–atom collision frequency at $T_e = 0.1$ eV is $\nu_{ea} = 1.5 \times 10^6$ s^{-1}. The electron mean free path is $l_{ei} = v_{Te}/\nu_{ei} = 0.25$ cm, which is much less than the interelectrode spacing. The minimum and maximum values of the magnetic field can be evaluated from the conditions for ions to be unmagnetized and for electrons to be magnetized. The first of these conditions leads to the inequality $v_i/\omega_i > d$, from which we obtain $B < 300$ G. The minimum value of the magnetic field is to be derived from the comparison of the electron gyroradius with the interelectrode spacing: $m_e c^2 E/eB^2 < d$. For the electric field $E_x = 50$ V/cm (at the anode potential $\varphi = 100$ V), we obtain $B > 10$ G. At $B_0 = 100$ G, the electron and ion cyclotron frequencies are $\omega_e = 1.7 \times 10^9$ s^{-1} and $\omega_i = 6 \times 10^3$ s^{-1}, respectively, and the Hall parameter is $\omega_e\tau = 30$, where $1/\tau$ stands for the total electron collision frequency, which is defined as $1/\tau = \nu_{ei} + \nu_{ea}$ (here, ν_{ei} and ν_{ea} are the electron–ion and electron–atom collision frequencies, respectively).

The plasma dynamics was simulated by using a system of one-dimensional time-dependent equations of two-fluid magnetohydrodynamics. The hydrodynamic approach is justified by the fact that the electrons are magnetized (i.e., the Debye radius is much less than the electron Larmor radius) and that the electron mean free path is small compared to the extractor interelectrode spacing. Both of these conditions are met at the initial instant. In the course of extraction, the electron temperature grows and the plasma can become collisionless. Nevertheless, even in this case, the electrons can be described within the hydrodynamic model because they remain magnetized in the plane perpendicular to the magnetic field. The hydrodynamic approach also applies to ions because their temperature is low. The magnetization conditions are violated near the electrodes. Strictly speaking, the hydrodynamic approximation is not valid there; however, the sheath thickness is so small that it insignificantly affects the dynamics of extraction. The boundary conditions are derived from the balance of unidirectional particle flows, ignoring the magnetic field and assuming the distribution function to be close to Maxwellian.

The plasma was described by a system of MHD equations in Eulerian coordinates:

$$\frac{\partial n_{iA}}{\partial t} + \frac{\partial}{\partial x}(n_{iA} v_{ixA}) = -\nu_{AB} n_{iA}, \tag{1}$$

$$M n_{iA}\left(\frac{\partial}{\partial t} v_{ixA} + v_{ixA}\frac{\partial}{\partial x} v_{ixA}\right) = -e n_{iA}\frac{\partial \varphi}{\partial x}, \tag{2}$$

$$\frac{\partial n_e}{\partial t} + \frac{\partial}{\partial x}(n_e v_{ex}) = \nu_i n_e, \tag{3}$$

$$e n_e \frac{\partial \varphi}{\partial x} - k\frac{\partial n_e T_e}{\partial x} - \frac{e}{c}\omega_e \tau v_{ex} n_e B_{0z} - \frac{v_{ex}}{\tau} m n_e = 0, \tag{4}$$

$$\frac{\partial^2 \varphi}{\partial x^2} = -4\pi e(n_{iA} + n_{iB} - n_e), \tag{5}$$

$$\begin{aligned}\frac{3}{2} k n_e\left(\frac{\partial T_e}{\partial t} + v_{ex}\frac{\partial T_e}{\partial x}\right) &= -\frac{\partial}{\partial x}\chi_\perp \frac{\partial T_e}{\partial x} + \frac{j_x^2}{\sigma_\perp} \\ &- k n_e T_e \frac{\partial v_{ex}}{\partial x} - (\nu_0 \Delta E + \nu_i I) n_e,\end{aligned} \tag{6}$$

$$\frac{\partial n_{iB}}{\partial t} + \frac{\partial}{\partial x}(n_{iB} v_{iBx}) = \nu_i n_e + \nu_{AB} n_{iA}, \tag{7}$$

$$M n_{iB}\left(\frac{\partial}{\partial t} v_{iBx} + v_{iBx}\frac{\partial}{\partial x} v_{iBx}\right) = -e n_{iB}\frac{\partial \varphi}{\partial x}. \tag{8}$$

Here, subscripts *i* and *e* stand for ions and electrons, respectively; subscripts *A* and *B* refer to the selectively produced ions of an isotope to be separated out and the ions originating due to electron-impact ionization and charge exchange; $\nu_{AB} = v_i \sigma_{AB} N_0$ is the charge exchange rate, where $\sigma_{AB} = 3 \times 10^{-14}$ cm^2 is the charge-exchange cross section; ν_0 is the rate at which the electron energy is transferred to the neutrals in excited states; ν_i is the rate of ionization of an atom by electron impact [7]; *I* is

the atom ionization energy; ΔE is the atom excitation energy; j_x is the density of the transverse electron current; $\chi_\perp = \frac{5}{2}(nT_e/m\nu_{ei})/(\omega_e\tau)^2$ is the transverse electron thermal conductivity; $\sigma_\perp = (ne^2\tau/m)/(\omega_e\tau)^2$ is the transverse electron conductivity; and $\tau = 1/(\nu_{ei} + \nu_{ea})$ is the electron mean free time.

In the equations of motion of the ion species A (2) and B (8), the friction between ions and neutrals is ignored because the corresponding collision frequencies are less than 10^4 s^{-1} and, hence, the collision times are longer than the characteristic time of the process, which is ~10^{-5} s.

The continuity equation (3) for electrons accounts for the secondary ionization of neutral atoms by electrons. The ionization rate is $\nu_i = \langle v_e\sigma_i\rangle N_0$, where σ_i is the ionization cross section, N_0 is the neutral atom density, and v_e is the electron thermal velocity.

In the equation of inertia-free electron motion (4), the Hall component of the electron velocity v_y is expressed through v_x using the equation of electron motion along the y-axis: $e/c(v_{ex}B_z) - m_e v_{ey}/\tau = 0$.

The continuity equation for ions incorporates the loss of primary ions of species A in the charge-exchange reactions. The production of B ions in the ionization and charge-exchange reactions is described the right-hand side of the continuity equation for the ions of species B. Equation (6) accounts for the change in the electron temperature due to heat conduction, Joule heating, plasma expansion, and inelastic collisions of electrons with atoms (including ionization).

The initial conditions are as follows: $n_i(x, 0) = n_e(x, 0) = 10^{11}$ cm^{-3}, $v_i(x, 0) = v_e(x, 0) = 0$, $n_{iB}(x, 0) = 0$, $v_{iB}(x, 0) = 0$, $T_i(x, 0) = T_e(x, 0) = 0.1$ eV, and $E_x(x, 0) = \varphi_0/L$. The boundary conditions are as follows: $\varphi(0, t) = \varphi_0$, $\varphi(L, t) = 0$, and $T_e(0, t) = T_e(L, t) = 0.1$ eV. The boundary conditions for the particle flows at the anode or the cathode depend on the sign of the potential jump $\Delta\varphi$ at the corresponding electrode. Thus, at $\Delta\varphi > 0$, the plasma electrons freely arrive at the anode, whereas the ion flow is limited by the Boltzmann exponential factor. In contrast, at $\Delta\varphi < 0$, the ions freely arrive at the anode, whereas the electrons have to overcome the potential barrier. The boundary conditions at the cathode are set in a similar way. The electron flow at the cathode is the sum of the two oppositely directed flows, namely, the electron flow from the plasma and the emission flow. Correspondingly, depending on the sign of $\Delta\varphi$, one of these flows freely passes the cathode region, whereas the other is limited by a Boltzmann exponential factor.

Therefore, the boundary conditions at the anode are set as follows:

$$j_{e0} = -0.25n_e(0)v_e(0) \text{ for } \Delta\varphi \geq 0,$$
$$j_{i0} = -0.25n_i(0)v_i(0)\exp(-e\Delta\varphi/kT_a) \text{ for } \Delta\varphi \geq 0,$$
$$j_{e0} = -0.25n_e(0)v_e(0)\exp(e\Delta\varphi/kT_{ea}) \text{ for } \Delta\varphi \leq 0,$$
$$j_{i0} = -0.25n_i(0)v_i(0) \text{ for } \Delta\varphi \leq 0.$$

The boundary conditions at the cathode are set as follows:

$$j_{e0} = J_{em}/e - 0.25n_e(L)v_e(L)\exp(-e\Delta\varphi/kT_{ec}) \text{ for } \Delta\varphi \geq 0,$$
$$j_{i0} = -0.25n_i(L)v_i(L) \text{ for } \Delta\varphi \geq 0,$$
$$j_{e0} = J_{em}/e\exp(e\Delta\varphi/kT_{ec}) + 0.25n_e(L)v_e(L) \text{ for } \Delta\varphi \leq 0,$$
$$j_{i0} = 0.25n_i(L)v_i(L)\exp(e\Delta\varphi/kT_c) \text{ for } \Delta\varphi \leq 0.$$

The boundary emission current from the cathode is set as $J_{em} = n_{e0}v_{Te}/(\omega_e\tau)$. Here, T_{ea} and T_{ec} are the electron temperatures near the anode and cathode, respectively; T_a and T_c are the anode and cathode temperatures, which are assumed to coincide with the ion temperatures near the anode and cathode; $v_e(0)$ and $v_e(L)$ are the electron thermal velocities near the anode and cathode; $v_i(0)$ and $v_i(L)$ are the ion velocities near the anode and the cathode; and $n_e(0)$, $n_e(L)$, $n_i(0)$, and $n_i(L)$ are the densities of electrons and ions near the anode and cathode.

3. IDEALIZED MODEL OF THE EXTRACTOR

First, we consider the feasibility of ion extraction from a magnetized plasma. To this end, we fix the temperature of the plasma electrons at the initial value. Then, the plasma mainly undergoes the action of electric forces. Secondary ionization and charge exchange are ignored. Thus, we solve the system of Eqs. (1)–(5), with the right-hand sides of Eqs. (1) and (3) being equal to zero. The Hall parameter and the accelerating voltage were taken equal to 10 (B = 33 G) and 50 V, respectively.

The results of numerical simulation are presented in Figs. 2 and 3. Here, mean ion mass velocity $\langle v_i(t)\rangle = \{\int v_i(x, t)n_i(x, t)dx\}/\{\int n_i(x, t)dx\}$ is introduced to determine the volume-averaged parameters of ion acceleration. The acceleration dynamics appears as follows. Initially, the electric field penetrates freely into the plasma. As the plasma electrons move toward the anode, a self-consistent emission current from the cathode arises, which compensates for the cathode potential drop caused by the ion space charge. The ions keep accelerating so that the ion current progressively increases (Fig. 2). As the ions propagate toward the cathode, an anode potential drop caused by the electron space charge arises, which shields the external electric field. When the densities of the ion current to the cathode and the electron current to the anode become equal to each other, the electric field inside the plasma drops to zero (Fig. 3, t = 1.8 μs). By that time, the ions throughout the entire plasma volume acquire a maximum velocity of 1.2×10^5 m/s (Fig. 2). Since the field inside the plasma is close to zero and the ion velocities in the bulk of the plasma substantially exceed the electron velocities, the motion of the plasma particles takes the form of ambipolar diffusion of ions and magnetized

electrons. The plasma ions drag the electrons via the ambipolar field, and the quasineutral plasma as a whole moves by inertia toward the cathode. In this stage, the ions are partially decelerated by the magnetized electrons; however, due to the large momentum of the plasma ion component, almost all of the ions leave the discharge gap (80% in 15 μs). An increase in the magnetic field up to 70 G leads to an increase in the decelerating effect of the magnetized electrons; as a result, in a time of 15 μs, slightly more than 50% of ions are extracted.

To derive analytical relationships between the parameters of the process and estimate the required field values, we interpret the obtained results taking into account the extraction phenomenology.

First of all, we estimate the time during which the electric field penetrates into the plasma with magnetized electrons. This enables us to determine the optimum values of the interelectrode voltage and magnetic field. Obviously, if the electrons are not magnetized, the electric field is shielded in a fraction of a nanosecond and the ions have no time to acquire any significant velocity toward a cathode. Alternatively, if the electrons are overmagnetized, their mobility is lower than that of ions and they decelerate the ions moving toward the cathode. Hence, the electron mobility should be slightly above the ion mobility so that the electron initial velocity is higher than the velocity acquired by the ions during acceleration (~10^5 cm/s). Ignoring the pressure term in the equation of electron motion, we obtain $v_{xe} = eE/m\omega^2\tau$, from which we can determine the values of $\omega_e\tau$, B, and U_0 at which the electron initial velocity is ~10^6 cm/s. For $U_0 = 100$ V, we have $\omega_e\tau = 30$ and $B = 100$ G and, for $U_0 = 50$ V, we have $\omega_e\tau = 20$ and $B = 70$ G. These values of $\omega_e\tau$ and B are obtained for an initial plasma density of 10^{11} cm^{-3}. Note that the initial electron velocity ~10^6 cm/s corresponds to reasonable values of the emission current (about 15 mA/cm^2). For an initial plasma density of 10^{12} cm^{-3}, the above values are as follows: for $U_0 = 100$ V, we have $\omega_e\tau = 10$ and $B = 300$ G and, for $U_0 = 50$ V, we have $\omega_e\tau = 7$ and $B = 200$ G.

To estimate the shielding time, we write the expression for the electric field in the bulk of the interelectrode volume (except the anode sheath):

$$E = E_0 - 2\pi e n_e \lambda^2/d. \quad (9)$$

Here, λ is the length of the anode sheath; d is the interelectrode spacing, which coincides with the length of the main interelectrode region under the assumption that the anode sheath length is negligibly small ($\lambda \ll d$); n_e is the electron density in the anode sheath; and $E_0 = U_0/d$ is the initial electric field in the plasma. Now, we assume that the electric field in the plasma decreases linearly with time:

$$E(t) = E_0(1 - t/t_0), \quad (10)$$

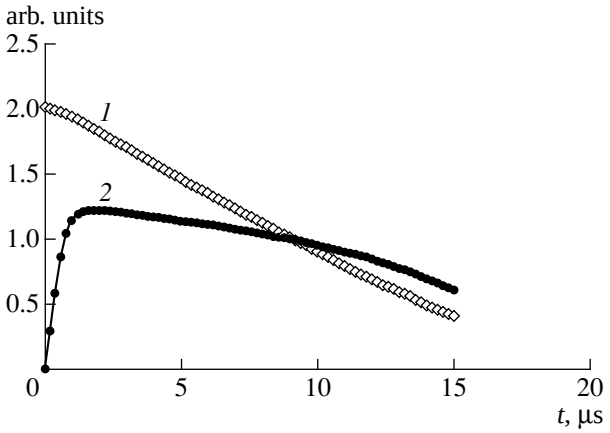

Fig. 2. Extraction dynamics in a cold plasma ($T_e = 0.1$ eV): (*1*) the number of ions (in units of $\times 10^{11}$ cm^{-2}) and (*2*) the mean ion mass velocity (in units of $\times 10^5$ cm/s) for the Hall parameter $\omega_e\tau = 10$, $U_0 = 50$ V, $N_0 = 10^{14}$ cm^{-3}, $n_{i0} = 10^{11}$ cm^{-3}, and $B = 33$ G.

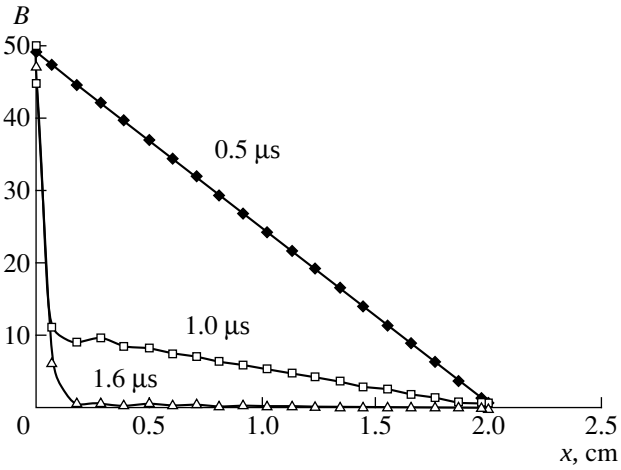

Fig. 3. Potential profiles in a cold plasma ($T_e = 0.1$ eV) at different times for the same conditions as in Fig. 2.

where t_0 is the shielding time.

We determine the λ value by integrating from 0 to t_0 the ion velocity in the linearly decreasing electric field:

$$\lambda = eE_0 t_0^2/3M. \quad (11)$$

The average electron density n_e in the anode sheath can be obtained from the balance between the ion flux in the interelectrode region and the electron flux from the anode sheath toward the anode:

$$n_{i0} eE_0 t_0/2M = n_e eE_0 d/m\lambda\omega_e^2\tau. \quad (12)$$

Both the anode sheath length λ_0 at which the electric field between the electrodes is completely shielded and the shielding time t_0 can be determined from expressions (9)–(12), in which n_{i0} is set to be equal to the initial

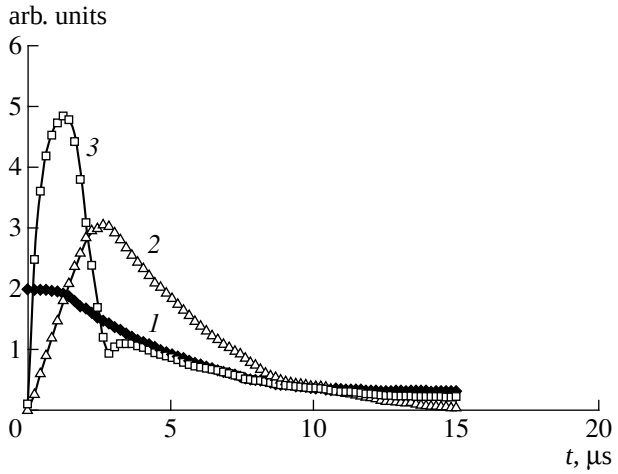

Fig. 4. Extraction dynamics with plasma heating and cooling taken into account: (*1*) the number of ions (in units of $\times 10^{11}$ cm^{-2}), (*2*) the mean ion mass velocity (in units of $\times 10^5$ cm/s), and (*3*) the mean electron temperature (eV) for the same conditions as in Fig. 2, except for the voltage U_0, which is cut off at $t = 3$ μs.

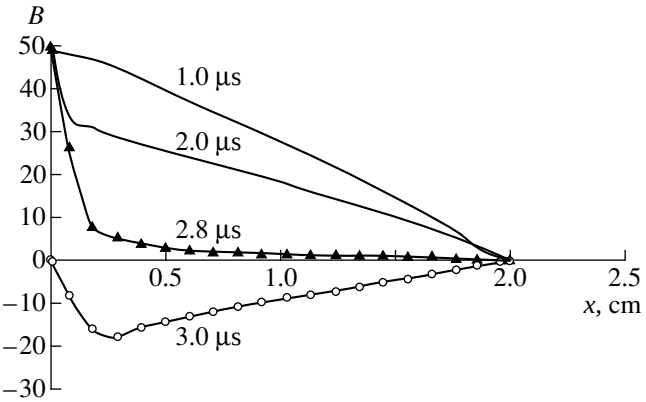

Fig. 5. Potential profiles at different times for the same conditions as in Fig. 4.

plasma density and it is assumed that $\tau = 1/\nu_{ea}$ because, in the anode sheath, $\nu_{ei} \simeq 0$. For the shielding time, which is one of the most important parameters of the extractor, we obtain $t_0^7 = 27/\pi(M/e)^4(d^2/U_0)^2/n_{i0}m\omega^2\tau$.

Therefore, the shielding time depends on the magnetic field as $t_{02} = t_{01}(B_2^2/B_1^2)^{1/7}$. In the above numerical solution for a cold plasma, the shielding time is 1.8 μs at $B = 35$ G. According to our estimate, for $B = 70$ G, with other parameters kept constant, this time should be 1.33 μs. Numerical simulations in this case give $t_0 = 1.44$ μs. Analogously, for $B = 100$ and 140 G, numerical simulations yield 1 and 0.8 μs, whereas the estimate gives 1.17 and 1 μs, respectively. Thus, the estimate provides the right dependence of the shielding time on the magnetic field. The dependence of the shielding time on the interelectrode voltage is the same. For $U_0 = 100$ V and $B = 35$ G, our estimate yields $t_0 = 1.33$ μs, whereas numerical simulations yield 1.4 μs. For $U_0 = 25$ V, we have 1.9 and 2 μs, respectively.

From expressions (9)–(12), we obtain the anode sheath length at which the electric field in the interelectrode region is completely shielded: $\lambda_0 = U_0/d(27/\pi)^{2/7}(M/e)^{1/7} \times (d^4/(n_{i0}m\omega^2\tau U_0^2))^{2/7}$.

The value of λ_0 depends on the magnetic field as $\lambda_{02} = \lambda_{01}(B_2^2/B_1^2)^{2/7}$. Numerical simulations for $B = 35$ G and $U_0 = 50$ V yield $\lambda_0 = 1.7$ mm, whereas for $B = 70$ G, we have $\lambda_0 = 1.1$ mm. According to the estimate, if we set λ_0 equal to 1.7 mm for $B = 35$ G, then, from the dependence of λ_0 on B, we obtain $\lambda_0 = 1.15$ mm for $B = 70$ G.

The dependence of λ_0 on U_0 has the form $\lambda_{01} = \lambda_{02}(U_{01}/U_{02})^{3/7}$, which is also confirmed by the numerical results. Thus, the simple ideas underlying relationship (10) lead to a good agreement with the numerical results and can be used to estimate the parameters of the process.

The above estimates are obtained under the assumption that the plasma is cold, so that the electric force exceeds the electron pressure, which is true at the initial temperature of 0.1 eV. At higher temperatures, the pressure effect leads to an increase in the shielding time (by a factor of 1.5–2). Nevertheless, the main tendencies in the dependences of the shielding time on B and U_0 are retained. For the given ion velocity in the extractor and the necessary shielding time, we can find the optimum values of the extractor parameters U_0 and B.

Now, we consider the effect of electron heating on the extraction dynamics. The plasma electrons are heated due to the current flowing through the discharge gap and cooled due to inelastic collisions with neutrals [see Eq. (6)]. Since the rate of plasma cooling due to inelastic collisions depends strongly on the gas species, numerical simulations were performed for ytterbium vapor (the scheme and technique for selective photoionization of ytterbium isotopes are fairly developed [8]).

The cross section and excitation rate $\langle v\sigma \rangle$ for the transition with energy ΔE were evaluated using the formula proposed in [7]. For ytterbium, the main contribution to excitation comes from inelastic collisions that excite an atom from the ground state 6^1S_0 to the 6^1P_1 and 7^1P_1 states with energies of 3.1 and 5.02 eV, respectively. For example, at $T_e = 10$ eV, these cross sections are equal to 6×10^{-16} and 1.1×10^{-16} cm^2, respectively. The power carried away by one electron is equal to $v_{Te}\sigma N_a \Delta E$, where σ is the total cross section of inelastic collisions with atoms. In order to take into account inelastic losses of the electron energy during the extraction, we add to the right-hand side of Eq. (6) the term

Pn_e, which describes the power density of inelastic losses. The ion and neutral densities were taken to be 10^{11} and 10^{14} cm^{-3}, respectively; the latter density was sufficiently high to regard the neutrals as an unlimited energy reservoir. The initial value of the Hall factor was set equal to 10 (B = 35 G), keeping in mind that the magnetization factor increases with the electron temperature. The applied voltage was 50 V. To lower the energy input into the plasma, the electric field was switched off after a time of 3 μs, which, according to numerical simulations, is the shielding time for the given parameters. To characterize the plasma heating, we introduced the mean electron temperature $\langle T_e(t)\rangle = \{\int T_e(x, t)\rho_e(x, t)dx\}/\{\int \rho_e(x, t)dx\}$, where $\rho_e = m_e n_e$ is the electron mass density.

The results of numerical simulations are presented in Figs. 4–6. The dynamics of the extraction process is shown in Fig. 4. It is seen that, in the initial stage, the plasma is accelerated and, for 3 μs, the ions acquire a velocity of 3.5×10^5 cm/s directed to the cathode. In this stage, the emission current with a density of 5 mA/cm^2 flows through the plasma and heats it for ~1 μs up to a temperature of 5 eV at the peak of the current. As the electric field in the plasma decreases, the temperature rapidly drops to about 1 eV and the electron pressure at the boundary between the anode sheath and the plasma begins to play an important role. As the temperature increases, the electron–ion collision frequency ν_{ei} decreases, thus increasing the electron magnetization factor. Simultaneously, the frequency of electron–neutral elastic collisions increases (at T_e = 1 eV, we have $\nu_{ei} = \nu_{ea}$). In this case, the electron–neutral collisions decrease the magnetization of the electrons, limiting the magnetization factor at $T_e \geq 1$ eV. Figure 5 presents the profile of the potential in the plasma at different times from 0.5 to 4 μs. It is seen that the dynamics of the potential is similar to that in the case of a cold plasma. It is seen that, in the stage of inertial plasma motion, the electric field arising due to electron magnetization decelerates the ions. The profiles of the electron temperature and ion density at t = 3 μs are shown in Fig. 6. It is seen that the Hall current mainly flows near the anode, where the electric field is high. The electron temperature also attains its maximum (5 eV) in this region. The increase in the electron pressure leads to both the suppression of plasma pinching and a decrease in the velocity and density gradients. It is also seen that electron emission does not significantly increase the temperature.

4. NUMERICAL SIMULATION WITH ALLOWANCE FOR PLASMA KINETICS

There are two basic mechanisms for the production of secondary ions, namely, resonant charge exchange and secondary ionization by electron impact. Let us consider each of them.

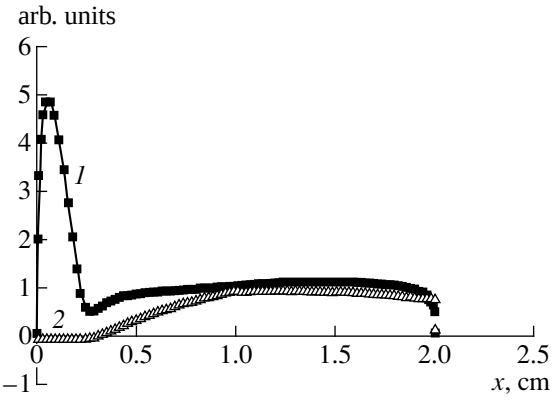

Fig. 6. Profiles of (*1*) the electron temperature (eV) and ion density (in units of $\times 10^{10}$ cm^{-3}) at t = 3 μs for the same conditions as in Fig. 4.

The effect of charge exchange is that an ion (in our case, the ion of an isotope to be separated out) colliding with a neutral atom captures an electron from the atom. The newborn ion can reach the collector. The cross section for the resonant charge exchange is extremely high and can vary by one order of magnitude for different elements, ranging from several units of 10^{-14} cm^2 to several units of 10^{-13} cm^2 (see, e.g., [8]).

As was shown above, two regions with different properties arise after the accelerating phase, which lasts for 1–3 μs: these are the region between the plasma and the anode, where the electric field is concentrated, and the region occupied by the plasma, where the electric field is near zero (or even slightly decelerates the ions; see Figs. 5, 6). Obviously, charge exchange proceeds most intensely in the field-free plasma region. Hence, after acceleration has terminated, charge exchange does not decrease the separation factor because it is not accompanied by momentum transfer between the moving ion and neutral atom. The discharged ion (i.e., neutral atom) of the desired isotope will continue its motion toward the collector, whereas the newborn ion will keep moving with the atomic beam and will even start to move toward the anode in the slightly decelerating field. Hence, the charge-exchange time is determined only by the time of plasma acceleration, which is equal to 1–3 μs. In this time interval, the ion travels a distance of ~0.3 cm. At the same time, for a charge-exchange cross section of 3×10^{-14} cm^2 and atom density of 10^{14} cm^{-3}, the charge-exchange length is 0.3 cm. Hence, if the atom density in the beam is less than 10^{14} cm^{-3}, charge exchange does not affect the extraction process. Correspondingly, at a higher cross section (as, e.g., for uranium or gadolinium [8]), it is necessary to operate with a lower atom density.

The secondary electron-impact ionization of the gas atoms can also lead to selectivity degradation. According to estimates [9], at the electron temperature T_e = 1 eV and neutral atom density of 10^{14} cm^{-3}, the rate of

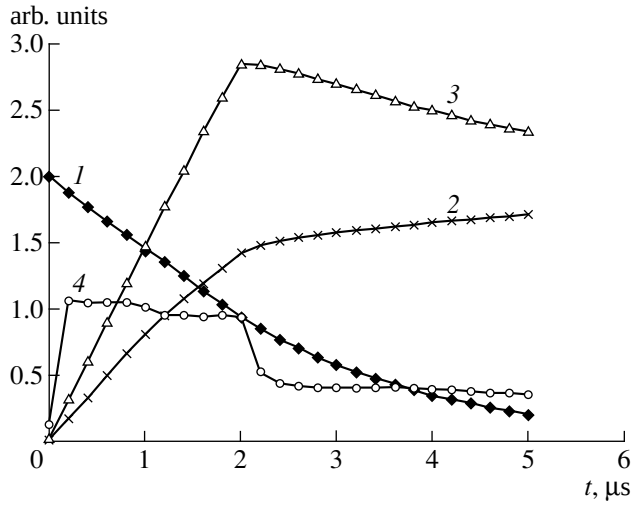

Fig. 7. Extraction dynamics with allowance for ionization and charge exchange: (*1*) the number of ions (in units of $\times 10^{11}$ cm^{-2}), (*2*) the number of secondary ions (in units of $\times 10^{11}$ cm^{-2}), (*3*) mean ion mass velocity (in units of $\times 10^5$ cm/s), and (*4*) mean electron temperature (eV) for the same conditions as in Fig. 2, except for the voltage U_0, which is cut off at $t = 2$ μs.

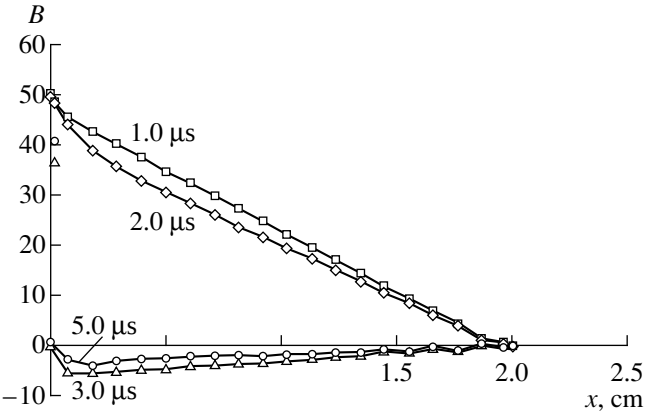

Fig. 8. Potential profiles at different times for the same conditions as in Fig. 7.

electron-impact ionization of neutral atoms is $\nu_i = \langle v_{Te}\sigma_i\rangle N_0 = 10^5$ s^{-1}, which means that, in a time of 10 μs, each electron ionizes, on average, one atom. Thus, in 10 μs, the selectivity will drop by half. The numerical simulation shows that secondary ionization is most intense during the plasma acceleration phase. After the acceleration phase, most of the electrons are in the plasma region, where the electric field is low and even decelerates the ions (Figs. 5, 6), whereas, in the anode zone, the electron density is low. Therefore, the secondary ions generated due to collisions with electrons from the high-energy tail of the electron distribution are not accelerated and cannot deteriorate the selectivity.

It follows from the above considerations that the electric field should be switched off when the ions have acquired a sufficiently high velocity. In this case, the secondary ions produced after the acceleration phase cannot reach the collector because there is no momentum transfer during secondary ionization and charge exchange and, thus, the extraction time is no longer of importance. The extraction dynamics with ionization and charge exchange taken into account is shown in Fig. 7. The ion and neutral densities are taken as 10^{11} and 10^{14} cm^{-3}, respectively. The initial value of the Hall factor is set at 10 ($B = 35$ G). The applied voltage is 50 V. The electric field is switched off after 2 μs. By this time, the ions are accelerated to a velocity of 3×10^5 cm/s. The maximum electron temperature is 1 eV. In 5 μs, about 90% of the ions are extracted. Although, as is seen from Fig. 7, more than 75% of the ions are *B* ions produced due to ionization and charge exchange, numerical simulations show that their velocities are one order of magnitude lower than those of *A* ions, in accordance with the above considerations. Generally speaking, the ion kinematic characteristics appear to be even better than those obtained without regard to charge exchange and ionization (see Fig. 4). This fact can be explained by Fig. 8, which presents the potential profiles in the gap at different times. Since ionization occurs mainly in the anode region, where the electron temperature is high, the shielding anode sheath does not form because it is neutralized by the ions produced due to ionization. Acceleration in this region proceeds as in a steady-state ion accelerator. Hence, to prevent an undesirable ion acceleration, it is important to switch off the electric field at the proper time.

The electron emission current required for the extractor operation can be produced by both heating the collector surface and using special emitting cathodes. In any case, the required emission current density is so small (5 mA/cm^2) that it can be readily achieved by heating the collector surface. Thus, according to the Richardson–Deshman formula, heating a uranium collector surface up to the melting point provides an emission current density of 10 mA/cm^2.

5. CONCLUSION

The high efficiency of a Hall-current plasma accelerator for ion extraction in laser isotope separation systems has been demonstrated through numerical simulations. Due to pulsed acceleration of the ions throughout the entire plasma volume, one can operate the accelerator at relatively low accelerating voltages and at extremely high densities of the vapor of the material to be separated. The required emission current density is so small (5–10 mA/cm^2) that it can be readily obtained by heating the collector surface. Although the Hall-current extractor is more complicated than the EE and there are problems related to both electron emission from the collector and closing the Hall current, this

type of extractor holds promise for use in laser isotope separation systems because of the lower acceleration time (by an order of magnitude) and better selectivity, which is related to the volume acceleration of the ions.

ACKNOWLEDGMENTS

We are grateful to A.A. Rukhadze for discussing the results obtained and to the staff of the Atomic Spectroscopy Laboratory of the Institute of General Physics for fruitful discussions.

REFERENCES

1. M. Murakami, Y. Ueshima, and K. Nishihara, Jpn. J. Appl. Phys., Part 2 **32** (10a), 221 (1993).
2. M. W. Grossman and T. A. Shepp, IEEE Trans. Plasma Sci. **19**, 1114 (1991).
3. G. S. Janes, US Patent No. 328954 (February 2, 1973).
4. N. S. Demidova and V. A. Mishin, J. Moscow Phys. Soc. **5**, 223 (1995).
5. I. I. Litvinov, J. Russ. Laser Res. **17** (14), 371 (1996).
6. A. Ohzu, Y. Suzuki, and T. Arisawa, in *Proceedings of the IEEE International Conference on Plasma Science, New York, 1993*, p. 84.
7. H. van Regemorter, Astrophys. J. **136**, 906 (1962); L. A. Vaĭnshteĭn, I. I. Sobel'man, and E. A. Yukov, in *Cross Sections for Excitation of Atoms and Ions by Electrons* (Nauka, Moscow, 1973), p. 45.
8. S. K. Borisov, M. A. Kuz'mina, and V. A. Mishin, Prikl. Fiz., No. 1, 65 (1995).
9. S. Sakabe, Y. Izawa, M. Hashida, *et al.*, Phys. Rev. A **45**, 252 (1992).

Translated by N. Ustinovskiĭ

Plasma Physics Reports, Vol. 26, No. 12, 2000, pp. 1054–1065. Translated from Fizika Plazmy, Vol. 26, No. 12, 2000, pp. 1126–1138.

LOW-TEMPERATURE PLASMA

Discharge Dynamics and the Production of Active Particles in a Cathode-Directed Streamer

S. V. Pancheshnyĭ, S. V. Sobakin, S. M. Starikovskaya, and A. Yu. Starikovskii

Moscow Institute of Physics and Technology,
Institutskiĭ per. 9, Dolgoprudnyĭ, Moscow oblast, 141700 Russia

Received March 23, 2000

Abstract—The emission spectroscopy technique is used to analyze a cathode-directed streamer discharge in air at atmospheric pressure in point–plane geometry at interelectrode distances of up to 100 mm and a high-voltage pulse amplitude of 18 kV. The densities of molecules in the $N_2(C^3\Pi_u, v = 0)$, $N_2^+(B^2\Sigma_u^+, v = 0)$, and $NO(A^2\Sigma^+, v = 0)$ states are determined, and the reduced electric field in the streamer head is estimated. It is shown that the increase in the average electric field in the discharge gap substantially intensifies the production of active particles in the discharge plasma and makes the plasma more homogeneous. This effect is only related to the increase in the fraction of regions with a high electric field in the discharge gap and, as a result, the reduction of the discharge energy losses via rapidly thermalized degrees of freedom. The active particles are only produced in the streamer head, including the case in which the interelectrode gap is bridged by the streamer channel. © *2000 MAIK "Nauka/Interperiodica"*.

1. INTRODUCTION

The ability of a streamer to propagate in a gap with a low external field (many times lower than the breakdown field) has attracted great interest since the discovery of the phenomenon of a streamer breakdown in an overvoltage gap [1]. Recently, interest in this type of electric discharge was stimulated by the possibility of using it in a number of plasmochemical applications, including the production of atoms, ions, and active radicals neutralizing harmful exhausts of thermal power plants and chemical factories (such as NO_x or SO_2) [2].

The existence of two clearly distinguished discharge regions with (i) a high electric field and low conductivity (streamer head) and (ii) a high conductivity and low electric field (streamer channel) is a distinctive feature of streamers as compared to other types of gas discharges. The basic parameters of a streamer discharge (such as the discharge shape, the electron density, the electric field in the streamer head, and the propagation velocity of the head) are determined by the processes occurring just in the streamer head; the role of the conducting channel is only to support the electric potential of the head.

Photoionization, electron-impact ionization, and charged particle drift in a high electric field of the streamer head play a decisive role in the development and propagation of a streamer. Generally, the streamer velocity and channel radius range within 10^7–10^8 cm/s and 10^{-2} –1 cm, respectively.

Numerous studies of streamer discharges and their efficiency in various plasmochemical technologies were conducted in flow-type reactors. The efficiency with which harmful additives were removed was measured under different parameters of a high-voltage pulse, geometry and material of the corona electrode, flow rate, and working mixture composition. The main result of the study of the streamer corona was a conclusion concerning the higher energy efficiency of the positive corona as compared to the negative one. Obviously, a further increase in the efficiency of plasmochemical applications is impossible without a detailed understanding of the processes occurring in a streamer discharge plasma.

Experimental studies of a streamer discharge have encountered a number of obvious difficulties: high rates of the processes (which call for subnanosecond time resolution), small size, unpredictable propagation trajectory, and high electromagnetic interference in the diagnostic facility. The use of contact diagnostics is hardly possible because the detector introduces strong perturbations in the field distribution in the discharge gap.

As a rule, the current–voltage characteristics are recorded in experiments, which, in particular, provide information about the energy input into the system. To determine spatiotemporal characteristics of the discharge, optical photography of a discharge with an image–converter tube or high-speed camera is usually used. These measurements provide information about the propagation velocity of the front of a glow, which is assigned to the processes of gas excitation in the streamer head (see, e.g., [3]). Synchronous measurements of electrodynamic and optical parameters of a discharge allow one to determine the time delay between the start of the discharge and the instant when

1063-780X/00/2612-1054$20.00 © 2000 MAIK "Nauka/Interperiodica"

the high-voltage pulse arrives at the electrode. These measurements reveal the formation and propagation of a second streamer discharge and the transformation of the streamer corona into an arc or spark channels as the duration of the high-voltage pulse and the electric field in the gap increases. In recent years, contactless spectroscopic diagnostics that enable one to resolve the spatiotemporal structure of a discharge and analyze kinetic processes in a streamer plasma have been widely used [4–6]. Thus, experimental investigations of the structure of a streamer discharge have been limited to studying its general electrodynamic and, to a lesser extent, radiative characteristics.

Up to now, numerical simulations of the streamer propagation and gas excitation in the plasma of the streamer channel have been practically the only method for studying the processes occurring in the streamer channel and its neighborhood. Numerical simulations are also necessary to more accurately interpret experimental data.

During recent decades, the potentialities of computer simulations of a streamer breakdown in an overvoltage electric field with various electrode configurations have been demonstrated. Almost all simulations were based on the hydrodynamic model for the electron component and Poisson's equation for self-consistent electric field. There are only a few works in which the electron motion was described using the Monte Carlo method. Although this method has substantially wider applications and allows one to obtain valid results even under conditions of extremely high electric fields and gradients, when the hydrodynamic approach fails, it requires too many computer resources, such that only the initial stages of the avalanche–streamer transition have been simulated so far with this technique [7].

The so-called "one-and-a-half-dimensional" (1.5D) models were proposed to simulate the streamer propagation in a long gap. The models incorporate one-dimensional balance equations for charged particles and two-dimensional equations for the electric field. This approach is widely used to describe the streamer propagation in weak fields and model plasmochemical processes in a streamer. Unfortunately, those models include an external parameter, namely, the diameter of the streamer channel, which almost entirely determines the dynamics and properties of a streamer. Taking the streamer channel diameter from measurements, one can achieve a reasonable agreement between the results of experiments and simulations. At the same time, for mixtures or conditions for which no experimental data are available, these models fail to provide reliable results.

An interesting version of a 1.5D model takes into account the ionization expansion of the streamer channel [8, 9]. Such a model allows one to accurately calculate the propagation velocity and the current of a streamer, provided that the level of gas preionization and the initial radius of the head are properly chosen. An important drawback of this model (as well as of all the 1.5D models) is the averaging of the plasma parameters over the channel cross section.

The impossibility of the self-consistent simulation of the discharge structure in the vicinity of the streamer head, which is characteristic of the 1.5D and 1.75D models, does not allow one to apply these models to a quantitative analysis.

This problem is absent for self-consistent 2D models, which now offer the greatest promise for investigating the structure of a streamer discharge. Such a model can incorporate all of the known mechanisms for the production and loss of charged particles. The model enables an automatic determination of both the radial and axial inhomogeneity of the channel plasma; the shape of an axisymmetric head is transformed consistently with the other parameters during the streamer development. Note that the measurements indicate the 3D nature of the discharge. In experiments, a solitary channel is rarely observed; as a rule, the so-called streamer "flash" takes place.

The available 3D model of a streamer discharge in air [10] fails to provide three-dimensional spatial distribution of the parameters due to the lack of both initial and boundary conditions with respect to an additional coordinate (azimuthal angle in cylindrical coordinates). Within the 3D approach with axisymmetric initial and boundary conditions, the solution must be axisymmetric as well, which provides no additional data on the physics of a discharge as compared to 2D simulations. This limitation is caused by the absence of a clear physical model that could substitute the axisymmetric description of a streamer by a fully 3D approach.

Unfortunately, the experiments and numerical simulations of a streamer discharge were compared only with respect to such global parameters as the propagation velocity, discharge current, and energy input, which provide no information about the internal structure and spatial distribution of the plasma parameters. Therefore, the existent numerical models are not able to quantitatively describe the development of a streamer discharge. Nevertheless, they can be used to better understand the physics of the streamer propagation and qualitatively analyze the efficiency of the use of a streamer discharge in various applications.

Usually, active particles are produced only at the streamer head, which, as was mentioned above, is fairly small (0.01–1 cm). In [11], based on numerical simulations, it was pointed out that there can exist a regime in which the electric field is fairly high throughout the entire channel, which results in the enhanced production of chemically active particles. According to [11], this regime is settled after the discharge gap is bridged with a streamer and exists within a time interval shorter than that required for the development of spark breakdown. One of the important accompanying phenomena is the formation of a return wave, which equalizes the electric field along the discharge gap. This result was

obtained from 1.5D numerical simulations in the regime in which the streamer bridged the discharge gap. In this case, in addition to the above uncertainties of a 1.5D model, uncertainties related to the interaction of a streamer discharge with the electrode surfaces appear.

The above result however contradicts the result obtained by Sigmond [12], who, based on the analysis of experimental data, developed a model of the transition of a streamer to an arc discharge. It is asserted in [12] that, when a cathode-directed streamer bridges an air discharge gap, the return wave glow, as a rule, is not observed; however, after the return wave has passed the discharge gap, the second streamer starts propagating from the high-voltage to low-voltage electrode due to the development of the attachment instability. The propagation of this streamer results in the formation of an arc channel.

A detailed study of the streamer–arc transition in nitrogen at a pressure of 300 torr in a uniform electric field between two 2-cm-spaced plane electrodes was carried out in [13] based on the analysis of spatiotemporal variations of the emission spectrum in the range 300–860 nm. In that paper, the absence of the return wave glow and the presence of the second streamer were also pointed out. The subsequent transition of the second streamer to an arc discharge is accompanied by the transformation of the line emission spectrum into a continuous spectrum, which is characteristic of a black body heated to several thousand degrees. Note that, despite a qualitative agreement between the above results and those obtained using the model [12], the mechanism for the onset of the instability proposed in [12] cannot be applied to describe the development of a spark discharge.

On the other hand, there are studies (see, e.g., [14]) in which the return wave glow was observed when high-voltage pulses of positive polarity were applied. As a rule, this occurs in long gaps (~1 m) on long time scales in a strongly nonuniform electric field.

When studying the efficiency of ozone generation in a streamer discharge in $N_2 : O_2$ mixtures [15], it was found that the electric field in the streamer channel is much less than that at the streamer head and is insufficient for the intense production of active particles. However, in such a field, an efficient excitation of both rotational and vibrational molecular states occurs, which, in turn, leads to the excitation of metastable molecular levels and a consequent increase in the rate with which chemically active particles are produced. Thus, the reduction of the "energy cost" of the ozone generation in the streamer channel by 30% is explained in [15] by the EV–conversion

$$N_2(X, v_1) + N_2(X, v_2) \longrightarrow N_2(A) + N_2(X, v_3),$$

which is followed by molecular oxygen dissociation

$$N_2(A) + O_2 \longrightarrow N_2(X) + O + O.$$

Summarizing the results of [11, 15], one can expect an increase in the efficiency of the production of active particles (due to one of the mechanisms discussed) in the regime in which the gap is bridged by a streamer.

The main purpose of this study is to investigate the spatiotemporal structure of the positive streamer corona in the range of interelectrode distances corresponding to both the regimes in which the gap is partially bridged by a streamer (without a transition to a spark discharge) and regimes with a freely propagating streamer. The measurements of the global discharge parameters (the discharge voltage and streamer velocity) are supplemented with synchronous measurements of the absolute densities of the plasma components.

Obviously, different plasmochemical applications require the efficient production of different chemically active particles. Here, the efficiency of the process was estimated by the production of molecules in the $NO(A^2\Sigma^+, v = 0)$, $N_2(C^3\Pi_u, v = 0)$, and $N_2^+(B^2\Sigma_u^+, v = 0)$ states, whose excitation thresholds from the ground states are 5.42, 11.2, and 18.6 eV, respectively.

2. EXPERIMENTAL SETUP

A schematic of the experimental setup and diagnostic facility is shown in Fig. 1. A rotating-interrupter generator designed at the Research and Production Corporation LIT was used as a pulsed voltage supply. The high-voltage pulses were fed through a 60-m-long RK-50-24-13 cable to the high-voltage connector of the discharge system. A calibrated back-current shunt placed in the break of the braiding of the feeding coaxial cable at a distance of 30 m from the discharge system was used to control the parameters of the pulses. The amplitude of the voltage pulse was U_{max} = 9 kV (positive polarity), the FWHM duration was $t_{1/2}$ = 75 ns, the rise time was t_{inc} = 25 ns, and the repetition rate was f = 1.2 kHz.

The discharge section had a conventional point–plane geometry; the interelectrode distance could be varied within 0–30 cm. The high-voltage electrode was a 300-mm-long cone with a tip radius of 0.5 mm, and the low-voltage electrode was a disc 8 mm thick and 550 mm in diameter (aluminum).

The active particles were detected with emission spectroscopy. The optical recording facility consisted of condensers, photomultipliers, monochromators, and a set of diaphragms. We used FEU-100 and SNFT-3 photomultipliers (with photocathode sensitivity ranges of λ = 170–830 and 300–800 nm, respectively) and MDR-12-1 and MUM-2 monochromators (with operating ranges of λ = 200–2000 and 200–800 nm, respectively). To measure the absolute emission intensity, the optical system was calibrated using a calibrated DDS-30 deuterium lamp (200–500 nm) and a SIRSH 8.5-200-1 tungsten incandescent lamp (350–700 nm).

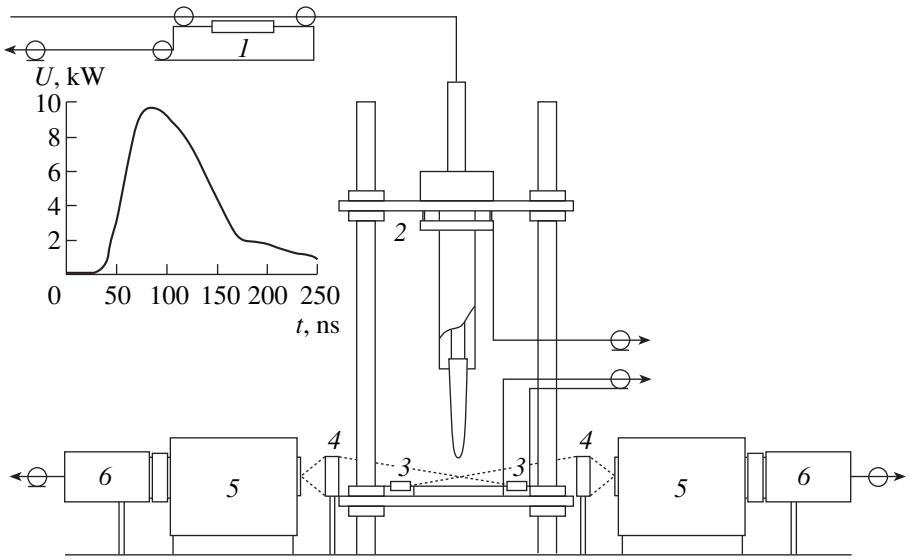

Fig. 1. Schematic of the optical diagnostics and the system for measuring the electric parameters of a discharge: (*1*) back-current shunt, (*2*) Rogowski coil, (*3*) current shunt, (*4*) quartz condenser, (*5*) MDR-12-1 and MUM-2 monochromators, and (*6*) FEU-100 and SNFT-3 photomultipliers.

To obtain the averaged emission characteristics of the discharge, we used the regime of signal accumulation (the time constant was varied within 0.1–1 s). Thus, at a pulse repetition rate of 1.2 kHz, the emission characteristics were averaged over 10^2–10^3 pulses, which enabled both an increase in the measurement accuracy and identification of weak bands and lines in the spectrum.

Spatiotemporal measurements were carried out with a 5-mm-high dielectric slit diaphragm, which could be shifted along the discharge gap with a micrometer mechanism up to 25 mm from the high-voltage electrode.

The signals were recorded by digital Tektronix TDS-380 (with a 400-MHz pass band) and S9-8 (in the accumulation regime) oscillographs.

3. MAIN RESULTS

It was established that, for the given parameters of the pulse—the voltage at the discharge gap $U_{gap} \simeq 18$ kV (with allowance for the doubling of the voltage at the high-voltage electrode) and $\tau_{1/2} \simeq 75$ ns—and interelectrode distances of $L \le 16$ mm, a spark channel developed in the discharge gap. In accordance with [12], the development of the spark channel was preceded by the second streamer propagating from the anode to the low-voltage electrode. At interelectrode distances of $L \ge 20$ mm, the development of a streamer flash rarely, if ever, led to a breakdown, although the discharge gap was bridged with streamers up to $L \simeq 24$ mm.

The spark breakdown was accompanied by a jump in the discharge current (up to 150–300 A). A transition from the streamer discharge to a pulsed breakdown was also accompanied by a radical change in the emission spectrum. In the case of a spark breakdown, the emission spectrum had a form characteristic of an arc channel; it contained numerous atomic lines, including lines of atoms and ions of the electrode material, which were superimposed on a intense continuum caused by both bremsstrahlung and recombination radiation of a quasi-equilibrium arc plasma.

Figure 2 presents the spectrum of a streamer flash, which is characteristic of the interelectrode distances $L \ge 20$ mm. Molecular bands of nitrogen (2^+ nitrogen system, $N_2(C^3\Pi_u, v') \longrightarrow N_2(B^3\Pi_g, v'')$ transition), nitrogen ions (1^- nitrogen system, $N_2^+(B^2\Sigma_u^+, v') \longrightarrow N_2^+(X^2\Sigma_g^+, v'')$ transition), and nitrogen monoxide (γ-band of nitrogen monoxide, $NO(A^2\Sigma^+, v') \longrightarrow NO(X^2\Pi, v'')$ transition), all with a clear vibrational structure, were readily identified in the discharge emission spectrum.

The following measurements were carried out for the bands:

(i) 2^+ nitrogen system, 0–0 transition with $\lambda = 337.1$ nm,

(ii) 1^- nitrogen system, 0–0 transition with $\lambda = 391.4$ nm, and

(iii) γ-band of nitrogen monoxide, 0–1 transition with $\lambda = 236.3$ and 237.0 nm.

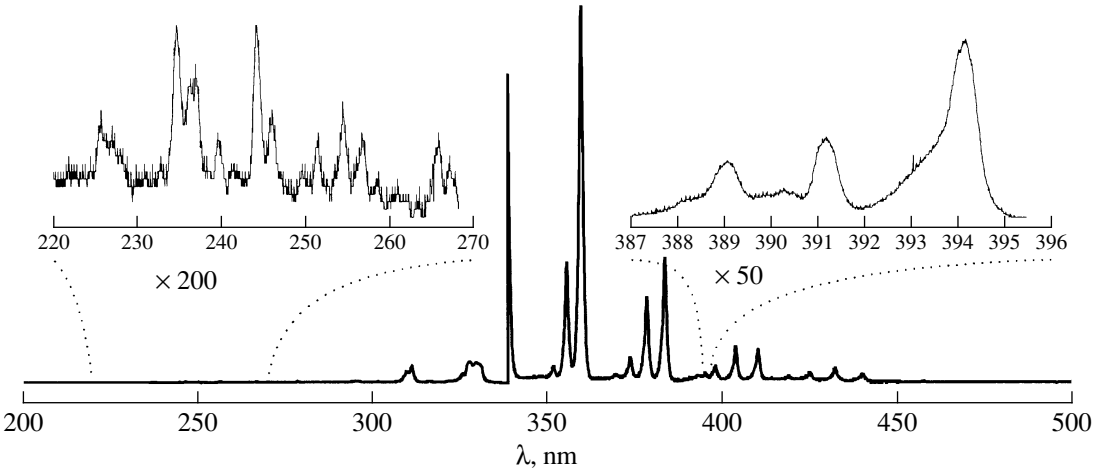

Fig. 2. Emission spectrum of the streamer flash for L = 24 mm.

Such a choice of bands was motivated by their relatively high intensity and the possibility of unambiguous identification of transitions due to the absence of overlapping with other intense bands.

The relation between the densities of excited particles and the emission intensity is determined (provided that there is no reabsorption in the band) by the transition frequency $\nu_{v'v''}$, the particle population at the upper level [N*], the radiative time of the transition τ_0, and the probability of the vibrational transition $A_{v'v''}$:

$$I_f = h\nu_{v'v''}\frac{[\mathrm{N}^*]}{\tau_0}A_{v'v''}. \quad (1)$$

The probability of a one-photon dipole transition is equal to

$$A_{v'v''} = \frac{q_{v'v''}\nu^3_{v'v''}}{\Sigma q_{v'v''}\nu^3_{v'v''}}. \quad (2)$$

All of the above values are presented in the table. The Franck–Condon factors $q_{v'v'}$ were taken from [16], and the radiation times τ_0 of the $N_2(C^3\Pi_u,\ v = 0)$, $N_2^+(B^2\Sigma_u^+,\ v = 0)$, and $NO(A^2\Sigma^+,\ v = 0)$ levels were taken from [17, 18]. Therefore, Eq. (1) allows us to unambiguously relate the instantaneous populations of the upper levels to the emission intensities of the corresponding transitions.

Parameters of the investigated transitions of 2^+ and 1^- systems of N_2 and γ-band of NO

	$2^+, 0 \longrightarrow 0$	$1^-, 0 \longrightarrow 0$	$\gamma, 0 \longrightarrow 1$
λ, nm	337.1	391.4	236.3
τ_0, ns	37	62	196
$A_{v'v''}$	0.523	0.718	0.298

3.1. Measurements of the Distributions of the Production of Active Particles along the Discharge Gap

The dynamics of the linear density of excited particles in the discharge gap was studied using time-resolved measurements. A set of 5-mm-high slit diaphragms separating out the emission from the desired regions of the discharge gap was used for this purpose. A micrometer mechanism provided the positioning of the diaphragms with an accuracy of no worse than 0.1 mm.

Shifting the diaphragm along the discharge gap, we measured the emission intensities of the transitions of interest. The rise and fall times of the radiation pulses corresponded to the time during which the streamer covered a distance equal to the length of the most intense region; the FWHM of the emission pulse corresponded to the time during which the streamer passed the slit height. Estimates based on these data (see below) showed that the emitting zone was a narrow strip 3 mm long. From here, we can draw an important conclusion that the production of active particles in the states under investigation mainly occurs in the streamer head and its vicinity. The subsequent analysis and conclusions concern just that part of the discharge, where most of the excited particles are produced.

The time, at which the high-voltage pulse arrived at the electrode was used as a reference point; this enabled us to synchronize different oscillograms and plot the diagrams of the streamer propagation through the discharge gap. Figure 3 shows the emission field (synchro-

nous emission intensity profiles in the different cross sections of the gap) of the second positive nitrogen system for an interelectrode distance of $L = 24$ mm.

3.2. Propagation Velocity of the Glow Front

It is convenient to present the dependence of the streamer velocity on the distance from the high-voltage electrode with the so-called *x–t* diagram (the time during which the emission intensity increases to 0.1 of the maximum intensity versus the coordinate). An analysis shows the existence of the three characteristic regions of the streamer propagation:

(i) the anode region, in which the streamer is formed and which is characterized by the extremely high velocity of the glow front ($l \le 7$ mm) in the high external field;

(ii) the main region, in which the streamer velocity is almost constant for discharge gaps no longer than $L =$ 42 mm and slightly decreases for higher L; and

(iii) the cathode region, in which the streamer velocity increases as the streamer approaches the low-voltage electrode (this region is observed only when streamer bridges the gap).

For the interval in which the streamer propagates with almost constant velocity, we can find the dependence of the streamer velocity on the gap length (Fig. 4). It is seen that the streamer velocity grows with decreasing gap length, ranging within $(2–3.5) \times 10^7$ cm/s under the given pulse parameters and geometry of the experiment.

The waveforms of the streamer-flash emission from the given cross sections can be characterized by the signal rise time and half-duration of the emission pulse. These parameters are in close relation to both the length of the emissive zone near the streamer head and the streamer velocity. The half-duration of the emission pulse corresponds to the time during which the streamer passes the slit diaphragm aperture, whereas the signal rise time is determined by the length of the emissive zone.

The signal rise time and half-duration of the emission pulse range within 10–20 and 20–30 ns, respectively. The measured values of the streamer propagation velocity indicate that the length of emissive zone is $l \simeq \langle v \times \Delta t \rangle \sim 3–4$ mm, which corresponds to the length of both the streamer head and the zone of the radially expanded channel just behind the head.

3.3. Peak Densities of Active Particles in the Streamer Head

Figure 5 presents the dependences of the peak (corresponding to the instant the streamer head passes through the given cross section of the gap) linear densities of the $N_2(C^3\Pi_u, v = 0)$, $N_2^+(B^2\Sigma_u^+, v = 0)$, $NO(A^2\Sigma^+,$

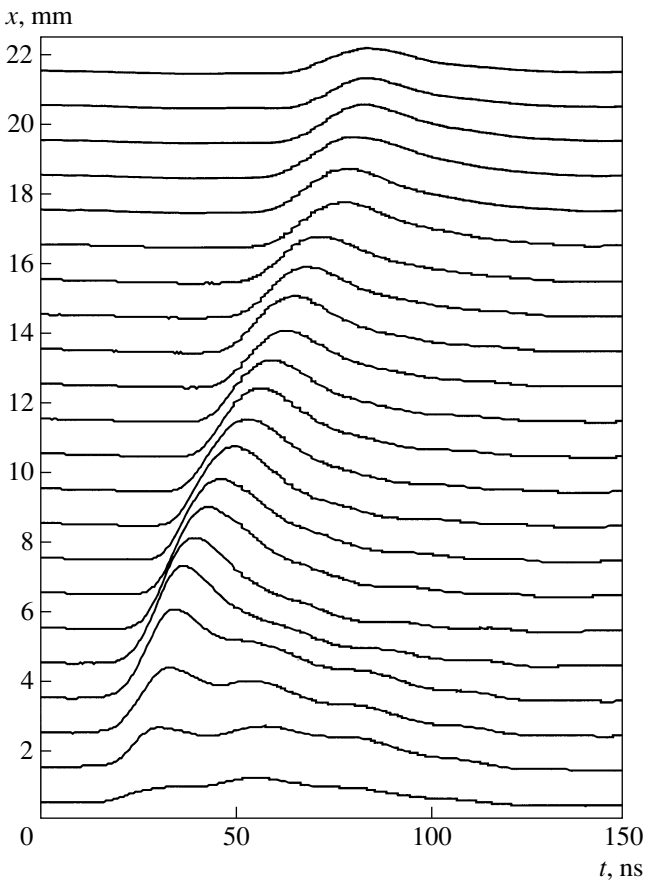

Fig. 3. Emission field of the second positive nitrogen band for $L = 24$ mm.

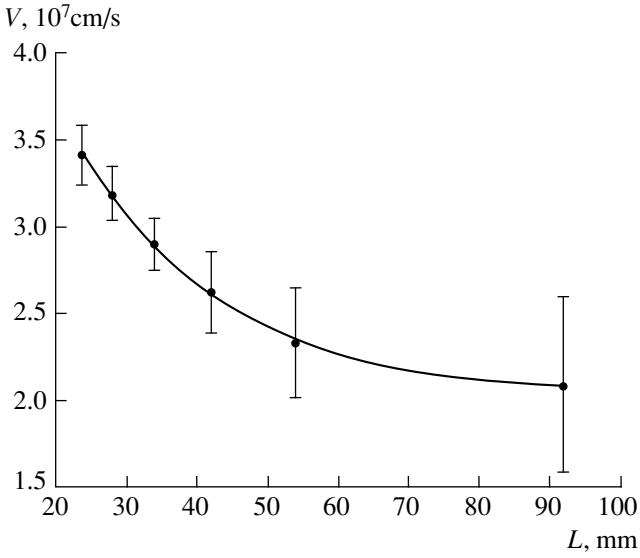

Fig. 4. Streamer velocity vs. the interelectrode distance.

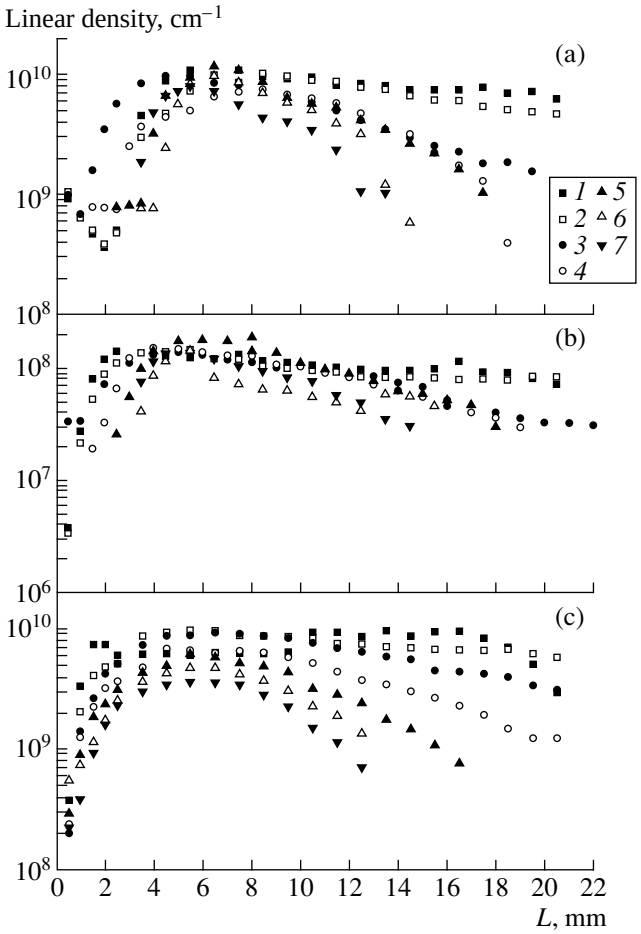

Fig. 5. Peak densities of (a) $N_2(C^3\Pi_u,\ v = 0)$, (b) $N_2^+(B^2\Sigma_u^+,\ v = 0)$, and (c) $NO(A^2\Sigma^+,\ v = 0)$ in the streamer head vs. the distance from the high-voltage electrode for different interelectrode distances: (*1*) 20, (*2*) 24, (*3*) 28, (*4*) 34, (*5*) 42, (*6*) 54, and (*7*) 92 mm.

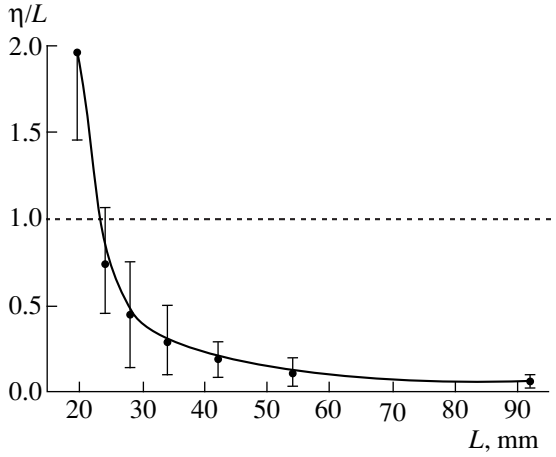

Fig. 6. Reduced damping length of the emission intensity vs. the interelectrode distance.

$v = 0$) states versus the distance from the high-voltage electrode for different interelectrode distances.

The results obtained show that, at distances up to $l_1 = 6$ mm from the high-voltage electrode (anode), the streamer corona is formed. In this stage, the glow front propagation is determined by the local electric field near the high-voltage electrode and depends only slightly on the distance from the low-voltage electrode (i.e., on the average field in the gap). In this region, the linear densities of excited particles reach their maximums, the typical values being $[N_2(C^3\Pi_u,\ v = 0)]_{max} \simeq (0.5–1.0) \times 10^{10}$ cm^{-1}, $[N_2^+(B^2\Sigma_u^+,\ v = 0)]_{max} \simeq (1.0–2.0) \times 10^8$ cm^{-1}, and $[NO(A^2\Sigma^+,\ v = 0)]_{max} \simeq (0.3–1.0) \times 10^{10}$ cm^{-1}.

For small interelectrode distances, when the streamer channel bridges the gap, the linear densities of active particles created in the discharge change slightly along the discharge gap.

For long gaps, the linear densities of active particles drop sharply beyond the zone where the streamer is formed. As is seen from Fig. 5, the longer the gap (at the same electrode voltage), the shorter the effective length of the region where active particles are produced.

The drop in the density of active particles (which will further be referred to as N*) along the gap can be approximated to a good accuracy by a decreasing exponential function of length. The linear density [N*] beyond the zone where the streamer is formed is represented as

$$[N^*](x) = [N^*]_{max} \exp\left(-\frac{(x - x_0)}{\eta}\right). \qquad (3)$$

Here, $[N^*]_{max}$ is the peak density, which is reached at the distance x_0, and η is the damping length of the emission intensity, which characterizes the uniformity of the production of active particles along the streamer corona.

It is seen from Fig. 6 that, for short interelectrode distances, when the streamer bridges the discharge gap, the damping length (normalized to the interelectrode distance) is $\eta/L > 1$ and the active particles are produced nearly uniformly throughout the discharge gap. This is true for interelectrode distances up to 24 mm; in this case, the average electric field in the gap is $E = 7.5$ kV/cm. In longer discharge gaps, the size of the region where the active particles are produced nearly uniformly becomes less than the gap length; thus, the production of active particles in the discharge gap becomes nonuniform (for $L > 65$ mm, we have $\eta/L < 0.1$)

3.4. Integral Production of Active Particles

The volume production of active particles in the discharge depends strongly on the interelectrode distance

and, thus, on the average electric field in the gap. The space- and time-resolved measurements showed that the active particles in the electronically excited states are mainly produced in the streamer head.

The experiments carried out for interelectrode distances in the range 16–50 mm (Figs. 7, 8) showed that the integral production of the active particles in different electronically excited states sharply decreases when passing over from the regime in which the streamer bridges the gap ($L \simeq 20$ mm) to the regime with a freely propagating streamer ($L \simeq 50$ mm). Thus, the integral production of $N_2(C^3\Pi_u, v = 0)$ decreases by one order of magnitude (Fig. 7). The integral productions of nitrogen ions in the electronically excited state $N_2^+(B^2\Sigma_u^+, v = 0)$ and nitrogen monoxide in the electronically excited state $NO(A^2\Sigma^+, v = 0)$ behave in the same manner. However, all these states have substantially different excitation energies: 5.42 eV for $NO(A^2\Sigma^+, v = 0)$, 11.2 eV for $N_2(C^3\Pi_u, v = 0)$, and 18.6 eV for $N_2^+(B^2\Sigma_u^+, v = 0)$. The difference in the excitation thresholds is clearly seen in Fig. 8, which presents the relative concentrations of active particles in electronically excited states as functions of the gap length.

The ratio $[N_2(C^3\Pi_u, v = 0)]/[NO(A^2\Sigma^+, v = 0)]$ depends slightly on the gap length and varies in the range 1–1.5. The ratio $[N_2(C^3\Pi_u, v = 0)]/[N_2^+(B^2\Sigma_u^+, v = 0)]$ changes from 50 to 60 as the gap length varies from 34 to 20 or 45 mm (Fig. 8). These relatively weak dependences can be explained by the fact that all the states are populated mainly in the streamer head, where the electric field is high and depends weakly on the average field in the gap.

3.5. Region Where Active Particles Are Produced

The relative concentrations of the particles in the excited states of interest measured in the integral regime (Figs. 7, 8) correspond to those obtained in the time-resolved measurements (Fig. 5). This is additional confirmation of the fact that the active particles are produced mainly in the streamer head.

No appreciable production of active particles in the streamer channel was observed for any interelectrode distances, including those corresponding to a partial bridging of the discharge gap with a streamer (down to those at which spark breakdown occurs). Thus, the proposed mechanism for a significant enhancement of the production of active particles in the streamer channel (see [11, 15]) was not confirmed. Perhaps, this effect could occur at greater interelectrode distances (of a few tens or hundreds of cm) and proper amplitudes of the high-voltage pulse on time scales comparable with the time during which the conducting channel decays. However, the available data on the dynamics of a streamer discharge under the above conditions show

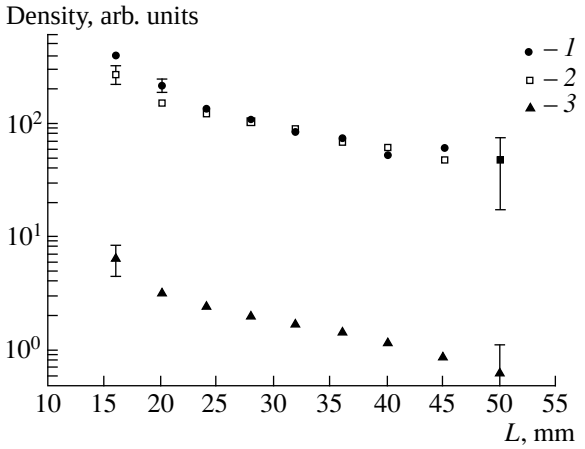

Fig. 7. Integral production of active particles in the discharge vs. the interelectrode distance: (*1*) $N_2(C^3\Pi_u, v = 0)$, (*2*) $NO(A^2\Sigma^+, v = 0)$, and (*3*) $N_2^+(B^2\Sigma_u^+, v = 0)$.

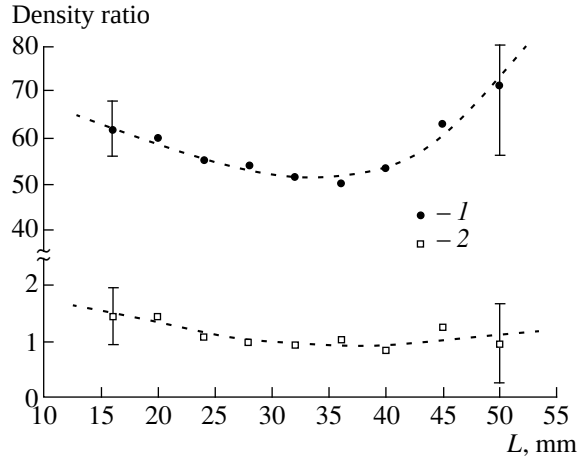

Fig. 8. Relative concentrations of (*1*) the $[N_2(C^3\Pi_u, v = 0)]/[N_2^+(B^2\Sigma_u^+, v = 0)]$ and (*2*) $[N_2(C^3\Pi_u, v = 0)]/[NO(A^2\Sigma^+, v = 0)]$ excited states vs. the interelectrode distance.

the existence of repeated discharges (both cathode- and anode-directed), which sustain a relatively high plasma density in the pseudopulsed mode. Therefore, it is questionable whether the regime with a nearly uniform electric field (sufficient for the production of active particles in the streamer channel) throughout the discharge gap [11] can exist; such a regime could be just a specific feature of 1.5D numerical simulations of a streamer discharge and a consequence of uncertainties in the boundary conditions at the electrode surfaces.

When the streamer arrives at the cathode, the cathode sheath, which is characterized by a high voltage

drop across a narrow spatial region, is formed near the cathode surface. The cathode sheath is known to substantially affect the discharges in which the gap is bridged. The strong influence of an uncertainty in velocities of electrons emitted from the cathode (due to both photoemission and electron–ion emission) on the cathode sheath parameters was pointed out in [19]. Although this result was obtained for a Xe–Cl mixture, it is natural to expect the same high sensitivity of the plasma parameters to the uncertainty in velocities of emitted electrons in air after the streamer has bridged the gap.

3.6. Electric Field in the Region Where Electronic States Are Efficiently Excited

The reduced electric field can be estimated by analyzing the population rates of the electronically excited states of molecular nitrogen. The populations of the $N_2(C^3\Pi_u, v=0)$ and $N_2^+(B^2\Sigma_u^+, v=0)$ excited states are determined by the processes of direct electron-impact excitation from the ground state of nitrogen

$$\begin{aligned} &N_2(X^1\Sigma_g^+) + e \longrightarrow N_2(C^3\Pi_u, v=0) \quad k_{ex}^c = f(E/N), \\ &N_2(X^1\Sigma_g^+) + e \longrightarrow N_2^+(B^2\Sigma_u^+, v=0) \quad k_{ex}^b = f(E/N); \end{aligned} \tag{4}$$

radiative depopulation

$$\begin{aligned} &N_2(C^3\Pi_u, v=0) \longrightarrow N_2(B^3\Pi_g, v'') + h\nu_{2^+} \\ &\tau_0^c = 37\ \text{ns}, \\ &N_2^+(B^2\Sigma_u^+, v=0) \longrightarrow N_2^+(X^2\Sigma_g^+, v'') + h\nu_{1^-} \\ &\tau_0^b = 62\ \text{ns}; \end{aligned} \tag{5}$$

quenching in collisions with heavy particles

$$\begin{aligned} &N_2(C^3\Pi_u, v=0) + N_2 \longrightarrow \text{products} \\ &k_c^{N_2} = 0.09\times10^{-10}\ \text{cm}^3/\text{s}, \\ &N_2(C^3\Pi_u, v=0) + O_2 \longrightarrow \text{products} \\ &k_c^{O_2} = 2.7\times10^{-10}\ \text{cm}^3/\text{s}, \\ &N_2^+(B^2\Sigma_u^+, v=0) + N_2 \longrightarrow \text{products} \\ &k_b^{N_2} = 2.1\times10^{-10}\ \text{cm}^3/\text{s}, \\ &N_2^+(B^2\Sigma_u^+, v=0) + O_2 \longrightarrow \text{products} \\ &k_b^{O_2} = 5.1\times10^{-10}\ \text{cm}^3/\text{s}; \end{aligned} \tag{6}$$

and associative conversion of the nitrogen ions

$$\begin{aligned} &N_2^+(B^2\Sigma_u^+, v=0) + N_2 + M \longrightarrow N_4^+ + M \\ &k_b^M = 5\times10^{-29}\ \text{cm}^6/\text{s}. \end{aligned} \tag{7}$$

The lifetimes and rate constants of the collisional bimolecular quenching of the levels in processes (5) and (6) are taken from [17]. At atmospheric pressure, the ion conversion process (7), whose rate constant at room temperature is fairly high [20], plays a significant role in depopulating the $N_2^+(B^2\Sigma_u^+, v=0)$ state. Note that the available data about this process are related to the ground electronic state of N_2^+; however, the conversion rate of ions in the $N_2^+(B^2\Sigma_u^+, v=0)$ state should differ insignificantly from that of the ions in the ground state because the polarization interaction, which is responsible for the production of N_4^+ ions, slightly depends on the electronic excitation of reagents.

The balance equation for excited particles $N^* = \{N_2(C^3\Pi_u, v=0), N_2^+(B^2\Sigma_u^+, v=0)\}$ has the form

$$\frac{d[N^*]}{dt} = k_{ex} n_e [N_2(X^1\Sigma_g^+)] - \frac{[N^*]}{\tau}. \tag{8}$$

Here, k_{ex} is the rate constant of the direct electron-impact excitation, n_e is the electron density, and τ is the total lifetime with allowance for radiative decay and collisional quenching:

$$\begin{aligned} \tau_c &= (1/\tau_0^c + k_c^{N_2}[N_2] + k_c^{O_2}[O_2])^{-1}, \\ \tau_b &= (1/\tau_0^b + k_b^{N_2}[N_2] + k_b^{O_2}[O_2] + k_b^M[N_2][M])^{-1}. \end{aligned} \tag{9}$$

To determine the electric field, we consider the ratio between the population rate constants of the $N_2(C^3\Pi_u, v=0)$ and $N_2^+(B^2\Sigma_u^+, v=0)$ levels. Taking into account that the time derivative on the left-hand side of Eq. (8) is much less than the population and depopulation rates on the right-hand side, we obtain

$$\frac{k_{ex}^c}{k_{ex}^b} = \frac{[N_2(C^3\Pi_u, v=0)]}{[N_2^+(B^2\Sigma_u^+, v=0)]}\frac{\tau_b}{\tau_c}. \tag{10}$$

On the one hand, the ratio of both peak densities to the inverse lifetimes of the $N_2(C^3\Pi_u, v=0)$ and $N_2^+(B^2\Sigma_u^+, v=0)$ levels can be directly determined from the experimental data:

$$f_{\text{exp}} = \frac{[N_2(C^3\Pi_u, v=0)]}{[N_2^+(B^2\Sigma_u^+, v=0)]}\frac{\tau_b}{\tau_c}. \tag{11}$$

On the other hand, the ratio of the population rate constants of the levels under consideration can be derived by solving the Boltzmann kinetic equation within the two-term approximation. Within this

approach, the rate constants $k_{ex}^{c,b}$ depend only on the reduced electric field E/N

$$f_{\text{calc}}(E/N) = \frac{k_{ex}^{c}}{k_{ex}^{b}}. \quad (12)$$

The electric field was estimated by comparing expressions (11) and (12). The obtained value of the electric field characterizes the zone corresponding to the outer boundary of the streamer head where the excitation rates of $N_2(C^3\Pi_u, v = 0)$ and $N_2^+(B^2\Sigma_u^+, v = 0)$ states are the highest. In a sense, this value may be treated as the peak value of the electric field in the streamer head.

A typical longitudinal profile of the reduced electric field E/N in the streamer head corresponding to the maximum rate of the production of electronically excited N_2 molecules is presented in Fig. 9 for the gap length $L = 24$ mm.

The reduced electric field $E/N \sim 10^3$ Td reaches its maximum near the high-voltage electrode. At a distance of 7 mm from the electrode, the formation of the streamer channel is completed and the electric field decreases to 400 Td. As the streamer head approaches the low-voltage electrode, the reduced electric field increases to 500 Td.

For longer discharge gaps, at distances from the high-voltage electrode of up to $x = 10$ mm, the electric field profiles are nearly the same as in Fig. 9. As is the case of $L = 24$ mm, the reduced electric field beyond the region where the streamer is formed changes within 400–500 Td. For very long gaps, at distances from the high-voltage electrode of longer than 12 mm, the emission intensity of the first negative nitrogen system becomes so weak that it does not allow accurate absolute measurements of the population rate of the $N_2^+(B^2\Sigma_u^+, v = 0)$ state.

Using a similar approach when treating the results of measurements in the integral regime (Figs. 7, 8), we can estimate the effective averaged reduced electric field in the streamer head during the propagation of the streamer along the discharge gap (in the regions where the excitation of electronic molecular states is the most efficient). The obtained dependence of E/N on the gap length L is presented in Fig. 10.

It is seen from the figure that, at $L = 24$ mm, the average reduced field is $E/N \simeq 490$ Td. This value is in good agreement with the results of time-resolved measurements, which yield a reduced electric field in the middle of the discharge gap of $E/N \simeq 400$–500 Td. Therefore, this approach can be used to estimate the electric field within an accuracy of 20%. This conclusion opens up the possibility of discharge optimization under conditions of industrial installations, when it is impossible to implement diagnostic systems with nanosecond time resolution.

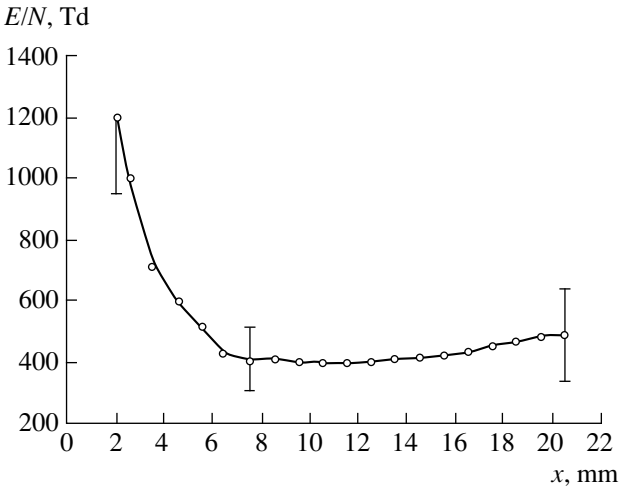

Fig. 9. Reduced electric field in the streamer head vs. the distance from the high-voltage electrode for $L = 24$ mm.

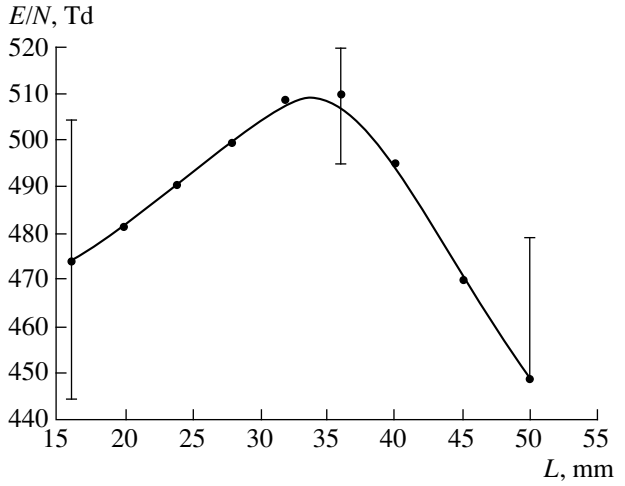

Fig. 10. Effective averaged (over the pulse) reduced electric field in the streamer head vs. the interelectrode distance.

It worth noting that, to determine the electric field, we need only the relative emission intensity of the transitions; hence, the accuracy of absolute calibration (~15%) influences only the measured values of the particle densities.

It follows from Fig. 10 that the average effective electric field reaches its maximum at an interelectrode distance of $L_{\max} = 34 \pm 3$ mm. Naturally, it is also the distance at which the relative production of excited molecules in the high-lying electronic states is maximum. It is seen from Fig. 8 that, as the interelectrode distance deviates from $L_{\max}$, the relative production of

the particles in both the $N_2^+(B^2\Sigma_u^+, v=0)$ and $NO(A^2\Sigma^+, v=0)$ states (with excitation thresholds of 18.6 and 5.42 eV, respectively) decreases, whereas the absolute densities of active particles decrease monotonically as the gap length increases. Apparently, this effect is related to the shape of the high-voltage pulse applied to the gap (Fig. 1). At small interelectrode distances, the streamer bridges the gap for a time that is less than (or close to) the rise time of the voltage pulse at the high-voltage electrode. At large interelectrode distances, the bridging time is longer and the streamer propagates in the average effective field that is stronger than in a short gap. This is illustrated in Fig. 10, which displays the average electric field in the streamer head. A further increase in the interelectrode distance decreases the average field in the gap. In this case, beyond the region where the streamer is formed, the streamer propagation velocity decreases and the average field in the vicinity of the streamer head somewhat decreases.

4. CONCLUSIONS

Detailed measurements of the parameters of a repetitive streamer discharge have been carried out in the point–plane geometry at interelectrode distances of 20–92 mm for the following high-voltage pulse parameters: the pulse amplitude is U_{max} = 18 kV (positive polarity), the FWHM duration is $t_{1/2}$ = 75 ns, the rise time is t_{inc} = 25 ns, and the repetition rate is f = 1.2 kHz.

Two characteristic regions of the discharge propagation have been revealed. The region in which a streamer flash is formed (up to $l_1 \le 7$ mm) is characterized by the maximum density of active particles, is almost independent of the interelectrode distance, and is determined by the electric field near the high-voltage electrode. The other region, where the formed streamer propagates in a weak external electric field, is characterized by a decrease in the density of active particles with increasing distance from the high-voltage electrode. This region is determined mainly by the position of the low-voltage electrode, i.e., by the average field in the gap.

It is shown that active particles are mainly produced in the streamer head and its vicinity. No appreciable production of electronically excited particles in the streamer channel was observed for any interelectrode distances, including those corresponding to the partial bridging of the discharge gap by a streamer (up to the distances at which the spark breakdown occurs).

The streamer channel parameters for an interelectrode distance ranging within 20–90 mm are the following: the propagation velocity of the glow front is $(2–3.5) \times 10^7$ cm/s and the maximum linear molecular densities along the discharge gap are $[N_2(C^3\Pi_u, v=0)] \simeq 3 \times 10^8–10^{10}$ cm^{-1}, $[N_2^+(B^2\Sigma_u^+, v=0)] \simeq 2 \times 10^7–2 \times 10^8$ cm^{-1}, and $[NO(A^2\Sigma^+, v=0)] \simeq 2 \times 10^8–10^{10}$ cm^{-1}.

The uniformity of the gas excitation by the streamer corona in the discharge gap is investigated as a function of the gap length. The relative decrease in the production of active particles along the discharge gap is η/L = 2.0, 1.0, and 0.1 for L = 20, 24, and 65 mm, respectively. This result indicates that the density of active particles becomes more uniform as the interelectrode distance decreases, which is due to the increase in the average electric field in the gap.

The dependence of the volume-integrated production of active particles on the interelectrode distance is obtained. It is shown that the production of active particles in the regime in which the streamer channel only partially bridges the gap (without a transition to a spark discharge) is one order of magnitude higher than that in the regime with a freely propagating streamer. This increase is related to the enhanced excitation of electronic states at the streamer head, which propagates in a higher external field.

The peak values of the reduced electric field in the region where the electronic states are efficiently excited are measured. It is shown that the reduced field varies along the gap from $E/N \sim 10^3$ Td in the region where the streamer is formed to $E/N \sim$ 400–500 Td in the region where it propagates in a weak external field.

ACKNOWLEDGMENTS

We are grateful to É.M. Bazelyan and N.L. Aleksandrov for fruitful discussions. This work was supported in part by the Énergiya–Kompleks Scientific and Technology Center, the Russian Foundation for Basic Research (project no. 99-03-32237), INTAS (grant no. 96-2120), the US Air Force Research Laboratory's Office of Scientific Research, and the European Office of Aerospace Research and Development (London) (grant no. SPC-99-4007).

REFERENCES

1. W. Rogowski, Arch. Elektrotech. (Berlin) **20**, 99 (1928).
2. *Non-Thermal Plasma Techniques for Pollution Control*, Ed. by M. Penetrante and E. Shultheis (Springer-Verlag, Berlin, 1993) [NATO ASI Ser., Ser. G, Vol. 34A].
3. H. Raether, *Electron Avalanches and Breakdown in Gases* (Butterworths, London, 1964; Mir, Moscow, 1968).
4. N. Spyrou and C. Manassis, J. Phys. D **22**, 120 (1989).
5. A. Gilbert and F. Bastien, J. Phys. D **22**, 1078 (1989).
6. M. Simek, V. Babicky, M. Clupek, *et al.*, J. Phys. D **31**, 2591 (1998).
7. C. Wu and E. E. Kunhardt, Phys. Rev. A **37**, 4396 (1988).
8. N. L. Alexandrov and E. M. Bazelyan, J. Phys. D **29**, 740 (1996).
9. J. M. Guo and J. Wu, IEEE Trans. Plasma Sci. **24**, 1348 (1996).
10. A. A. Kulikovsky, Phys. Lett. A **245**, 445 (1998).

11. N. L. Aleksandrov, É. M. Bazelyan, and V. A. Vasil'ev, in *Proceedings of the XVII Scientific Conference of the Moscow Institute for Physics and Technology, Dolgoprudnyĭ, 1999*, Part 4, p. 149.

12. R. S. Sigmond, J. Appl. Phys. **56**, 1355 (1984).

13. P. Stritzke, I. Sander, and H. Raether, J. Phys. D **10**, 2285 (1977).

14. J. J. Kritzinger, in *Proceedings of the 6th International Conference on Phenomena in Ionized Gases, Paris, 1963*, Vol. 2, p. 295.

15. A. Knijnik, B. Potapkin, S. Korobtsev, *et al.*, in *Proceedings of the 14th International Symposium on Plasma Chemistry, Prague, 1999*, Vol. 5, p. 2319.

16. N. E. Kuz'menko, L. A. Kuznetsova, and Yu. Ya. Kuzyakov, *Frank–Condon Factors of Diatomic Molecules* (Mosk. Gos. Univ., Moscow, 1984).

17. S. V. Pancheshnyĭ, S. M. Starikovskaya, and A. Yu. Starikovskii, Fiz. Plazmy **23**, 664 (1997) [Plasma Phys. Rep. **23**, 616 (1997)].

18. H. Okabe, *Photochemistry of Small Molecules* (Wiley, New York, 1978; Mir, Moscow, 1981).

19. A. Belasri, J. P. Boeuf, and L. C. Pitchford, J. Appl. Phys. **74**, 1553 (1993).

20. *Physical Quantities: Handbook*, Ed. by I. S. Grigor'ev and E. Z. Meĭlikhov (Énergoatomizdat, Moscow, 1991).

Translated by N. Ustinovskiĭ

Plasma Physics Reports, Vol. 26, No. 12, 2000, pp. 1066–1075. Translated from Fizika Plazmy, Vol. 26, No. 12, 2000, pp. 1139–1148.

LOW-TEMPERATURE PLASMA

Experimental Study of a Low-Pressure Glow Discharge in Air in Large-Diameter Discharge Tubes: I. Conditions for the Normal Regime of a Glow Discharge

V. A. Lisovskiy* and S. D. Yakovin**

**Kharkov National University, pl. Svobody 4, Kharkov, 61077 Ukraine*

***Scientific Physics and Technology Center, ul. Novgorodskaya 1, Kharkov, 61145 Ukraine*

Received March 16, 2000; in final form, June 22, 2000

Abstract—The initiation and characteristics of a low-pressure glow discharge in air in large-diameter discharge tubes are studied. A deviation from the Paschen law is observed: the breakdown curves $U_{dc}(pL)$ shift toward the higher values of U_{dc} and pL as the interelectrode distance L increases. It is shown that the normal regime of a glow discharge is accompanied by gas ionization in the anode sheath. This takes place only for pL values lying to the right of the inflection point in the breakdown curve. The cathode-sheath characteristics in the normal and abnormal regimes of an air discharge for a duralumin cathode are determined. The axial profiles of the ion density, electron temperature, and plasma potential, as well as the anode voltage drop, are measured at various air pressures. © *2000 MAIK "Nauka/Interperiodica".*

1. INTRODUCTION

DC glow discharges are widely used to produce thin polymer and oxide films, clean material surfaces, and pump gas-discharge lasers. Glow discharges are also used in plasma display panels and gas-discharge switches, which are key elements in radio-electronic and electrotechnical devices. Therefore, studies of the breakdown conditions, discharge regimes, and structure of a glow discharge are of considerable interest.

As is known [1–7], dc glow discharges can occur in both normal and abnormal regimes. In the abnormal regime, the entire cathode is occupied by the discharge. In this case, the increase in the discharge current I_{dc} is accompanied by an increase in both the voltage drop U_c across the cathode sheath and the discharge voltage U_{dc}, as well as a decrease in the cathode sheath length d_c. Such behavior of the cathode voltage drop is observed for U_c values higher than the so-called normal cathode voltage drop, which depends on the type of gas and cathode material. The normal regime of a glow discharge is characterized by the conditions $U_c = U_n$ and $pd_c = pd_n$. In this regime, only part of the cathode surface may be occupied by the discharge. As the discharge current decreases, the cathode voltage drop U_c and the cathode-sheath length d_c remain constant, whereas the cathode area S occupied by the discharge decreases, so that the current density $j = I_{dc}/S$ does not change. In [8, 9], it is asserted that, at pressure values lying to the left of the minimum of the breakdown curve $pL < (pL)_{\min}$, where p is the gas pressure and L is the distance between the electrodes, a glow discharge can occur only in the abnormal regime, whereas the normal regime is observed for $pL \geq (pL)_{\min}$.

Experiments [1, 2, 10–13] were largely conducted in long ($L \sim 50$ cm) and narrow (~2–3 cm in diameter) discharge tubes. However, technological plasma devices often use discharge chambers in which the cathode diameter is much larger than the distance between the cathode and anode (below, such discharge chambers will be referred to as large-diameter tubes). Hence, it is of interest to clarify the properties of a glow discharge in large-diameter discharge tubes.

In this study, we measured the breakdown curves and *I–V* characteristics of a glow discharge in air in large-diameter discharge tubes. The axial profiles of the plasma density, electron temperature, and plasma potential, as well as the cathode and anode voltage drops, were measured using the probe technique. It is shown that the normal discharge regime occurs at pressure values lying to the right of the inflection point in the breakdown curve. The normal regime of a discharge in air is accompanied by ionization in the anode sheath; in the absence of such ionization, the abnormal regime of a glow discharge takes place.

2. EXPERIMENTAL TECHNIQUES

Experiments were carried out at air pressures of $p = 10^{-2}$–10 torr, in the range of dc voltages $U_{dc} \leq 1000$ V and discharge currents $I_{dc} \leq 100$ mA. A duralumin cathode was at the potential of a dc voltage source. A 1.5-kΩ resistor was connected in series to the discharge circuit between the cathode and the dc voltage source. A stainless-steel anode was grounded.

1063-780X/00/2612-1066$20.00 © 2000 MAIK "Nauka/Interperiodica"

Fragments of a quartz tube 100 mm in diameter were inserted and sealed between the cathode and anode. The use of a set of such quartz tubes of different lengths allowed us to discretely vary the distance between the cathode and anode within the range L = 11–54 mm. The outer cathode and anode diameters were equal to 160 mm; i.e., they were larger than the inner discharge-tube diameter. Such a design of the discharge chamber allowed us to create a highly uniform electric field in a vacuum (in the absence of a discharge), thereby eliminating the edge effects during gas breakdown and measurements of the breakdown curves of a glow discharge.

The plasma parameters (electron temperature T_e, plasma density n_i, and plasma potential φ_{pl}) were measured with the help of single cylindrical nichrome probes 5 mm in length and 0.18 mm in diameter. In the pressure range under investigation, all three (collisionless, transition, and collisional) regimes of probe operation can occur: at different pressures, the gas ions pass through the probe sheath either without colliding with gas molecules (at low pressures of $p \le 0.05$ torr) or colliding several times (at intermediate pressures) or frequently (at $p > 1$ torr) with neutrals. For this reason, the plasma density n_i was determined from the ion branch of the probe *I–V* characteristic and from the measured values of the electron temperature T_e using the procedure described in [14, 15]. The plasma potential φ_{pl} was derived from the zero of the second derivative of the probe current with respect to the probe voltage and also from measured values of the probe floating potential φ_f and the electron temperature T_e using the formula $\varphi_{pl} = \varphi_f + CT_e$, where C is a constant depending on the type of gas [6].

The electron temperature T_e was determined from the linear regions in the probe *I–V* characteristic and in the second derivative of the probe current with respect to the probe voltage (plotted on the semilogarithmic scale). The T_e values determined by these two methods differed by no more than 10–20%. When measuring the second derivative of the probe current with respect to the voltage, d^2I_{pr}/dU_{pr}^2, we used the second-harmonic method: the probe current was modulated with a low-frequency ($f_{lf} \sim$ 1–3 kHz) voltage, and a signal at a frequency of $2f_{lf}$ was detected. Since, in the pressure range under study, electrons collide with gas molecules near the probe, the method of determining T_e from the slope of the *I–V* characteristic can give an overestimated value of the electron temperature. However, as was shown in [6, 16], the electron temperature in the collisional regime can be determined from the slope of the linear region in the *I–V* characteristic (plotted on the semilogarithmic scale) near the probe floating potential [17], rather than near the plasma potential. In our experiments, the method for determining T_e proposed in [17] was used for the entire pressure range under study. The electron temperature determined in this way was usually 2–3 times lower than the T_e determined from the slope of the linear region in the probe *I–V* characteristic near the plasma potential.

3. ANALYSIS OF EXPERIMENTAL RESULTS

3.1. Conditions for the Normal Regime of a Glow Discharge

In this section, we present results from studies of the relation between the breakdown curves and the *I–V* characteristic of a glow discharge. In particular, we determine the lowest pressure for which the effect of the normal current density can exist.

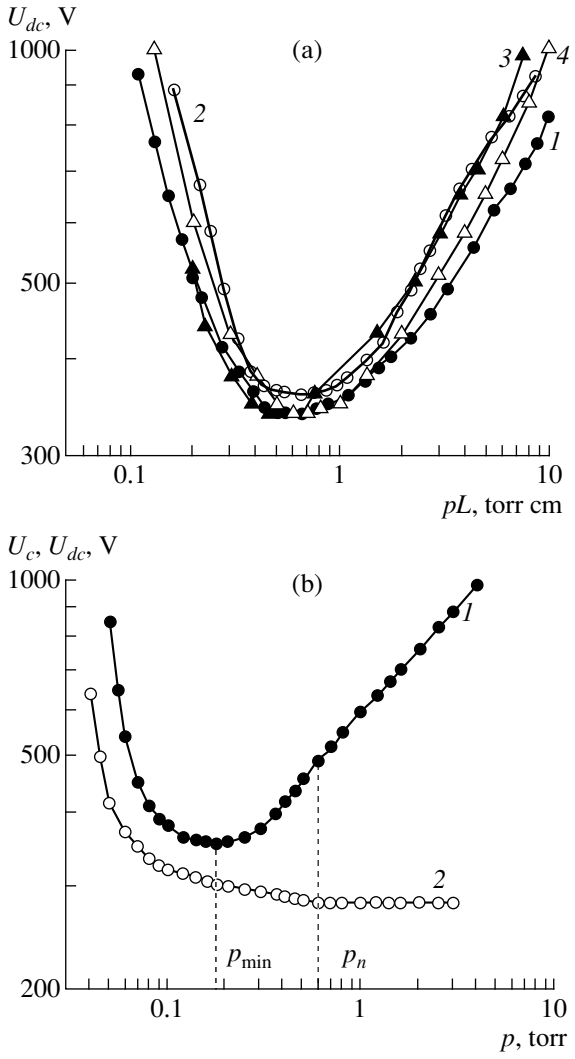

Fig. 1. (a) Breakdown curves of a glow discharge in air: (*1*) L = 11, (*2*) L = 54 mm, (*3*) experiment [19], and (*4*) experiment [16]; (b) (*1*) breakdown curve of a glow discharge and (*2*) dependence of the minimum value of the cathode voltage drop on the air pressure for L = 32 mm.

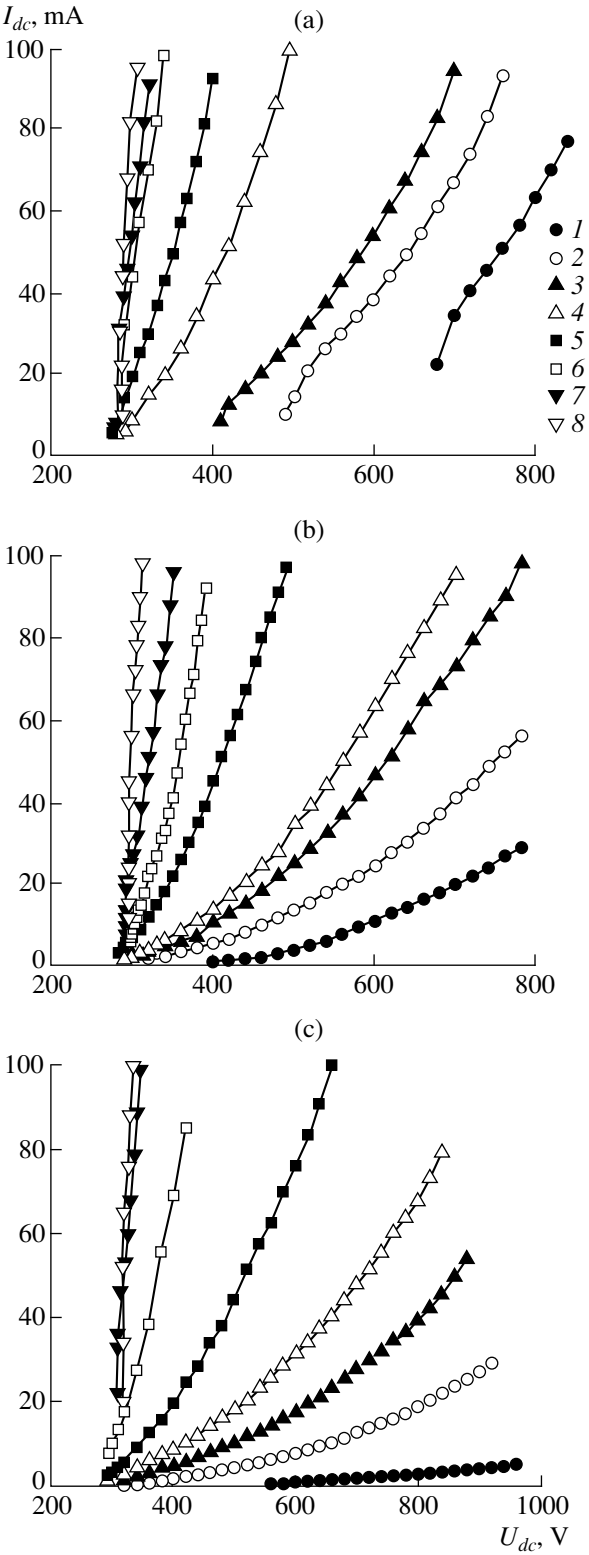

Fig. 2. *I–V* characteristics of a glow discharge for (a) L = 11 mm at p = (*1*) 0.1, (*2*) 0.15, (*3*) 0.2, (*4*) 0.4, (*5*) 0.6, (*6*) 1, (*7*) 1.5, and (*8*) 2 torr; (b) for L = 32 mm at p = (*1*) 0.06, (*2*) 0.1, (*3*) 0.15, (*4*) 0.2, (*5*) 0.4, (*6*) 0.6, (*7*) 1, and (*8*) 2 torr; and (c) for L = 54 mm at p = (*1*) 0.04, (*2*) 0.1, (*3*) 0.15, (*4*) 0.2, (*5*) 0.3, (*6*) 0.6, (*7*) 1.25, and (*8*) 2 torr.

Figure 1 shows the breakdown curves of a glow discharge in air, $U_{dc}(pL)$, measured by us for different distances L between the cathode and anode. It is seen from the figure that, as L increases, the minimum of the breakdown curve shifts toward higher values of the product pL. For example, for L = 1.1 cm, we have $p_{min} \approx$ 0.55 torr and $(pL)_{min} \approx$ 0.61 torr cm; for L = 5.4 cm, we have $p_{min} \approx$ 0.12 torr and $(pL)_{min} \approx$ 0.65 torr cm. At the same time, the breakdown voltage U_{dc} increases over the entire range of pL as the distance L between the cathode and anode increases. Thus, for pL = 0.6 torr cm (near the minimums of the breakdown curves), a glow discharge arises at U_{dc} = 334 V for L = 1.1 cm and U_{dc} = 360 V for L = 5.4 cm. The same dependence $U_{dc}(L)$ at pL = const was observed for other pL values. Hence, an increase in L leads to the shift of the breakdown curves toward higher values of both pL and the breakdown voltage U_{dc}. An increase in the breakdown voltage $U_{dc}(pL)$ was also indicated in [18, 19]. Such a deviation from the Paschen law can be attributed to the fact that the loss of charge particles due to diffusion toward the side walls of the discharge tube increases as the distance between the cathode and anode increases. A theoretical description of this effect is given in [20, 21].

Figure 1a also demonstrates the breakdown curves obtained by other authors [22, 23]. Note that curves *3* and *4* in Fig. 1a were obtained by averaging many experimental breakdown curves for different values of the interelectrode distance and the discharge-tube diameter. It is seen from the figure that our breakdown curves agree satisfactorily with the results of [22, 23].

Now, we specify the values of pL at which different structural components of a glow discharge are observed. At $pL < (pL)_{min}$ and over the entire range of U_{dc}, the glow discharge consists of a cathode sheath and a negative glow. At low values of U_{dc}, the cathode sheath occupies almost the entire discharge gap and the negative glow is adjacent to the anode. As U_{dc} increases, the length of the cathode sheath decreases, whereas almost the entire remaining part of the discharge gap becomes occupied by the negative glow. In this range of pL, the anode sheath is almost invisible, especially at higher values of the applied voltage U_{dc}.

At $pL \approx (pL)_{min}$ and low values of U_{dc}, a Faraday dark space appears; however, at a higher U_{dc}, the Faraday dark space disappears and the glow discharge again consists of the cathode sheath and the negative glow.

For $(pL)_{inf} = e(pL)_{min}$ (where e is the base of the natural logarithm), the Townsend breakdown criterion predicts the occurrence of an inflection point in the breakdown curve of a glow discharge [6, 20, 23]. Experimentally, such a point is sometimes absent in the breakdown curve. At $pL \geq (pL)_{inf}$, the glow discharge includes not only the cathode sheath, the negative glow, and the Faraday dark space, but also the anode sheath with the anode glow.

At $pL > 50$ torr cm (i.e., at $pL \gg (pL)_{min}$), a positive column arises. No inflection points are observed on the breakdown curve in this case.

Figure 2 shows the *I–V* characteristics of a glow discharge, $I_{dc} = f(U_{dc})$, for different distances L between the cathode and anode. It is seen from Fig. 2a that, for a short interelectrode distance ($L = 1.1$ cm), the discharge current is relatively high ($I_{dc} \geq 5$ mA) even at low gas pressures. At the minimum applied voltage U_{dc}, the discharge only partially occupies the cathode and anode surfaces. As U_{dc} increases, the discharge current I_{dc} increases and the electrode area occupied by the discharge increases rapidly until it occupies the entire electrode surface. At low pressures ($pL \leq (pL)_{inf}$), the effect of the normal current density is not observed because the increase in the discharge current is always accompanied by an increase in the discharge voltage. For $L = 1.1$ cm, the effect of the normal current density is observed at $p \approx 1.5$ torr, i.e., $(pL)_n \approx 1.65$ torr cm. Since, for this value of L, the minimum of the breakdown curve lies at $(pL)_{min} \approx 0.61$ torr cm, we obtain that $(pL)_n \approx 2.71\ (pL)_{min}$.

If at $pL \geq (pL)_{inf}$, the discharge voltage is reduced after breakdown, then the discharge is first observed to occur in the abnormal regime and to uniformly occupy the entire area of the electrodes. Then, the discharge arrives at the normal regime, in which case it is located near the dielectric side wall of the discharge tube, whereas the discharge at the center of the cathode is quenched. As the current I_{dc} decreases, the discharge in the normal regime first takes the shape of a torus. Then, a break in the torus appears and the discharge takes the shape of a toroidal segment. After this, the discharge is quenched.

The *I–V* characteristics for long interelectrode distances L are shown in Figs. 2b and 2c. At low values of the gas pressure and the voltage U_{dc}, the discharge current is low and, before quenching, the discharge occupies the entire cross section of the discharge tube. For $L = 3.2$ cm, the effect of the normal current density appears at $p \approx 0.6$ torr, i.e., $(pL)_n \approx 3.2\ (pL)_{min}$. As for $L = 1.1$ cm, for this distance, the normal discharge regime is observed at a gas pressure such that an anode glow (clearly visible and uniform over the entire anode surface) arises near the anode. As the pressure increases, the anode glow first appears near the wall of the discharge tube; then, the glow expands over the anode surface into the central region. When the anode glow at the minimum discharge voltage uniformly covers the entire anode surface, the effect of the normal current density appears.

This result is very interesting. Before, it was commonly accepted that the processes occurring in the cathode sheath are only important for the effect of the normal current density; i.e., it is necessary that the voltage drop across the cathode sheath become equal to the normal cathode voltage drop $U_c = U_n$ and the cathode-sheath length be equal to the normal length $d_c = d_n$. At the same time, little attention was given to the shape of the discharge and the processes occurring in the entire discharge gap, rather than only in the cathode sheath.

The anode glow appears when the voltage drop across the anode sheath becomes close to the ionization potential for neutral gas particles. Hence, it may be concluded that the voltage drop across the anode sheath becomes comparable with the ionization potential when the effect of the normal current density takes place in large-diameter discharge tubes; i.e., the gas molecules in the anode sheath are ionized by electron impact. A comparison of $(pL)_n$ values for $L = 1.1$ and 3.2 cm allows us to conclude that $(pL)_n \approx (pL)_{inf}$; i.e., the normal regime of a glow discharge can occur only within the pressure range to the right of the inflection point in the breakdown curve (at $pL > (pL)_{inf}$).

Figure 2c shows the *I–V* characteristics of a discharge at $L = 5.4$ cm. Qualitatively, they are similar to the characteristics shown in Fig. 2b, but there are some differences. For $L = 5.4$ cm, the anode glow appears at $p \approx 0.3$ torr, i.e., $pL \approx 1.62$ torr cm ($pL \approx 2.5(pL)_{min}$). The normal discharge regime appears at an air pressure of $p \approx 1$ torr (for $pL \approx 8.3\ (pL)_{min}$); i.e., there is a substantial difference in pL between the appearance of the anode glow and the effect of the normal current density. However, as is the case for shorter distances L, the normal regime takes place only after a clearly visible anode glow appears near the anode surface.

We also carried out a series of experiments in argon and nitrogen and obtained the following results. For argon at $L = 1.1$ cm, the anode glow and the effect of the normal current density appear at $pL \approx (pL)_n \approx 2.68(pL)_{min}$; for $L = 2.2$ cm, the anode glow is observed at $pL \approx 2.72\ (pL)_{min}$ and the normal discharge regime appears at $(pL)_n \approx 2.8\ (pL)_{min}$. For nitrogen at $L = 1.1$ cm, the anode glow and the effect of the normal current density are observed starting from $pL \approx (pL)_n \approx 2.73\ (pL)_{min}$. For $L = 2.2$ cm, we have $pL \approx 2.7\ (pL)_{min}$ for the appearance of the anode glow and $(pL)_n \approx 2.75(pL)_{min}$ for the appearance of the normal discharge regime. For $L = 3.3$ cm, the anode glow is observed starting from $pL \approx 2.69\ (pL)_{min}$ and the effect of the normal current density appears at $(pL)_n \approx 2.85\ (pL)_{min}$. This allows us to conclude that, over the entire range of the interelectrode distances L under investigation, the anode glow in different gases appears at $pL \approx (pL)_{inf}$, i.e., at the inflection point in the breakdown curve of a glow discharge. With short interelectrode distances $L \leq 3$ cm, the normal discharge regime is observed at $(pL)_n \geq (pL)_{inf}$, whereas for large values of L, the effect of the normal current density exists only at $(pL)_n > (pL)_{inf}$. As the distance L increases, the ratio $(pL)_n/(pL)_{inf}$ also increases.

3.2. Characteristics of the Cathode Sheath

The processes occurring in the cathode sheath play a decisive role in sustaining a glow discharge. Therefore, it is not surprising that, in studying a glow discharge, much attention is frequently paid to the characteristics of the cathode sheath (see, e.g., [3, 7, 24–31]). We also measured such important characteristics as the cathode voltage drop U_c (i.e., the voltage drop across the cathode sheath) and the cathode-sheath length d_c.

The voltage drop across the cathode sheath was determined by measuring the plasma potential φ_{pl} with respect to the anode with the help of a cylindrical probe positioned parallel to the cathode surface at the visible boundary of the sheath. In this case, the cathode voltage drop U_c is equal to the difference between the applied voltage U_{dc} and the plasma potential; i.e., $U_c = U_{dc} - \varphi_{pl}$. All of the probe measurements were made for the interelectrode distance $L = 3.2$ cm.

Figure 1b shows the dependence of a minimum cathode voltage drop on the gas pressure p. By a minimum cathode voltage drop, we mean the voltage drop across the cathode sheath before quenching the discharge. It is seen from the figure that, as the gas pressure increases, the minimum cathode voltage drop decreases, reaching the minimum value $U_c = U_n = 280 \pm 2$ V at $p \sim 0.6$ torr. As the pressure increases further, this value remains almost unchanged and is equal to the normal cathode voltage drop for the air–duralumin cathode system. From the same figure, it also follows that the cathode voltage drop reaches the minimum value U_n at $pL = (pL)_n$, i.e., when the effect of the normal current density takes place. For comparison, the breakdown curve of a glow discharge is also shown in Fig. 1b. It is easy to see that the cathode voltage drop becomes equal to its "normal" value at $pL > (pL)_{\inf}$, rather than at $pL > (pL)_{\min}$ as was stated in [8, 9].

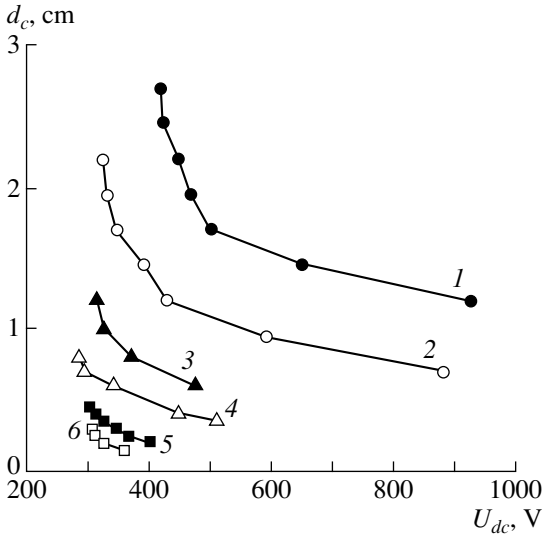

Fig. 3. The cathode-sheath length as a function of the constant voltage applied to the electrodes for $L = 32$ mm at $p =$ (*1*) 0.05, (*2*) 0.1, (*3*) 0.2, (*4*) 0.3, (*5*) 0.6, and (*6*) 1 torr.

Figure 3 shows the dependence of the cathode-sheath length d_c on the applied voltage U_{dc} for different air pressures. It follows from the figure that, at low pressures and low voltages U_{dc}, the cathode-sheath length is only slightly shorter than the interelectrode distance L, whereas at sufficiently high pressures, it covers only a small fraction of the discharge gap. The cathode-sheath length decreases rapidly with increasing applied voltage U_{dc}.

Figure 4a shows the cathode voltage drop U_c for different values of the product pd_c. It is seen from the figure that the product of the normal sheath length and air pressure is $pd_n \approx 0.3$ torr cm. All the experimental points fall reasonably well on one curve (which is analogous to the left branch of the Paschen curve).

Figure 4b shows the ratio j/p^2 as a function of the cathode voltage drop U_c. It is seen from this figure that, first, the minimum (normal) value of this ratio is equal to $(j/p^2)_n \approx 0.21$ mA/cm^2 torr^2 and, second, all of the measured values of $j/p^2(U_c)$ also fall on one curve.

For comparison, we present the results obtained by other authors for air [1]: $U_n = 229$ V for an aluminum cathode and $U_n = 269$ V for an iron cathode, $(j/p^2)_n \approx 0.33$ mA/cm^2 torr^2, and $pd_n \approx 0.25$ torr cm. These characteristics of the normal regime of a glow discharge coincide reasonably well with our results.

3.3. Axial Structure of a Glow Discharge

Here, we consider the axial profiles of the plasma parameters (ion density, plasma potential, and electron temperature) for two fixed values of the air pressure: 0.1 torr (the left branch of the breakdown curve) and 0.6 torr (the right branch of the breakdown curve, when the effect of the normal current density takes place). Note that the z-coordinate in all of the axial profiles is measured from the anode; i.e., the anode is on the left (at $z = 0$), and the cathode is on the right (at $z = 3.2$ cm).

Figure 5 shows the axial profiles of the positive-ion density $n_i(z)$. For $p = 0.1$ torr, the glow discharge consists of the cathode sheath, negative glow, and almost invisible anode sheath. From Fig. 5a, it is seen that, at low discharge voltages, the cathode sheath covers a significant fraction of the discharge gap and the cathode-sheath length decreases rapidly with increasing U_{dc}. Near the anode, the ion density begins to fall rapidly starting from $z \approx 4$–5 mm.

For $p = 0.6$ torr (Fig. 5b) and the minimum applied voltage $U_{dc} = 300$ V, the normal regime takes place and the glow discharge consists of the cathode sheath (with length $d_c \le 0.5$ cm), negative glow, Faraday dark space, and anode sheath with the anode glow. The length of

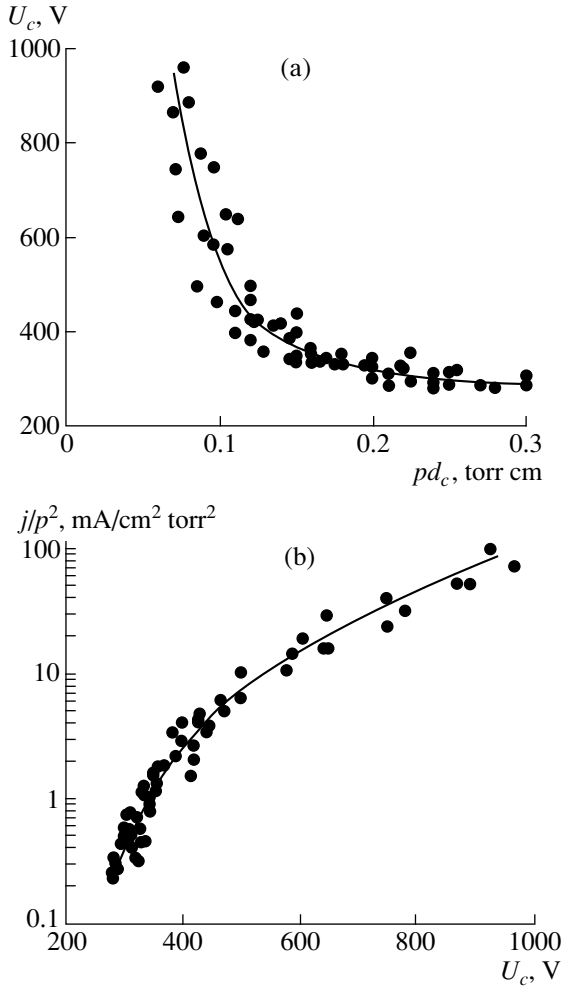

Fig. 4. (a) The cathode voltage drop as a function of the product pd_c and (b) the ratio j/p^2 as a function of the cathode voltage drop for L = 32 mm.

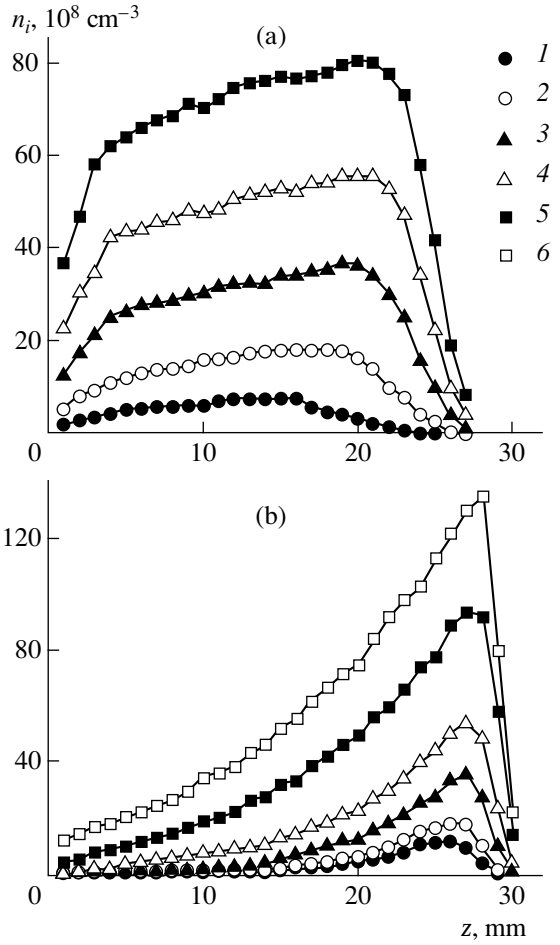

Fig. 5. Axial profiles of the plasma density in a glow discharge for L = 32 mm (a) at p = 0.1 torr and U_{dc} = (*1*) 350, (*2*) 400, (*3*) 500, (*4*) 600, and (*5*) 700 V and (b) at p = 0.6 torr and U_{dc} = (*1*) 300, (*2*) 325, (*3*) 350, (*4*) 375, (*5*) 400, and (*6*) 425 V.

the anode glow is no more than 1–1.5 mm, and the anode-sheath length is $d_a \approx 4$ mm. As the applied voltage U_{dc} increases, the plasma density increases monotonically throughout the discharge gap and the negative glow expands toward the anode. First, the Faraday dark space disappears. When the boundary of the negative glow reaches the anode sheath, the anode glow decays and also disappears. The maximum plasma density is observed near the boundary of the cathode sheath in the negative glow of the discharge. At p = 0.1 torr, the plasma density between the cathode and anode sheaths varies slightly (by no more than 30% for the range of voltages U_{dc} under study), but at p = 0.6 torr, the plasma density n_i decreases from the cathode sheath to the anode sheath by a factor of 7–10.

Figure 6 shows the axial profiles of the plasma potential $\varphi_{pl}(z)$. At the air pressure p = 0.1 torr, the plasma potential with respect to the anode in the negative glow was no more than 2 V, while the remainder of the voltage drop fell at the cathode sheath. The plasma potential in the negative glow slightly increased with applied voltage. In this case, the field in the anode sheath was nearly equal to the field in the negative glow. At p = 0.6 torr and low values of U_{dc}, a significant voltage drop (~10–12 V) was observed in the anode sheath. In this case in the Faraday dark space together with the negative glow, the voltage drop was no more than 5–8 V. As the voltage U_{dc} increased, the plasma potential with respect to the anode decreased to low values (~2–3 V) almost throughout the entire discharge gap (except for the cathode sheath); at the same time, a nearly constant plasma potential was observed in the negative glow (i.e., the electric field in the negative glow almost vanished).

Figure 7 shows the axial profiles of the electron temperature $T_e(z)$. At p = 0.1 torr (Fig. 7a) and low voltages U_{dc}, the electron temperature near the anode reaches the value $T_e \approx 2$ eV and decreases with distance from the

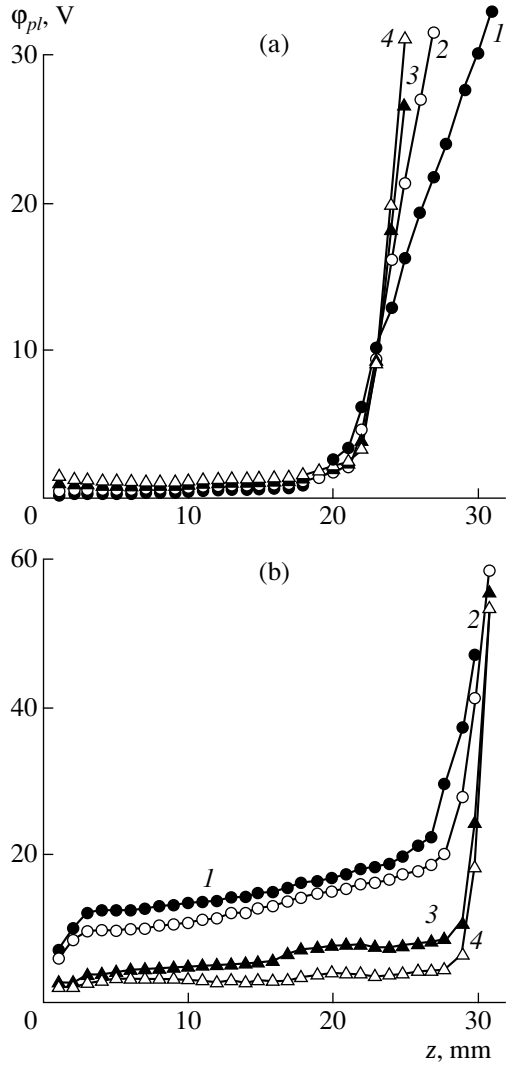

Fig. 6. Axial profiles of the plasma potential in a glow discharge for L = 32 mm (a) at p = 0.1 torr and U_{dc} = (*1*) 400, (*2*) 500, (*3*) 600, and (*4*) 700 V and (b) at p = 0.6 torr and U_{dc} = (*1*) 300, (*2*) 350, (*3*) 400, and (*4*) 425 V.

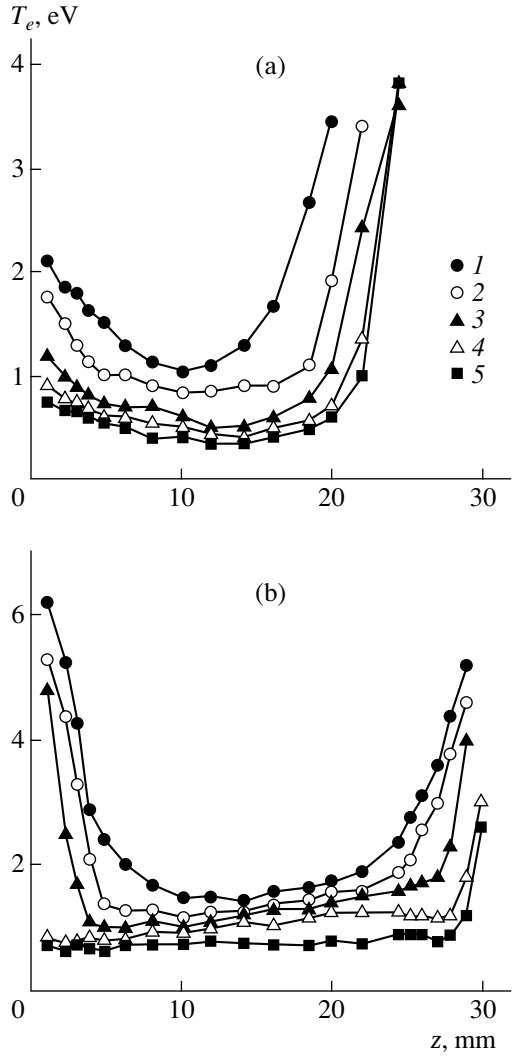

Fig. 7. Axial profiles of the electron temperature in a glow discharge for L = 32 mm (a) at p = 0.1 torr and U_{dc} = (*1*) 350, (*2*) 400, (*3*) 500, (*4*) 600, and (*5*) 700 V and (b) at p = 0.6 torr and U_{dc} = (*1*) 300, (*2*) 325, (*3*) 350, (*4*) 400, and (*5*) 425 V.

anode. Near the boundary of the cathode sheath and in the sheath itself, T_e rapidly increases. At high discharge voltages, the electron temperature is $T_e < 1$ eV almost throughout the entire discharge gap (except for the cathode sheath) and it somewhat increases near the anode.

At p = 0.6 torr (Fig. 7b) and low discharge voltages, the electron temperature near the anode reaches the value $T_e \approx 6$ eV, whereas at the boundary of the anode sheath, it is $T_e \approx$ 2–3 eV. In the Faraday dark space and negative glow, the electron temperature is $T_e < 2$ eV. As the voltage U_{dc} increases, the anode glow disappears and the electron temperature in the anode sheath decreases sharply. At high values of U_{dc}, the electron temperature in the anode sheath and negative glow varies slightly with distance from the anode and is about $T_e \leq 1$ eV.

We note that the sharp increase in the electron temperature near the boundary of the cathode sheath was also observed experimentally in [2, 32–35] and was predicted theoretically in [26, 36, 37]. This is associated primarily with an increase in the electric field and, as a result, with heating of electrons from the low-energy part of the electron Maxwell distribution. Let us estimate how rapidly the electrons that acquire a higher temperature T_e due to heating near the boundary of the cathode sheath will lose energy as they move deep into the negative glow. The mean free path of electrons in air at p = 0.6 torr is nearly equal to $\lambda_e \approx 0.2$ mm [6]. The energy-relaxation length is equal to $\Lambda_u \approx 0.8\lambda_e/\sqrt{\delta}$ [6],

where δ is the fraction of energy lost by an electron in a collision with a gas molecule. For a collision between an electron with energy $\varepsilon_e \approx 4$ eV and a nitrogen molecule, we take $\delta \approx 0.05$ [38]. Then, we obtain $\Lambda_u \approx 1.8$ mm, which agrees with the results of our measurements. Electrons with energies $\varepsilon_e \geq 6.2$ eV can excite the electronic levels of nitrogen molecules [6], which increases δ and, in turn, decreases the energy-relaxation length for electrons.

Now, we consider the reason why the electron temperature increases near the anode. As will be shown below, the anode voltage drop at low air pressures is small ($U_a \approx$ 1–2 V); consequently, near the anode surface, the ratio of the electric field strength to the gas pressure at $p = 0.1$ torr is no more than $E/p = 30$ V/(cm torr). For this value of E/p, the electron temperature near the anode can reach a value of $T_e =$ 2–3 eV [39] (which is seen in Fig. 7a). For the air pressure $p = 0.6$ torr and voltage $U_{dc} = 300$ V, we obtain $E/p = 200$ V/(cm torr) near the anode surface, which corresponds to an electron temperature of $T_e =$ 6–8 eV [39, 40] and agrees with the results of our experiments. At a higher discharge voltage U_{dc}, when the fast electrons accelerated in the cathode sheath reach the anode and the anode glow disappears, the anode voltage drop sharply decreases, which results in a decrease in E/p near the anode surface and a decrease in the electron temperature in the anode sheath. The increase in the electron temperature as the anode is approached was predicted theoretically in [11, 41–43] and observed experimentally in [11, 43].

3.4. Anode Voltage Drop

Figure 8 shows the measured voltage drop U_a across the anode sheath. At low levels of air pressure, as the voltage U_{dc} increases, the anode voltage drop slightly decreases, reaches its minimum, and then slightly increases; its value is $U_a \leq$ 2–3 V. As the air pressure increases, the anode voltage drop increases (at a fixed value of U_{dc}). With the appearance of the anode glow, the voltage drop across the anode sheath sharply increases: $U_a \geq 10$ V. At the air pressure $p = 0.6$ torr, the normal regime of a glow discharge is observed. In this case, the anode voltage drop is $U_a \geq 12$ V and the electron temperature at the boundary of the anode sheath is $T_e \approx 3$ eV; therefore, a certain fraction of the electrons moving toward the anode can acquire an energy that is sufficient to ionize gas molecules (for nitrogen molecules, the ionization energy is $U_i = 15.6$ eV; for oxygen molecules, it is $U_i = 12.2$ eV).

The anode voltage drop decreases as the voltage U_{dc} increases. At U_{dc} values such that the boundary of the negative glow approaches the anode sheath, the anode glow disappears and the anode voltage drop sharply decreases to $U_a \approx$ 3–5 V and remains almost unchanged as U_{dc} further increases. The higher the air pressure, the higher the voltage U_{dc} at which the boundary of the negative glow approaches the anode sheath. Once the anode glow disappears, U_a falls abruptly.

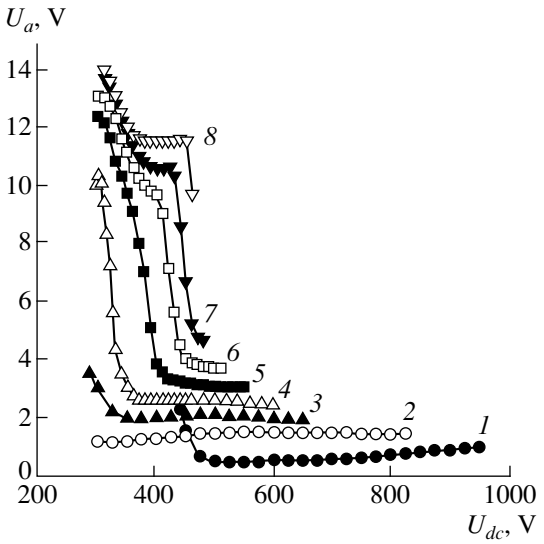

Fig. 8. Dependence of the anode voltage drop on the discharge voltage for $L = 32$ mm at air pressures $p =$ (*1*) 0.05, (*2*) 0.2, (*3*) 0.4, (*4*) 0.5, (*5*) 0.6, (*6*) 0.7, (*7*) 0.8, and (*8*) 1 torr.

In a glow discharge, the anode acts as a collector of electrons that makes the electron current in the external circuit equal to the total discharge current. As is seen from Fig. 8, the value of the anode voltage drop depends strongly on the anode position in the discharge. If the anode is inside the negative glow or in the adjacent region of the Faraday dark space, then the anode voltage drop is small and increases slightly as the gas pressure or the discharge voltage U_{dc} increases. In this region of the discharge gap, there is a significant flux of fast electrons emitted from the cathode surface and accelerated in the cathode sheath [26, 28]. In addition, the plasma density is maximum in the negative glow (see Fig. 5 and also [1, 2]). Therefore, if the anode is inside the negative glow, then it collects a high diffusion electron current and a flow of fast electrons. These two electron flows can reach the anode surface even at relatively low values of the anode voltage drop (as is seen in Fig. 8). This is what usually takes place at sufficiently low gas pressure values lying near and to the left of the minimum of the breakdown curve of a glow discharge.

Another situation takes place when the anode lies sufficiently deep in the Faraday dark space (on the anode side of the Faraday dark space). In this region of glow discharge, the diffusion electron current is low (which is seen from Fig. 5). Most of the fast electrons accelerated in the cathode sheath cannot penetrate into this region of the discharge, because they lose a great deal of energy in inelastic and elastic collisions with gas molecules and are thermalized. In such a situation, an additional ionization in the anode sheath is required

to make the electron current in the external circuit equal to the total discharge current. Hence, the anode voltage drop should be comparable with the ionization potential of gas molecules by electron impact. In this case, the anode glow is observed near the anode surface. As follows from the results of this study, this situation takes place at gas pressure values lying to the right of the inflection point of the breakdown curve of a glow discharge and moderate discharge voltages U_{dc}. As U_{dc} increases, the boundary between the negative glow and the Faraday dark space shifts toward the anode. At sufficiently high values of U_{dc}, when the anode is located inside the negative glow, the anode glow disappears and the voltage drop across the anode sheath sharply decreases.

In our experiments, the value of the anode voltage drop was always positive. However, as was shown in [10], the anode voltage drop becomes negative at sufficiently low gas pressures. For the negative anode voltage drop to be obtained in our discharge tubes, a glow discharge should be presumably ignited in the pressure range $p < 0.01$ torr at discharge voltages $U_{dc} > 1000$ V (however, this was beyond our experimental conditions).

4. CONCLUSIONS

In this paper we have examined the initiation and characteristics of a glow discharge in air in large-diameter discharge tubes. The main results can be summarized as follows:

(i) As the interelectrode distance L increases, the breakdown curves $U_{dc}(pL)$ shift toward higher values of U_{dc} and pL; i.e., a deviation from the Paschen law is observed.

(ii) The range of pL for the normal regime of a glow discharge is determined more exactly. It is shown that regimes with a normal current density are characterized not only by certain "normal" values of the cathode sheath parameters ($U_c = U_n$, $pd_c = pd_n$, $j/p^2 = (j/p^2)_n$), but also by the presence of ionization in the anode sheath. The normal discharge regime takes place at low air pressures only for pL values such that the cathode sheath, negative glow, Faraday dark space, and anode sheath with the anode glow are present simultaneously in the discharge. These conditions refer only to pL values lying to the right of the inflection point in the breakdown curve.

(iii) The cathode glow in the normal regime of an air discharge (for a duralumin cathode) is characterized by the following parameters: $U_n = 280 \pm 2$ V, $pd_n \approx 0.3$ torr cm, and $(j/p^2)_n \approx 0.21$ mA/cm^2 torr^2.

(iv) The axial profiles of the ion density, plasma potential, and electron temperature, as well as the anode voltage drop, are measured at various air pressure values lying both to the left and to the right of the minimum of the breakdown curve. It is shown that, in the normal discharge regime, the anode voltage drop and electron temperature at the boundary of the anode sheath are sufficiently high for the electron-impact ionization of gas molecules in the anode sheath.

REFERENCES

1. G. Frencis, in *Handbuch der Physik*, Ed. by S. Flugge (Springer-Verlag, Berlin, 1956), Vol. 22, p. 53.
2. V. L. Granovskiĭ, *Electric Current in a Gas: Steady-State Current* (Nauka, Moscow, 1971).
3. Yu. P. Raĭzer, Teplofiz. Vys. Temp. **24**, 984 (1986).
4. V. N. Melekhin and N. Yu. Naumov, Pis'ma Zh. Tekh. Fiz. **12**, 99 (1986) [Sov. Tech. Phys. Lett. **12**, 41 (1986)].
5. Yu. P. Raĭzer and S. T. Surzhikov, Pis'ma Zh. Tekh. Fiz. **13**, 452 (1987) [Sov. Tech. Phys. Lett. **13**, 186 (1987)].
6. Yu. P. Raizer, *Gas Discharge Physics* (Nauka, Moscow, 1987; Springer-Verlag, Berlin, 1991).
7. G. G. Lister, J. Phys. D **25**, 649 (1992).
8. B. N. Klarfeld, L. G. Guseva, and A. S. Pokrovskaya-Soboleva, Zh. Tekh. Fiz. **36**, 704 (1966) [Sov. Phys. Tech. Phys. **11**, 520 (1966)].
9. B. N. Klarfeld, L. G. Guseva, and V. V. Vlasov, in *Proceedings of the X International Conference on Phenomena in Ionized Gases, Oxford, 1971*, Contrib. Pap., Vol. 1, p. 97.
10. B. N. Klarfeld and N. A. Neretina, Zh. Tekh. Fiz. **30**, 186 (1960) [Sov. Phys. Tech. Phys. **5**, 169 (1960)].
11. Yu. B. Golubovskiĭ and Sh. Kh. al Hawat, Zh. Tekh. Fiz. **57**, 44 (1987) [Sov. Phys. Tech. Phys. **32**, 25 (1987)].
12. Yu. B. Golubovskiĭ, V. I. Kolobov, and Sh. Kh. al Hawat, Zh. Tekh. Fiz. **58**, 1729 (1988) [Sov. Phys. Tech. Phys. **33**, 1046 (1988)].
13. Yu. B. Golubovskiĭ, V. S. Nekuchaev, and N. S. Ponomarev, Zh. Tekh. Fiz. **68** (3), 25 (1998) [Sov. Phys. Tech. Phys. **43**, 288 (1998)].
14. V. A. Nemchinskiĭ, Zh. Tekh. Fiz. **40**, 416 (1970) [Sov. Phys. Tech. Phys. **15**, 317 (1970)].
15. G. J. Schulz and S. C. Brown, Phys. Rev. **98**, 1642 (1955).
16. O. V. Kozlov, *Electric Probe in a Plasma* (Atomizdat, Moscow, 1969).
17. N. A. Gorbunov, N. B. Kolokolov, and A. A. Kudryavtsev, Fiz. Plazmy **15**, 1513 (1989) [Sov. J. Plasma Phys. **15**, 881 (1989)].
18. J. M. Meek and J. D. Craggs, *Electrical Breakdown of Gases* (Clarendon, Oxford, 1953; Inostrannaya Literatura, Moscow, 1960).
19. L. Jacques, W. Bruynooghe, R. Boucique, and W. Wieme, J. Phys. D **19**, 1731 (1986).
20. V. I. Kolobov and A. Fiala, Phys. Rev. E **50**, 3018 (1994).
21. V. A. Lisovskiy and S. D. Yakovin, Zh. Tekh. Fiz. **70** (6), 58 (2000) [Tech. Phys. **45**, 727 (2000)].
22. T. W. Dakin, J. Gerhold, Z. Krasucki, *et al.*, in *Proceedings of the International Conference on Large High Voltage Electric Systems, Paris, 1977*, p. 1.
23. V. A. Lisovskiy and V. D. Yegorenkov, J. Phys. D **27**, 2340 (1994).
24. V. A. Shveĭgert and I. V. Shveĭgert, Fiz. Plazmy **14**, 347 (1988) [Sov. J. Plasma Phys. **14**, 204 (1988)].

25. V. A. Shveĭgert and I. V. Shveĭgert, Fiz. Plazmy **15**, 621 (1989) [Sov. J. Plasma Phys. **15**, 363 (1989)].
26. Yu. P. Raĭzer and M. N. Shneĭder, Fiz. Plazmy **15**, 318 (1989) [Sov. J. Plasma Phys. **15**, 184 (1989)].
27. T. J. Sommerer, W. N. G. Hitchon, and J. E. Lawler, Phys. Rev. A **39**, 6356 (1989).
28. Yu. P. Raĭzer and M. N. Shneĭder, Teplofiz. Vys. Temp. **29**, 1041 (1991).
29. V. I. Kolobov and L. D. Tsendin, Phys. Rev. A **46**, 7837 (1992).
30. A. P. Korzhavyĭ and V. I. Kristya, Zh. Tekh. Fiz. **63** (2), 200 (1993) [Tech. Phys. **38**, 156 (1993)].
31. Yu. P. Raĭzer and M. N. Shneĭder, Teplofiz. Vys. Temp. **35**, 19 (1997).
32. J. M. Anderson, J. Appl. Phys. **31**, 511 (1960).
33. G. S. Solntsev, A. I. Orlov, and V. A. Dovzhenko, Radiotekh. Élektron. (Moscow) **15**, 1980 (1970).
34. L. Protin, G. Fleury, and C. Vautier, Vacuum **34**, 791 (1984).
35. H. Sasaki, K. Nanbu, and M. Takahashi, Rep. Inst. Fluid Sci. **10**, 259 (1997).
36. D. B. Graves and K. F. Jensen, IEEE Trans. Plasma Sci. **14**, 78 (1986).
37. G. Lapenta, F. Iinoya, and J. U. Brackbill, IEEE Trans. Plasma Sci. **23**, 769 (1995).
38. L. G. Christophorou and J. G. Carter, Chem. Phys. Lett. **2**, 607 (1968).
39. J. J. Lowke and R. Morrow, IEEE Trans. Plasma Sci. **23**, 661 (1995).
40. C. S. Lakshminarasimha and J. Lucas, J. Phys. D **10**, 313 (1977).
41. J. J. Lowke, J. H. Parker, and C. A. Hall, Phys. Rev. A **15**, 1237 (1977).
42. Yu. B. Golubovskiĭ, Sh. Kh. al Hawat, and L. D. Tsendin, Zh. Tekh. Fiz. **57**, 1285 (1987) [Sov. Phys. Tech. Phys. **32**, 760 (1987)].
43. V. A. Shveĭgert, Fiz. Plazmy **14**, 1363 (1988) [Sov. J. Plasma Phys. **14**, 801 (1988)].

Translated by N. Larionova

Plasma Physics Reports, Vol. 26, No. 12, 2000, pp. 1076–1078. Translated from Fizika Plazmy, Vol. 26, No. 12, 2000, pp. 1149–1151.

BRIEF COMMUNICATIONS

Production of C_2^* Radicals in a Transverse Volume Discharge

A. K. Shuaibov, L. L. Shimon, A. I. Dashchenko, and I. V. Shevera

Uzhgorod State University, Pidgirna str. 46, Uzhgorod, 88000 Ukraine

Received February 24, 2000; in final form, June 12, 2000

Abstract—Conditions for producing stable transverse volume discharges in freon-containing media (CCl_4/air mixtures at a pressure of P = 0.1–2 kPa) are studied. It is shown that a transverse discharge produced in the CCl_4/air = (1–2)/0.03 kPa mixture at a moderate discharge voltage (U_{ch} = 8–15 kV) and an interelectrode distance of d = 2.2 cm is a selective source of $C_2(d^3\Pi_g–a^3\Pi_u)$ 468.0- and 516.5-nm radiation and C(2*p*–3*s*) 247.9-nm radiation. The brightness of the $C_2(d–a)$ band is comparable with that of the $N_2(C–B)$ 337.1- and 357-nm bands. The transverse discharge in CCl_4 is of interest for generating pulsed emission via the *d–a* transitions of C_2 molecules in the blue–green region of the visible spectrum. © *2000 MAIK "Nauka/Interperiodica".*

In connection with the problem of developing high-power chemically pumped sources of induced and spontaneous radiation [1], it is of interest to study the production of C_2^* molecules in pulsed low-temperature plasmas. In [2], the chemical excitation and emission of carbon molecules produced during the mixing of Mg or Na vapor with CCl_4 vapor was studied. An abnormal spectral intensity distribution at the edges of the $C_2(d^3\Pi_g, v \le 6)$ bands was indicated. Under the action of the radiation from a 9.6-μm TEA CO_2 laser (E_{dep} = 2 J/cm^2) on CCl_3F/C_2H_2 or CCl_3F/C_2H_6 mixtures at pressures of $P \ge 1.3$ kPa, intense chemiluminescence of C_2^* molecules in the visible spectrum was observed over the entire cell length [3]. In experiments on the ablation of graphite by a XeCl laser [4], nonequilibrium $C_2(d–a)$ 508-nm radiation was also observed. The characteristics of emission and the mechanism for the production of C_2^* molecules and C* atoms in continuous and pulsed longitudinal discharges were studied in detail in [5, 6]. Experiments were carried out in a He/CO = 0.2–1.0 kPa mixture at an average current of 10–100 mA and CO concentration of less than 3%. It was found that the increase in the pressure was accompanied by the selective population of $C_2(d^3\Pi_g, v = 6)$ states through reactions with the participation of long-lived particles $C_2O + C \longrightarrow C_2^* + CO$ ($k = 3 \times 10^{-10}$ cm^3/s) [6]. When He/CO(N_2, Xe) mixtures were excited in a transverse volume discharge (TVD) of submicrosecond duration, no C_2^* molecules were detected [7]. In a TVD in pure freon-12 (CF_2Cl_2) at P = 0.1–3 kPa, the plasma emission spectra showed an efficient production of C_2^* molecules [8].

In this study, the CCl_4 molecule, which is less stable against destruction in the discharge, was chosen to be a carbon carrier. To examine the efficiency with which C_2^* molecules are produced in the presence of $N_2(C)$ molecules, which are an active medium of TVD-pumped $N_2(C–B)$ lasers, a small amount of air was admixed into the CCl_4 vapor.

A TVD with an automatic spark preionization was ignited in the $18 \times 0.7 \times 2.2$ cm volume (the interelectrode distance being d = 2.2 cm) using a double LC-circuit with a main 30-nF capacitor and sharpening capacitors with a total capacity of 9.4 nF. A TGI 1 1000/25 thyratron was used as a switch. The inductance of the main supply circuit for the discharge was less than 10 nH. The maximum energy deposition in the TVD plasma was 10–20 mJ/cm^3. The scheme of the emitter and the diagnostic technique for recording the discharge characteristics are described in [9].

Figure 1 shows the emission spectrum of a TVD in a CCl_4/air mixture. The most intense emissions in the UV and visible spectral regions were the emission via 2^+ transitions of the N_2, CN(*B–X*), $C_2(C^1\Pi_g–A^1\Pi_u)$ system and C(2*p*–3*s*) 247.9-nm emission. The intensities of Swan bands were comparable with the intensities of the $N_2(C–B)$ 337.1- and 357.6-nm laser bands, which indicates the efficient production of $C_2(d^3\Pi_g)$ molecules in the plasma under study. A comparison of the intensities of Swan bands with the intensity of the XeF 353-nm band in a Ar/Xe/SF_6 = 100/3/0.3 mixture at P = 7 kPa and the discharge voltage U_d = 10 kV showed that the intensity of emission via carbon-molecule transitions was less than 5–10% of the intensity of the XeF(*B–X*) excimer band. The Deslandres–d'Azambuja band with a C_2^* 385.2-nm edge was observed in the short-wavelength wing of the CN(*B–X*) bands. Weaker CN(*B–X*) bands were also observed in the 410- to 420-nm range. In the vibrational structure of the Swan-band sequence with $\Delta v = +1$, an inverse population was

1063-780X/00/2612-1076$20.00 © 2000 MAIK "Nauka/Interperiodica"

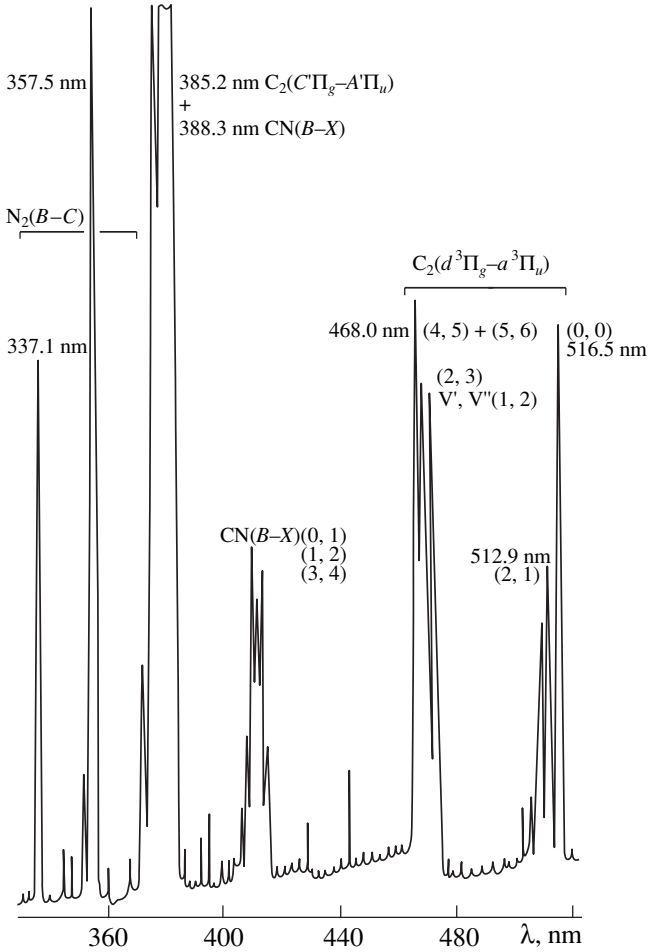

Fig. 1. Emission spectrum of the plasma of a TVD in the CCl_4/air = 800/25 Pa mixture at U_d = 15 kV.

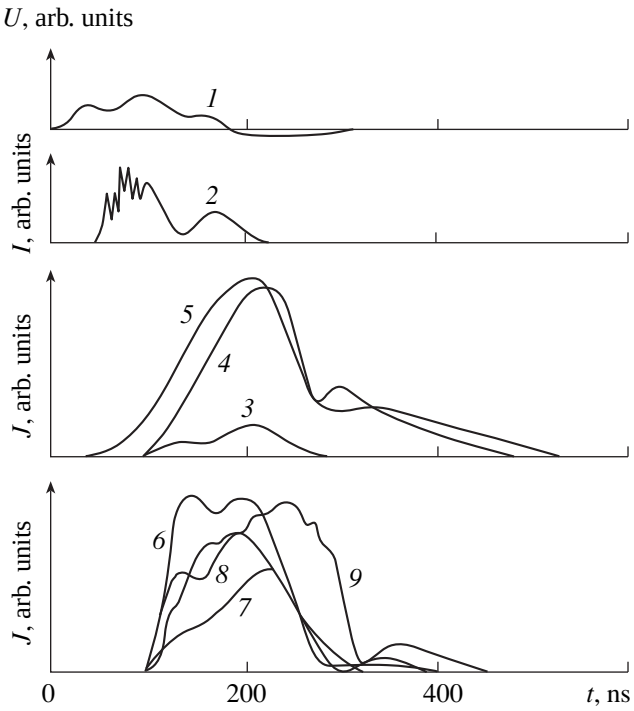

Fig. 2. Waveforms of the (*1*) voltage, (*2*) current, and intensities of emission from the plasma of a TVD in the CCl_4/air = 1200/25 Pa mixture in the (*3*) C($2p$–$3s$) 247.9-nm, (*4*) C_2(d–a)(6, 5) 468.0-nm, (*5*) C_2(d–a)(0, 0) 516.5-nm, (*6*) N_2(C–B)(0, 0) 337.1-nm, (*7*) $Cl^+(4p'^3P_3–5s'^3D_3^0)$ 414.7-nm, (*8*) $Cl(4s^4P_{5/2}–5p^4D_{5/2}^0)$ 426.4 nm, and (*9*) CN(B–X)(0, 0) 388.3-nm bands.

observed for levels of the $d^3\Pi_g$ state of C_2 molecules. The maximum intensity was observed for the set of unresolved bands with λ = 467.8–468 nm corresponding to the v = 6–5 and 5–4 transitions of the C_2(d–a) system. Such an anomalous distribution of the intensity of the electronic–vibrational Swan-band sequence Δv = +1 was observed in a CF_4 plasma jet at a lower translational temperature ($T \le 4000$ K) [10, 11]. This was explained by the occurrence of chemical reactions such that the transitions from different levels were initiated with different probabilities. Simultaneously with the Swan bands, low-intensity bands (λ = 491–494 nm) of CF_3^* and C_2F^* radicals were observed in the spectra. We obtained no information concerning the appearance of the emission from radicals of the C_2Cl^* type that are probably produced in a CCl_4 plasma. The emission from CCl_3^* radicals is usually recognized by a wide band in the 400–600-nm spectral region with a maximum at λ = 470 nm [12]. In the spectrum shown in Fig. 1, this band of CCl_3^* molecules is probably present in the continuum.

Figure 2 shows the waveforms of the voltage, current, and intensity of emission from the products of destruction of the plasma of a TVD in the CCl_4/air mixture. All of the excited plasma products showed up immediately in the afterglow following the pumping current. This emission intensity had two maximums (like the TVD current) and was associated primarily with chemical reactions. The emission of the Swan-band sequence with Δv = 0 was observed earlier (by 40–50 ns) than the emission of the band sequence with Δv = +1. The most probable reactions leading to the population of the $C_2(d^3\Pi_g)$ state in the plasma under study are the following:

$$C_2Cl + C \longrightarrow C_2(^5\Pi_g, v) + CCl, \quad (1)$$

$$C_2(^5\Pi_g, v) + M \longrightarrow C_2(^5\Pi_g, 0) + M, \quad (2)$$

$$C_2(^5\Pi_g, 0) + M \longrightarrow C_2(d^3\Pi_g, 6) + M, \quad (3)$$

where $C_2(^5\Pi_g)$ is the metastable state of a C_2 molecule and M designates CCl_4, N_2, or O_2. In the production of $C_2(d^3\Pi_g, 0)$, the reaction $C_2 + e \longrightarrow C_2(d^3\Pi_g, 0)$ plays an important role in the initial stage of a TVD.

In this study, we have shown that a CCl_4 TVD plasma is a selective source of pulsed (150–200 ns) emission from C_2^* molecules in the blue–green region of the visible spectrum. In the Swan-band sequence with $\Delta v = +1$, the inverse population of vibrational levels with $v \leq 6$ (C_2^* 468.0-mn transitions) is observed. The CCl_4 TVD plasma may find an application in pulsed sources of $C_2(d–a)$ 468.0- and 516.5-nm radiation.

REFERENCES

1. V. F. Gavrikov, A. N. Dvoryankin, A. A. Stepanov, *et al.*, Tr. Fiz. Inst. Akad. Nauk SSSR **194**, 171 (1989).
2. E. D. Bugrim, A. I. Lyutyĭ, V. S. Rassikhin, and I. L. Tsikora, Opt. Spektrosk. **20**, 568 (1966).
3. M. O. Bulanin, S. F. Bureĭko, and I. L. Danilov, Opt. Spektrosk. **51**, 563 (1981) [Opt. Spectrosc. **51**, 313 (1981)].
4. A. V. Demyanenko, V. S. Letokhov, A. A. Puretskiĭ, and E. A. Ryabov, Kvantovaya Élektron. (Moscow) **24**, 1012 (1997).
5. G. M. Grigoryan, Yu. Z. Ionikh, and N. V. Chernyshova, Opt. Spektrosk. **70**, 309 (1991) [Opt. Spectrosc. **70**, 180 (1991)].
6. Yu. Z. Ionikh, I. N. Kostyukevich, and N. V. Chernyshova, Opt. Spektrosk. **74**, 455 (1993) [Opt. Spectrosc. **74**, 274 (1993)]; Opt. Spektrosk. **76**, 406 (1994) [Opt. Spectrosc. **76**, 361 (1994)]; Opt. Spektrosk. **80**, 590 (1996) [Opt. Spectrosc. **80**, 527 (1996)].
7. A. K. Shuaibov, A. I. Dashchenko, A. A. Sinishin, and V. S. Shevera, Pis'ma Zh. Tekh. Fiz. **23** (19), 71 (1997) [Tech. Phys. Lett. **23**, 765 (1997)].
8. A. K. Shuaibov, Pis'ma Zh. Tekh. Fiz. **24** (23), 30 (1998) [Tech. Phys. Lett. **24**, 919 (1998)].
9. A. K. Shuaibov, Kvantovaya Élektron. (Moscow) **26**, 127 (1999).
10. V. G. Khalturin, I. S. Fishman, and B. P. Khalepp, Zh. Obshch. Khim. **58**, 1351 (1988).
11. V. G. Khalturin, Zh. Prikl. Spektrosk. **54**, 285 (1991).
12. Yu. S. Kravchenko, V. S. Osadchuk, A. F. Sergienko, *et al.*, Teplofiz. Vys. Temp. **25**, 151 (1987).

Translated by N. Larionova

Plasma Physics Reports, Vol. 26, No. 12, 2000, p. 1079. Translated from Fizika Plazmy, Vol. 26, No. 12, 2000, p. 1152.

NEW BOOKS

V. B. Krasovitskiĭ, *Nonlinear Regular Oscillations in Nonequilibrium Plasma and Gaseous Media* (Folio, Kharkov, 2000), Vols. 1, 2

Vol. 1: *Instabilities of a Relativistic Electron Beam in a Plasma* (Folio, Kharkov, 2000), 268 p.

Vol. 2: *Self-Focusing of Relativistic Electron Bunches in a Plasma* (Folio, Kharkov, 2000), 255 p.

The first volume is devoted to the nonlinear theory of the collective interaction between a modulated beam of relativistic charged particles and narrow electromagnetic and Langmuir wave packets in plasma or gas slow-wave systems. Regular oscillations excited by a relativistic beam under the conditions of the Cherenkov resonance and the anomalous Doppler effect can be used to generate coherent microwave radiation and accelerate charge particles in a plasma.

The main subject of the second volume is the nonlinear theory of the electrostatic focusing of an electron beam split into bunches under conditions when the plasma permittivity at the modulation frequency is negative and the effective Coulomb force acting on the electron bunches is reversed. Conditions for the spatial equilibrium between the bunch and plasma emission, as well as the dynamics of the formation of focused bunches, are confirmed by solving (both analytically and numerically) the self-consistent set of equations.

Results are also presented from investigations on nonlinear plasma theory, including the propagation of Langmuir and helicon solitons in a plasma with a charged particle beam under the conditions of the Cherenkov and cyclotron resonances, the collective acceleration of ions by a relativistic electron beam, and the propagation of Langmuir perturbations in a weakly ionized gas described by the Davydov kinetic equation.

The beam instability is frequently encountered in laboratory, geophysical, and astrophysical plasma studies. Therefore, the book will be of interest to experts in plasma physics and related sciences, as well as to all those who are interested in the problems of modern physics. To solve the applied problems of plasma physics, the general methods of macroscopic electrodynamics are used. Most of the chapters are supplemented by appendices that contain detailed mathematical derivations and may be useful for lecturers and students.

1063-780X/00/2612-1079$20.00

Plasma Physics Reports, Vol. 26, No. 12, 2000, pp. 991–999. Translated from Fizika Plazmy, Vol. 26, No. 12, 2000, pp. 1059–1067.

Investigation of the Possibility of Exceeding the Greenwald Density Limit during ECRH in T-10

V. V. Alikaev, A. A. Borshchegovskiĭ, V. V. Volkov, M. M. Dremin, Yu. V. Esipchuk, A. M. Kakurin, N. A. Kirneva, A. Ya. Kislov, D. A. Kislov, I. V. Klimanov, V. A. Kochin, V. A. Krupin, S. V. Krylov, T. B. Myalton, A. Yu. Novikov, G. E. Notkin, Yu. D. Pavlov, V. V. Piterskiĭ, V. I. Poznyak, I. N. Roĭ, P. V. Savrukhin, M. M. Stepanenko, A. V. Sushkov, V. M. Trukhin, E. V. Trukhina, and V. V. Chistyakov

Nuclear Fusion Institute, Russian Research Centre Kurchatov Institute, pl. Kurchatova 1, Moscow, 123182 Russia

Received March 31, 2000; in final form, May 30, 2000

Abstract—In T-10 experiments, attempts were made to significantly exceed the Greenwald limit $\bar{n}_{\mathrm{Gr}}$ during high-power (P_{ab} = 750 kW) electron-cyclotron resonance heating (ECRH) and gas puffing. Formally, the density limit $(\bar{n}_e)_{\mathrm{lim}}$ exceeding the Greenwald limit ($(\bar{n}_e)_{\mathrm{lim}}/\bar{n}_{\mathrm{Gr}}$ = 1.8) was achieved for q_L = 8.2. However, as q_L decreased, the ratio $(\bar{n}_e)_{\mathrm{lim}}/\bar{n}_{\mathrm{Gr}}$ also decreased, approaching unity at $q_L \approx 3$. It was suggested that the "current radius" (i.e., the radius of the magnetic surface enclosing the bulk of the plasma current I_p), rather than the limiter radius, was the parameter governing the value of $(\bar{n}_e)_{\mathrm{lim}}$. In the ECRH experiments, no substantial degradation of plasma confinement was observed up to $\bar{n}_e \sim 0.9(\bar{n}_e)_{\mathrm{lim}}$ regardless of the ratio $(\bar{n}_e)_{\mathrm{lim}}/\bar{n}_{\mathrm{Gr}}$. In different scenarios of the density growth up to $(\bar{n}_e)_{\mathrm{lim}}$, two types of disruptions related to the density limit were observed.

1. INTRODUCTION: THE GOAL OF THE EXPERIMENTS

1. In previous electron-cyclotron-resonance-heating (ECRH) experiments with gas puffing in T-10 [1], it was shown that the density limit $(\bar{n}_e)_{\mathrm{lim}}$ increased with increasing the microwave power P_{ab} absorbed in the plasma:

$$(\bar{n}_e)_{\mathrm{lim}}^{\mathrm{HF}} = (\bar{n}_e)_{\mathrm{lim}}^{\mathrm{OH}} \sqrt{\frac{P_{\mathrm{tot}}}{P_{\mathrm{OH}}}},$$

where $P_{\mathrm{tot}} = P_{\mathrm{ab}} + P_{\mathrm{OH}}$.

At a sufficiently high microwave power ($P_{\mathrm{ab}} \sim$ 1 MW), a nearly twofold increase in the density limit was achieved. However, because of the poor wall condition in these experiments, the density limit in ohmically heated plasmas dropped significantly when gyrotrons began to operate. As a result, although $(\bar{n}_e)_{\mathrm{lim}}$ doubled during ECRH, attempts to substantially exceed the Greenwald limit [2]

$$\bar{n}_{\mathrm{Gr,\,20}} = \frac{I_p[\mathrm{MA}]}{\pi a^2[\mathrm{m}]}$$

were unsuccessful.

At present, as a result of the improved conditioning and backing of the chamber, the plasma state has been substantially improved and the density limit of the ohmically heated plasma decreases only slightly when gyrotrons begin to operate. This was confirmed by testing experiments in which $(\bar{n}_e)_{\mathrm{lim}}$ was determined for an ohmically heated plasma both at the beginning and at the end of each day of ECRH experiments.

For this reason, it became relevant to pose the problem of verifying the possibility of significantly exceeding the Greenwald limit in experiments with gas puffing and high-power ECRH (P_{ab} = 0.8 MW).

The experiments were also aimed at answering the following questions:

(i) Does the degradation of energy and/or particle confinement occur near $(\bar{n}_e)_{\mathrm{lim}}$?

(ii) If this is the case, then in which density range Δn with respect to $(\bar{n}_e)_{\mathrm{lim}}$ and $(\bar{n}_{\mathrm{Gr}})$ does it occur?

(iii) What is the cause of confinement degradation and how large is this degradation?

2. Experiments were carried out at three values of the plasma current:

(i) I_p = 230 kA (q_L = 3.2, $\bar{n}_{\mathrm{Gr}} = 8.1 \times 10^{19}$ m^{-3}),

(ii) I_p = 150 kA (q_L = 4.8, $\bar{n}_{\mathrm{Gr}} = 5.3 \times 10^{19}$ m^{-3}), and

(iii) I_p = 90 kA (q_L = 8.2, $\bar{n}_{\mathrm{Gr}} = 3.2 \times 10^{19}$ m^{-3}).

Microwaves at a frequency of f = 140 GHz (the second ECR harmonic, X-mode) were launched into the tokamak at an angle of $\psi = 21°$ to the direction of the

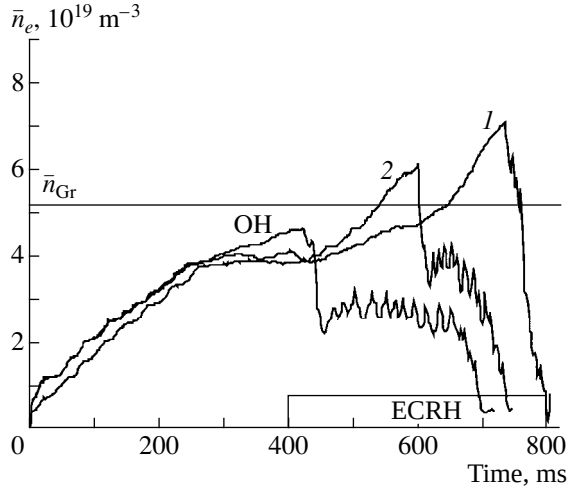

Fig. 1. Scenario of the growth of the line average density $\bar{n}_e$ at I_p = 150 kA and B_T = 2.42 T in regimes with different values of the heating power P_{ab} = (*1*) 800 and (*2*) 380 kW.

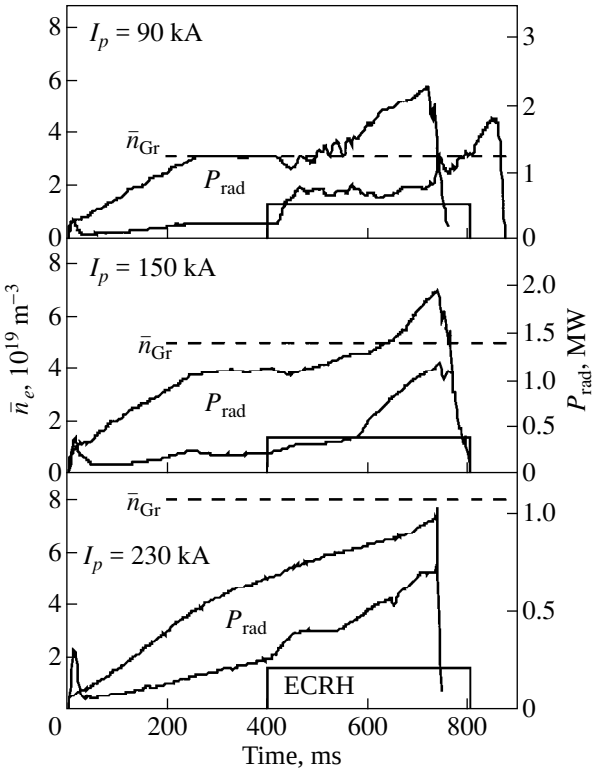

Fig. 2. Time evolutions of the line average $\bar{n}_e$ at P_{ab} = 0.6–0.75 MW in regimes with different values of I_p. The dashed lines indicate the Greenwald limit $\bar{n}_{Gr}$.

major radius R. In all cases, the toroidal magnetic field was equal to B_T = 2.42 T, which corresponded to the resonant absorption of microwaves near the center of the plasma column, provided that the plasma density was not too high and the microwave refraction did not markedly disturb the profile of the absorbed power (see Section 2). In these experiments, the limiter radius was a_L = 30 cm.

2. DEPENDENCE OF THE RATIO $(\bar{n}_e)_{lim}/\bar{n}_{Gr}$ ON q_L

1. Figure 1 shows the scenarios of the density growth in the regimes with different values of the auxiliary heating power and I_p = 150 kA (q_L = 4.8). It is seen that, as in the previous T-10 experiments [1], the density limit grows as the total heating power P_{tot} increases.

Figure 2 illustrates the time evolutions of the plasma density for the three regimes; the dashed lines show the Greenwald limit $\bar{n}_{Gr}$. It is seen that, for low values of the safety factor ($q_L \simeq 3.2$), the value of the density limit $(\bar{n}_e)_{lim}$ is close to $\bar{n}_{Gr}$; however, as q_L increases, the ratio $(\bar{n}_e)_{lim}/\bar{n}_{Gr}$ grows, reaching the value ~1.8 at q_L = 8.2.

2. As is seen from Fig. 2, in all three regimes, the radiation power P_{rad} grows as the density increases and, when the latter reaches $(\bar{n}_e)_{lim}$, the value P_{rad} becomes nearly equal to the total heating power P_{tot}. Unfortunately, the radiation power profile was not measured; therefore, we cannot characterize the role of the multifaceted asymmetric radiation from the edge (MARFE) near $(\bar{n}_e)_{lim}$. However, the profile of $\Phi(h) = \int n_e\, dl$ (where h is the observation chord) presented in Fig. 3 indicates that the MARFE effect is not so strong. Furthermore, in the regimes with the maximum heating power, the density profile becomes peaked as the density approaches $(\bar{n}_e)_{lim}$ (Fig. 13).

3. Thus, the T-10 experiments reveal that the excess of the density limit $(\bar{n}_e)_{lim}$ over the value $(\bar{n}_e)_{Gr}$ predicted by the Greenwald formula depends on q_L (see Fig. 4).

In T-10, both in ohmically heated plasmas and in ECRH plasmas, the profiles of the temperature T_e and, consequently, the plasma current density j become peaked as q_L increases. In addition, it should be noted that, in previous experiments on studying the density limit in T-10 [1], it was shown that, as $\bar{n}_e$ approaches the limit $(\bar{n}_e)_{lim}$, the amplitude of the m = 2 MHD mode gradually grows. The formation of an island is explained by the fact that, as the density approaches $(\bar{n}_e)_{lim}$, cooling occurs predominantly at the edge of the plasma column and the current channel becomes narrower. Consequently, the current flowing outside of the magnetic surface q = 2 decreases, which ultimately results in a discharge disruption. With such a disruption

mechanism, the limiter radius should not be regarded as an adequate parameter determining the density limit $(\bar{n}_e)_{\rm lim}$.

The new data presented in Fig. 4 do not contradict this disruption mechanism. This allows us to suggest that an adequate parameter for determining the density limit is the "current radius" a_C, i.e., the radius of the magnetic surface enclosing the bulk of the plasma current.

In this case, the Greenwald limit can be presented in the form

$$(\bar{n}_e)_{\rm Gr}^{\rm mod} = \frac{I_p}{\pi a_C^2}. \quad (1)$$

Since the current radius is difficult to determine precisely, for definiteness, we took the radius of the magnetic surface enclosing 95% of the total current: $a_C = r(I = 0.95I_p)$. The current profile $j(r)$ was calculated by the ASTRA code [3] assuming that the conductivity is neoclassical and using experimental profiles $T_e(r)$ and $n_e(r)$.

The ratio of the density limit $(\bar{n}_e)_{\rm lim}$ to the Greenwald limit modified according to (1), $(\bar{n}_e)_{\rm lim}/(\bar{n}_e)_{\rm Gr}^{\rm mod}$, is plotted in Fig. 4 as a function of I_p. It is seen that, in this representation, the ratio $(\bar{n}_e)_{\rm lim}/(\bar{n}_e)_{\rm Gr}^{\rm mod}$ remains constant over the entire range of q_L under investigation and is equal to $(\bar{n}_e)_{\rm lim}/(\bar{n}_e)_{\rm Gr}^{\rm mod} \simeq 0.9$.

Note that, according to the above considerations, the experimental curve $(\bar{n}_e)_{\rm lim}/\bar{n}_{\rm Gr}$ should asymptotically approach 0.9. A sharper dependence in the vicinity of I_p = 230 kA is explained by the fact that the microwave power in this regime was lower than in other cases ($P_{\rm ab}$ = 600 kW instead of $P_{\rm ab}$ = 820 kW).

At I_p = 150 kA, experiments in which the density limit $(\bar{n}_e)_{\rm lim}$ was attained were also carried out at a reduced limiter radius, a_L = 25 cm. According to the Greenwald formula, the density limit in these experiments might be expected to increase as $(\bar{n}_e)_{\rm Gr} \sim 1/a_L^2$ (i.e., by a factor of 1.4). However, $(\bar{n}_e)_{\rm lim}$ remained almost at the same level as for a_L = 30 cm because the current radius a_C changed slightly. This result is consistent with the above considerations.

Thus, based on the above considerations, we can suggest that, in the T-10 experiments with gas puffing, in spite of a rather high microwave power ($P_{\rm ab}$ to 0.85 MW), our attempts to exceed the physical limitations underlying the Greenwald limit were not successful.

Note that, at densities so high that $n_e(0)$ can approach the cutoff level (Fig. 13), microwave refraction plays an important role, which causes the profile of the absorbed power $P_{\rm ab}(r)$ to change. Figures 5 and 6 illustrate the ray trajectories calculated by the TORAY code [4] for two values of the line averaged density. It is seen that, for $\bar{n}_e = 0.9(\bar{n}_e)_{\rm lim}$, microwave refraction becomes so strong that the single-pass microwave-power absorption is close to zero. The power reflected from the walls is absorbed after several passes; however, the profile of $P_{\rm ab}$ should change significantly: it should broaden and maybe even become hollow (off-axis heating). Computations of the $P_{\rm ab}(r)$ profile formed after multiple reflections from the chamber walls are still lacking.

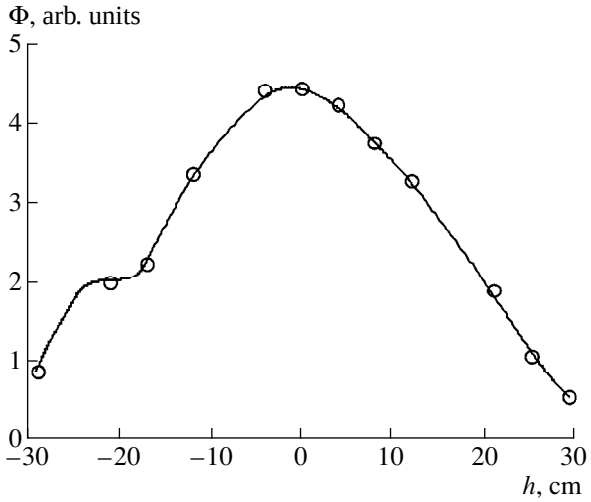

Fig. 3. Profile of $\Phi(h)$ before the disruption related to the density limit in the regime with I_p = 150 kA and $P_{\rm ab}$ = 0.7 MW.

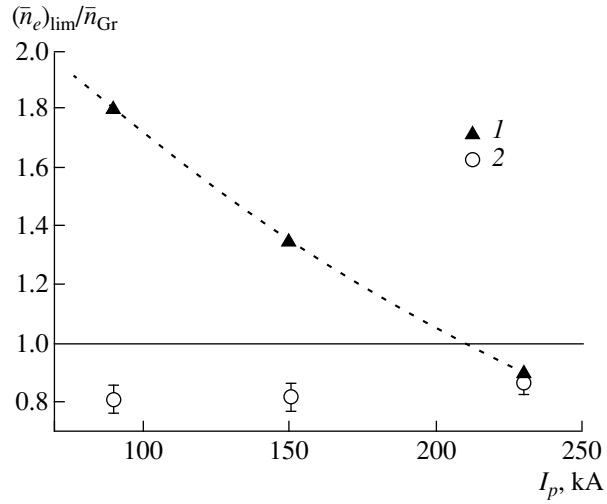

Fig. 4. Dependence of the enhancement factors (*1*) $(\bar{n}_e)_{\rm lim}/\bar{n}_{\rm Gr}$ and (*2*) $(\bar{n}_e)_{\rm lim}/\bar{n}_{\rm Gr}^{\rm mod}$ on I_p.

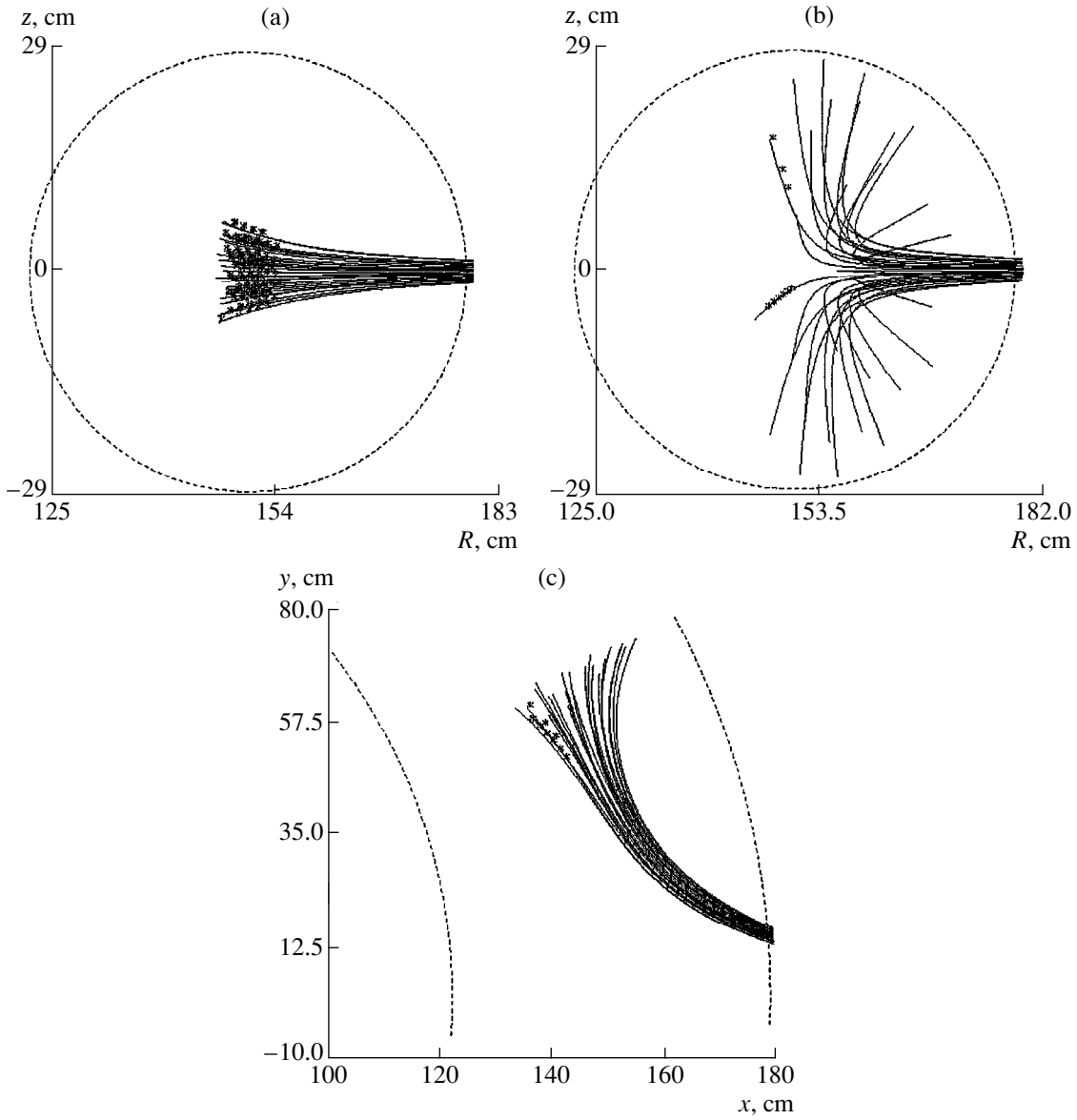

Fig. 5. Results of ray tracing calculations for various plasma densities (Fig. 13, shot no. 24 454) illustrating how the refraction of microwaves increases as the density increases for (a) $\bar{n}_e = 4.9 \times 10^{19}$ m^{-3} $\simeq 0.67(\bar{n}_e)_{\rm lim}$ (Fig. 13b, t = 500 ms) and (b, c) $\bar{n}_e = 6.8 \times 10^{19}$ m^{-3} $\simeq 0.96(\bar{n}_e)_{\rm lim}$ (Fig. 13b, t = 630 ms). The plots present the projections of ray trajectories onto (a, b) meridional and (c) equatorial planes. The asterisks indicate the microwave absorption region.

However, it should be noted that the results of calculations presented in Figs. 5 and 6 are typical for all of the investigated regimes, both for those with $(\bar{n}_e)_{\rm lim}/(\bar{n}_e)_{\rm Gr} = 1.8$ (I_p = 90 kA) and those with $(\bar{n}_e)_{\rm lim}/(\bar{n}_e)_{\rm Gr} \simeq 1$ (I_p = 230 kA). Therefore, it is unlikely that strong microwave refraction near $(\bar{n}_e)_{\rm lim}$ can change the above suggestion about the role of the current radius. Furthermore, the disruption related to the density limit is caused by cooling of the edge plasma, whereas the additional microwave power hinders such cooling. Therefore, it is important that the microwave power be absorbed in the region outside of which the change in the energy balance leads predominantly to cooling of the edge plasma.

3. DETERIORATION OF CONFINEMENT NEAR THE DENSITY LIMIT

Figure 7 shows the time dependences of the density and β_p (which is deduced from the plasma equilibrium)

for regimes with the current I_p = 150 kA. The data are presented for two different scenarios of the density behavior: the rapid growth of $\bar{n}_e$ (Fig. 7a) and the slightly varying density (Fig. 7b). The figure demonstrates the general features that were also observed in all of the other experiments. No matter what scenario of the density growth is used, no decrease in β_p (i.e., the deterioration of confinement) is observed up to $\bar{n}_e \approx 0.9(\bar{n}_e)_{\rm lim}$. Only in the immediate vicinity of the density limit do we see a small degradation of confinement that shows up as a small decrease in β_p by at most 5%, which corresponds to a decrease in the energy confinement time by no more than 10%.

Hence, the results obtained in T-10 show that degradation of confinement does not take place as the density increases up to $\bar{n}_e \approx 0.9(\bar{n}_e)_{\rm lim}$.

4. TWO TYPES OF DISRUPTIONS AT THE DENSITY LIMIT

1. The experiments demonstrate that the plasma behavior depends on the scenario according to which the density grows to $(\bar{n}_e)_{\rm lim}$, which is most clearly seen for ohmically heated plasmas. These data show that there may be two types of disruptions that occur at $(\bar{n}_e)_{\rm lim}$ depending on the scenario of the density growth. In ohmically heated plasmas, the value of $(\bar{n}_e)_{\rm lim}$ is also different for different scenarios $\bar{n}_e(t)$.

Figure 8 illustrates the behavior of the line average density $\bar{n}_e$ and the intensity of the X-ray signal (for the central viewing chord) $I_{\rm SXR}(0)$ for two Ohmic discharges. In the first case (shot no. 22 277), the plasma density grew steadily up to $(\bar{n}_e)_{\rm lim}$. In such a scenario, we observed a disruption of the type that is usual for T-10 and is described in item 3 of Section 2. This type of disruption has the following characteristics:

(i) predominant cooling of the plasma edge, as shown in Fig. 9;

(ii) monotonic growth of the m = 2 MHD-mode, i.e., the broadening of the m = 2 island (Fig. 10) before the disruption; and

(iii) narrowing of the current channel, which is followed by the disruption.

As is seen from Fig. 8, sawtooth oscillations are observed in this regime up to the instant at which the density reaches $(\bar{n}_e)_{\rm lim}$, i.e., until the disruption occurs.

2. In the second case (Fig. 8, shot no. 24 440), the plasma density is kept constant and lower than in the first case (other parameters being the same). However, ~200 ms after the density arrives at the plateau, a disruption occurs. Hence, in this scenario, the density limit $(\bar{n}_e)_{\rm lim}$ turns out to be lower (by 15%) than in the previous case (shot no. 22277).

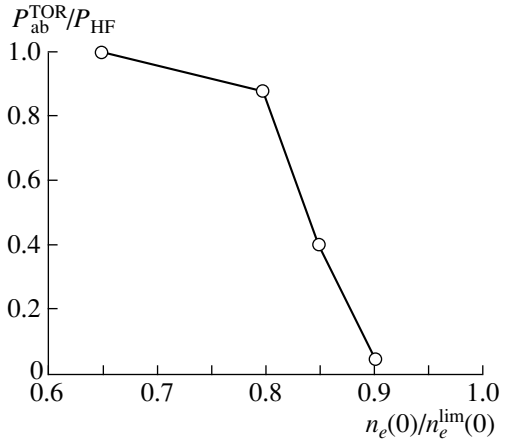

Fig. 6. A decrease in the single-pass microwave absorption with increasing plasma density (Fig. 13b, shot no. 24454). $P_{\rm ab}^{\rm TOR}$ is the power absorbed during a single pass, $P_{\rm HF}$ is the input power, $n_e(0)$ is the central plasma density, and $n_e^{\rm lim}(0)$ is the central density for $(\bar{n}_e)_{\rm lim}$ (Fig. 13b, instant *4*).

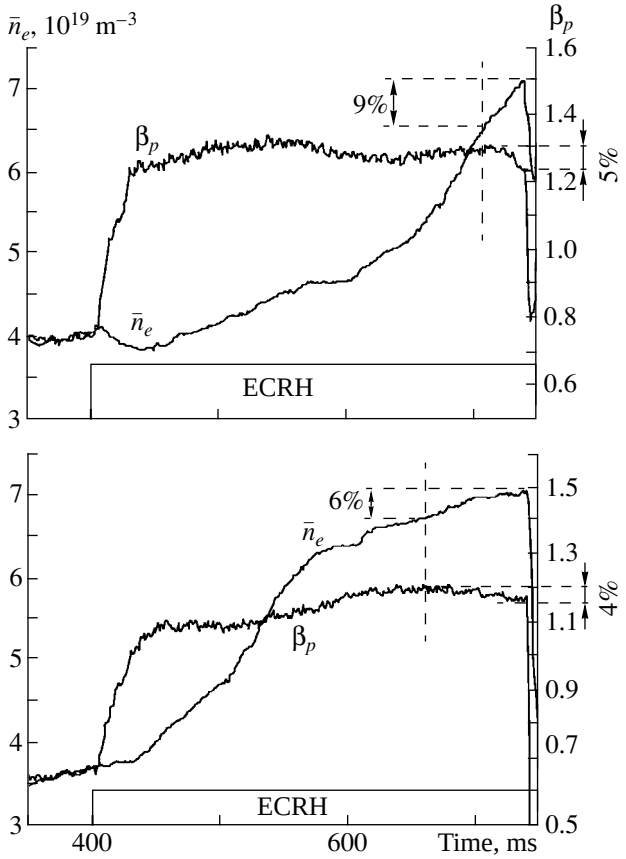

Fig. 7. Variations in β_p near the density limit $(\bar{n}_e)_{\rm lim}$ in the regime with I_p = 150 kA. The data are presented for two different scenarios of the density growth ($\bar{n}_{\rm Gr} = 5.3 \times 10^{19}$ m^{-3}). The upper plot presents shot no. 24189 ($P_{\rm ab}$ = 0.8 MW); the lower plot presents shot no. 24 454 ($P_{\rm ab}$ = 0.6 MW).

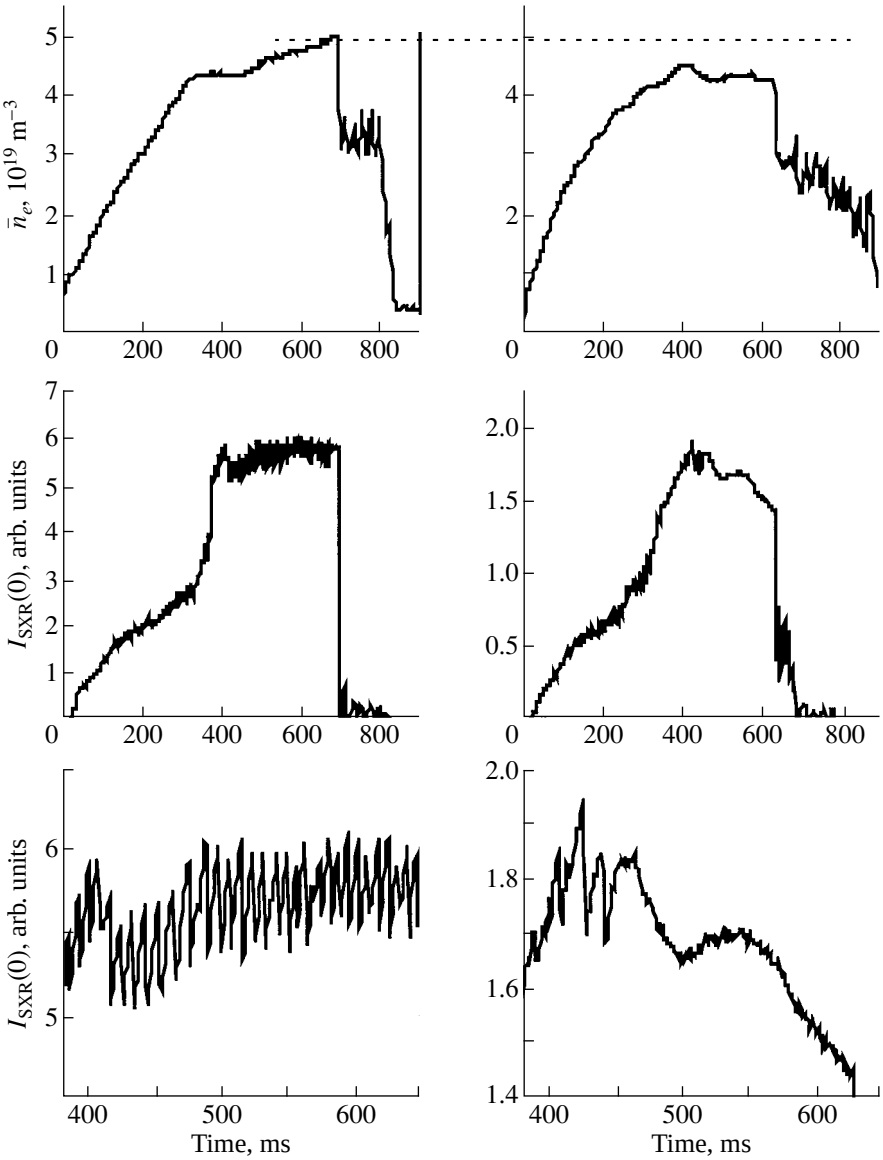

Fig. 8. Traces of $(\bar{n}_e)_{lim}$ and $I_{SXR}(0)$ for different scenarios of the density growth $\bar{n}_e(t)$ for ohmically heated plasmas (I_p = 150 kA). The left plots present shot no. 22 277; the right plots present shot no. 24440.

The characteristic features of the scenario with a constant density in ohmic discharges are the following.

(i) A comparison of the radiation power P_{rad}, the loop voltage V_0, and the intensities of the D_α and C_{III} lines shows that, by the instant at which the density reaches $(\bar{n}_e)_{lim}$, these values are even lower than in the case of growing density (shot no. 22277). Therefore, there were no additional changes at the edge that might lead to a disruption.

(ii) At 300 ms (Fig. 8, shot no. 24440), the intensity $I_{SXR}(0)$ of X-ray emission from the center of the plasma column sharply increases, which is characteristic of the transition to the so-called B-mode [5], which is characterized by improved impurity confinement. The accumulated impurities expel a fraction of the current from the plasma core. As a result, the sawtooth oscillations disappear (see Fig. 8). This suggests that, in the regime with a constant density, the current density profile flattens in the plasma core.

As is seen in Fig. 8, the transition to the B-mode also occurs in shot no. 22277. However, the subsequent density growth suppresses impurity accumulation, and the sawtooth oscillations take place up to the disruption.

(iii) Figure 11 demonstrates the time dependences of the amplitude and frequency of the $m = 2$ and $m = 3$ MHD modes in the regime under consideration.

We can see that, unlike the regime with the usual type of disruption, the phase of gradual growth of the $m = 2$ mode near $(\bar{n}_e)_{\lim}$ does not occur. A sharp increase in both the $m = 2$ and $m = 3$ modes is observed only during the disruption. Note that, before the disruption, the frequency of the modes changes only slightly; i.e., locked modes cannot cause the disruption in this case.

In addition to the aforesaid, we note that, although the density limit $(\bar{n}_e)_{\mathrm{Gr}}$ in this regime turns out to be lower, it is high enough to suggest that the predominant cooling of the edge plasma begins. The contraction of the current channel at the edge takes place simultaneously with the flattening of the current density in the core, which suggests that this type of disruption can be related to the instability of the current profile against the $m = 2$ and $m = 3$ MHD-modes.

3. Calculations of the MHD-instability parameter Δ' show that the initial profile is unstable against the $m/n = 2/1$ mode with $\Delta'\rho_S = 2.14$, where $\rho_S = r_S/a_L = 0.53$, with r_S being the radius of the $q = 2$ magnetic surface. The other MHD modes are stable. When the current profile is flattened in the central region corresponding to an increase in $q(0)$ to 1.08, the value $\Delta'\rho_S$ for the $m = 2$ mode doubles and the $m/n = 3/2$ mode ($\Delta'\rho_S = 0.02$ for $\rho_S = 0.39$) becomes unstable. Apparently, the value of $\Delta'\rho_S$ for the $m/n = 3/2$ mode is small. However, there is a pronounced tendency for this mode to be more unstable as the current profile in the core flattens. Calculations show that the flattening of the current profile in the plasma core affects the stability of MHD modes more strongly than a small narrowing of the current channel. These results do not contradict the above suggestion but, at the same time, cannot be regarded as support for our hypothesis because variations in $\Delta'\rho_S$ are relatively small.

4. Based on the above said, we can suggest that the different plasma behaviors in the scenarios with growing and almost constant densities can take place only in ohmically heated plasmas. This difference should disappear if the ECRH power is sufficiently high. Note that all of the experiments under discussion were carried out using the electron-cyclotron current drive in the direction of the Ohmic current in order to prevent the disappearance of sawtooth oscillations and the flattening of the current profile in the plasma core. Indeed, first, switching on the microwave power in the regime where $\bar{n}_e$ was constant and the disruption was related to the density limit prevented the disruption; in this case, the sawtooth oscillations remained to the end of the discharge. Second, as is seen in Fig. 12, at the maximum value of microwave power $P_{\mathrm{ab}} \simeq 0.8$ MW, the density limit $(\bar{n}_e)_{\lim}$ was the same both for the growing and almost constant densities. Nevertheless, different plasma behaviors in the plasma core (i.e., either an increase in the period T_s of sawtooth oscillations or the

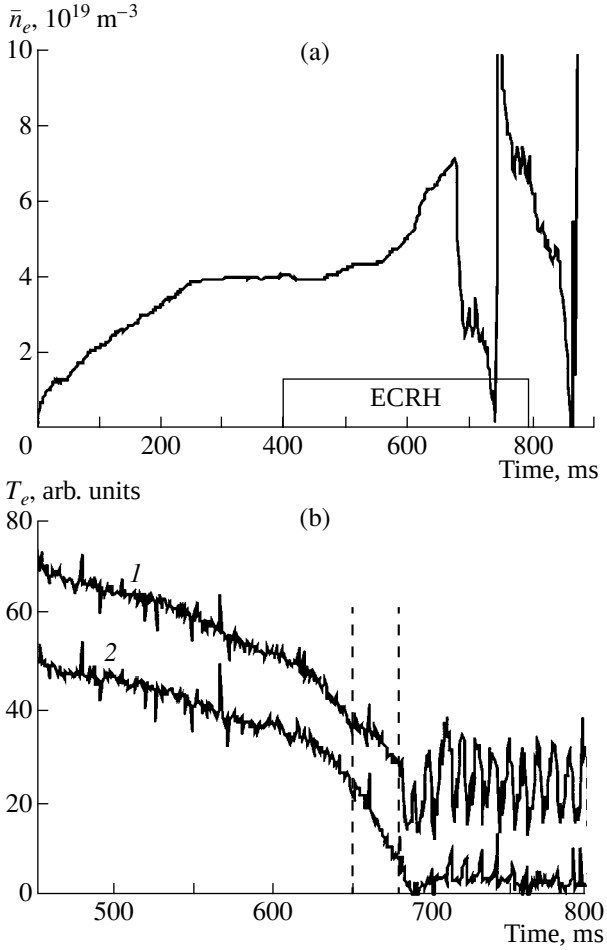

Fig. 9. Predominant cooling of the edge plasma in the regime with a growing density: time dependences of (a) the line average density and (b) electron temperature (ECE measurements) at r = (*1*) 2.7 and (*2*) 14.4 cm (shot no. 24190, I_p = 150 kA, P_{ab} = 0.8 MW). The dashed lines indicate the time interval from the beginning of cooling to the instant of disruption.

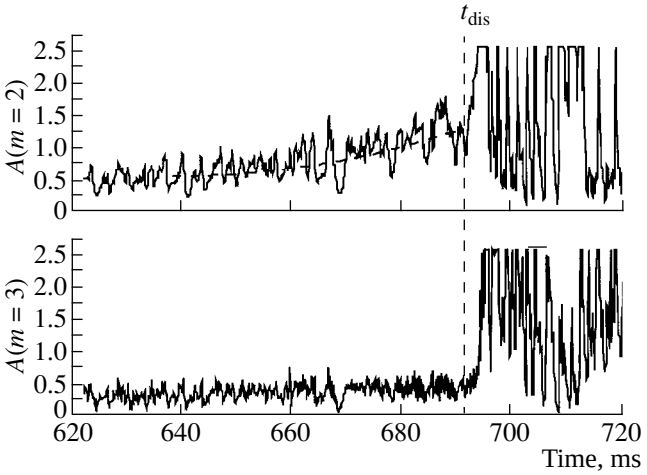

Fig. 10. The growth of the $m = 2$ island before the disruption; t_{dis} is the instant of disruption; $A(m = 2)$ and $A(m = 3)$ are the amplitudes of the $m = 2$ and $m = 3$ MHD modes (Fig. 8, shot no. 22277).

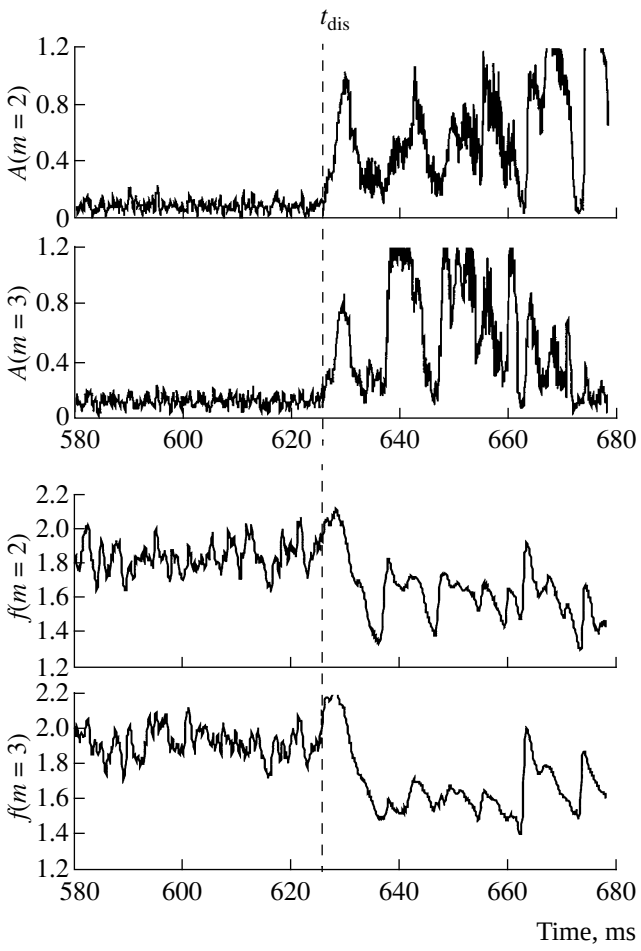

Fig. 11. Time evolutions of the amplitude A and frequency f (in arb. units) of the $m = 2$ and $m = 3$ MHD modes in the scenario with a constant density (Fig. 8, shot no. 24440).

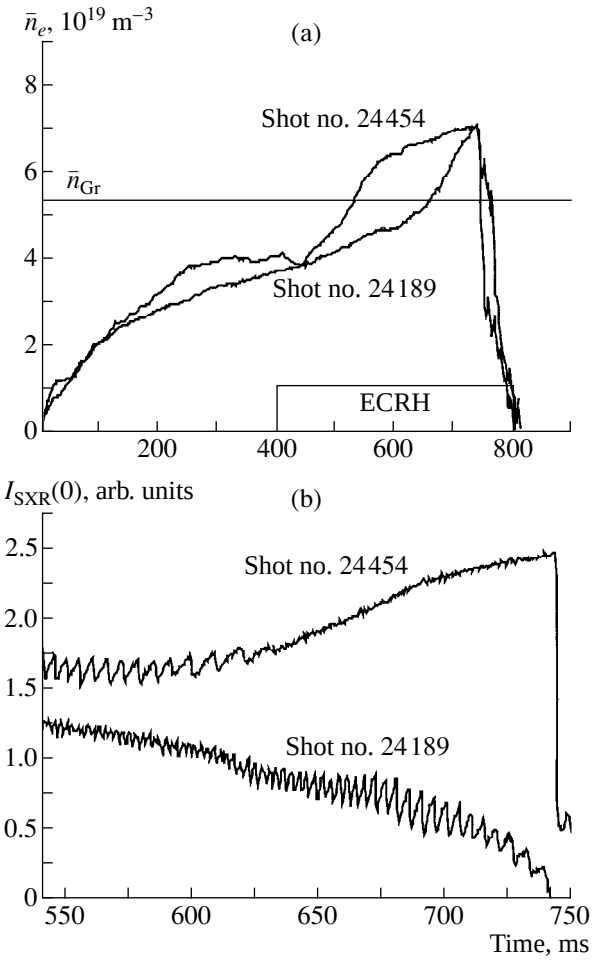

Fig. 12. Time evolutions of (a) the density $\bar{n}_e$ and (b) X-ray signal during ECRH for different scenarios of the density growth at I_p = 150 kA and P_{ab} = 0.8 MW.

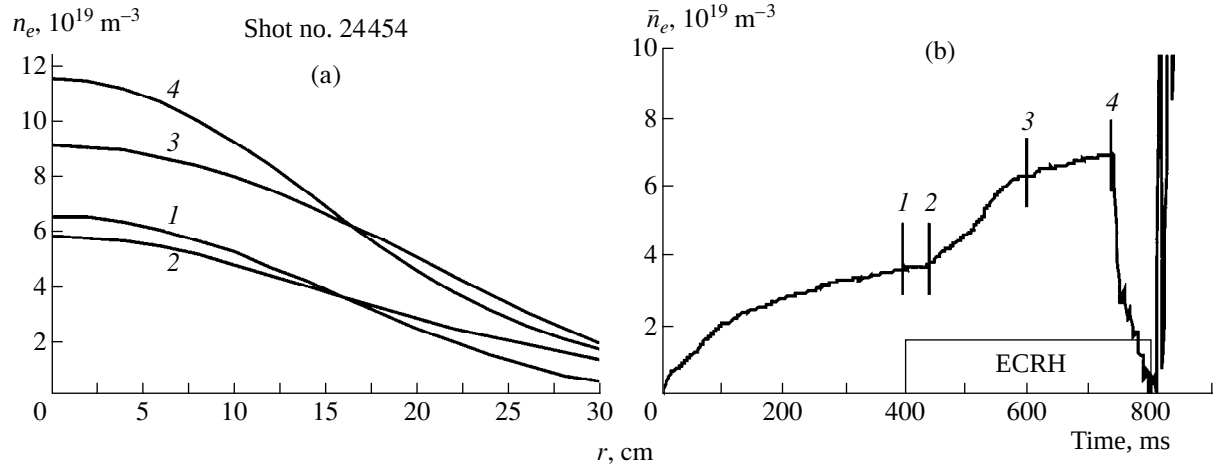

Fig. 13. (a) Evolution of the plasma density profile as the line average approaches $(\bar{n}_e)_{lim}$ and (b) time behavior of $\bar{n}_e$ (shot no. 24454, I_p = 150 kA, P_{ab} = 0.6 MW). The density profiles in plot (a) are shown for the instants marked in plot (b).

disappearance of them near the density limit ($\bar{n}_e)_{\rm lim}$) were observed (see Fig. 12b).

5. Figure 13a shows the plasma density profiles for different instants indicated in Fig. 13b. It is seen that, as the density approaches the limiting value, the profile $n_e(r)$ becomes more peaked. As a result, before the disruption, the density at the edge near the limiter is lower than it was150 ms before. It follows from here that the edge density probably is not an adequate characteristic of the density limit.

5. CONCLUSIONS

(i) In T-10 experiments with gas puffing and an ECRH power $P_{\rm ab}$ up to 0.85 MW, it is found that the ratio $(\bar{n}_e)_{\rm lim}/\bar{n}_{\rm Gr}$ of the density limit to the Greenwald limit depends on q_L. The value of $(\bar{n}_e)_{\rm lim}/\bar{n}_{\rm Gr}$, which attains 1.8 for $q_L = 8.2$, drops to ~1 for $q_L \approx 3$.

(ii) The fact that the value of $(\bar{n}_e)_{\rm lim}/(\bar{n}_e)^{\rm mod}_{\rm Gr}$ is independent of q_L (when the current radius a_C is used instead of the limiter radius a_L) apparently suggests that our attempts to exceed the physical limitations that underlie the Greenwald limit did not succeed in T-10 experiments with gas puffing and high-power ECRH.

(iii) No substantial (>10%) degradation of plasma confinement was observed up to $\bar{n}_e \sim (\bar{n}_e)_{\rm lim}$.

(iv) Depending on the scenario of plasma density growth, two types of disruptions related to the density limit were observed in T-10.

ACKNOWLEDGMENTS

This work was supported in part by the Ministry of Atomic Energy of the Russian Federation (agreement no. 69F) and the Ministry of Science and Technology of the Russian Federation (under the federal program “Controlled Fusion and Plasma Processes”).

REFERENCES

1. V. V. Alikaev, A. A. Bagdasarov, A. A. Borschegovskij, *et al.*, in *Proceedings of the 17th EPS Conference on Plasma Physics and Controlled Fusion, Amsterdam, 1990*, Vol. 14B, Part III, p. 1080.
2. M. Greenwald, J. L. Terry, S. M. Wolfe, *et al.*, Nucl. Fusion **28**, 2199 (1988).
3. G. V. Pereverzev, P. N. Yushmanov, A. Yu. Dnestrovskij, *et al.*, Report No. IAE-5358/6 (Kurchatov Institute of Atomic Energy, Moscow, 1992).
4. R. H. Cohen, Phys. Fluids **31**, 421 (1988).
5. V. V. Alikaev, A. A. Bagdasarov, E. L. Berezovskij, *et al.*, Plasma Phys. Controlled Fusion **30**, 381 (1988).

Translated by N. Larionova